Numerical Investigation of Thermo-acoustic Instabilities Using Detailed Chemistry Approaches

A thesis accepted by the Faculty of Aerospace Engineering and Geodesy of the University of Stuttgart in partial fulfillment of the requirements for the degree of Doctor of Engineering Sciences (Dr.-Ing.)

by

Antonio Filosa

born in Formia

main referee:	Prof. Dr.-Ing Manfred Aigner
co-referee:	Prof. Dr.-Ing Franz Joos
Date of defence	01/09/2016

Institute of Combustion Technology for Aerospace Engineering
University of Stuttgart

2017

Acknowledgments

At the end of my thesis, I would like to acknowledge all the people I got to know in this important period of my life, who helped me to growth both from an intellectual and human point of view.

I want to thank Prof. Dr.-Ing M. Aigner for providing me with the opportunity to complete my PhD thesis at the Institute of Combustion Technology in Stuttgart. I especially want to thank my advisors on the spot, Dr.-Ing habil B. Noll and Dr.-Ing Di Domenico, whose support and guidance made my thesis work possible. They have been actively interested in my work and have always been available to advise me. I am very grateful for their patience, motivation, enthusiasm and immense knowledge in the field of turbulent-combustion.

I thank all the people working in the THETA-group and in other departments for their constant friendly support and for the useful scientific discussions. A special thanks for Bastian, Yann and Alex for the good times we spent together enjoying the taste of italian coffees.

I would also like to say a heartfelt thank you to my Mum, Dad and Sister for always believing in me and encouraging me to follow my dreams. They deserve a warm and special acknowledgment for their love and care. Vi Voglio BENE!

I am also extremely indebted to all my Stuttgart-friends: Ivano, Paola, Mauro, Andrea, Simone, Eleonora, Ekaterina, Giovanna, Mohammed, Maher, for helping in whatever way they could during this challenging period!!!Grazie Ragazzi!

Contents

List of Figures

List of Tables

Nomenclature

Roman symbols

A_r, E_{a_r}, $\Re$	pre-exponential factor, activation energy, universal gas constant
$\tilde{c}$	progression variable
CD	cross diffusion
C_{D1}, C_{D2}, C_{EDC}	constants for the EDC model
C_1, C_2, C_3 C_μ	constants for the $k-\varepsilon$ model
$C_{\varepsilon 1}$, $C_{\varepsilon 1}$	constants for the $k-\varepsilon$ model in the Low-Re formulation
C_λ, B_λ, A_λ	constants in the k_θ-ε_θ model
C_{P1}, C_{P2}, C_{D1}, C_{D2}	constants for the $k_\theta - \varepsilon_\theta$ model
C_p	specific heat
c_p	specific heat capacity
C_s	Smagorinsky constant
C_w	Wale constant
D,H,W	geometrical parameters: depth, height, width
D_i	diffusion coefficient for the species i
f	frequency
F_1,F_2	blending functions
$f_{\varepsilon 1}$, $f_{\varepsilon 2}$, f_μ	damping functions for the $k-\varepsilon$ model in the Low-Re formulation
f_{P1},f_{P2},f_{D1},f_{D2},f_λ	Damping functions expressions for the AKN or DWX model in the Low-Re formulation
h	specific enthalpy
h	heat transfer coefficient
I	turbulent intensity

k	turbulent kinetic energy
k_f, k_b	forward and backward rate constant
k_θ	temperature fluctuation
L	integral length scale
L_{VK}	Von Karman length scale
l_{mix}	characteristic length
L_t	turbulent length scale
M	molecular weigth
$\dot{m}$	mass flow
N_η, γ_η	number of subgrid dissipative eddies generated in each cell, ratio between N_η and the total number of scales generated locally
p	pressure i
$\mathcal{P}_{\varepsilon_\theta}$, $\tilde{\mathcal{P}}$, $\mathcal{P}_\theta$	production term in the ε_θ equation, production rate due to the mean shear, production rate due to the temperature
P_k	production term in the k equation
Pr,Pr_t	Prandtl number and turbulent Prandtl number
$\dot{q}$	heat flux
R	geometrical parameter: radius
R	time scale ratio between τ_t and τ_θ
Re	Reynolds number
RR	reaction rate
R_T	Pope factor
R_T, R_y	dimensionless parameters in the Low-Re formulation
Sc	Schmidt number
S_{ij}	mean strain rate tensor
S_T	turbulent burning velocity
S_w	swirl number
t	time
T	temperature

t_η	Kolmogorov time scale
T_f	sufficiently long time for the RANS averaging
t_j	pressure tensor
t_L	integral time scale
T_{P0}	Temperature in the cell point next to the surface
T_{sol}	Temperature of the outer wall in the solid region
$\mathbf{U}$	velocity vector of a fluid element
e	specific internal energy
u_η	Kolmogorov velocity scale
u_{mix}	characteristic velocity
u_τ	skin friction velocity
$\mathbf{x}$	position vector of a fluid element
Y_i	species mass fraction of i-component mixture
y^+, u^+	dimensionless wall distance and velocity
y^*	dimensionless wall distance based on the Kolmogorv velocity scale

Greek letters

α_t	turbulent diffusivity
β_k	constant for the $k-\omega$ model
χ_p, χ_{lim}	vortex shedding invariant and limiter
σ_k, σ_ε	constants for the $k-\varepsilon$ model
σ_k, σ_ω	constants for the $k-\omega$ model
$\widehat{\zeta}$, σ_ϕ	constants for the SST-SAS $k-\omega$ model
$\delta_{0.5}$	spreading rate
δ	dimension of the boundary layer
Δ_g	filter size
ε_θ	dissipation rate of the temperature fluctuations
η	Kolmogorov length scale
γ	length of the fine scale
γ_h	heat capacity ratio

κ	thermal conductivity
κ_V	Von Karman costant
λ	air excess ratio
λ_s	frequent of stirring event
μ	molecular dynamic viscosity
μ_t	turbulent dynamic viscosity
ν	molecular kinematic viscosity
ν_t	turbulent kinematic viscosity
Ω	vorticity
ω	specific dissipation rate
ω_i	source term for the species i
$\overline{\Omega}_{ij}$	mean rotation tensor
ω_θ	specific dissipation rate of the temperature fluctuations
ϕ	generic variable
ρ	density
Ω_s	invariant measure of the strain rate
σ_T	temperature variance
τ_{ij}	sspecific Reynolds-stress tensor
τ_t	turbulent heat transfer time scale
τ^*	residence time in the fine scale
τ_t	turbulent time scale
τ_t	characteristic time scale related to k_θ and ε_θ
τ_w	wall shear stress
ε	dissipation rate of the turbulent kinetic energy

Abbreviations

AKN	Abe Kondoh Nagano model
AKN_t	Abe Kondoh Nagano thermal model
DWX	Deng et al. model
EDC	Eddy Dissipation Concept Model

EDM	Eddy Dissipation Model
FM	Fractal Model
HB	Huag-Bradshaw model
IRZ	Inner Recirculation Zone
LB	Lam Brenhorst model
$N-S$	Navier Stokes
ORZ	Outer Recirculation Zone
PDF	Probability Density Function
PIV	Particle Image Velocimetry
$PLIF$	Planar Laser Induced Fluorescence
PVC	Precessing Vortex Core
$RANS$	Reynolds-Averaged Navier Stokes
SST	Shear Stress Traspost model

Zusammenfassung

Die numerische Untersuchung turbulenter reagierender Strömungen ist heutzutage für Gasturbinenanwendungen von großer Bedeutung. Sie trägt auch dazu bei, die Anzahl erforderlicher Tests für das Brennkammerdesign und für Optimierungen der Brennkammer zu reduzieren. Neue Verbrennungskonzepte müssen entwickelt werden, um die Schadstoffemissionsanforderungen für eine Bandbreite von Bedingungen zu erfüllen. Einer der Abstriche zur Erzielung geringer Emissionen insbesondere im Falle magerer, vorgemischter Verbrennung sind Instabilitäten, welche zu Strukturvibrationen, erhöhtem Wärmeübergang, Verlöschen und Flammenrückschlag führen können. Verbrennungsinstabilitäten sind selbsterregte Druckfluktuationen, die durch instationäre Verbrennung auftreten, wenn Druck- und Wärmefreisetzungsschwankungen in der Brennkammer wechselwirken. Besonders akustische Schwingungen verursachen Fluktuationen der Wärmefreisetzungsrate und transportieren damit Energie ins akustische Feld.

Um das Wissen über selbsterregte Schwingungen im Verbrennungsprozess zu vertiefen und um die möglichen Effekte in der Brennkammer zu untersuchen, wurde von Jim Kok et al. [5, 6] ein akademischer Modellbrenner entworfen, der ein verbrennungsgetriebenes Rijke Rohr abbildet. Dieser Brenner wurde im Rahmen des von der EU geförderten Projektes „LIMit cycles of thermoacOUstic oscillationS in gas turbINE combustors“ - abgekürzt „LIMOUSINE“ - untersucht. Aufgrund ihrer Geometrie können in der Brennkammer selbsterregte Schwingungen des Druckfeldes infolge der Rückkopplung zwischen Akustik und Verbrennung auftreten. In der vorliegenden Arbeit wurde die Brennkammer numerisch untersucht.

Experimentell wurde das akustische Verhalten des Brenners unter stabilen und instabilen Bedingungen bestimmt, indem die Druckschwankungen an verschiedenen Positionen aufgenommen wurden. Die Flammenfront und die Verbrennungszone wurden mittels OH* Chemilumineszenz erfasst. Zusätzlich wurden Temperaturwerte der Gasphase anhand der Coherent Anti-Stokes Raman Scattering (CARS) Technik aufgenommen.

Mit dem Ziel das dynamische Verhalten des LIMOUSINE Brenners genau vorherzusagen wurden mehrere numerische Ansätze mit unterschiedlichen Modellen detaillierter Verbrennungschemie (Fractal Model *FM*, Eddy Dissipation Concept Model *EDC*) und thermische Modelle (Abe et al. AKN_t, Huag and Bradshaw HB model) in den DLR Verbrennungscode

THETA implementiert. Die Modelle wurden zunächst anhand einfacher Testfälle für stationäre und dann für instationäre Bedingungen validiert. Für die numerische Verifizierung der Verbrennungsmodelle wurden Simulationen einer Strahlflamme (H3-Flame [7]) sowie eines Drahlbrenners für kleine Industriegasturbinen im realen Maßstab durchgeführt (G30-Dry Low Emission Combustor [8]).

Um die Leistungsfähigkeit der thermischen Modelle zu verstehen, wurden verschiedene Berechnungen zur Vorhersage der Wärmeübertragung in einer Kavität, in einer Rohrerweiterung, in einer rückspringenden Stufe sowie in einer oszillierenden Strömung durchgeführt [9]. Die zuletzt genannte Strömung wurde untersucht, um den erhöhten Wärmeübergang unter instationären Bedingungen nachzuweisen. Die numerischen Ergebnisse haben eine verbesserte Genauigkeit der berechneten übertragenen Wärme bei Verwendung der thermischen Modelle gezeigt.

Um das akustische Verhalten des LIMOUSINE Brenners beim Auftreten thermo-akustischer Schwingungen zu simulieren, wurden unterschiedliche numerische Simulationen durchgeführt. Zunächst wurde eine einfache Berechnung mit globaler Chemie durchgeführt (Eddy Dissipation Model *EDM*). Dann wurden Berechnungen mit detaillierter Chemie (Eddy Dissipation Concept model *EDC*) und dem thermischen Modell von Huag and Bradshaw (*HB* Modell) realisiert.

Die Berechnung mit dem *EDC* Verbrennungsmodell zeigt eine verbesserte Darstellung der akustischen Charakteristika verglichen mit dem *EDM* Modell. Im Einzelnen wurden Frequenzen von 250Hz mit dem *EDM* bzw. 185Hz mit dem *EDC* Modell ermittelt. Der letztgenannte Wert zeigt eine gute Übereinstimmung mit der experimentell bestimmten Frequenz von 181Hz. Des weiteren wurden Simulationen mit dem *EDC* Modell in Verbindung mit dem *HB* Modell für einen weiteren Betriebspunkt durchgeführt. Das Hauptziel dabei war es, den Einfluss detaillierter Chemie und instationärer Wärmeübertragung auf das akustische Verhalten zu bewerten. Die Ergebnisse zeigten abermals, dass die Verwendung detaillierter Chemie erforderlich ist, um die Akustik in der Brennkammer genau zu simulieren. Zudem zeigten sie, dass der instationäre Wärmeübergang mit dem thermischen *HB* Modell von Huag und Bradshaw unter Berücksichtigung einer nicht konstanten turbulenten Prandtl-Zahl besser simuliert wird.

Abstract

The numerical investigation of turbulent reacting flows in gas turbine related configurations is nowadays of high interest. This contributes to reduce the number of tests required for the design and for the optimization of the combustion chamber. New combustion concepts must be developed in order to meet the requirements concerning the pollutant emission in a wide range of conditions. One of the trade-off for achieving low emissions is represented by instabilities especially in the lean premixed combustion, which can lead to structure vibration, enhancement of heat transfer, blow-off and flame flash back. Combustion instabilities are self-excited pressure fluctuations which occur during unsteady combustion, where pressure and heat release oscillations interact in the combustion chamber. Here, in particular acoustic oscillations drive the heat release rate to fluctuate and thus to feed energy to the acoustic field.

In order to gain more knowledge on self-excited oscillations in a combustion process and to study the possible effects that this may generate in the burner, an academic model combustor was designed to represent a combustion-driven Rijke tube by Jim Kok et al. [5, 6]. This combustor was investigated under the EU-funded project “LIMit cycles of thermoacOUstic oscillationS in gas turbINE combustors”, abbreviated as "LIMOUSINE". Due to its geometry, self-excited oscillations of the pressure field can occur in the combustor as a result of the closed feedback between acoustics and combustion. In the present work a numerical study of this combustor was performed.

Experimentally, the acoustic behaviour of the combustor was determined under stable and unstable conditions, recording the pressure oscillations at different positions. The flame front and the combustion region were detected by mean of the OH* chemiluminescence technique. Additionally gas-phase temperature values were taken using the Coherent Anti-Stokes Raman Scattering (CARS) technique.

With the intent to predict accurately the dynamics behavior of the LIMOUSINE combustor, several numerical tools consisting of various detailed chemistry combustion models (Fractal Model FM, Eddy Dissipation Concept Model EDC), and ad-hoc thermal methods (Abe et al. AKN_t, Huag and Bradshaw HB model) were implemented in the DLR combustion code THETA. The models were validated first with simple test-cases for steady and

then for unsteady conditions. For the numerical verification of the combustion models, simulations were performed considering a jet flame test case (H3-Flame [7]) and a real scale swirl combustor for small industrial gas turbines (G30-Dry Low Emission Combustor [8]).

To elucidate the performance of the thermal models instead, various computations were carried out to predict the heat transfer in a cavity, in a pipe expansion, in a backward facing step and also in an oscillating flow [9]. The latter was investigated in order to prove the heat transfer enhancement in unsteady conditions. The numerical results have shown an improvement of the accuracy of the heat transfer when the thermal models are used.

In order to simulate the acoustic behaviour of the LIMOUSINE combustor under thermo-acoustic oscillations, various numerical simulations were performed. First, a simple calculation was run with global chemistry (Eddy Dissipation Model *EDM*). Later computations with detailed chemistry (Eddy Dissipation Concept Model *EDC*) and with the thermal model (Huag and Bradshaw *HB* model) were carried out.

The computation with the *EDC* combustion model shows an improvement in the determination of the acoustic characteristics (in terms of acoustic frequency and amplitude of oscillations) compared to the case with the *EDM*. In detail, a main frequency of 250Hz and 185Hz was found with the *EDM* and *EDC* respectively. The latter is in good agreement with the experimental value of 181Hz. Furthermore, simulations at a different operative condition were performed using the *EDC* in conjunction with *HB* (Huag and Bradshaw *HB* model). The main goal was to assess the influence of detailed chemistry and unsteady heat transfer on the acoustic behaviour. The results show again that the use of detailed chemistry is necessary to simulate accurately the acoustics of the combustor. Also the unsteady heat transfer is better predicted by considering a non-constant turbulent Prandtl number using the Huag and Bradshaw *HB* thermal model.

1 Introduction and Motivation

Combustion instabilities constitute a key issue for the next generation of gas turbines as they can deteriorate the combustion process and even represent a severe threat for the structure lifetime. Lean premixed combustion is required to reduce NOx emissions and it is well known that lean premixed combustion can produce acoustic oscillations in the combustion chamber. These oscillations can also result in other effects as the enhancement of heat transfer, blow-off and flash-back. These instabilities are excited through a feedback loop between several combustion processes and one of the natural modes of the structure [10]. In this loop, for example, the fluctuation in the velocity field produces an oscillation in the heat release rate which, in turn, excites the acoustic oscillations and these acoustic oscillations finally close the loop by driving the velocity perturbations [4]. The causes of these mechanisms are not completely known yet and a more in depth research is needed. The study of the heat transfer occurring during a cycle of a pressure oscillation has not been sufficiently investigated so far, even though it represents an important issue for the thermal load of the combustor liner and it will give more insights on the heat loss of combustion in a chamber. Thus the pressure fluctuations can generate a perturbed thermal boundary layer which can lead to a thermal fatigue and, consequently, to the failure of the combustor liner.

A model combustor has been designed and built in the framework of the EU-funded project LIMOUSINE to study the self-excited oscillation in an academic configuration [5, 6, 11, 12]. The LIMOUSINE burner is basically similar to the Rijke tube (an open cylinder resonator) with heat transfer. It operates with one end closed, turning heat into sound by creating a self-amplifying standing wave. This phenomenon was first described in 1850 by the German physicist Karl Friedrich Julius Sondhauss [13] and explained mathematically by Lord Rayleigh in 1896 [14].

In order to investigate these problems, some numerical tools were implemented in the DLR-THETA code for evaluating accurately the behavior of the burner under unstable combustion. To achieve this point, an appropriate estimation of the thermal field in the center region and near the wall is necessary. Its prediction depends in fact, on the accuracy of the turbulent-combustion models in modeling the right turbulent-chemistry interactions, flame heat release rate and wall regions. It is necessary therefore to consider detailed chemistry

mechanisms and thus, combustion models that can handle a large number of species and chemical reactions. On the other hand, the wall heat transfer is influenced by all the characteristics of the turbulent boundary layer, which must be modeled with ad-hoc thermal models. The main aim of this work is therefore to get a better insight into the dynamics of the thermo-acoustic instabilities and the heat transfer process through the coupling of both the numerical methods, combining the effects of the detailed turbulent-combustion models with the efficient estimation of the near-wall region. Summarizing, to model appropriately the acoustic behavior of the burner and the corresponding wall heat transfer, the following models have to be used:

1. a turbulent combustion model that accounts for detailed chemistry mechanism for the fuel oxidation in air;

2. a thermal model for evaluating the temperature fluctuation variance without the assumption of a constant turbulent Prandtl number;

3. a model capable of determining conjugate wall heat transfer.

A brief description of the physical problems that arise in the combustor during thermo-acoustic instabilities and the numerical strategies adopted to model them within the present work is presented in Fig.1.0.1.

The present work is divided into 7 sections. In each section the validation of the considered models for turbulent-combustion or wall heat transfer will be presented. More in detail, in Chapter 2 a brief description of the most promising techniques for solving turbulent reacting flows and a literature overview of turbulent boundary layer modeling in oscillating flows are presented. It is pointed out the state of the art for both turbulent and combustion modeling, with a large description of the combustion models that have been implemented. Three new turbulence-combustion models were investigated and later implemented: Eddy Dissipation Concept (EDC) [15],[16], Fractal Model (FM) [17],[18] and an extension of the Linear Eddy Mixing Model (LEM) [7] for solving the turbulent-chemistry interaction. The models are based on the turbulent kinetic cascade of Kolmogorov and assume that the reactions occur in the dissipative region of the spectrum, called "fine structures". These structures can be treated like a Perfectly Stirred Reactor (PSR) assuming a constant pressure. The dimension of the fine structure γ is normally only a part of the numerical cell, therefore a modeling for this structure is required. Once known the relative size, this information can be used for evaluating the turbulent-chemistry interaction. To solve the PSR reactor equations, a stiff solver was implemented in the DLR-THETA combustion code.

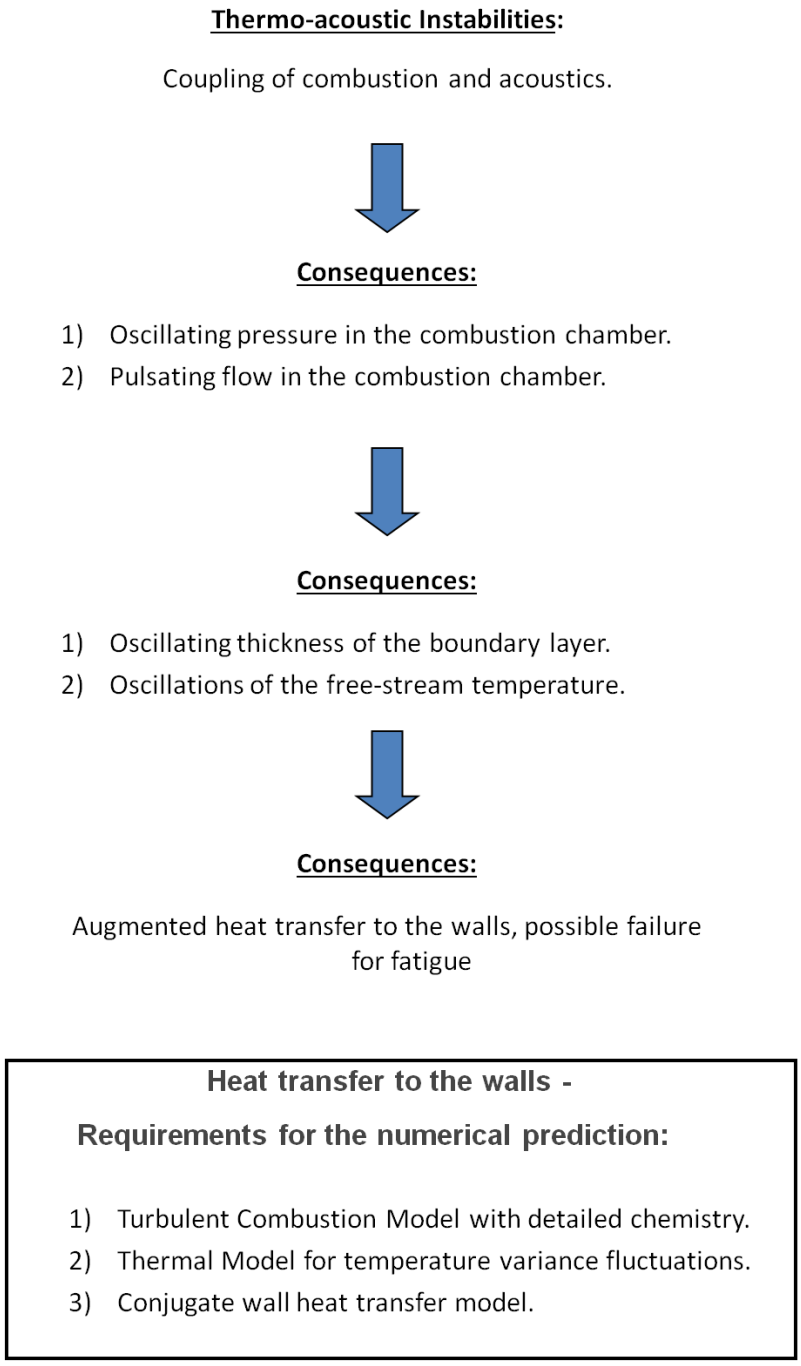

Figure 1.0.1: Thermo-acoustic instabilities and its consequences, as well as suited numerical models.

A numerical validation of the PSR reactor model for a 0D case is reported in Chapter 3. Here an initial discussion of the oxidation mechanisms used in this work is provided and eventually, the results obtained from the stiff-solver are compared in terms of the time-ignition delay for the hydrogen-air and methan-air system with both a direct-integration (non-stiff)

solver and the CANTERA software [19].

In Chapter 4 the ability of these combustion models for simulating turbulent combustion problems is investigated. A first test case considered for the validation of the models is a non-premixed, turbulent hydrogen-air flame, the H3-jet flame, which is a standard test case of the Turbulent Non-Premixed Flame 'TNF' workshop [7],[20]. A second test case is a typical gas-turbine combustor configuration, the GT burner G30 DLE (Dry Low Emission) developed by Siemens Industrial Turbomachinery in Lincoln, UK [8],[21]. This is a real-size industrial burner that operates at a thermal power of 1MW. The aim was to examine the capability of the URANS/LES SAS approach and of various combustion models for the prediction of turbulent swirling flows.

Chapter 5 deals, instead, with the theory and the numerical validation of the thermal models developed by Abe et al. (AKN_t) [22] and by Huag and Bradshaw (HB) [23]. These approaches are able to consider the turbulent boundary layer in near-wall regions, solving for the temperature fluctuation variance equation and its dissipation or specific dissipation rate. The models can predict in fact, the turbulent Prandtl number and, thus, the turbulent heat fluxes generated close to the solid boundary. Different test cases for stationary conditions are presented with the intent to investigate the ability of the AKN_t and HB thermal model to predict the wall heat transfer under different configurations and conditions, such as the heat transfer predictions in a cavity, in a pipe expansion, in a backward facing step and finally in oscillating flows.

The last chapter treats numerical investigations of the thermo-acoustic instabilities in a model combustor. The main purpose of this section is to present a numerical study on a fully premixed methane flame in an academic burner that resembles acoustically a Rijke tube. The research focuses on the determination of the flame dynamics and the corresponding flame reaction zone under stable regime and during thermo-acoustic oscillations. As a matter of fact due to the geometry of the burner, self-excited oscillations of the pressure can take place in the combustor, modifying the structure of the flow field and causing fluctuations of heat release and also of the heat flux at the wall. Phase locked measurements of the OH* chemiluminescence were performed and used to understand the structure of the flame. Several simulations were performed varying systematically the thermal boundary conditions, the turbulent-combustion model and finally the equivalence ratio with the aim to reproduce the main acoustic features of the burner correctly. Particular attention was paid to the achievement of accurate solutions for unsteady heat transfer due to thermo-acoustic instabilities.

2 Theory and Numerical Implementation

:

2.1 Introduction to turbulence

The first works on turbulence are dated back to the end of the 18th Century, thanks to the experiments of Osborne Reynolds (1883). He introduced a dimensionless quantity, the Reynolds number, defined as the ratio between the inertial (destabilizing) force and the viscous damping (stabilizing) force, that identifies the occurrence of laminar or turbulent condition:

$$Re = \frac{\text{Inertial Forces}}{\text{Viscous Forces}} = \frac{\rho U L}{\mu} \tag{2.1.1}$$

A turbulent regime represents a state of the flow motion, that is a solution of the Navier Stokes equations but it presents a high level of complexity compared to a laminar flow regime. In this condition the macroscopic transport predominates on the microscopic transport enhancing the diffusivity and conductibility with values of orders of magnitude larger than in laminar conditions. The problem consists in the determination of the more suitable description of this state, both for the comprehension of the physical phenomena and for the modeling necessary to their qualitative prediction.

The main features of turbulent flows are:

- **Irregularity**. The most striking feature of turbulent flows is the temporal and spatial irregularity presented by all the variables involved. At high Re, the viscous forces are not sufficient to contrast the inertial forces, and the fluid particles travel in a chaotic and stochastic way, without observable pattern and no definite layers.

- **Rotationality**. They present normally three dimensional structures, characterized by high levels of vorticity and by a strong three-dimensional vortex generation mechanism known as vortex stretching. Vortex stretching is the core mechanism, which the turbulence energy cascade relies on.

- **Spatial and time scales**. They are characterized by the presence of motions with different spatial and temporal scales. In other words, different vortical structures are present simultaneously whose geometrical dimensions and characteristic times scale are very different among them.

Another common feature to all turbulent flows is the non-reproducibility of the experiments.

2.1.1 Turbulent energy cascade

The theory of the "turbulent energy cascade", developed in 1941 by Andrei N. Kolmogorov for locally isotropic turbulence, is well recognized as the most important work in turbulence. It describes:

- how energy is transferred from large-scale structures to smaller scale structures by means of an inertial and essentially inviscid mechanism;
- how much energy is contained by eddies of a given size;
- how much energy is dissipated by eddies of each size.

Briefly, the mechanical energy is supplied to the turbulent fluctuations at the integral length scale L, that is constrained by the characteristic length of the problem. The vortices with size $l_{EI} = L/6 < L < 6L$ represent the largest scales in the energy spectrum and are quite unstable. Eventually they may break up, transferring their energy to smaller eddies. These undergo a similar break-up process and transfer their energy to yet smaller eddies. This region of the turbulent spectrum is referred to as inertial sub-range. According to Kolmogorov the statistics of the scales (or better the characteristics of the structures) in this range are universally and uniquely determined by the rate of energy dissipation ε [24]. The energy cascade, in which energy is transferred to successively smaller and smaller eddies, continues until the small scale structures are small enough that their kinetic energy can be transformed by the fluid's molecular viscosity into heat. When this condition occurs, the smallest scale η (Komlogorov scale) of turbulence is reached.

Another important concept of Kolmogorov's theory regards the modeling of the small scale quantities (length η, velocity u_η and time scales t_η), and the ratio between large and small scale processes in a turbulent flow as a function only of the Reynolds number:

$$\frac{L}{\eta} = Re^{\frac{3}{4}}, \quad \frac{U}{u_\eta} = Re^{\frac{1}{4}}, \quad \frac{t_L}{t_\eta} = Re^{\frac{1}{2}} \tag{2.1.2}$$

2.2 Turbulence modeling

In literature several turbulence models are available for solving the Navier-Stokes equations. Since no single turbulence model is universally accepted as being superior for all classes of problems, three main approaches have been progressively developed in the past years:

- **Direct Numerical Solution (DNS)**. This represents ideally the most simple approach and consists of the direct numerical integration of the Navier Stokes equations without any turbulence model [1]. The aim is to solve exactly the whole range of spatial and temporal scales of the turbulence. The only error introduced by the model is due to the numerical approximation of the partial differential equations. On the other hand, to solve all the turbulent energy spectrum, a high computational cost even at low Reynolds numbers is required. As matter of fact, according to eq. 2.1.2 the ratio between the large and the small scale structures is equal to $Re^{3/4}$: thus, the number N of points to resolve the small scales along a given mesh direction will be proportional to the same factor $Re^{3/4}$; for a three-dimensional DNS it would require a number of mesh points N^3, that is to $Re^{9/4}$. DNS is obviously far from being feasible for a high Reynolds number and thus for many real technical systems.

- **Large Eddy Simulation (LES)**. Contrary to the DNS approach, the LES model resolves exactly only one portion of the spectrum: the large scale structures that are responsible of the turbulent energy cascade. The small scale processes are instead modeled with an additional method based on the turbulent viscosity [25]. The basic advantage is that the larger scales, in the inertial range, are simulated and thus it is possible to derive a unique model that is suited for all kinds of turbulent flows (jet flows, jet in crossflow, ...) without calibrating the model parameters at the problem of interest. To filter the small scales of the solution, a low-pass filter is applied to the Navier-Stokes equations. This reduces the computational cost of the simulation and unfortunately the accuracy of the solution with respect to a DNS simulation. Defining a filter function $G(x)$:

$$\overline{u}(x,t) = \int u(y,t)G(x-y,t)dy \tag{2.2.1}$$

it is possible to separate the filtered velocity and the sub-grid part:

$$u(x,t) = \overline{u}(x,t) + u^{'}(x,t) \tag{2.2.2}$$

For an accurate solution of the LES, the $G(x)$ function should capture and consent to

simulate vortices up to the inertial sub-range.

Most of the LES models are based on the Boussinesq hypothesis, which defines a simple relationship between the SGS stresses and velocity gradients through the eddy viscosity (similar to molecular viscosity):

- Smagorinsky model: it is the most common and used model, for the sake of simplicity and accuracy:
$$\nu_{SGS} = (C_s \Delta)^2 \left|\bar{S}\right| \tag{2.2.3}$$
- Germano dynamic model: this method is similar to the Smagorinsky one but the parameter C_s represents an unknown of the problem and therefore an additional filtering operation for determining C_s is required;
- One equation model for k:
$$\nu_{SGS} = C_k \Delta k_{SGS}^{1/2} \tag{2.2.4}$$

- **Reynolds Averaged Navier-Stokes (RANS)**. This model represents the most economic approach for computing complex turbulent industrial flows, providing information limited to the averaged characteristics of the flow field. Compared to the DNS approach, where all the turbulent characteristics are captured instantaneously without modeling, the RANS loses most of this information due to the time averaging of the flow field and requires modeling of every quantity from the integral scales in the dissipation range. Only mean quantities are directly computed and the approach is nearly independent of Re. More in detail, using the Reynolds decomposition, a generic variable ϕ can be split as follows [26]:

$$\phi(x,t) = \overline{\phi(x,t)} + \phi^{'}(x,t) \tag{2.2.5}$$

where the mean quantity $\overline{\phi(x,t)}$ and the fluctuating component $\phi^{'}(x,t)$ are defined as:

$$\overline{\phi(x,t)} = \lim_{T_f \to \infty} \frac{1}{T_f} \int_t^{t+T_f} \phi(x,t) dt, \quad \phi^{'}(x,t) = \phi(x,t) - \overline{\phi(x,t)} \tag{2.2.6}$$

T_f is a sufficiently long time to make the averaging independent upon the time. After some mathematical manipulations, the equations for a turbulent flow in an incompressible case may be written as:

$$\frac{\partial \overline{u_i}}{\partial x_i} = 0, \tag{2.2.7}$$

$$\frac{\partial \rho \overline{u_i}}{\partial t} + \overline{u_i}\frac{\partial \rho \overline{u_i}}{\partial x_j} = -\frac{1}{\rho}\frac{\partial \overline{p}}{\partial x_i} + \frac{\partial}{\partial x_j}\left[\mu \frac{\partial \overline{u_i}}{\partial x_j} - \rho \overline{u_i' u_j'}\right] \tag{2.2.8}$$

$$\frac{\partial \rho c_p \overline{T}}{\partial t} + \overline{u_i}\frac{\partial \rho \overline{T}}{\partial x_j} = \frac{\partial}{\partial x_j}\left[\kappa \frac{\partial \overline{T}}{\partial x_j} - \rho \overline{u_i' T}\right] \tag{2.2.9}$$

The above time-averaged equations represent the continuity, momentum and energy equations in the RANS formulation. They are formally identical to the Navier-Stokes equations with the exception for the cross-products of the fluctuation terms:

$$\overline{u_i' u_i'}, \quad \overline{u_j' u_j'}, \quad \overline{u_k' u_k'}, \quad \overline{u_i' u_j'}, \quad \overline{u_i' u_k'}, \quad \overline{u_j' u_k'} \tag{2.2.10}$$

However, they introduce additional unknowns represented by the turbulent fluxes $\overline{u_i' T}$ and the turbulent fluctuations $\overline{u_j' u_j'}$. The latter have an effect equivalent to the viscous stresses, they diffuse momentum due to the turbulent motions, and are therefore called "turbulent stresses" or Reynolds stresses. Being the number of the unknowns greater than the number of equations, the problem is not mathematically solvable, if not introducing new equations or relations for modeling the Reynolds stresses in terms of the known variables (mean quantities of the flow).

The most popular correlation for closing the problem is based on the Boussinesq hypothesis [27]. This assumption states that the momentum transfer caused by turbulent eddies can be modeled with an eddy viscosity. Mathematically, it expresses the Reynolds stresses as function of the mean rate of strain tensor of the mean flow and a positive parameter, known as turbulent viscosity μ_t.

Models that try to provide expressions for μ_t are known in literature as eddy viscosity models. However, the Boussinesq hypothesis is not the unique correlation for closing the NS system; a huge amount of RANS formulations are available in literature [28].

2.2.1 (U)RANS-Approach

In the following section the standard and widely used two equation turbulence models will be briefly described, highlighting the physical meaning of the formulations and discussing their advantages and limitations.

2.2.1.1 Standard k-ε Model

The k- ε model is one of the most used and common model in Computational Fluid Dynamics (CFD) to simulate turbulent flows. The first contribution to the method is attributed to Chou

in 1945, whereas the first significant formulation was proposed only years later by Launder and Jones [29] [30]. The model consists of two additional equations that transport the main characteristics of turbulence: the turbulent kinetic energy k and its dissipation ε. Considering that the turbulent fluctuations are described by the turbulent kinetic energy:

$$k = \frac{1}{2}\overline{u_i' u_i'} \tag{2.2.11}$$

and turbulent energy dissipation is proportional to the dynamic viscosity μ:

$$\varepsilon = \mu \overline{\frac{\partial u_i'}{\partial x_k}\frac{\partial u_i'}{\partial x_k}} \tag{2.2.12}$$

it results that the transport equation for k can be derived directly from the Navier-Stokes equations and it is written as follows:

$$\frac{\partial \rho k}{\partial t} + u_j \frac{\partial \rho k}{\partial x_j} - \frac{\partial}{\partial x_j}\left[\left(\mu + \frac{\mu_t}{\sigma_k}\right)\frac{\partial k}{\partial x_j}\right] = P_k - \rho\varepsilon \tag{2.2.13}$$

The source terms on the right hand side of eq.2.2.13 represent the production P_k and the dissipation $\rho\varepsilon$ of the turbulent kinetic energy.

An exact equation for the rate of dissipation of the turbulent kinetic energy can be obtained by the Navier-Stokes equations. The physical interpretation of the different terms, however, is complex and even their modeling could be difficult to obtain. Therefore, we may use an expression for ε similar to the k equation that includes convective, production, diffusion and dissipative terms. A detailed discussion about its derivation and meaning can be found in [1] and [25]. The ε-equation is written as follows by empirical considerations:

$$\frac{\partial \rho\varepsilon}{\partial t} + u_j \frac{\partial \rho\varepsilon}{\partial x_j} - \frac{\partial}{\partial x_j}\left[\left(\mu + \frac{\mu_t}{\sigma_\varepsilon k}\right)\frac{\partial \varepsilon k}{\partial x_j}\right] = C_{\varepsilon 1}\frac{\varepsilon}{k}G_k - C_{\varepsilon 2}\rho\frac{\varepsilon^2}{k} \tag{2.2.14}$$

Closure coefficient of the standard k-ε model are [29]:

$$C_1 = 1.44, \quad C_2 = 1.92, \quad C_\mu = 0.09, \quad \sigma_k = 1.0, \quad \sigma_\varepsilon = 1.3 \tag{2.2.15}$$

The turbulent viscosity is expressed as a combination of the turbulent kinetic energy k and its dissipation ε:

$$\mu_t = C_\mu' \sqrt{k} l_c = C_\mu' C_D k^{\frac{1}{2}} \frac{k^{\frac{3}{2}}}{\varepsilon} = C_\mu \frac{k^2}{\varepsilon} \tag{2.2.16}$$

The k-ε formulation is relatively simple and probably represents the best compromise between generality and accuracy of results, ease of implementation and computational stability.

Best results have been found for free-shear layer flows as well as for wall-bounded and internal flows with relatively small pressure gradients at high Reynolds number [31]. All these characteristics make it an attractive choice for many industrial problems. However, the model is not so perfect and shows its limits under particular flow conditions. It has been demonstrated the inability of the model to provide good accuracy for flows with large adverse pressure gradients. Other limitations appear in the classic problems of the back flow facing step with the systematic underestimation of the reattachment length in separate streams or in jet flows with the overestimation of the spreading rate, known as round jet/plane anomaly [32], [33]. Compared with a LES or DNS, this approach is strongly dependent on the model parameters: the standard values that perform well in one flow condition do not always perform well when the flow condition is altered. Therefore, the values have to be re-calibrated depending on the problem to solve. Moreover, the model is based on the assumption of isotropic and homogeneous turbulence at high Reynolds number. In proximity of the wall this "standard" formulation fails (due to the flow anisotropy and the low velocity) and provides erroneous results as a consequence. Therefore, new formulations have been developed for overcoming the near-wall problem with the so called "Low-Reynolds Number Models" that can be considered valid everywhere in the computational domain. An alternative approach is represented by the theory of the Wall functions, which will be briefly described in the next section.

Wall Functions Approach

Because of the intrinsic assumptions of the RANS models of isotropic turbulence and equilibrium, the integration of the above equations through the near-wall region yields unsatisfactory results in term of velocity, friction coefficient, heat transfer. A way to overcome this deficiency is to introduce special damping functions with the intent to decrease the turbulent viscosity in the boundary layer. This approach is called low-Reynolds-number formulation and will be outlined in Chap.5. In this section instead, an alternative and still widely employed method is described that provides the right estimation of the turbulent parameters near the solid boundaries. The method, known as wall-functions modeling, models the laminar sublayer in order to match the experimental observations at the boundary without the need for a very fine mesh.

It assumes two main hypotheses:

- Validity of the logarithmic law of the wall. The first grid point is assumed to be in the logarithmic layer ($y^+ > 11$) and the velocity is assumed to be described by:

$$u^+ = \frac{1}{\kappa_V} \ln y^+ + C \tag{2.2.17}$$

where κ_V is the Von Karman constant ($\kappa_V = 0.41$) and C is equal to 5.2;

- Local equilibrium in the boundary layer (production=dissipation).

The assumption of local equilibrium between the production of turbulent kinetic energy k and its dissipation rate ε is defined as:

$$\varepsilon = \rho P_k \quad \rightarrow \quad \mu_t \frac{\partial \overline{u}}{\partial y}\frac{\partial \overline{u}}{\partial y} = -\rho \overline{u_i' u_j'} \frac{\partial \overline{u_i}}{\partial x_j} \tag{2.2.18}$$

In the boundary layer theory it is common to refer to non-dimensional quantities for studying the evolution of the velocity in the near-wall regions [32]. We can introduce a non-dimensional velocity and wall distance as follows:

$$y^+ = \frac{\bar{u}_\tau y}{\nu} \tag{2.2.19}$$

$$u^+ = \frac{u}{\bar{u}_\tau} \tag{2.2.20}$$

where the $\bar{u}_\tau$ is the skin friction velocity:

$$\bar{u}_\tau = \sqrt{\frac{\tau_w}{\rho}} \tag{2.2.21}$$

The definition of the wall shear stress τ_w is:

$$\tau_w = \mu_t \frac{\partial u}{\partial x_n} \tag{2.2.22}$$

The y+ value represents the distance from the wall measured in viscous lengths (similar to a local Reynolds) and its magnitude determines the relative importance of viscous and turbulent processes [33]

Combining the above expressions under the local equilibrium assumption, it is possible to determine a value for the turbulent dissipation energy ε at the wall:

$$\varepsilon_w = \frac{C_\mu^{3/4} k^{3/2}}{y \kappa_V} \tag{2.2.23}$$

Concerning the turbulent kinetic energy, a zero-gradient condition is assumed on the wall:

$$\frac{dk_w}{dn} = 0 \tag{2.2.24}$$

Wall functions for the momentum equations have been found to provide good predictions of the near-flow behavior, although there are documented cases where they failed, especially

if they are employed for the heat transfer calculation [34].

2.2.1.2 Standard k-ω Model

The $k-\omega$ turbulence model dates back to the studies of Kolmogorov and is nowadays used in the form proposed by Wilcox [25]. This is a two-equation turbulence model where, in addition to the transport equation for the turbulent kinetic energy k, an equation for the specific dissipation rate ω is considered. The unknown ω has the dimension of an inverse time scale and represents the time that elapses between the production and the dissipation of the turbulent structures.

$$\omega = \frac{\beta_k \varepsilon}{k} \tag{2.2.25}$$

This model has been modified numerous times in the attempt to improve its accuracy. As for the $k-\varepsilon$ formulation, the transport equation for k is:

$$\frac{\partial \rho k}{\partial t} + \frac{\partial \rho u_j k}{\partial x_j} = \tau_{ij}\frac{\partial u_i}{\partial x_j} + \frac{\mu_t}{\rho^2}\frac{\partial \rho}{\partial x_j}\frac{\partial p}{\partial x_j} - \beta_k \rho \omega k + \frac{\partial}{\partial x_j}\left[\left(\mu + \frac{\mu_t}{\sigma_k}\right)\frac{\partial k}{\partial x_j}\right] \tag{2.2.26}$$

The ω transport equation can be derived by a combination of physical reasoning and dimensional analysis as shown in [25]

$$\frac{\partial \rho \omega}{\partial t} + \frac{\partial \rho u_j \omega}{\partial x_j} = \gamma\frac{\omega}{k}\tau_{ij}\frac{\partial u_i}{\partial x_j} + \frac{\gamma}{\rho}\frac{\partial \rho}{\partial x_j}\frac{\partial p}{\partial x_j} - \beta_k \rho \omega^2 + \frac{\partial}{\partial x_j}\left[\left(\mu + \frac{\mu_t}{\sigma_\omega}\right)\frac{\partial \omega}{\partial x_j}\right] \tag{2.2.27}$$

The first terms on the right hand side of eq. 2.2.26 and 2.2.27 represent respectively the generation of turbulent kinetic energy and the production of the specific dissipation rate that arises due to mean velocity gradients, defined in the same manner like in the $k-\varepsilon$ model.

The turbulent viscosity is related to the turbulent quantities k and ω as follows:

$$\mu_t = \rho\frac{k}{\omega} \tag{2.2.28}$$

Although the k-ω formulation is not as popular as the k-ε model, it has shown good prediction in results for transitional flows and in flows with adverse pressure gradients. It has greater accuracy in case of wall-bounded and low Reynolds number flows. The standard approach does not require damping functions and it is numerically stable since it tends to converge to the solutions more rapidly than the k-ε. The main weakness lies in the strong dependency of its results on the free-stream value of ω [35]. Indeed, the model does not predict very well the transition between turbulent and free-shear flow, since low values of k and ω in the free-shear flow deeply affect the turbulent part of the flow. To reduce this sensitivity

a new model that combines the positive effects of the k-ε and k-ω has been proposed, which is described in the next section.

2.2.1.3 Shear Stress Transport k-ω Model

The SST (Shear Stress Transport) model is an eddy-viscosity model introduced by Menter et al. [36] with the intent to improve the weaknesses of the standard k-ε and k-ω formulations. As already mentioned, the standard k-ε performs well under particular conditions but fails in the determination of shear stress in adverse pressure gradient flows due to too low dissipation, requiring particular modifications such as low-Re models, wall functions, etc. The k-ω provides better results instead, however it does not consider the use of any wall damping functions and is quite dependent on the free-stream value of ω [37]. To overcome these limitations, Menter came up with the idea to combine the two models, blending automatically between the Wilcox k-ω turbulence model near to the walls and the standard k-ε formulation in the outer region outside of the boundary layer. For industrial problems, the SST-method is quite useful since it provides accurate results for flows with large recirculation and separation. This improvement has been obtained with a particular limitation of the shear stress in adverse pressure gradient and assuming it proportional to the turbulent kinetic energy [36].

In order to combine the two models, the k-ε formulation is converted into a k-ω model and the transport equations are defined as follows:

$$\frac{\partial \rho k}{\partial t} + u_j \frac{\partial \rho k}{\partial x_j} - \frac{\partial}{\partial x_j}\left[\left(\mu + \frac{\mu_t}{\sigma_k}\right)\frac{\partial k}{\partial x_j}\right] = P_k - \beta_k \rho k \omega \tag{2.2.29}$$

$$\frac{\partial \rho \omega}{\partial t} + u_j \frac{\partial \rho \omega}{\partial x_j} - \frac{\partial}{\partial x_j}\left[\left(\mu + \frac{\mu_t}{\sigma_\omega}\right)\frac{\partial \omega}{\partial x_j}\right] = \alpha \frac{1}{\nu_t} P_k - \beta_k \rho \omega^2 + 2(1 - F_1)\rho \sigma_{\omega 2} \frac{1}{\omega}\frac{\partial k}{\partial x_j}\frac{\partial \omega}{\partial x_j} \tag{2.2.30}$$

The blending function F_1 is defined by:

$$F_1 = \tanh\left\{\left\{\min\left[\max\left(\frac{\sqrt{k}}{\beta_k \omega y}, \frac{500\nu}{y^2\omega}\right), \frac{4\rho\sigma_{\omega_2} k}{CD_{kw} y^2}\right]\right\}^4\right\} \tag{2.2.31}$$

with:

$$CD_{kw} = \max\left(2\rho\sigma_{\omega_2}\frac{1}{\omega}\frac{\partial k}{\partial x_j}\frac{\partial \omega}{\partial x_j}, 10^{-10}\right) \tag{2.2.32}$$

F_1 is equal to zero far away from the surface (k-ε model), and switches over to one inside the boundary layer (k-ω model).

As mentioned, the k-ω formulation performs better than the k-ε model in predicting adverse pressure gradient flows because it predicts lower shear stress values, but still larger than the

experiments. Thus to reduce its value, Menter suggested a new expression for the turbulent viscosity:

$$\mu_t = \frac{a_1 k}{\max\left(a_1\omega, \Omega_s F_2\right)} \tag{2.2.33}$$

where $\Omega_s$is the invariant measure of the strain rate and F_2 is a second blending function defined by:

$$F_2 = \tanh = \left[\left[\max\left(\frac{2\sqrt{k}}{\beta^*\omega y}, \frac{500\nu}{y^2\omega}\right)\right]^2\right] \tag{2.2.34}$$

More information about the theoretical background can be found in [36]. The values of the model constants accordingly to [37] have been chosen to blend the behavior of k-ω in the inner region and k-ε formulation in the outer region.

2.2.2 Turbulent Boundary Layer

The concept of the boundary layer was introduced by Prandtl to simplify the calculation of the problems of interaction between a moving fluid and a solid wall. The boundary layer is defined as a small region of fluid where the effects caused by the proximity of a wall are much more marked with respect to the free stream. Outside this region, the flow viscosity can be neglected without significant effects on the solution and the flow field can be approximated by solving the Euler equation. Inside the boundary layer large velocity fluctuations reside and the effects of the viscous stresses must be taken into consideration. Moreover, the majority of the heat transfer to and from a body takes place within this region. The thickness of the velocity boundary layer can be defined as the distance from the solid body at which the viscous flow velocity is 99% of the free-stream velocity [38].

From Prandtl's studies, the turbulent boundary layer has been subdivided into two sub-layers, called outer and inner layer respectively. In the first of these two regions the viscous effects and heat transfer are negligible. The flow field is governed with a good approximation by the Euler equations. The second region, in general very small, is characterized on the other hand by high spatial and temporal gradients of flow and by relevant viscous effects. This is, in turn, decomposed in three sub-layers:

- Log-law region ($y^+ > 40$): it extends from $y^+ = 40$ to about $y^+ = 400$, with approximately constant shear stress. The classical logarithmic law of velocity is valid in this region, which assumes the linear behavior with the adoption of semi-log scales.

$$u^+ = \frac{1}{\kappa_V}\ln(y^+) + C = \frac{1}{\kappa_V}\ln(Ey^+) \tag{2.2.35}$$

- Viscous-linear sublayer ($0 < y^+ < 5$): extends from the wall boundary until 5 y^+ and is characterized by a linear distribution of the velocity.

$$u^+ = y^+ \tag{2.2.36}$$

- Buffer layer: between the log-law region (characterized by turbulent motion) and viscous sublayer (controlled by molecular diffusion). In this zone, no law for the velocity can be determined, since the profile varies from the linear trend of the viscous substrate to the logarithmic behavior of the overlap region.

Fig.2.2.1 illustrates clearly the subdivision of the turbulent boundary layer at high Reynolds numbers.

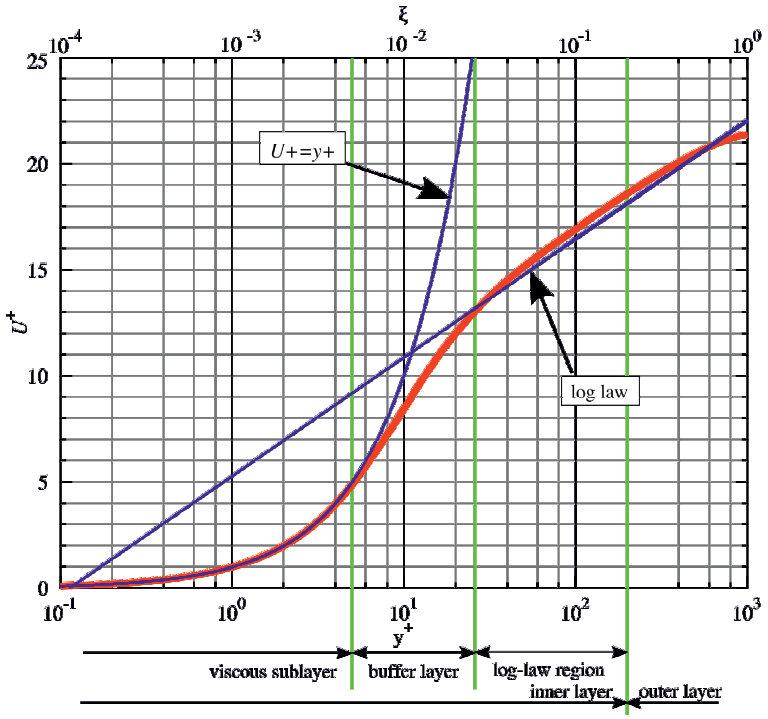

Figure 2.2.1: Illustration of the theoretical subdivision of the turbulent boundary layer. [1]

2.2.3 Hybrid (U)RANS/LES methods

Hybrid modeling methods of turbulent flows have received increasing attention over the past decade to fill up the gap between (U)RANS and LES computations for applications at industrially relevant Reynolds numbers. These approaches represent an alternative to RANS and LES simulations for unsteady turbulent flows in complex geometries, that try to combine the best aspects of both strategies. As matter of fact, LES simulations suffer from the fine resolution of the near-wall region at high Reynolds numbers. On the other hand,

(U)RANS simulations for unsteady flows often do not provide accurate results for industrial applications, since most of the energy spectrum is modeled. Thus the hybrid URANS/LES method is nowadays considered the best compromise in terms of computational time and accuracy of the solution and probably more suited for the calculations of complex geometries typical of gas-turbine combustors. In this work the SST-SAS hybrid model, developed by Menter and coworkers [39] [40], has been intensively used since it proved to be an interesting technique for solving unsteady flows around a bluff body configuration. The theory of the model is briefly described in the following section.

2.2.3.1 Scale Adaptive Simulation Method (SST-SAS)

The idea behind the SST-SAS model was to combine the positive characteristics of the RANS and LES formulations for resolving with great accuracy the near wall and far field regions. The model ideally provides a URANS solution in stable flow regions while resolving turbulence in transient instabilities, such as massive separation zones. Indeed, the SST-SAS model captures regions with relatively coarse grid by URANS whereas flow regions with fine grid are simulated in an LES-like mode. It uses the SST $k-\omega$ turbulence model formulation and includes an additional production term $Q_{SST-SAS}$ in the ω equation, which is sensitive to unsteady fluctuations. This term is a function of the second derivative of the turbulent kinetic energy k and of the turbulent dissipation ω and depends also on the ratio between the turbulent and the Von Karman length scale L_t/L_{VK} as shown below:

$$\begin{aligned} Q_{SST-SAS} &= max\left[\widehat{\zeta}\kappa_V S^2 \frac{L_t}{L_{VK}} - C\cdot\frac{2}{\sigma_\phi}k \right. \\ &\left. \cdot max\left(\frac{1}{\omega^2}\frac{\partial\omega}{\partial x_j}\frac{\partial\omega}{\partial x_j}, \frac{1}{k^2}\frac{\partial k}{\partial x_j}\frac{\partial k}{\partial x_j}\right), 0\right]. \end{aligned} \tag{2.2.37}$$

Here $\widehat{\zeta} = 3.51$, $C = 2$, $\kappa_V = 0.41$, $\sigma_\phi = 2/3$ are the modeling constants.

The $Q_{SST-SAS}$ term is able to detect flow unsteadiness depending on the local ratio L_t/L_{vK}. If the grid has a fine resolution (in regions where the flow equations solve the small-scale movement) the von Karman length scale, based on the ratio of the first to the second velocity gradients, is smaller for an unsteady velocity profile than for a steady velocity one and leads consequently to high values for the ratio L_t/L_{vK}. An increase of the SAS-term results in an enhancement of the production of the dissipation rate ω and thus in a reduced value for the turbulent kinetic energy k and the turbulent viscosity μ_t. Due to the reduction of μ_t, its dissipating effect on the solved fluctuations becomes smaller, allowing the model to work in an "LES-like" mode and to solve turbulence in the crucial zones of interest [39],[40].

2.2.4 Large Eddy Simulation Modeling

The Large Eddy Simulation is a mathematical model for turbulence used in computational fluid dynamics. The main feature is its capability to solve directly the largest scales of the motion and to model the small vortices up to the inertial range of the energy spectrum. Mathematically, this corresponds to a filtering operation of the NS-equations in order to eliminate the small scales of the solution. The resulting equations are similar to the RANS equations but they have a completely different meaning: RANS equations are time-averaged or ensemble-averaged, the LES formulation is based on space-filtering. As in other turbulence models, new unknowns arise from the non-linear advection terms $\overline{u_i u_j}$ after the separation of the small and the large scales. These new quantities represent the effect of the non-resolved small scale in the flow motion, which is unknown and must be modeled. The filtered advection term can be split up, following the work of Leonard [41] as:

$$\overline{u_i u_j} = \tau_{ij}^r + \overline{u}_i \overline{u}_j \tag{2.2.38}$$

where τ_{ij}^r is defined as sub-grid stress tensor.

The first LES model employed the Boussinesq hypothesis to provide an adequate expression of the SGS stress tensor as function of the filtered variables:

$$\tau_{ij}^r - \frac{1}{3}\tau_{ij}\delta_{ij} = -2\nu_t \bar{S}_{ij} \tag{2.2.39}$$

where $\nu_t = \mu_t/\rho$ is the turbulent eddy viscosity and $\bar{S}_{ij} = \frac{1}{2}\left(\frac{\partial \bar{u}_i}{\partial x_j} + \frac{\partial \bar{u}_j}{\partial x_i}\right)$ is the rate-of-strain tensor.

2.2.4.1 WALE Model

The WALE model is also based on the eddy dissipation concept but represents a better alternative to the Smagorinsky model in the near-wall regions. It was developed to recover the scaling law of the wall without the necessity of using a wall function approach [42]. The eddy viscosity formulation of the WALE model is able to ensure a behavior of $\mu_t \approx y^{+^3}$ close to the wall, improving the accuracy of the solution in this region.

In the WALE model the eddy viscosity is modeled by:

$$\mu_t = \rho \Delta_g^2 \frac{(S_{ij}^d S_{ij}^d)^{3/2}}{(\overline{S}_{ij}\overline{S}_{ij})^{5/2} + (S_{ij}^d S_{ij}^d)^{5/4}} \tag{2.2.40}$$

Where C_w is a model constant taken equal to 0.5, Δ is the filter width corresponding to the root of the cell volume. Further details concerning the WALE model can be found in literature [42].

2.3 Combustion modeling

The state of the art for the combustion modeling was given by Joos in his work [43]. In the following section, the theoretical description of the combustion models used for the present numerical simulations will be given.

2.3.1 Eddy dissipation model for global chemistry: EDM

In non-premixed flames, turbulence slowly convects and (or) mixes fuel and oxidizer into the reaction zones where they quickly burn. In such cases, the combustion is said to be mixing-limited, and the complex chemical kinetic rates can be safely neglected [44]. This condition is referred to as Fast Chemistry, where the chemical reactions are assumed to occur infinitely fast compared to the time scale of the transport process. The EDM model (Eddy Dissipation Model) [45] is based on the previous hypothesis. Under this assumption the chemical reaction rate is controlled, as in the eddy-breakup model of Spalding [46], by the turbulent mixing time-out τ_t. The latter is defined as:

$$\tau_t = \frac{k}{\varepsilon} \tag{2.3.1}$$

According to this model, the rate of production of the species i due to the turbulent mixing rate RR_t is given by the following expression:

$$RR_t = A\rho\frac{\varepsilon}{k}\min\left(\min_R\left(\frac{Y_R}{\nu'_{R,j}M_R}\right), B\frac{\sum_P Y_P}{\sum_k^N \nu'_{k,j}M_k}\right). \tag{2.3.2}$$

where Y_R refers to the mass fraction of a particular reactant and Y_P is the mass fraction of any product species.

In cases where chemistry is relatively slow, a possible solution is to combine the mixing model with a finite-rate chemistry formulation, eq. 2.3.3: the kinetic rate is taken as the minimum of the mixing rate and the chemically controlled terms. If chemistry is much faster than the turbulent mixing processes, the reaction rate is controlled by the turbulent mixing RR_t, whereas if mixing is much faster than chemistry finite rate effects RR_c are included. Thus, for a 1-step global reaction it follows:

$$RR_c = A_r T^{\alpha_r}\exp\left(-\frac{-E_{a_r}}{\Re T}\right)\prod_j [C_j]^{\nu_{j_r}} \tag{2.3.3}$$

One of the most significant limitation is the fact that only global reaction schemes can be considered.

2.3.2 Eddy Dissipation Model for detailed chemistry: EDC

The EDC model was developed in the past years by Magnussen and coworkers [16] as an extension of the previous model for detailed chemistry. The model is based on the theory of the energy cascade by Kolmogorov, in which the turbulent kinetic energy is transferred from larger to smaller scales and finally dissipated at the Kolmogorov scale. The idea is to assume that the chemical reactions occur in the finest scales of the energy spectrum where the dissipation of turbulent energy takes place. Normally, in case of RANS or LES simulations these scales are not resolved from the turbulence model since they are smaller than the grid spacing; thus the numerical cells cannot model the energy transfer mechanism and its dissipation due to the molecular diffusion. A modeling of these scales is therefore required. According to the model, the computational cell may be conceptually split up into two sub-zones [15]:

- surrounding fluid;
- fine zone or fine structure.

As mentioned, the fine scale represents the portion of the grid cell, in which the homogeneous chemical reactions occur. Due to the intense mixing in the dissipative region, they can be treated as an adiabatic, isobaric Perfectly Stirred Reactor with initial conditions taken as the current species and temperature values in the cell. The surrounding fluid is the adjacent region where the turbulent transport convects the fresh and reacting mixture into the fine scale.

The length of the fine structures has been determined in [47] and is strictly dependent on the local turbulence. It is defined as [15]:

$$\gamma = \left(\frac{3C_{D2}}{4C_{D1^2}}\right)^{1/4} \left(\frac{\nu\varepsilon}{k^2}\right)^{1/4} \tag{2.3.4}$$

where ν is the kinematic viscosity, C_{D1} and C_{D2} are model constants related to the turbulence model used. The volume fraction occupied by the fine structures is therefore the cube of the length γ.

Once determined an expression for γ, it is opportune to determine the mean residence time in which mass is transferred between the fine structures and the surrounding flow. This quantity is proportional to the Kolmogorov time scale [16]:

$$\tau^* = \left(\frac{C_{D2}}{3}\right)^{1/2} \left(\frac{\nu}{\varepsilon}^{1/2}\right) \tag{2.3.5}$$

This mean residence time is roughly equivalent to the characteristic chemical time whereby the fresh mixture reacts in the fine scale with a net mean reaction rate for the transport equation:

$$\omega_i^* = \frac{\gamma^2}{\tau}\left(Y_i^* - Y_i^0\right) \tag{2.3.6}$$

In the above equation the subscript $*$ and 0 represent respectively the scalar value in the fine and surrounding regions.

In order to relate the mean mass quantity and the state in the fine and surrounding structures, Magnussen proposed a relation that links the sub-grid processes with the mean flow as follows [47]:

$$\tilde{\Phi} = \gamma^3\chi\Phi^* + \left(1 - \gamma^3\chi\right)\Phi^0 \tag{2.3.7}$$

The factor χ, referred to as the fraction of γ where reactions take place, is commonly set to 1 for detailed chemistry, as indicated by the analysis of Orszag in [48]. Thus by solving the equation 2.3.7 for Φ^0, following is an expression for the scalar quantity in the surrounding region:

$$\Phi^0 = \frac{\tilde{\Phi} - \gamma^3\chi\Phi^*}{1 - \gamma^3\chi} \tag{2.3.8}$$

Substituting eq. 2.3.8 in 2.3.6:

$$\omega_i^* = \frac{\gamma^2}{\tau}\left(Y_i^* - \frac{\tilde{Y}_i - \gamma^3\chi Y_i^*}{1 - \gamma^3\chi}\right) \tag{2.3.9}$$

Rearranging the previous equation and considering a detailed chemistry mechanism ($\chi = 1$), the mean reaction rate for each species can be expressed as:

$$\omega_i* = \rho\frac{\gamma^2}{1 - \gamma^3\chi}\frac{Y_i^* - \tilde{Y}_i}{\tau} \tag{2.3.10}$$

As proposed by Gran [15], the value of Y_i^* corresponds to the integration in time of the species i over the time scale τ^*. The integration is performed considering the "fine regions" as a homogeneous, adiabatic PSR reactor with constant pressure and the governing equations are:

$$\begin{cases} \dfrac{dY_i^*}{dt} = \omega_i^* + \dfrac{Y_i * - \tilde{Y}_i}{\tau^*} \\ \dfrac{dh}{dt} = 0 \\ \dfrac{dp}{dt} = 0 \end{cases} \tag{2.3.11}$$

The numerical integration of the system 2.3.11 is computationally expensive, since the detailed chemistry mechanism involves the evolutions of species with a largely different time scale (stiff problem).

2.3.3 Fractal Model FM

A similar model based always on Kolmogorov's energy cascade theory is the Fractal model [17], [18]. The model, developed by Giacomazzi et al., is able to ensure the closure for the turbulence and combustion problem estimating the values for the turbulent viscosity and the mean reaction rate. Based on the Kolmogorov theory, this predicts an algebraic closure for the turbulent viscosity μ_t. Briefly, considering that due to the energy/vortex cascade, N_η subgrid dissipative eddies are generated in each cell (from the local grid cell size to the dissipative scale η), the local enhancement of the turbulent viscosity due to the turbulence can be expressed as function of N_η and the molecular viscosity μ:

$$\mu_t \propto N_\eta \mu \tag{2.3.12}$$

In his work [18], Giacomazzi provides an expression, based on the local grid size and the dissipative scale, to evaluate the number of the scales N_η generated by the turbulent energy cascade.

The combustion problem closure is treated similarly to the EDC model and makes use of the fractal geometry for evaluating the turbulent-chemistry interaction. As in the EDC model, the model assumes that the molecular mixing and chemical reactions occur at the finest scale of the turbulence "fine structure" that occupies only a fraction of the cell size. The fraction of the cell (volume fraction) interested by the dissipative process is related to the ratio of the cell size and the local Kolmogorov scale:

$$\gamma^* = \gamma_\eta \left(\frac{\Delta}{\eta} \right)^{D_3 - 1} \tag{2.3.13}$$

where γ_η is the ratio between the number N_η scales and the total number of scales generated locally, D_3 the local fractal dimension, Δ the characteristic dimension of the problem (the

local grid size) and η the dissipative scale. The determination of γ_η is difficult to obtain and in [17] an estimation of the value for saving computational time in the calculation has been proposed:

$$\gamma_\eta = 1 - \frac{0.36\,(\Delta/\eta - 1)}{1 + 0.0468\,(\Delta/\eta - 1)^{2.7}} \tag{2.3.14}$$

The fractal dimension is instead defined as follows:

$$D_3 = 1 + \frac{\ln N_\eta}{\ln\,(\Delta/\eta)} \tag{2.3.15}$$

The trend of γ with the Reynolds number assumes high values close to 1 in the laminar region, decreases until a minimum and grows slightly approaching an asymptotic value for high turbulence. Further details can be found in [18]. The net reaction rate for the filtered species equations in the fractal model is expressed as:

$$\tilde{\omega_i} = \gamma \omega_i^* \tag{2.3.16}$$

The reacting fine structures are treated again as adiabatic PSR reactors with constant pressure that react over a time scale τ^*. The governing equations for the 0D reactors are expressed by the stiff differential system in 2.3.11 and provide after $t = \tau^*$ the value for Y_i^* necessary for the calculation of ω_i^*.

The time scale τ^* has a different formulation compared to the EDC. This matches the eddy turnover time of the dissipative vortices η:

$$\tau^* = N_\eta \left(\frac{\nu_\eta}{\nu_\Delta}\right)^{1/2} \frac{\tau_\Delta}{Re_\Delta^{1/2}} \tag{2.3.17}$$

2.3.4 Assumed PDF model

The finite-rate combustion model is able to describe the oxidation of the reacting mixture using detailed chemistry. This formulation considers the solution of a transport equation for each reacting species involved in the chemical mechanism. Under laminar conditions, it provides an exact solution for the chemical source term and accurate description of the flame characteristics, leading obviously to an enhancement of the computational cost for the high number of scalar equations to solve. In a mixture of N_r elementary reactions, the source term of a species i is computed using Arrhenius expressions:

$$\omega_i = M_i \sum_{r=1}^{N_r} \left(\nu_{i_r}^{''} - \nu_{i_r}^{'}\right) \left(k_{f_r} \prod_{\beta=1}^{N_{sp}} C_\beta^{\nu_{\beta_r}^{'}} - k_{b_r} \prod_{\beta=1}^{N_{sp}} C_\beta^{\nu_{\beta_r}^{''}}\right) \tag{2.3.18}$$

When turbulent flows are considered, an expression for the Favre-averaged source term is difficult to obtain, since turbulence fluctuations of the species and temperature strongly modify the net production rate with a non linear dependency on T and Y_i. Approximating the averaged source term with that computed with its mean values may lead to erroneous results:

$$\overline{\omega_i} \neq M_i \sum_{r=1}^{N_r} \left(\nu_{i_r}^{''} - \nu_{i_r}^{'}\right) \left(\overline{k_{f_r}} \overline{\prod_{\beta=1}^{N_{sp}} C_\beta^{\nu_{\beta r}^{'}}} - \overline{k_{b_r}} \overline{\prod_{\beta=1}^{N_{sp}} C_\beta^{\nu_{\beta r}^{''}}} \right) \tag{2.3.19}$$

The turbulence chemistry interaction can be evaluated by means of presumed PDF approach for the species and temperature fluctuations. By means of this model the average source term for the species equation can be computed considering a PDF for the unknown quantities:

$$\overline{\omega_i} = \int \omega_i \left(T, Y_1, \cdots, Y_N\right) P\left(T, Y_1, \cdots, Y_N\right) dT dY_1 \cdots dY_N \tag{2.3.20}$$

Such a PDF includes the correlations for temperature, species and density. A common approach, but often questionable, is to assume statistical independence of the stochastic variables [49]. The previous PDF can be re-written as the product of species and temperature PDF as follows:

$$P\left(T, Y_1, \cdots, Y_N\right) = P_T(T) P_Y\left(Y_1, \cdots, Y_N\right) dT dY_1 \cdots dY_N \tag{2.3.21}$$

For the PDF of the temperature often a Gaussian distribution function is considered and limited in a specific range of validity between T_{min} and T_{max} for avoiding unphysical values:

$$P(T,\overline{T},\sigma_T) = C_{min}\delta\left(T_{min}\right) + f_g(T,T_g,\sigma_g) + C_{max}\delta\left(T_{max}\right) \tag{2.3.22}$$

$$f_g(T,T_g,\sigma_g) = \frac{1}{\sqrt{2\pi\sigma_g}} \exp\left[-\frac{\left(T-\overline{T}\right)^2}{2\sigma_g}\right] \tag{2.3.23}$$

The coefficient C_{min} and C_{max} are chosen, as mentioned, to clip the distribution of the previous PDF, whereas T_g and σ_g are moments of the unclipped PDF. The latter are found with an iterative process described in [49].

Thus, the averaged Arrhenius reaction rate is obtained as the integration in the temperature space of the reaction rate in combination of the temperature PDF:

$$\overline{k_{f_r}} = \int_{T_{min}}^{T_{max}} k_{f_r}\left(T\right) P(T,\overline{T},\sigma_T) dT \tag{2.3.24}$$

Normally the averaged values are stored in a lookup table for reducing the computational cost during the time integration. These tables contain the Arrhenius coefficients as function of the mean temperature and temperature variance, requiring however high memory for storage [50]. To reduce the memory problem, in the THETA-code the $\overline{k_{f_r}}$ are instead cast into a canonical Arrhenius form as function of the temperature fluctuation intensity I_T [49]:

$$\overline{k_{f_r}} \approx A_{f_r}\left(I_T\right)\overline{T}^{\alpha_r(I_T)}\exp\left(-\frac{-E_{a_r}\left(I_T\right)}{\Re\overline{T}}\right) \tag{2.3.25}$$

where I_T:

$$I_T = \frac{\sqrt{\sigma_T}}{T} \tag{2.3.26}$$

and:

$$\sigma_T = \overline{T''^2} \tag{2.3.27}$$

The latter is the temperature variance and represents an important parameter, unfortunately unknown, that determines the shape of the Gauss-distribution. To solve σ_T, an additional transport equation was proposed [49],[51]:

$$\frac{\partial\overline{\rho}\sigma_T}{\partial t} + \frac{\partial\left(\overline{\rho}\widetilde{u_k}\sigma_T\right)}{\partial x_k} = \frac{\partial}{\partial x_k}\left[\frac{\mu_t}{Pr_{\sigma_T}}\frac{\partial\sigma_T}{\partial x_k}\right] + \overline{S_{\sigma_T}} \tag{2.3.28}$$

For the species fluctuations the multi-variate β-PDF was used as proposed by Girimaji [52]:

$$P(\mathbf{Y},\overline{\mathbf{Y}},\sigma_Y) = \frac{\Gamma\left(\sum_{j=1}^{N_s}\beta_j\right)}{\prod_{j=1}^{N_s}\Gamma\left(\beta_j\right)}\prod_{j=1}^{N_s}\left(Y_j\right)^{\beta_j-1}\delta\left(1-\sum_{j=1}^{N_s}Y_j\right) \tag{2.3.29}$$

the PDF depends on the turbulent scalar energy σ_Y:

$$\sigma_Y = \sum_{j=1}^{N_s}\overline{Y_j''^2} \tag{2.3.30}$$

and on β_j, that is function of mean mass fractions [49].

In order to determine the species PDF a transport equation for σ_Y has to be solved also [50].

2.3.5 Burning Velocity Model BVM

The BVM models the propagation of a premixed or partially premixed flame by solving a scalar transport equation for the mean reaction progress variable $\tilde{c}$. The progress variable

c describes the probability of the reacted state of the fluid along the time. Burnt regions are treated similar to diffusion flames whereas the unburnt fluid is represented by the cold mixture. The filtered source term in the scalar equation is closed with an algebraic expression depending on turbulent flame speed and is expressed as follows:

$$\tilde{\omega} = \rho_u S_T \left|\nabla \tilde{c}\right| \tag{2.3.31}$$

where ρ_u is the density of the unburnt mixture, $\nabla \tilde{c}$ is the gradient of the progress variable and S_T is the turbulent flame velocity. The model is completed with the closure for the turbulent burning velocity S_T given by Zimont et al. [53]. Further details concerning the model can be found in [54].

2.3.6 Linear Eddy Mixing Model LEM

The Linear Eddy Model LEM has been developed by Menon et al. [55, 56, 57] for turbulent flames. The main feature of this model is to solve the large eddy scales by means of an LES- or Hybrid RANS/LES approach and also to solve the effects of the small scale processes in a one-dimensional domain within the grid cells. According to the model, all the physical processes occuring in every computational cell (i.e., convective transport, turbulent and molecular diffusion, chemical reactions) are solved using a one-dimensional grid. This ensures the capability to capture most of the unsteadiness of the flow and to perform an affordable DNS for turbulent-reacting flows.

A brief description of the main aspects of the combustion model is presented here. Due to the turbulence, the velocity field can be seen as the sum of the contribution of the resolved velocity $\tilde{u}$ and modeled subgrid scale turbulent fluctuations u':

$$u = u' + \tilde{u} \tag{2.3.32}$$

The idea behind the LEM is to solve each physical phenomena at their corresponding time scale, thus, to solve the large scale advection (the resolved field) and the small scale processes (not resolved by the solver and modeled on a one-dimensional grid) separately. A non-filtered scalar equation for the generic variable ϕ (eq. 2.3.33) is written as:

$$\rho \frac{\partial \phi}{\partial t} + \rho u_i \frac{\partial \phi}{\partial x_i} + \frac{\partial}{\partial x_i}\left[-D_\phi \frac{\partial \phi}{\partial x_i}\right] = \dot{\omega}_\phi \tag{2.3.33}$$

Substituting the decomposition of the velocity eq. 2.3.32 into the previous equation, it is easy to obtain two different equations that describe the *large scale* (eq. 2.3.34) and *small scale* (eq. 2.3.35) processes:

$$\rho\frac{\phi^* - \phi}{\Delta t} + \rho\tilde{u_i}\frac{\partial\phi}{\partial x_i} = 0 \tag{2.3.34}$$

$$\rho\frac{\partial\phi^*}{\partial t} + \rho u_i'\frac{\partial\phi^*}{\partial x_i} + \frac{\partial}{\partial x_i}\left[-D_\phi\frac{\partial\phi^*}{\partial x_i}\right] = \dot{\omega_\phi} \tag{2.3.35}$$

Where ϕ^* is an intermediate solution between the large and small scales time step.

Eq. 2.3.35 solves a reaction-diffusion problem in every computational cell in a one-dimensional domain (LEM-1D domain), which is aligned along the normal to the maximum scalar gradient. The length of the 1D grid corresponds to the cell size. This is discretized with a number of elements whose dimension corresponds to the smaller scale in the turbulent spectrum, the Kolmogorov scale.

The convective term $F_k = u_i'\frac{\partial\phi^*}{\partial x_i}$ in the small scale equation represents an unknown term, since the velocity field is not resolved up to the dissipative scale. Thus, Kerstein modeled the effect of the turbulent convection (also called stirring-effect [55]) on the scalar field using a numerical algorithm called "triplet maps" [58]. This provides a stochastic re-arrangement event of the scalar field, reproducing the action of a vortex of a given size acting on the flow. The re-arrangement creates a spatial redistribution and also an increase of the scalar gradients. The algorithm creates three copies of the portion of the scalar field affected by the vortex, compresses each portion by a factor of three and reverses the middle segment. Mathematically, this is expressed by:

$$\phi\left(x,t_0\right) = \begin{cases} \phi\left(3x - 2x_0,t_0\right) & x_0 \leq x \leq x_0 + l/3 \\ \phi\left(-3x + 4x_0 + 2l,t_0\right) & x_0 + l/3 \leq x \leq x_0 + 2l/3 \\ \phi\left(3x - 2x_0 - 2l,t_0\right) & x_0 + 2l/3 \leq x \leq x_0 + l \\ \phi\left(x,t_0\right) & \text{otherwise} \end{cases} \tag{2.3.36}$$

where l is the length of the vortex ranging from the Kolmogorov scale η to the cell size Δ, x_0 is the location where the vortex occurs and t_0 is the time of the event. These parameters have to be defined in order to simulate the effect of an eddy upon the scalar field. The location x_0 is chosen randomly inside the LEM-domain (1D), whereas the frequency at which the vortex occurs (eq. 2.3.37) depends on the local turbulence conditions (sub-grid turbulent Reynolds number Re_Δ , Kolmogorov scale η, integral scale Δ). A higher value of the turbulent Reynolds number corresponds in frequent vortex events. The vortex frequency per unit length is expressed by [55]:

$$\lambda_s = \frac{54}{5}\frac{\nu Re_\Delta}{C_\lambda\Delta^3}\left[\frac{\left(\Delta/\eta\right)^{5/3} - 1}{1 - \left(\Delta/\eta\right)^{4/3}}\right] \tag{2.3.37}$$

Once the frequency is known, it is easy to obtain the characteristic time interval Δt_{stirr} between two vortexes (also known as "stirring" time [55], [56])

$$\Delta t_{stirr} = \frac{1}{\lambda_s \Delta} \tag{2.3.38}$$

The length of the eddy l on the other hand, is calculated by means of a PDF distribution $f(l)$, eq. 2.3.39, given by [58], that ensures a higher probability to get an eddy size close to the Kolmogorov scale η rather than to the integral length scale Δ:

$$f(l) = \frac{5}{3} \frac{l^{-8/3}}{\eta^{-5/3} - \Delta^{-5/3}} \qquad \eta \leq l \leq \Delta \tag{2.3.39}$$

In summary, the reaction-diffusion equation, eq. 2.3.35, is integrated using a time-step determined by the chemical process Δt_c. At each time-step, the stirring time interval Δt_{stirr}, the total stirring time t_{stirr} and the total integration time t_{int} are calculated:

$$t_{int} = t_{int} + \Delta t_c \tag{2.3.40}$$

$$t_{stirr} = t_{stirr} + \Delta t_{stirr} \tag{2.3.41}$$

During the time integration it may occur that the total stirring time is greater than the total time:

$$t_{stirr} > t_{int} \tag{2.3.42}$$

if the above condition is verified, a vortex event (triplet mapping algorithm) is applied to the scalar field, modeling thus explicitly the turbulent convection F_k at the sub-grid scales.

The large scale process is modeled by eq. 2.3.34 and represents the mass transfer among the cells due to the resolved velocity and the turbulent fluctuations. It couples the subgrid mixing process with the large scale transport processes. In its original formulation the equation is not resolved numerically, but modeled in a lagrangian way, where portions of the cells in the LEM-domain are transferred to neighboring grid cells. This is called as "splicing algorithm" [58] and is illustrated in Fig. 2.3.1.

In this work the lagrangian transport of the LEM-cells is not considered and another formulation has been used in order to reduce both the computational efforts and the numerical implementation. The species scalar equation, eq. 2.3.35, is solved in the LEM domains and integrated until the sub-grid integration time t_{int} matches the solver time-step Δt: $t_{int} = \Delta t$. When this occurs, the integration provides the distribution of the species mass fraction along

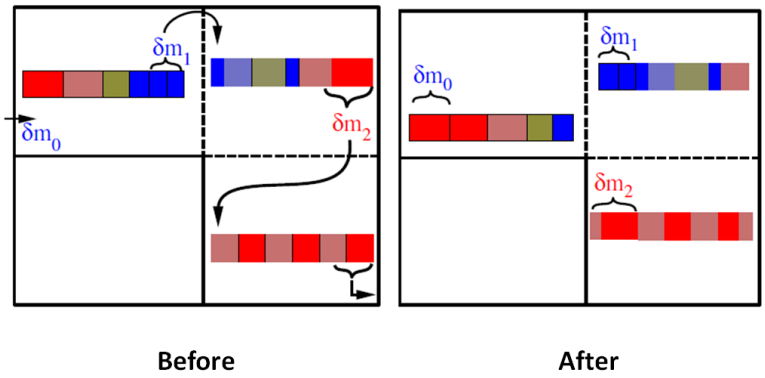

Figure 2.3.1: Schematic representation of the large scale process according to the original LEM formulation [2].

the one-dimensional domains at each solver time-step. Therefore, one can derive that for every computational cell a single value for the species mass fraction in the LEM-domains $\bar{Y}^*_{LEM,i}$ that takes into account all the sub-grid processes. This is computed as a weight-averaged value of the mass fraction with the local density:

$$\bar{Y}^*_{LEM,i} = \frac{\sum_{k=1}^{N_{lem}} \rho_k Y_{k,i}}{\sum_{k=1}^{N_{lem}} \rho_k} \tag{2.3.43}$$

where k indicates the k-th LEM-cell, i indicates the species mass fraction, N_{lem} is the number of the LEM-cells in every cell. In this alternative formulation of the LEM model the $\bar{Y}^*_{LEM,i}$ is used to calculate the source term for the filtered species mass fraction equation, in the same way as the source term is modeled within the Eddy Dissipation Concept Model (EDC) or the Fractal Model (FM). This for the species i is expressed as follows:

$$\tilde{\omega}_i = \rho \frac{\bar{Y}^*_{LEM,i} - Y^n_i}{\Delta t} \tag{2.3.44}$$

where Y^n_i is the mass fraction of the species i of previous time-step n of the main flow-solver and is the input condition for the sub-grid integration.

To reduce considerably the computational time, in this work a conjunction of the LEM and EDC formulation (hybrid LEM/EDC-model) is considered. The model works very simply, dividing the fluid region into two parts: one part of the domain solved by the LEM and the remaining by the EDC model. The LEM model is activated only in the region where the turbulent chemistry interaction occurs (i.e., flame front). This zone can be empirically defined as the portion of the computational domain where the concentration of the radical OH is higher than 600ppm [59].

2.4 Numerical Approach

The numerical simulations, presented and discussed in the thesis, are calculated by means of the commercial code ANSYS CFX v14[60] and by the DLR in-house code THETA (**T**urbulent **H**eat **E**xtension of the **TA**U)[49, 61]. The commercial ANSYS CFX software is a CFD code that can simulate a wide range of physical phenomena considering the high choice of models. Thus, it can solve the interactions between flow, turbulent mixing, heat release and chemical reactions. It uses an implicit finite volume approach and a compressible solver for solving the Navier-Stokes equations. More details can be found in [60]. The THETA code was developed at the Institute of Combustion Technology of the German Aerospace Center (DLR) for the simulation of complex combustion problems. The solver is based on a finite-volume formulation on unstructured meshes and a low-Mach number formulation of the transport equations. It can run on multiproccessors thanks to a domain-based parallelization. A variety of the most popular turbulence models is implemented according to three different approaches: unsteady Reynolds-Averaged Navier-Stokes (URANS), Scale-Adaptive Simulations (SAS) [39], and Large-Eddy Simulations (LES). The code provides also several models for turbulence-combustion coupling. Thus, a simple Eddy-Dissipation Model (EDM) [45] and a more complex assumed probability density function method (APDF) [49] can be used. Eventually, a Lagrangian Monte-Carlo method for the solution of the transported PDF model equations is also available[20].

3 Validation of the 0D reactive code

In this chapter a validation of a 0D-code for the calculation of the auto-ignition process of perfectly homogeneous mixtures is discussed. This validation is necessary since the code is used in the EDC and FM combustion models for the 3D calculations. The chemical oxidation mechanism under investigations regard the hydrogen-air and methane-air system.

3.1 Stiff Problems in chemical kinetics

Chemical kinetics problems are often mathematically represented by a stiff system [62]. A kinetic mechanism is composed by a large number of chemical species, whose concentrations grow (or decay) over time with largely different rates depending on different time scale. This means that the characteristic lifetimes of some species involved in the reaction process can be many orders of magnitude shorter than those of other species whose evolution in time slowly changes. This causes considerable problems for the numerical solver, since the time integration should take into account the time scale whereby the fast species evolve [63]. The stiffness in chemical problems is essentially due to the large scale separation and as a consequence different dynamics of the species over the time. To solve efficiently such a stiff system, the following two approaches can be considered:

1. an automatic adaption of the time-step as the solution proceeds, based on the estimated error at a particular point in time (stiff ODE solver) [64];

2. a reduction of the stiffness in the system by opportunely treating short-lived species, present in small amounts (this is normally a cause of stiffness) and approximating their time evolution by a slower reacting component present in proportionally larger amount (QSSA approximation, CSP,...) [65], [66].

In this work only the first method has been used and an open source software CVODE [67] was implemented in the DLR-THETA combustion code for the numerical integration of the chemical kinetics problems.

3.2 A stiff solver for chemical kinetics problems: SUNDIALS-CVODE

CVODE is a solver for systems of ordinary differential equations (ODEs). It belongs to the SUNDIALS (SUite of Nonlinear and DIfferential/ALgebraic equation Solvers) [67] solvers package for the resolution of numerical problems. These families of solvers are suitable for either integration methods for ODEs or sensitivity analysis or for systems of non-linear algebraic equations. CVODE contains methods for the solution of both stiff and nonstiff initial value problems. In the case of stiff problems, the linear systems can be solved by direct (dense or band) methods (in serial environments only), or by a preconditioned Krylov method, GMRES [64]. In the direct cases, the user can supply the Jacobian system or let the solver generate it internally. In the case of GMRES, the user can either supply a preconditioner or use one that is included with the package. The latter is a block-banded preconditioner based on domain decomposition. This code has been implemented in the DLR-in house THETA code and adapted for solving chemical kinetics problems for the ignition of hydrogen and methane in air. In the following paragraph a numerical validation of the code is given, the numerical results are compared with those obtained using a direct-integration solver with constant time-step and using a open source stiff solver CANTERA [19].

3.3 Numerical validations of the SUNDIALS-stiff solver

The numerical validation of the SUNDIAL-CVODE stiff solver, implemented in the THETA code, is performed considering the typical ignition delay time problems for a perfectly stirred reactor PSR. This is necessary since the turbulent-combustion models, which will be used for the simulations of the combustion process, are based on the numerical integration of a PSR in each computational cell. The computations were conducted by means of a direct integration solver, which solves the ODE equations with a constant time-step approach, with the CANTERA software [19] and with the SUNDIALS-CVODE solver. The problem under investigation regards the ignition of the hydrogen-air and methane-air system, analyzed at different initial temperature and pressure conditions.

The combustion process of the hydrogen-air mixture is captured in approximately twenty elementary reactions and about ten species [68]. The oxidation mechanism of methane in air on the other hand, involves several species and hundreds of reactions. Most of them are present as reaction intermediates in the processes of combustion of more complex hydrocarbons. According to the DRM-19 mechanism (derived from GRI-3.0 mechanism) [69], the oxidation of pure-methane presents 19 species with 84 reversible reactions.

The numerical results for the hydrogen-air mixture are reported in Fig. 3.3.1.a-b, respec-

tively for $p = 1$bar and $p = 2$bar. The initial temperature values considered are $T_i = 900$K, $T_i = 1200$K and $T_i = 1500$K. With the increase of the T_i the ignition-time delay decreases significantly due to the higher level of energy at which the chemical reactions occur. The computation with the SUNDIALS solver matches perfectly those performed with CANTERA and with the direct-integration both for low and higher pressures. In order to demonstrate the speed-up in the time-integration of the PSR equations, the number of the integration steps required for the previous solvers are reported in Fig. 3.3.2. The stiff solver is able to obtain a numerical solution with almost 4000 iterations, conversely, both CANTERA and the direct-integration solver require a larger number of iterations, especially at low temperature values. Analogous results are obtained for the methane-air mixture. The simulated ignition time delays and the speed up comparisons are illustrated in 3.3.3 and 3.3.4.

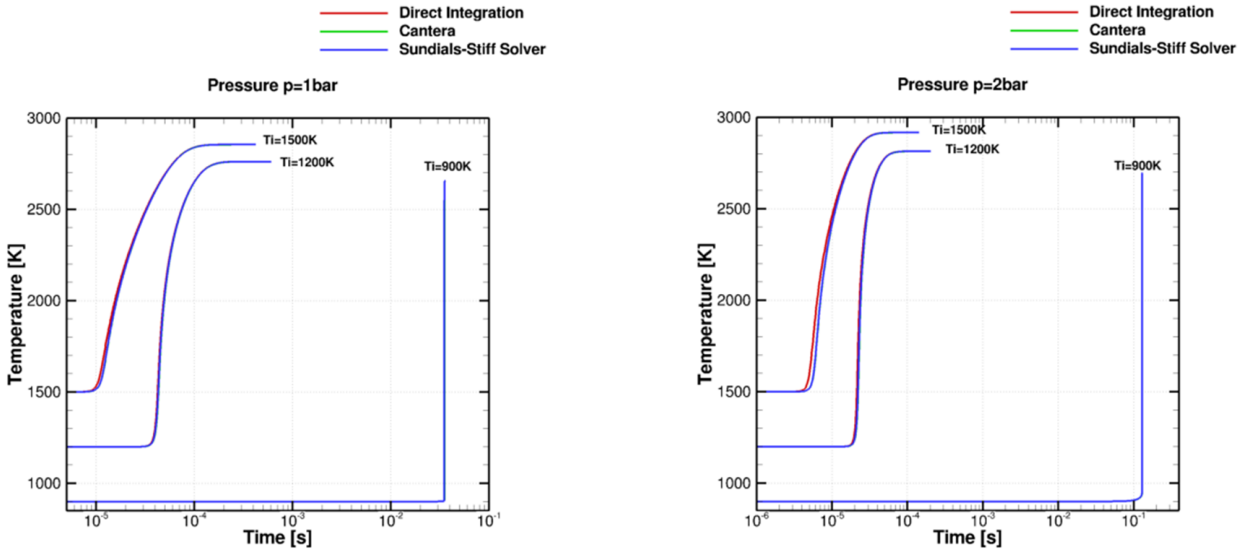

(a) (b)

Figure 3.3.1: Ignition time delay for the hydrogen-air mixture at different initial temperatures and pressures: p=1bar (a) and p=2bar (b).

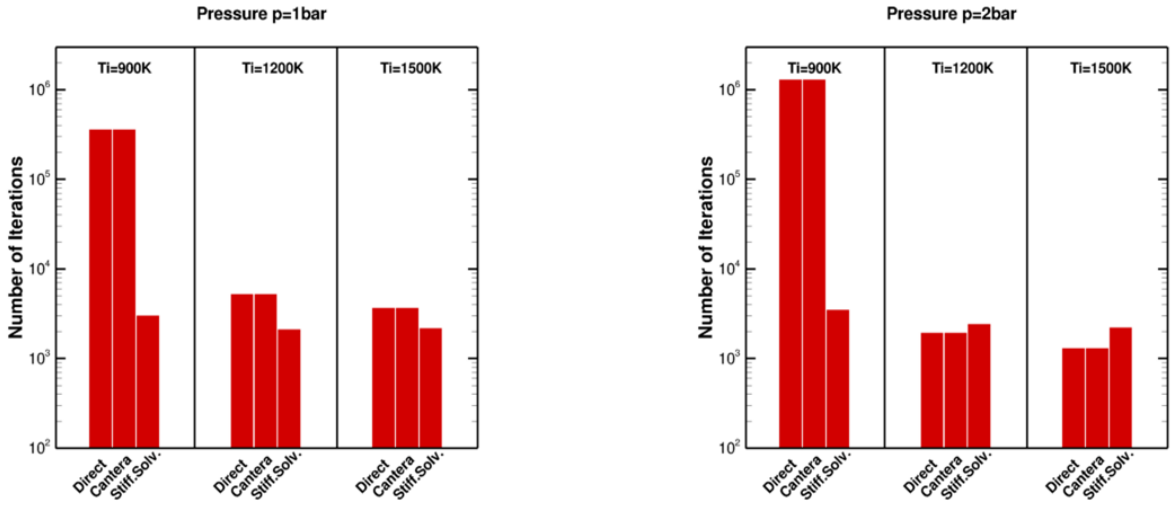

(a) (b)

Figure 3.3.2: Comparison of the speed-up of the stiff solver in respect to CANTERA software and direct integration for the hydrogen-air mixture: p=1bar (a) and p=2bar (b).

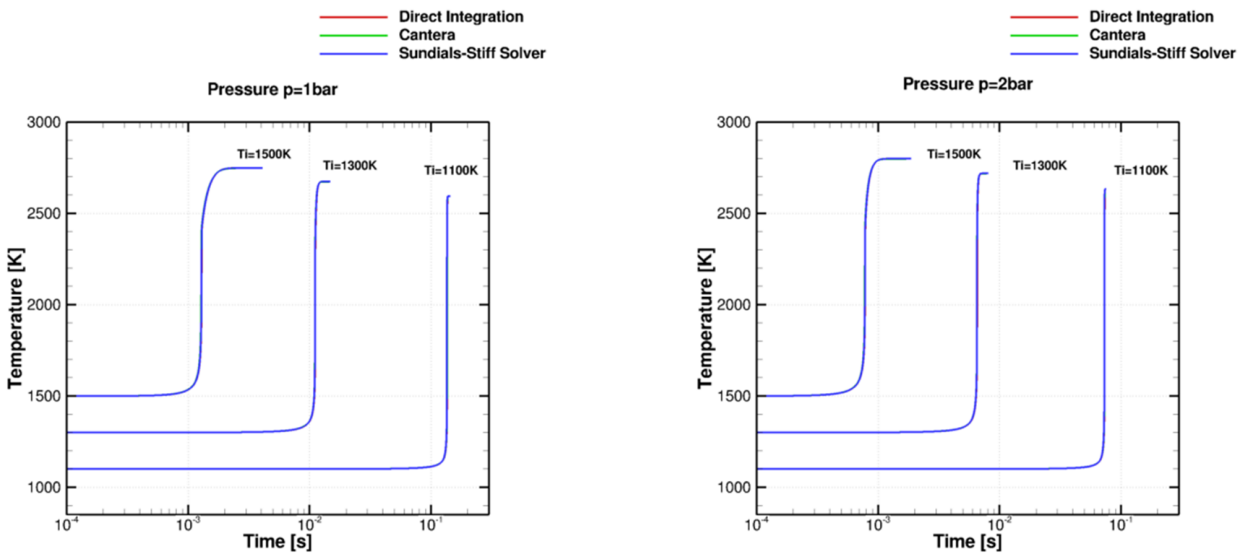

(a) (b)

Figure 3.3.3: Ignition time delay for the methane-air mixture at different initial temperatures and pressures: p=1bar (a) and p=2bar (b).

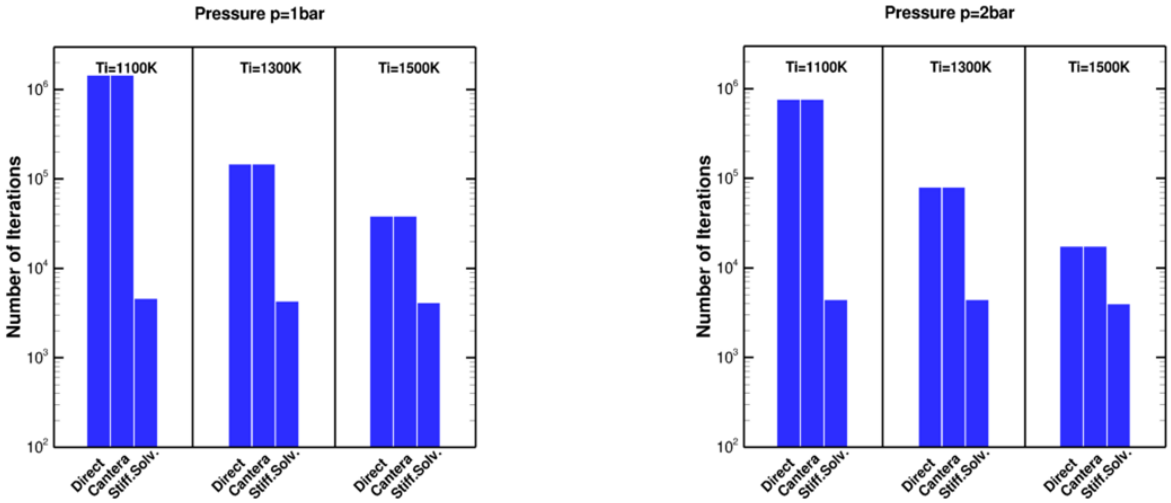

(a) (b)

Figure 3.3.4: Comparison of the speed-up of the stiffsolver in respect to CANTERA software and direct integration for the methane-air mixture: p=1bar (a) and p=2bar (b).

4 Validation combustion Models

4.1 Test case 1: Non-premixed, Turbulent Hydrogen-air Flame (H3-Flame)

The first test case considered here is a non-premixed, unconfined, turbulent hydrogen-air flame: the "H3-Flame" [7]. The burner has a very simple geometry. It presents two coaxial cylindrical pipes: the innermost tube represents the fuel injector, with a diameter of only 8mm and an outer one that injects pure air as a coflow. Fuel consists of a mixture of hydrogen diluted with 50% of nitrogen. Its velocity at the fuel nozzle is approximately 34.8 m/s. On the other hand, air presents a significantly lower velocity value (0.2 m/s) at the air coflow outlet, due to the geometry of the cylindrical tube, whose diameter is several times larger than the inner fuel pipe one.

The two flows come into contact after the injection and a diffusion flame evolves, which is stabilized at the edge of the smaller pipe. Fig. 4.1.1 shows a sketch of the test flame.

The numerical simulations were performed on a simplified version of the real geometry, using the computational domain proposed in the work of Fiolitakis at al. [20]. This includes a long fuel pipe to generate a fully developed turbulent velocity profile at the injection in the chamber and a small sector of the coflow for the flame stabilization. Due to the symmetry of the problem, only a 10 degree azimuthal sector is considered for the simulations [7]. The computational domain is illustrated in Fig. 4.1.2.

The simplified geometry was meshed with an in-house developed algorithm. Due to its regularity and simple shape, a structured mesh following a uniform pattern was considered. The mesh presents 16840 hexahedral and 410 prismatic cells resulting in 35089 nodes.

Since the fuels injected is a mixture of hydrogen and nitrogen, the O'Connaire mechanism [70] developed for modeling the hydrogen oxidation was considered for the numerical simulations. Temperature and species mass fractions were measured using the Raman technique, whereas the velocity field was measured by LDA [71].

Figure 4.1.1: Sketch of the H3 test flame [3].

4.1.1 Numerical Results: Influence of the combustion models

Steady state simulations were carried out with a RANS approach using the standard $k-\varepsilon$ model. Combustion was solved by means of the EDC, FM and hybrid $LEM-EDC$ models. Numerical convergence was assessed following the residual criteria: for the following CFD calculations, an RMS residual level lower than 1E-8 was considered, indicating solutions converged. The constant parameters of the $k-\varepsilon$ model have a deep influence on the prediction of the characteristics of the flame in terms of flame position and temperature peak [59]. The over-prediction of the $k-\varepsilon$ model for the spreading rate in plane jets is well known [72] and is usually removed by modifying the C_1 constant in the ε transport equation. According to the work of Launder and Spalding [73], the standard optimum value was set to $C_1 = 1.44$. Unfortunately this constant does not have a universal value and it may vary depending on the particular problem of interest.

In the following section, the simulations are performed with two values for C_1: the reference value of 1.44 and a slightly higher one, 1.6. The choice of $C_1 = 1.6$ is motivated in order to prove the high sensitivity of the test case on this model constant and to reduce the error introduced by the model in the prediction of the spreading rate.

Regarding the EDC method, two variants for the calculations of the length of the fine scale structures were introduced in the code. The normal formulation is based on the formula:

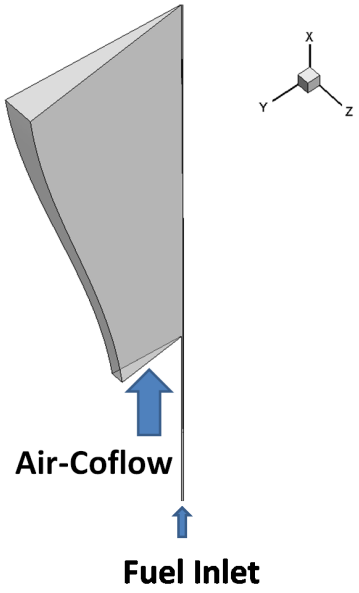

Figure 4.1.2: Simplified geometry for the numerical simulations.

$$\gamma = \left(\frac{3C_{D2}}{4{C_{D1}}^2}\right)^{1/4} \left(\frac{\nu\varepsilon}{k^2}\right)^{1/4} \tag{4.1.1}$$

whereas the alternative approach consists in introducing a different rate of diffusivity for the momentum and mass. This can be taken into account by replacing the expression for the molecular viscosity with $\mu = Sc \cdot \rho \cdot D$ where Sc is the Schmidt number:

$$\gamma = \left(\frac{3C_{D2}}{4{C_{D1}}^2}\right)^{1/4} \left(\frac{\rho DSc}{k^2}\right)^{1/4} \tag{4.1.2}$$

4.1.1.1 Axial Profiles with the standard $k-\varepsilon$ approach

The results shown from Fig. 4.1.3 to Fig. 4.1.8 illustrate the axial behavior of the main characteristics of the flame. In the following plots, the red line represents the simulation with the Fractal Model, blue and green lines simulations with the EDC model, using respectively for the definition of the fine scale length eq. 4.1.1 and eq. 4.1.2, and the orange line calculation with the hybrid LEM-EDC model. On the left hand side the simulation with $C_1 = 1.44$ is shown, whereas the calculation with $C_1 = 1.6$ is illustrated on the right.

The axial profiles of the velocity are presented in Fig. 4.1.3 and compared against the experimental data. The numerical values are extracted along the main axis of the burner: from the fuel nozzle position until a distance equal to 100 times the fuel pipe diameter. The velocity trend shows a maximum at the exit of the fuel nozzle. After this point, the cross sectional dimension of the burner increases rapidly, the velocity reduces and the mixing

process between the $H_2 - N_2$ fuel mixture and the oxidizer occurs. This mechanism favors the flame stabilization in combination with the slow laminar coflow velocity.

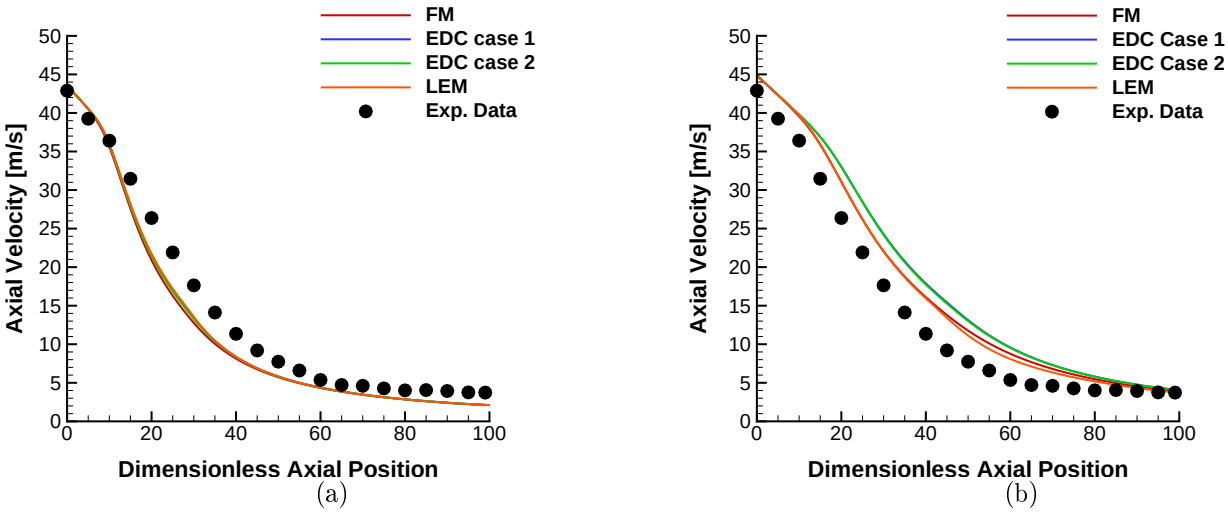

Figure 4.1.3: Velocity axial profiles with C_1=1.44 (a) and C_1=1.6 (b). Red line simulation with the Fractal Model, blue and green lines simulations with the EDC model with different definition for γ, orange line calculation with the hybrid LEM-EDC model, black circle experimental data.

The velocity profiles match the experimental data quite well in the region close to the fuel injection and further downstream where everything is burnt. In the central region, the velocity obtained from the simulations tends, depending on the value of the C_1 constant, to underestimate or overestimate the experimental data. All calculations, performed respectively with FM, EDC, LEM-EDC model, exhibit approximately the same curve trend. This indicates how strong the dependency is for this test case from the turbulence models with respect to the combustion models. The turbulence models in fact, can produce erroneous results for the flow field, so that the combustion models cannot be tested reliably.

In Fig. 4.1.4 the temperature profiles obtained with the numerical simulations are presented. The temperature increases from the constant inlet value of 300 K due to the combustion process, reaches a maximum at approximately 20 diameters from the fuel nozzle and thereafter decreases significantly approaching again the inflow value. The C_1 constant is responsible again of the flame characteristics and in particular of the temperature peak position. The maximum in the numerical simulations presents a pronounced shift in respect to the real measured peak: the position is shifted to the left with $C_1 = 1.44$ and to the right side with 1.6.

Fig. 4.1.5 shows the H_2 mass fractions profiles. The values of the H_2 mass fractions are under- or overestimated depending on the C_1 constant, as discussed previously. The

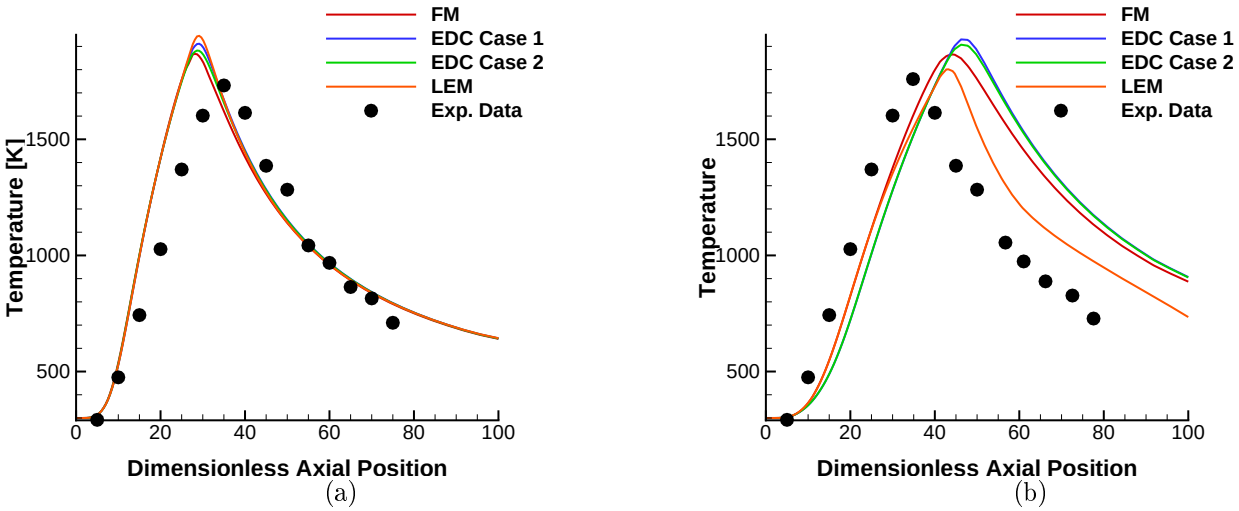

Figure 4.1.4: Temperature axial profiles with C_1=1.44 (a) and C_1=1.6 (b). Red line simulation with the Fractal Model, blue and green lines simulations with the EDC model with different definition for γ, orange line calculation with the hybrid LEM-EDC model, black circle experimental data.

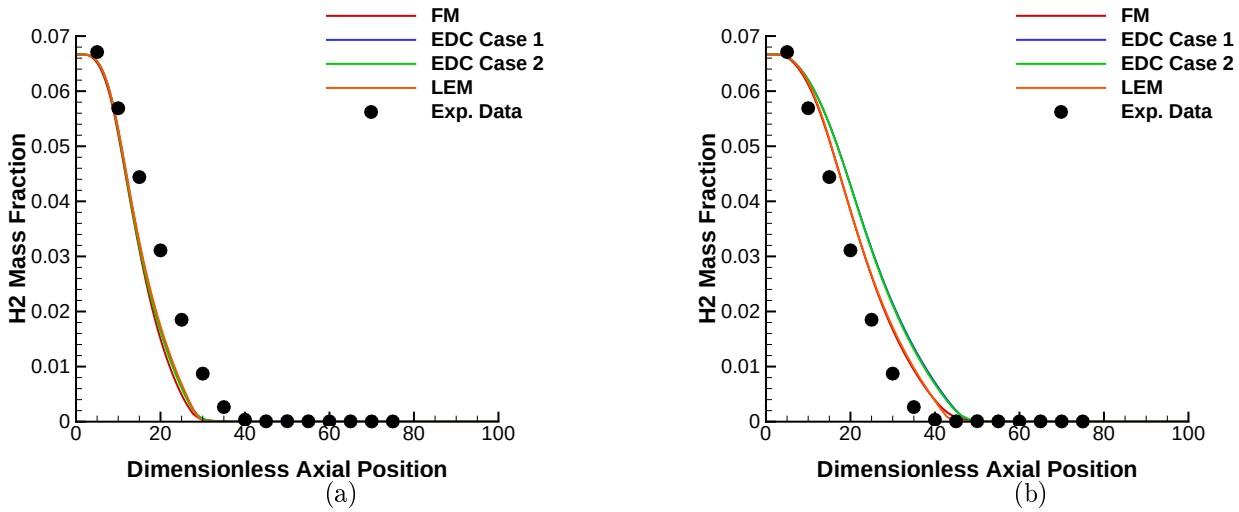

Figure 4.1.5: Y_{H2} axial profiles with C_1=1.44 (a) and C_1=1.6 (b). Red line simulation with the Fractal Model, blue and green lines simulations with the EDC model with different definition for γ, orange line calculation with the hybrid LEM-EDC model, black circle experimental data.

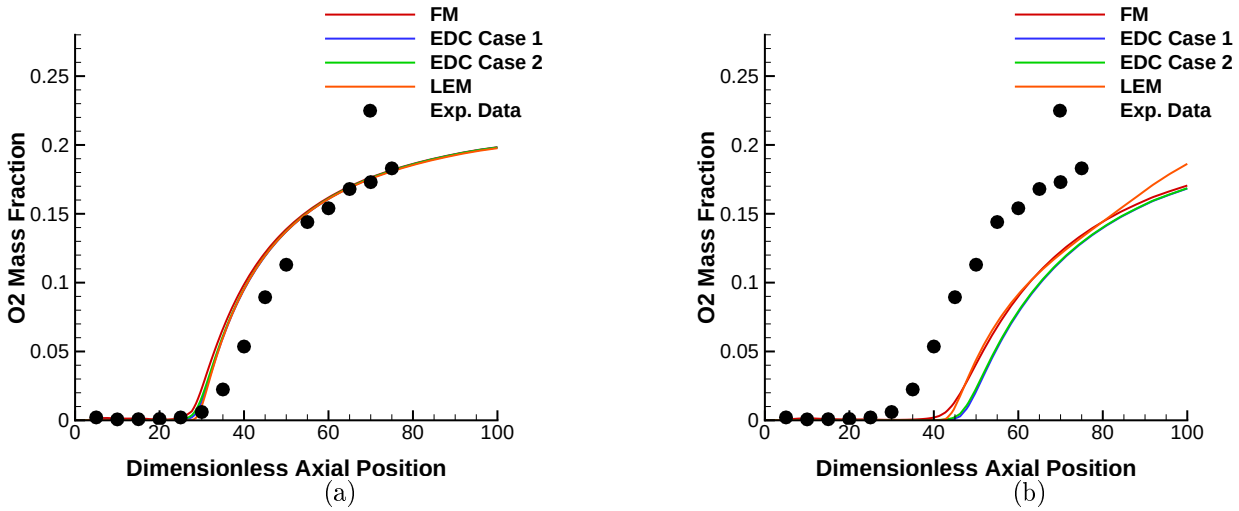

(a) (b)

Figure 4.1.6: Y_{O2} axial profiles with C_1=1.44 (a) and C_1=1.6 (b). Red line simulation with the Fractal Model, blue and green lines simulations with the EDC model with different definition for γ, orange line calculation with the hybrid LEM-EDC model, black circle experimental data.

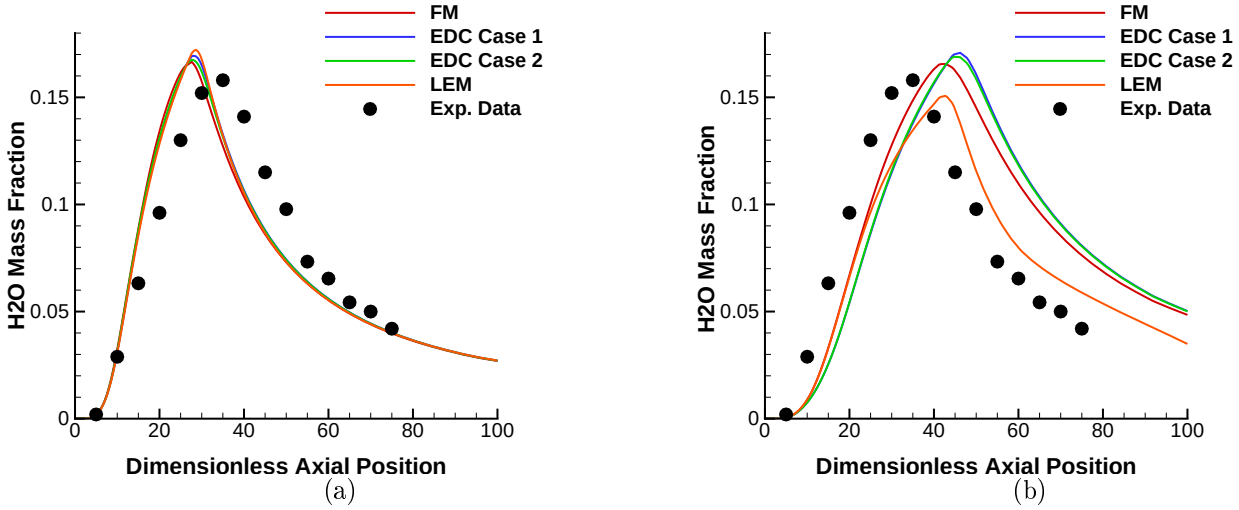

(a) (b)

Figure 4.1.7: Y_{H2O} axial profiles with C_1=1.44 (a) and C_1=1.6 (b). Red line simulation with the Fractal Model, blue and green lines simulations with the EDC model with different definition for γ, orange line calculation with the hybrid LEM-EDC model, black circle experimental data.

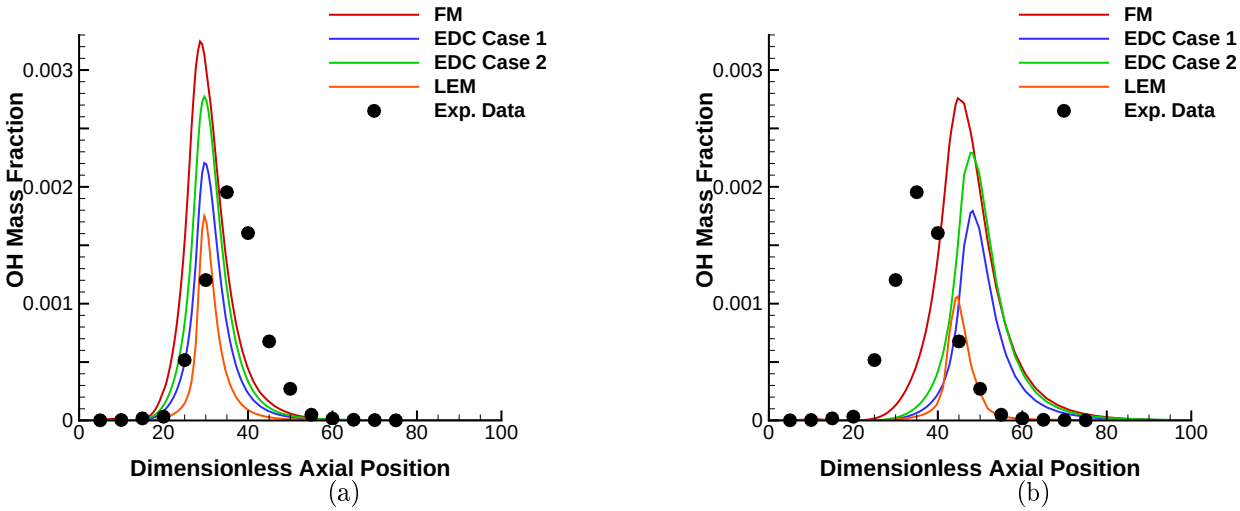

Figure 4.1.8: Y_{OH} axial profiles with C_1=1.44 (a) and C_1=1.6 (b). Red line simulation with the Fractal Model, blue and green lines simulations with the EDC model with different definition for γ, orange line calculation with the hybrid LEM-EDC model, black circle experimental data.

sensitivity with this constant is also clear in Fig. 4.1.7, Fig. 4.1.6 and Fig. 4.1.8 where the axial profiles for the O_2, H_2O and OH mass fractions are presented.

In general the modeling of the spreading rate with $C_1 = 1.6$ leads to a worsening of the results in the downstream region, whereas the use of the reference value provides better results in term of the flow characteristics. Regarding the combustion modeling, the test-case is less sensitive to the turbulent-chemistry interaction and it is strongly dependent on the turbulence model. The use of different combustion models leads to slightly different axial values.

4.1.1.2 Radial Profiles with the standard $k-\varepsilon$ approach

The results presented from Fig. 4.1.9 to Fig. 4.1.13 are the radial profiles for the velocity at different locations downstream of the injection. The profiles are extracted at $x = 5d$, $20d$, $40d$, $60d$, $80d$ respectively. The first position $x = 5d$ is closer to the pipe and it feels the effect of the high inflow velocity. Observing the results at locations $x = 20d$ and $x = 40d$, the velocity deviates from the measurements especially in the axis region, but recovers the agreement in the coflow region. On the other hand the last two locations show that the flow field tends to homogenize, since the velocity close to axis decreases and enhances in the upper part. All of the results computed with $C_1 = 1.6$ reveal a substantial deviation in the whole radial region, whereas the runs with $C_1 = 1.44$ predict the velocity trend better.

The temperature radial profiles are illustrated from Fig. 4.1.14 to Fig. 4.1.18. The plots

at the position $x = 5d$ exhibit a monotonic increase for the temperature from the axis to a particular point, where a peak can be observed, then it follows a strong reduction until the coflow value is approached. At $x = 20d$, the flame shows the same behavior as at $x = 5d$, characterized by a minimum at the axis, a maximum in the domain and a progressively reduction to the coflow value. For the further downstream locations, respectively at $x = 40d$, $x = 60d$ and $x = 80d$, the temperature reveals instead the maximum on the axis and it progressively reduces radially. The calculations with $C_1 = 1.6$, show again the worst results with large discrepancies with respect to the experimental measurements.

In conclusion, the reason of the under/over-prediction of the simulations is to attribute to the turbulence model with its inexact estimation of the spreading rate in jet-flows.

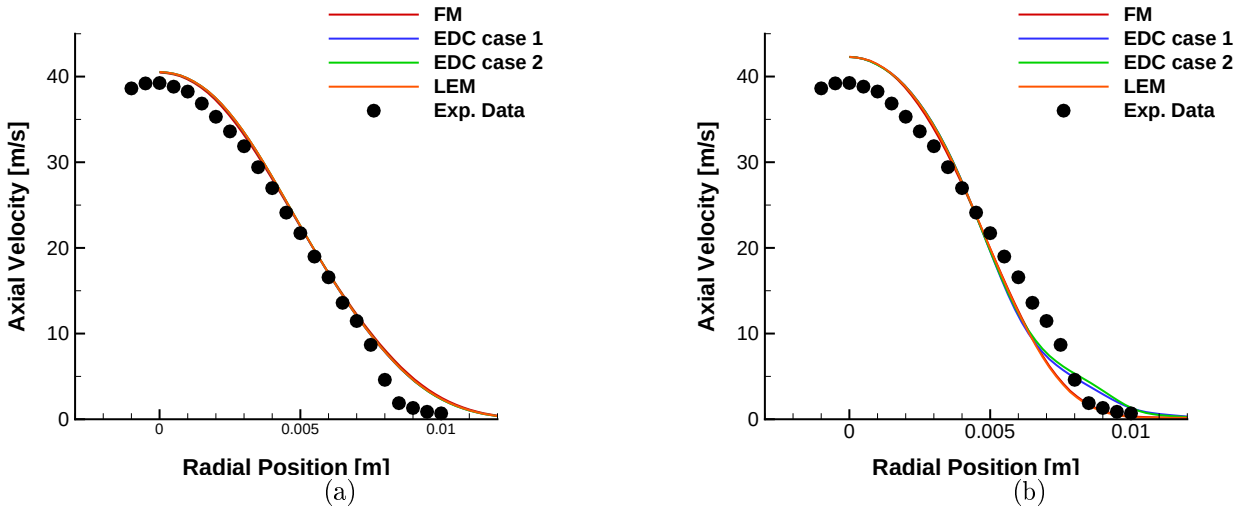

Figure 4.1.9: Velocity radial profiles with C_1=1.44 (a) and C_1=1.6 (b) at x=5d. Red line simulation with the Fractal Model, blue and green lines simulations with the EDC model with different definition for γ, orange line calculation with the hybrid LEM-EDC model, black circle experimental data.

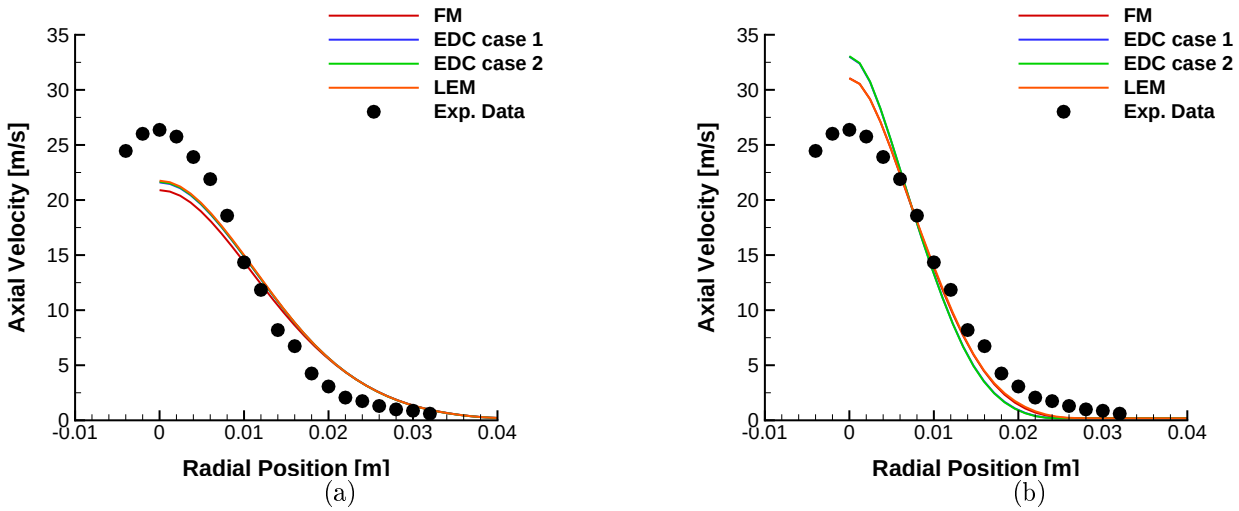

Figure 4.1.10: Velocity radial profiles with C_1=1.44 (a) and C_1=1.6 (b) at x=20d. Red line simulation with the Fractal Model, blue and green lines simulations with the EDC model with different definition for γ, orange line calculation with the hybrid LEM-EDC model, black circle experimental data.

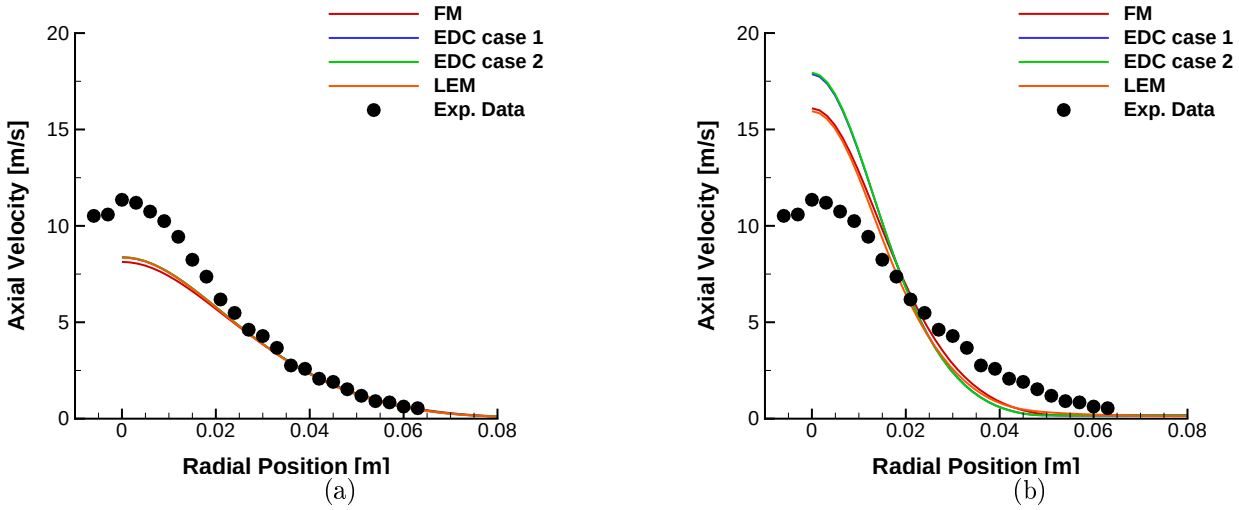

Figure 4.1.11: Velocity radial profiles with C_1=1.44 (a) and C_1=1.6 (b) at x=40d. Red line simulation with the Fractal Model, blue and green lines simulations with the EDC model with different definition for γ, orange line calculation with the hybrid LEM-EDC model, black circle experimental data.

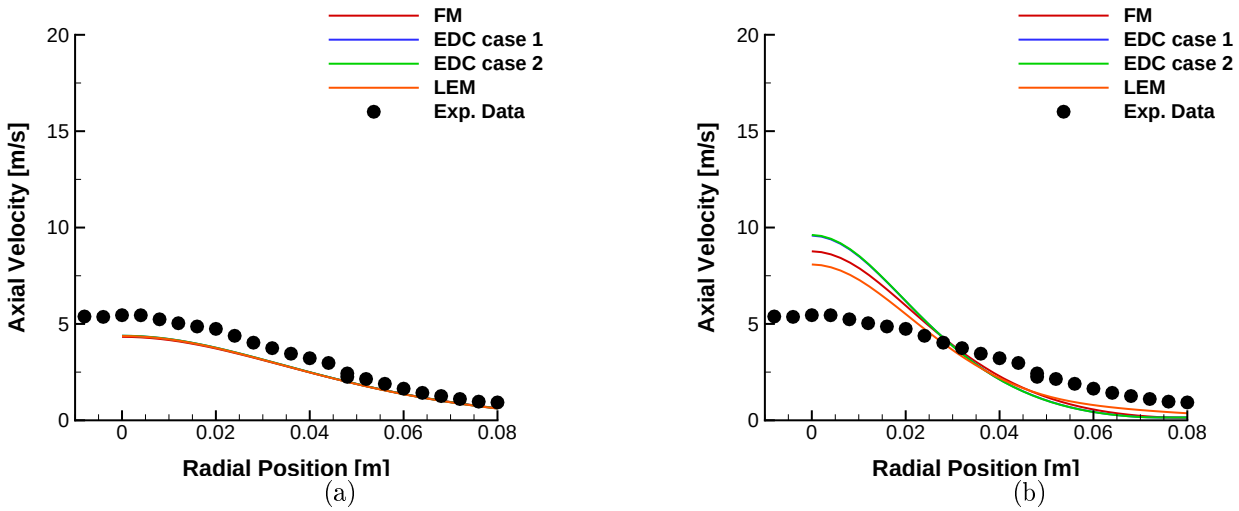

(a) (b)

Figure 4.1.12: Velocity radial profiles with C_1=1.44 (a) and C_1=1.6 (b) at x=60d. Red line simulation with the Fractal Model, blue and green lines simulations with the EDC model with different definition for γ, orange line calculation with the hybrid LEM-EDC model, black circle experimental data.

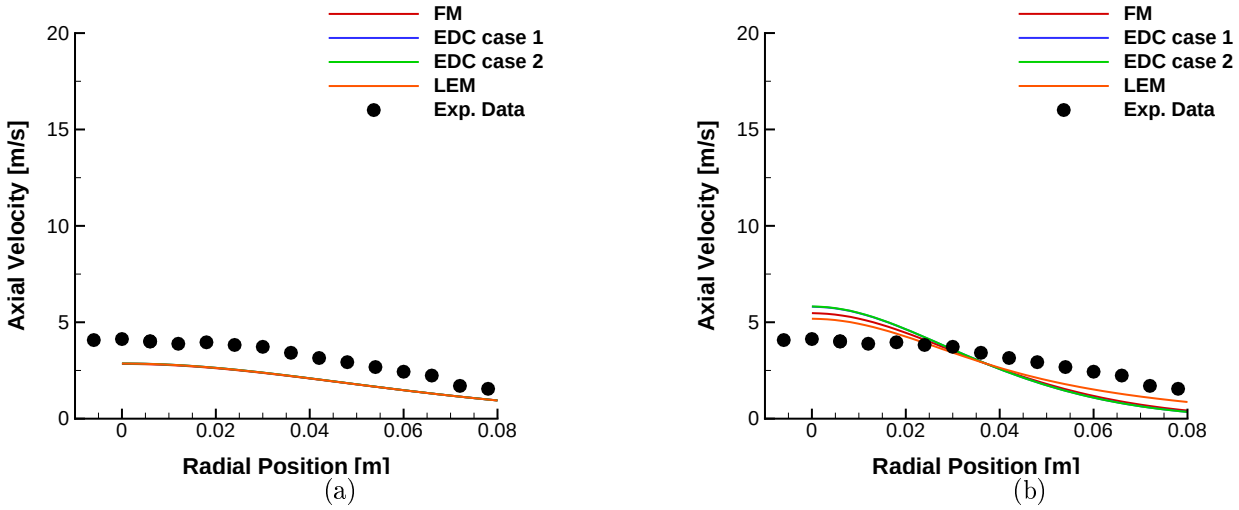

(a) (b)

Figure 4.1.13: Velocity radial profiles with C_1=1.44 (a) and C_1=1.6 (b) at x=80d. Red line simulation with the Fractal Model, blue and green lines simulations with the EDC model with different definition for γ, orange line calculation with the hybrid LEM-EDC model, black circle experimental data.

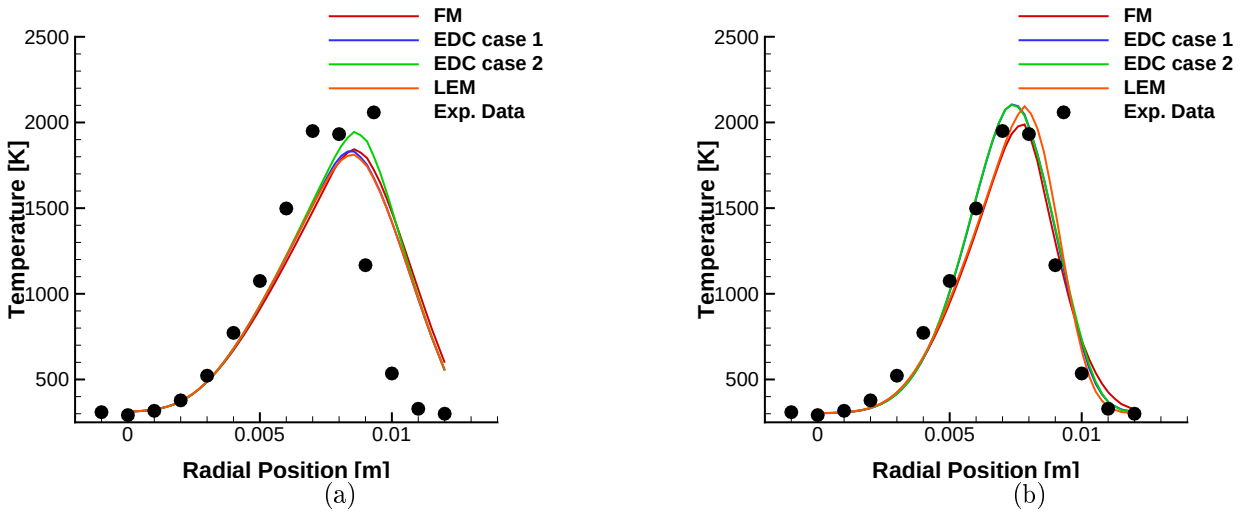

Figure 4.1.14: Temperature radial profiles with C_1=1.44 (a) and C_1=1.6 (b) at x=5d. Red line simulation with the Fractal Model, blue and green lines simulations with the EDC model with different definition for γ, orange line calculation with the hybrid LEM-EDC model, black circle experimental data.

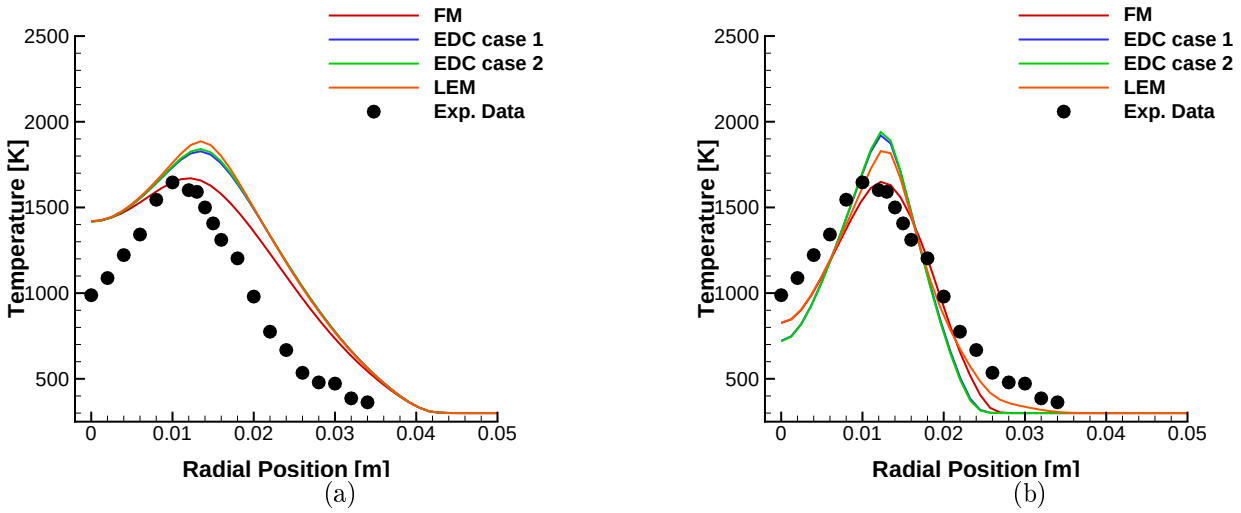

Figure 4.1.15: Temperature radial profiles with C_1=1.44 (a) and C_1=1.6 (b) at x=20d. Red line simulation with the Fractal Model, blue and green lines simulations with the EDC model with different definition for γ, orange line calculation with the hybrid LEM-EDC model, black circle experimental data.

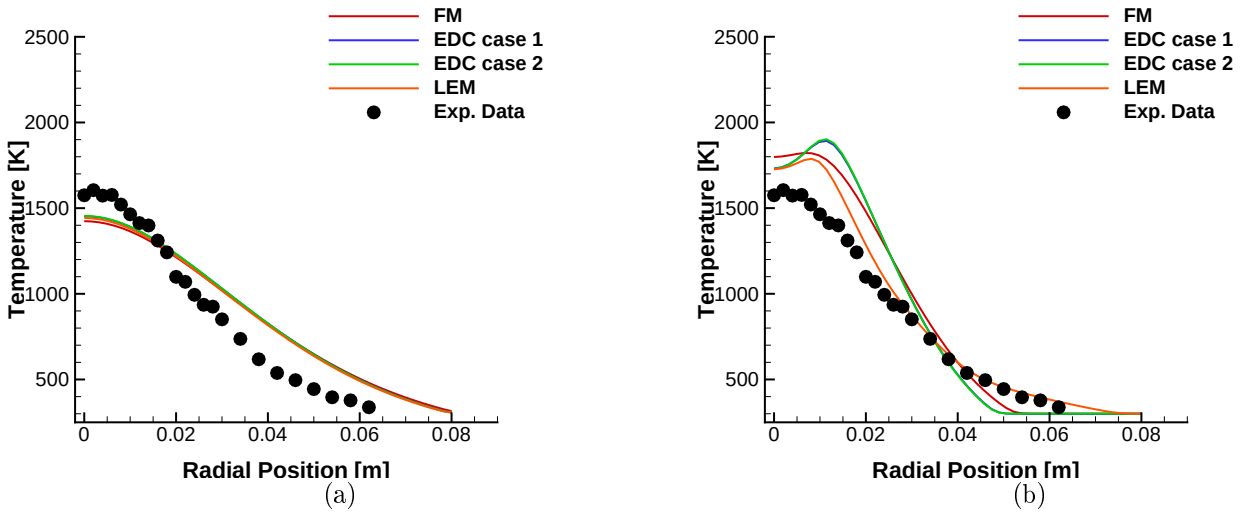

(a) (b)

Figure 4.1.16: Temperature radial profiles with C_1=1.44 (a) and C_1=1.6 (b) at x=40d. Red line simulation with the Fractal Model, blue and green lines simulations with the EDC model with different definition for γ, orange line calculation with the hybrid LEM-EDC model, black circle experimental data.

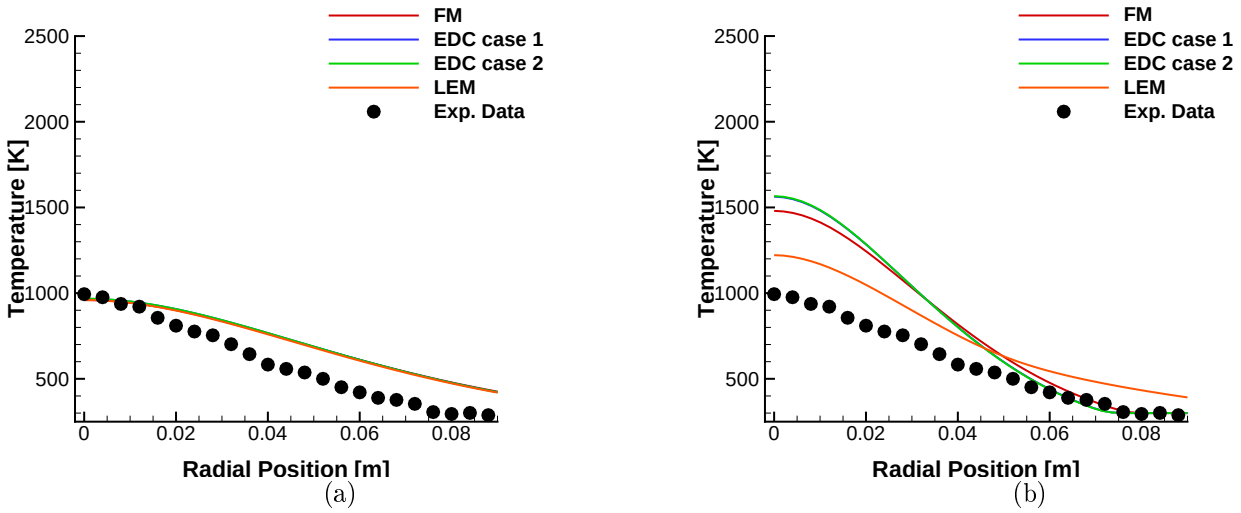

(a) (b)

Figure 4.1.17: Temperature radial profiles with C_1=1.44 (a) and C_1=1.6 (b) at x=60d. Red line simulation with the Fractal Model, blue and green lines simulations with the EDC model with different definition for γ, orange line calculation with the hybrid LEM-EDC model, black circle experimental data.

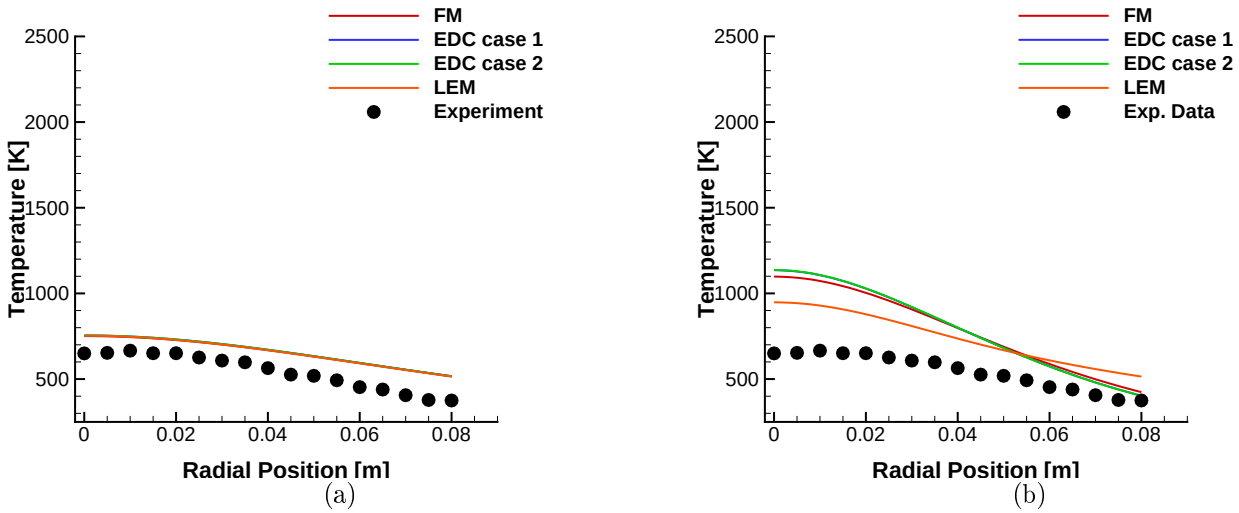

Figure 4.1.18: Temperature radial profiles with C_1=1.44 (a) and C_1=1.6 (b) at x=80d. Red line simulation with the Fractal Model, blue and green lines simulations with the EDC model with different definition for γ, orange line calculation with the hybrid LEM-EDC model, black circle experimental data.

4.1.2 Numerical Results: Influence of the Turbulence Models

The previous paragraph has shown a small sensitivity of the results for the "H3-Flame" test case on the combustion models. It was observed that when the reference value for the C_1 constant of the $k-\varepsilon$ model is used, a fairly good agreement against the experimental data was found. The axial velocity and temperature profiles present in fact, a remarkable shift upwards/downward with respect to the experimental data depending on the value of this constant, indicating the significant inefficiency of the turbulence model for the simulations. In this paragraph an alternative approach will be first discussed theoretically and then applied for new calculations. Steady-state RANS computations will be run employing the $k-\varepsilon$ formulation in conjunction with Pope's jet-round correction [74]. Results will be compared with those obtained with the SST $k-\omega$ model, with the intent to test the capability of the latter in simulating jet-flows. Convergence was assessed by the residual criteria. A target level of 1e-8 was sought in all the simulations.

4.1.2.1 Theory: Pope jet-round correction

Since the standard $k-\varepsilon$ formulation relies strictly on the C_1 and C_2 constants values used in the dissipation rate equation ε, an appropriate estimation of their values is therefore necessary. The choice is unfortunately not unique, depending on the test-case, they can be re-calibrated and optimized to present a better agreement with the experimental data. The reference values of $C_1 = 1.44$ and $C_2 = 1.92$ are not suited for the simulation of all kinds of turbulent flows. The main reason for the inaccuracy lies especially in the rate of destruction of the dissipation $C_2\varepsilon^2/k$, which produces an inexact evaluation of the spreading rate in round-jet flows [74]. To reduce this inadequacy, Pope suggested the introduction of an additional term in the dissipation rate equation ε. The idea behind it was to consider the vortex stretching mechanism occurring in any turbulent flow, acting as the main activator for the turbulent energy cascade from large to small structures. Due to this process, the rate of energy transferred is increased and thus also the dissipation. To account for this phenomenon, the turbulence constant C_2 was adjusted with a function dependent on the vortex shedding invariant χ_p [61].

4.1.2.2 Results: Pope jet-round correction and SST $k-\omega$ model.

In this section the numerical results with Pope's correction for the $k-\varepsilon$ model are presented. To assess the performance of Pope's formulation against other turbulence models, the results are compared with:

- the $k-\varepsilon$ model without POPE jet-round correction using the Fractal Model as combustion model (reference results);

- those obtained using the SST-$k-\omega$ turbulence model using the FM and EDC as combustion model (SST-$k-\omega$ results).

Due to the large computational time required by the LEM-EDC method, no computations have been carried out with this hybrid model. In Fig. 4.1.19(a) and (b) the behavior of the axial velocity is illustrated: runs with Pope's correction show an excellent agreement with the experimental points, whereas the simulations with SST-$k-\omega$ model under-predict the right velocity value as the reference computation with the $k-\varepsilon$ model. The temperature axial profiles are shown in Fig. 4.1.20(a) and (b), the calculations with the correction predict accurately the position of the peak with a small difference for the value of the maximum. Using the SST $k-\omega$ instead, the position remains slightly shifted on the left hand side. The behavior for H_2 mass fraction, Fig. 4.1.21, is reproduced very well with Pope's correction exhibiting the right rate of fuel-consumption. The same occurs for the O_2, Fig. 4.1.22, whose enhancement along the axis follows perfectly the experimental data. The SST formulation instead provides worse results, indicating that this model also suffers the incorrect prediction of the spreading rate in round-jet flows. About the sensitivity of the combustion models, this appears evident in the OH mass fraction, observing the different curve trends shown by the simulations with EDC/FM. The best agreement has been found using the EDC model for combustion in conjunction with Pope's correction.

The radial velocity profiles are shown from Fig. 4.1.25 to Fig. 4.1.29. The calculations with Pope's correction show an excellent agreement with the experimental data, reproducing the radial velocity accurately.

Fig. 4.1.30 to Fig. 4.1.34 illustrate the behavior of the radial temperature profiles. As expected, the simulations with Pope's modification provide again the best agreement against the experimental data. In contrast, the results with the SST model present a very poor agreement with the data and a larger discrepancy against the measurements is observable.

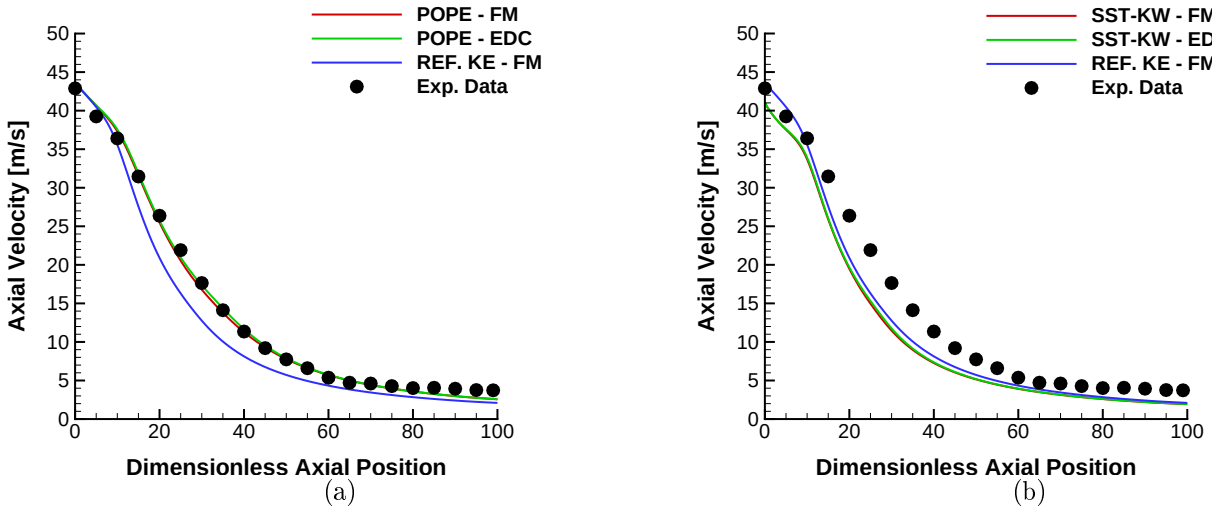

Figure 4.1.19: Axial velocity profiles with POPE jet-round correction (a) and SST-$k-\omega$ model (b). Red line simulation with the Fractal Model, green line simulation with the EDC model, blue line reference simulation with the $k-\varepsilon$ model without POPE jet-round correction using the Fractal Model, black circle experimental data.

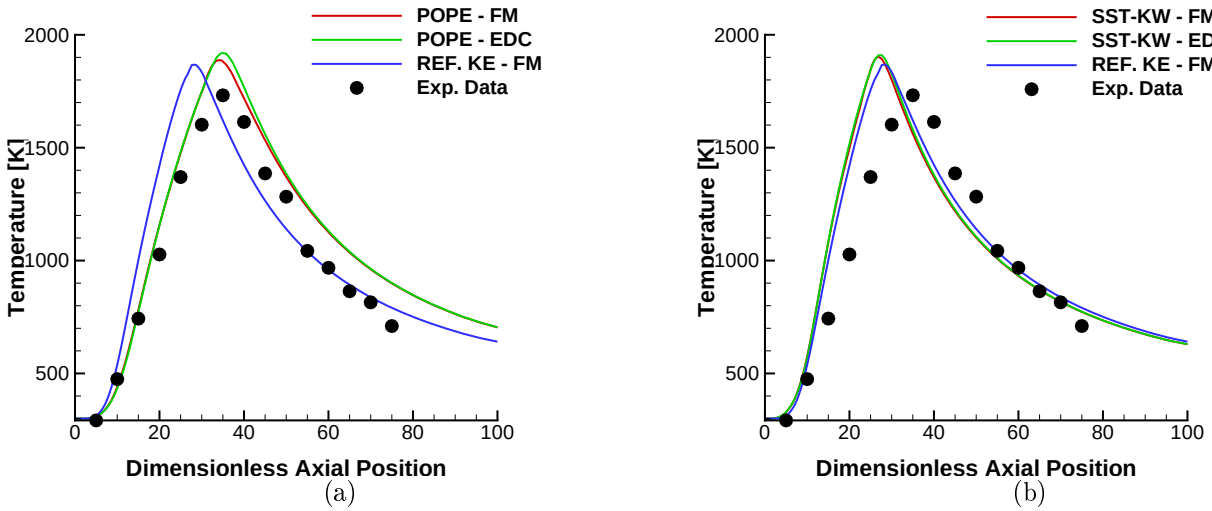

Figure 4.1.20: Axial temperature profiles with POPE jet-round correction (a) and SST-$k-\omega$ model (b). Red line simulation with the Fractal Model, green line simulation with the EDC model, blue line reference simulation with the $k-\varepsilon$ model without POPE jet-round correction using the Fractal Model, black circle experimental data.

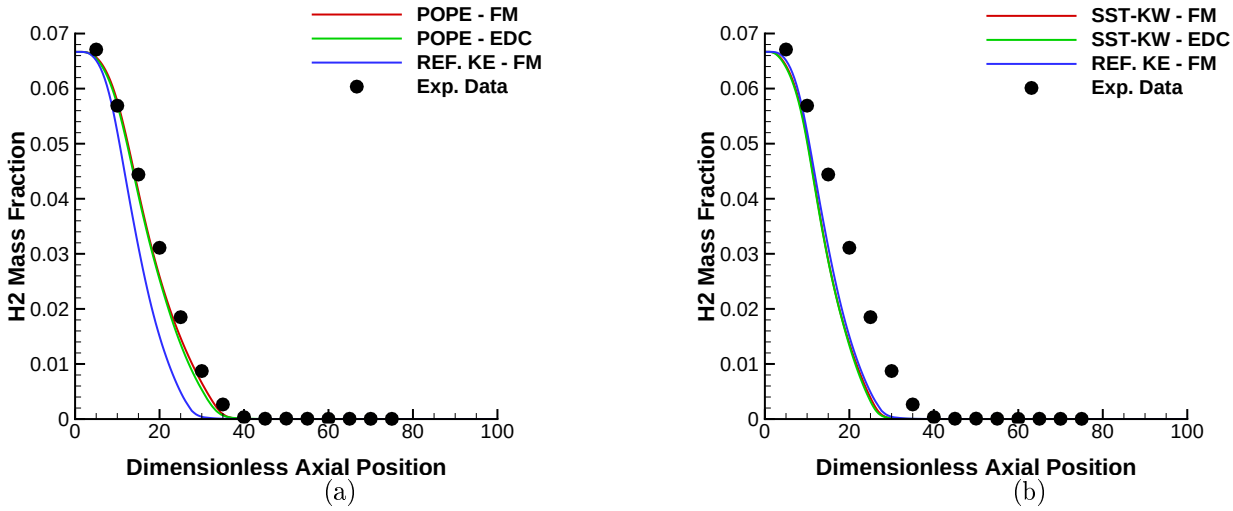

Figure 4.1.21: Axial Y_{H_2} profiles with POPE jet-round correction (a) and SST-$k-\omega$ model (b). Red line simulation with the Fractal Model, green line simulation with the EDC model, blue line reference simulation with the $k-\varepsilon$ model without POPE jet-round correction using the Fractal Model, black circle experimental data.

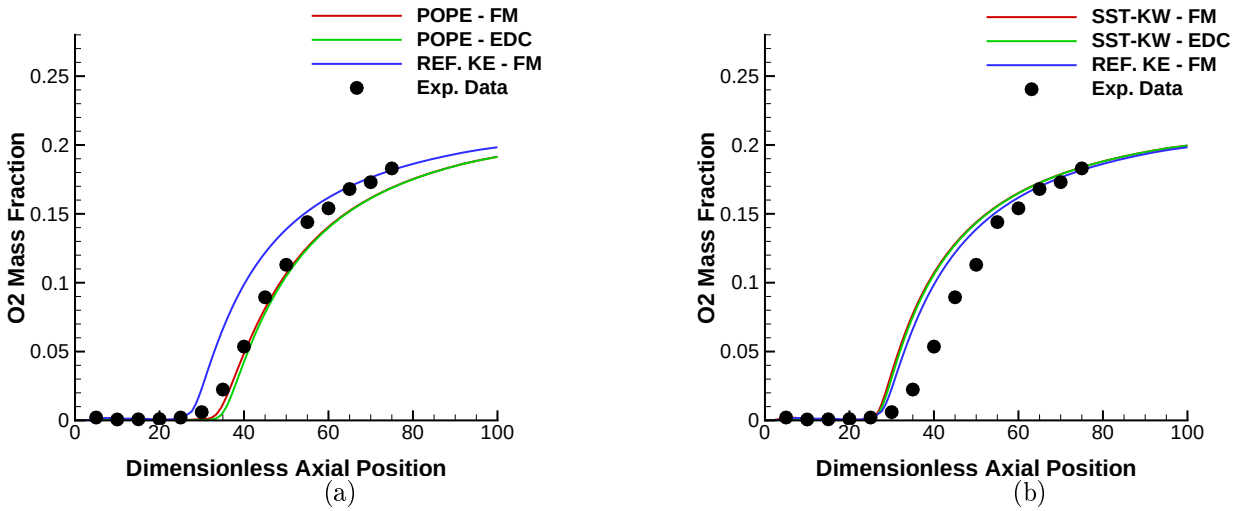

Figure 4.1.22: Axial Y_{O2} profiles with POPE jet-round correction (a) and SST-$k-\omega$ model (b). Red line simulation with the Fractal Model, green line simulation with the EDC model, blue line reference simulation with the $k-\varepsilon$ model without POPE jet-round correction using the Fractal Model, black circle experimental data.

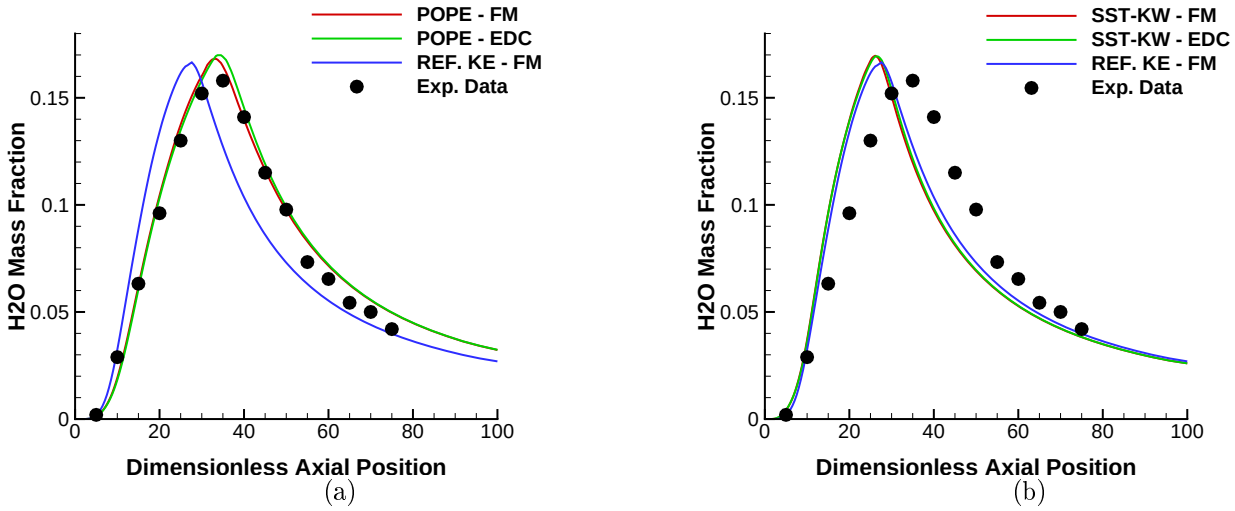

Figure 4.1.23: Axial Y_{H2O} profiles with POPE jet-round correction (a) and SST-$k-\omega$ model (b). Red line simulation with the Fractal Model, green line simulation with the EDC model, blue line reference simulation with the $k-\varepsilon$ model without POPE jet-round correction using the Fractal Model, black circle experimental data.

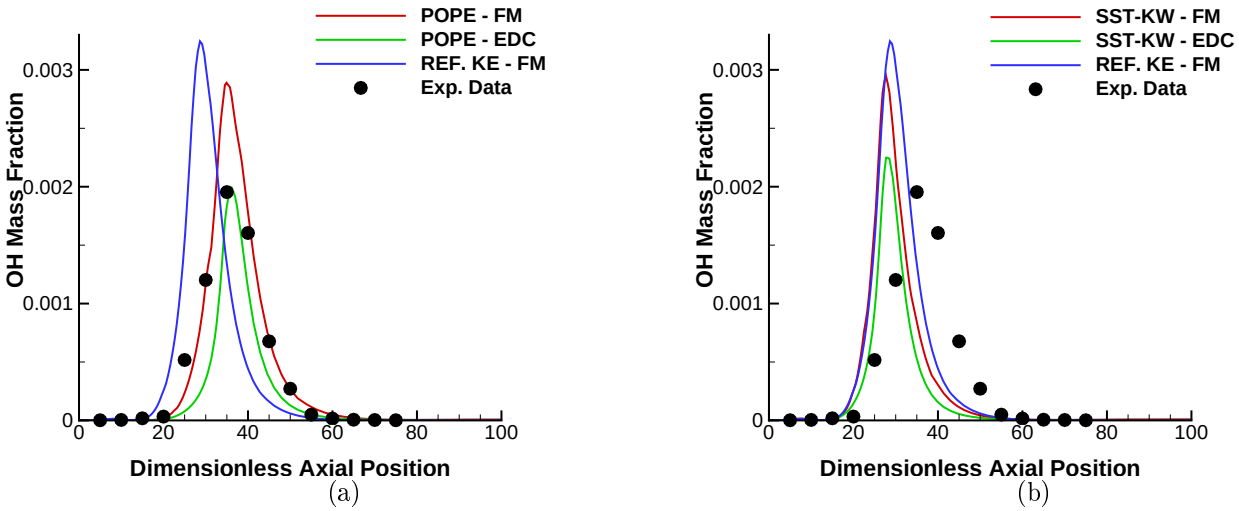

Figure 4.1.24: Axial Y_{OH} profiles with POPE jet-round correction (a) and SST-$k-\omega$ model (b). Red line simulation with the Fractal Model, green line simulation with the EDC model, blue line reference simulation with the $k-\varepsilon$ model without POPE jet-round correction using the Fractal Model, black circle experimental data.

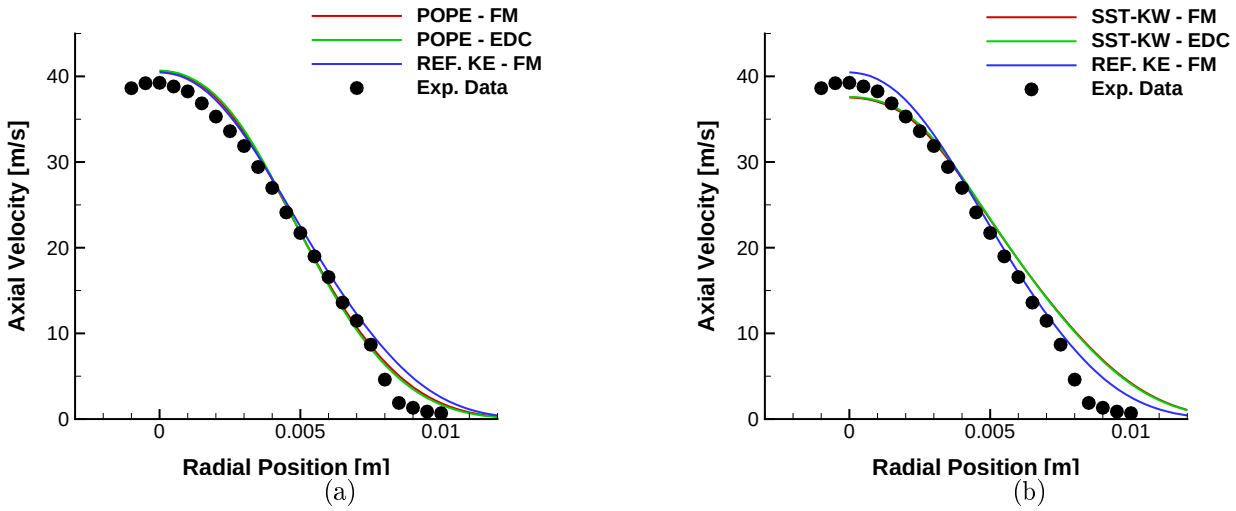

Figure 4.1.25: Radial profiles for the velocity with POPE jet-round correction (a) and SST-$k-\omega$ model (b) at x=5d. Red line simulation with the Fractal Model, green line simulation with the EDC model, blue line reference simulation with the $k-\varepsilon$ model without POPE jet-round correction using the Fractal Model, black circle experimental data.

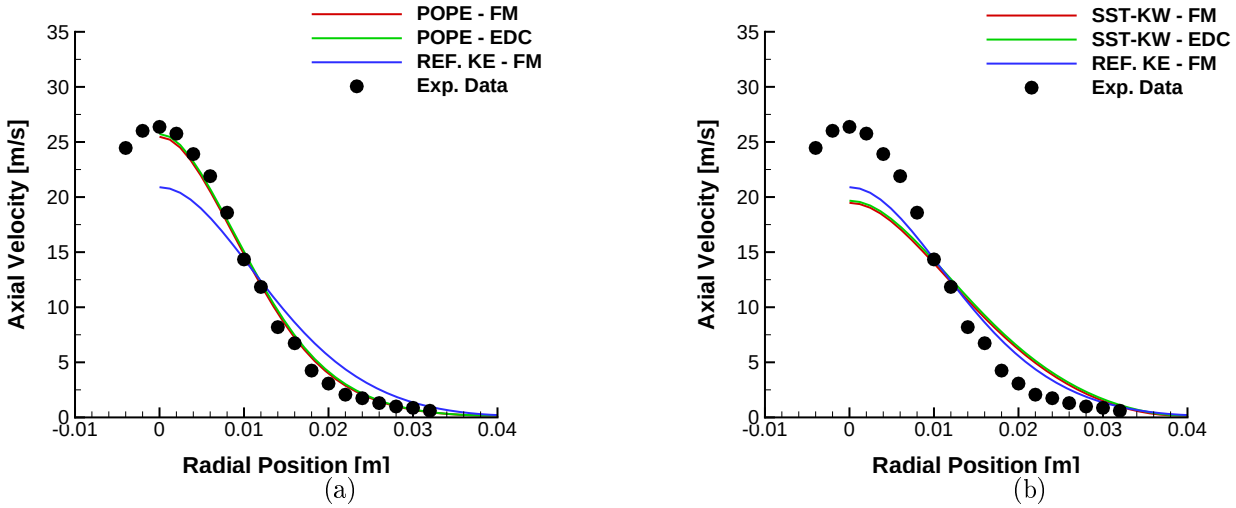

Figure 4.1.26: Radial profiles for the velocity with POPE jet-round correction (a) and SST-$k-\omega$ model (b) at x=20d. Red line simulation with the Fractal Model, green line simulation with the EDC model, blue line reference simulation with the $k-\varepsilon$ model without POPE jet-round correction using the Fractal Model, black circle experimental data.

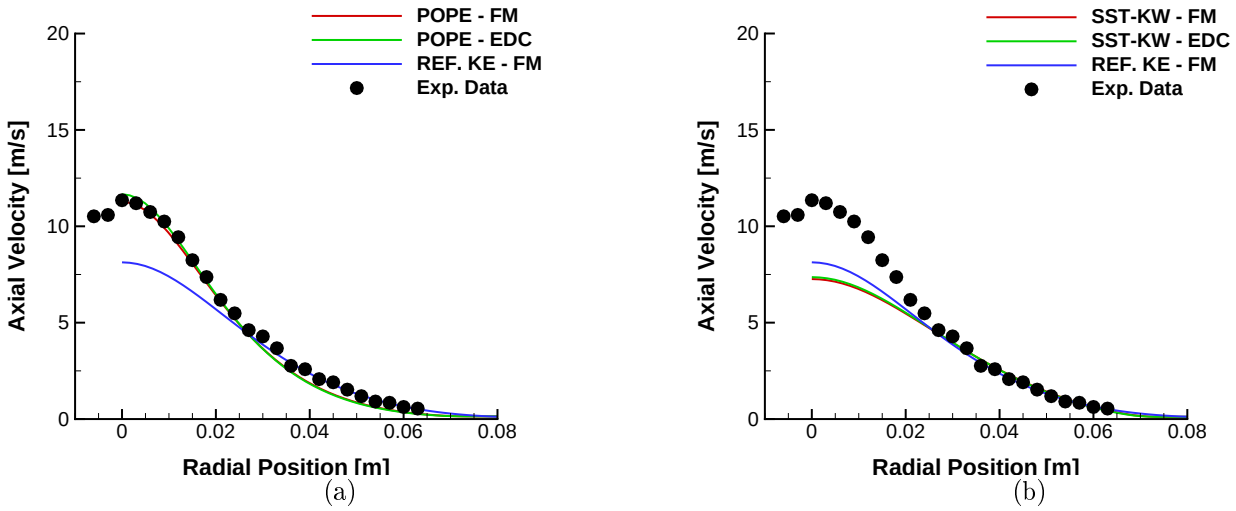

Figure 4.1.27: Radial profiles for the velocity with POPE jet-round correction (a) and SST-$k-\omega$ model (b) at x=40d. Red line simulation with the Fractal Model, green line simulation with the EDC model, blue line reference simulation with the $k-\varepsilon$ model without POPE jet-round correction using the Fractal Model, black circle experimental data.

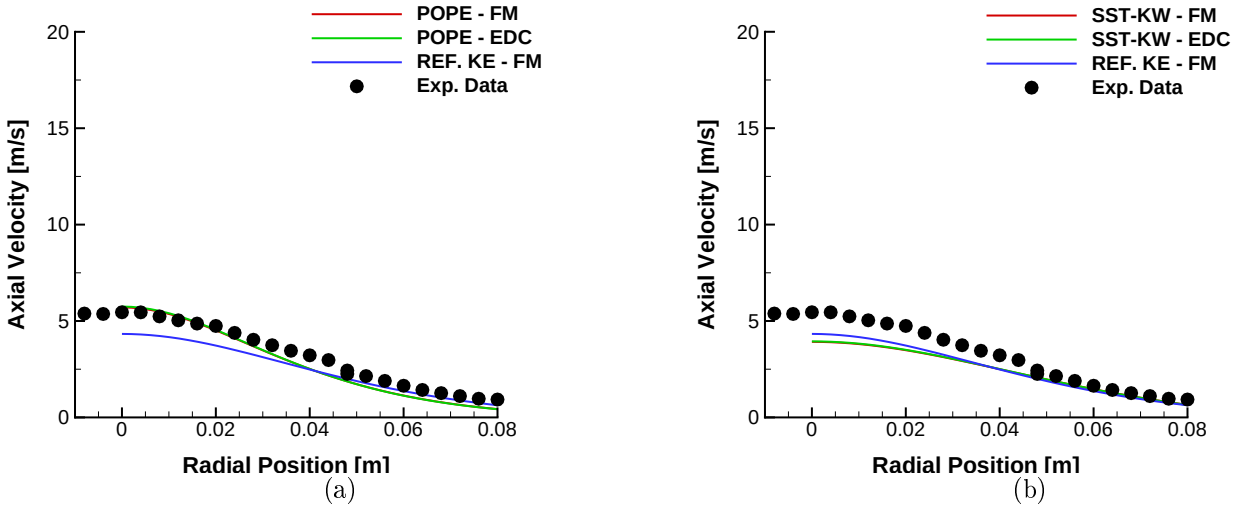

Figure 4.1.28: Radial profiles for the velocity with POPE jet-round correction (a) and SST-$k-\omega$ model (b) at x=60d. Red line simulation with the Fractal Model, green line simulation with the EDC model, blue line reference simulation with the $k-\varepsilon$ model without POPE jet-round correction using the Fractal Model, black circle experimental data.

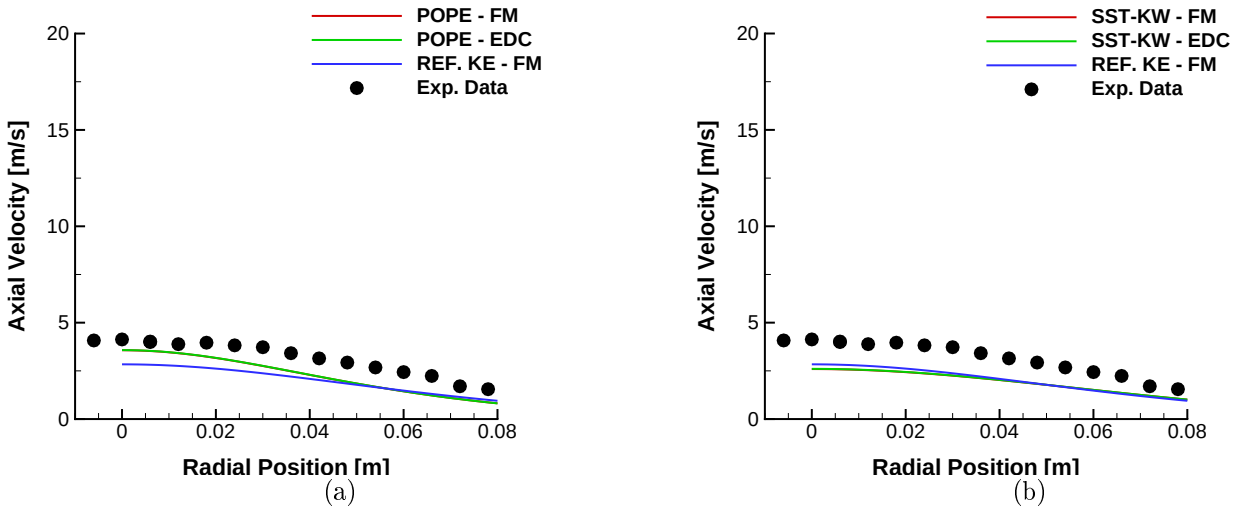

Figure 4.1.29: Radial profiles for the velocity with POPE jet-round correction (a) and SST-$k-\omega$ model (b) at x=80d. Red line simulation with the Fractal Model, green line simulation with the EDC model, blue line reference simulation with the $k-\varepsilon$ model without POPE jet-round correction using the Fractal Model, black circle experimental data.

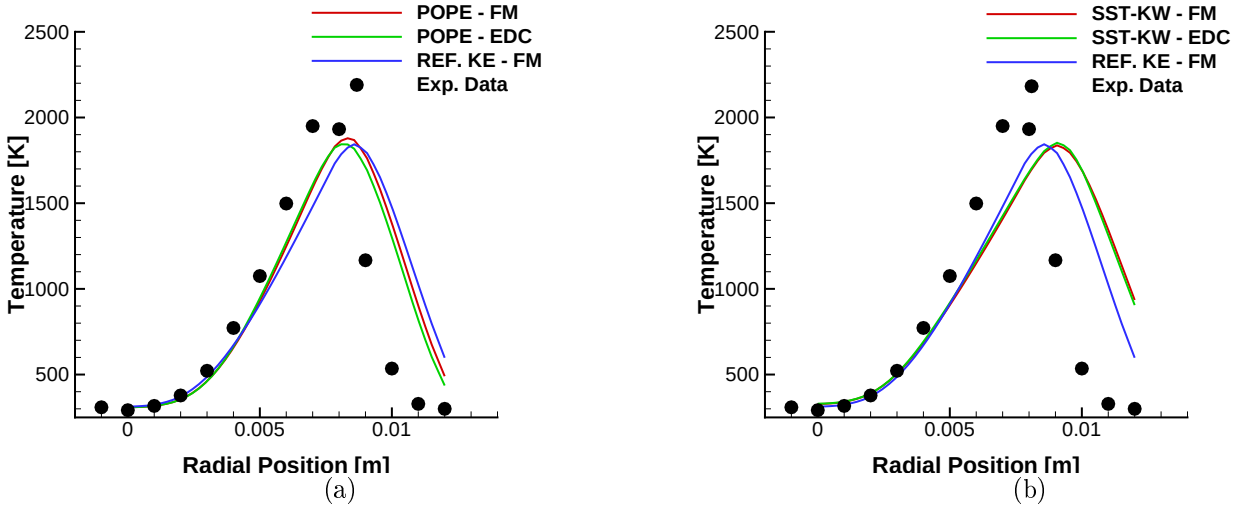

Figure 4.1.30: Radial profiles for the temperature with POPE jet-round correction (a) and SST-$k-\omega$ model (b) at x=5d. Red line simulation with the Fractal Model, green line simulation with the EDC model, blue line reference simulation with the $k-\varepsilon$ model without POPE jet-round correction using the Fractal Model, black circle experimental data.

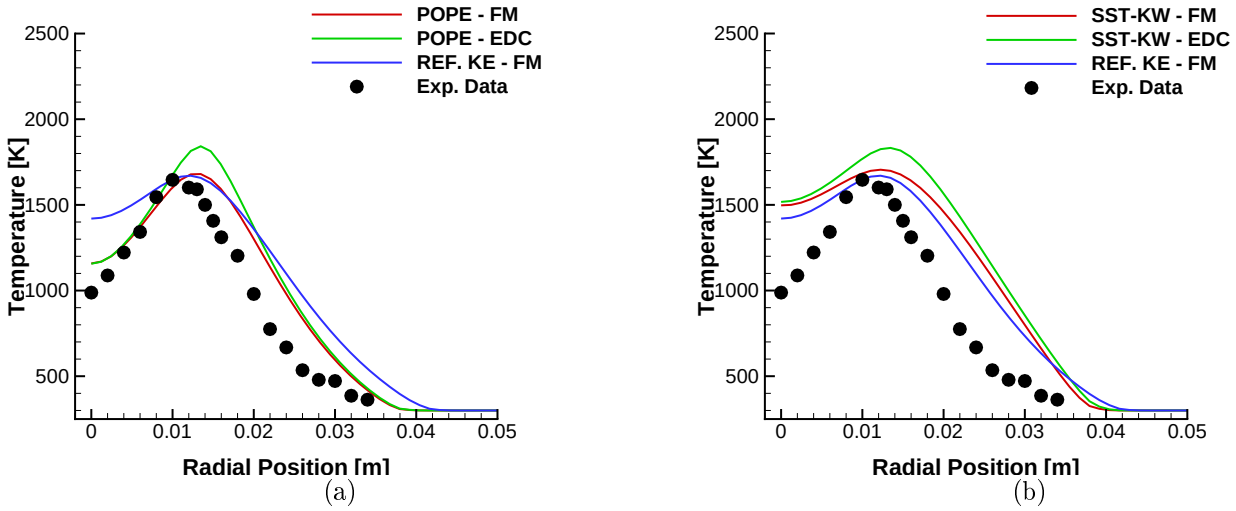

(a) (b)

Figure 4.1.31: Radial profiles for the temperature with POPE jet-round correction (a) and SST-$k-\omega$ model (b) at x=20d. Red line simulation with the Fractal Model, green line simulation with the EDC model, blue line reference simulation with the $k-\varepsilon$ model without POPE jet-round correction using the Fractal Model, black circle experimental data.

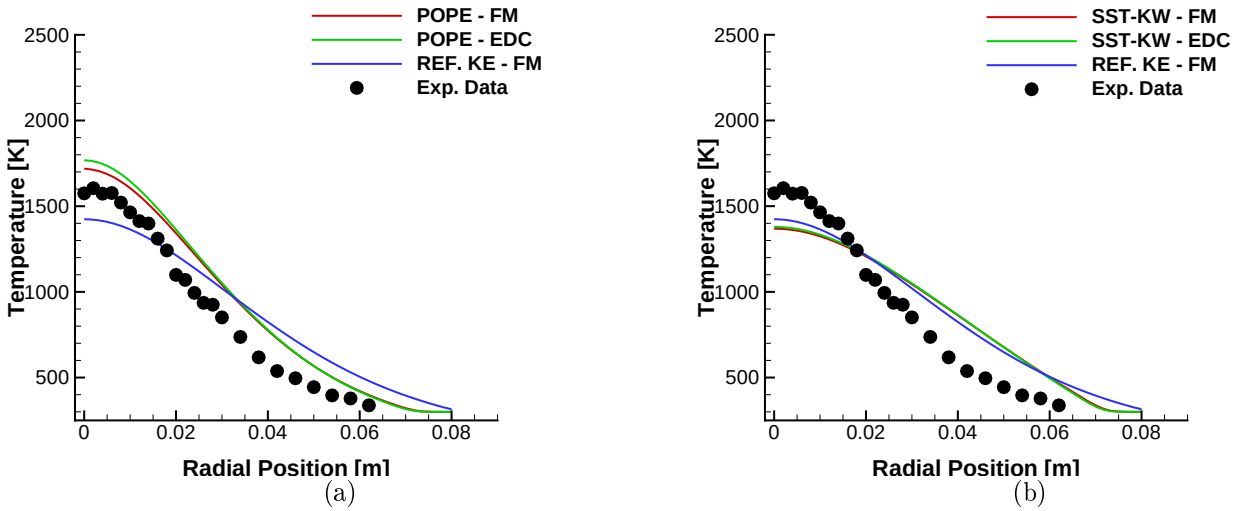

(a) (b)

Figure 4.1.32: Radial profiles for the temperature with POPE jet-round correction (a) and SST-$k-\omega$ model (b) at x=40d. Red line simulation with the Fractal Model, green line simulation with the EDC model, blue line reference simulation with the $k-\varepsilon$ model without POPE jet-round correction using the Fractal Model, black circle experimental data.

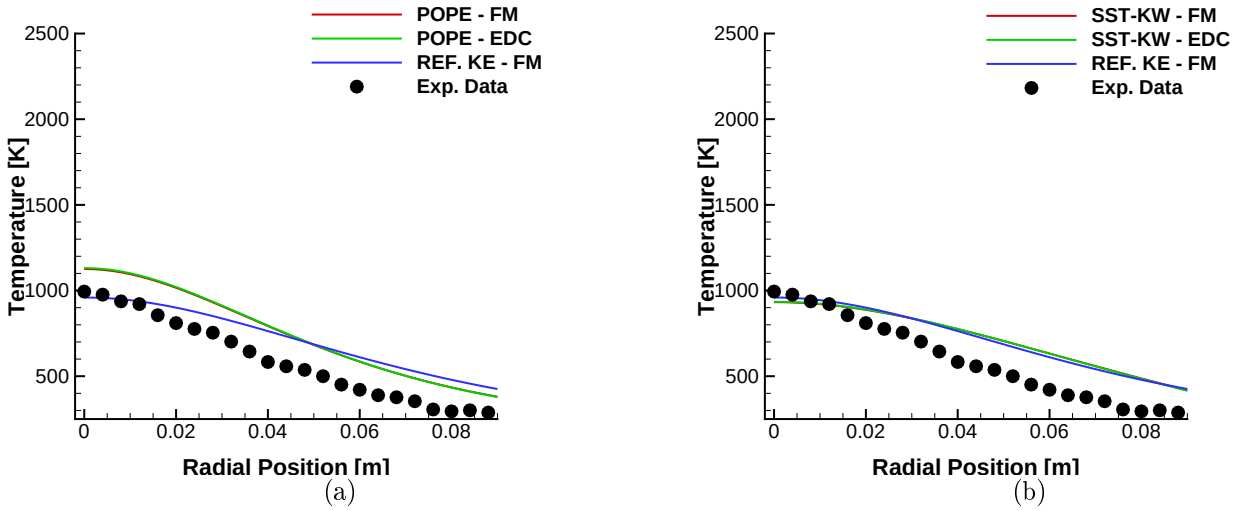

Figure 4.1.33: Radial profiles for the temperature with POPE jet-round correction (a) and SST-$k-\omega$ model (b) at x=60d. Red line simulation with the Fractal Model, green line simulation with the EDC model, blue line reference simulation with the $k-\varepsilon$ model without POPE jet-round correction using the Fractal Model, black circle experimental data.

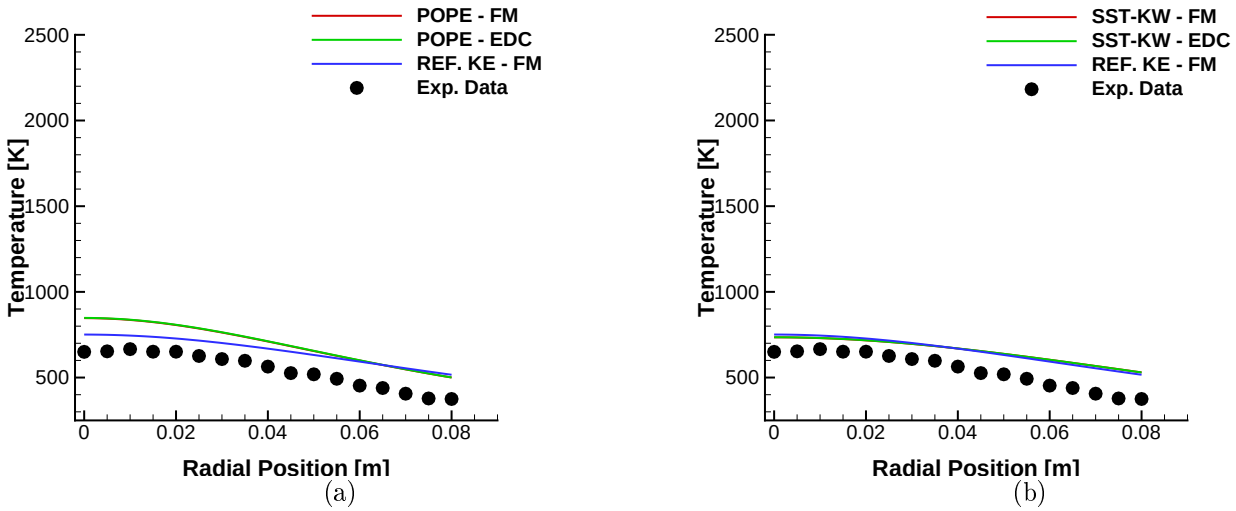

Figure 4.1.34: Radial profiles for the temperature with POPE jet-round correction (a) and SST-$k-\omega$ model (b) at x=80d. Red line simulation with the Fractal Model, green line simulation with the EDC model, blue line reference simulation with the $k-\varepsilon$ model without POPE jet-round correction using the Fractal Model, black circle experimental data.

4.2 Test case 2: Swirling Flames

A second test case that was considered, in order to validate the capability of the combustion models (EDC/FM), is a real size gas turbine (GT) combustor. A GT combustor is a crucial component for the gas turbine system, since it has to produce energy from the heat of combustion under high thermal and pressure loads. It has to ensure a target outlet temperature to avoid particular thermal stresses to the turbine, to produce a level of pollutant emissions lower than the requirements and to present the highest value for the global efficiency of the system. These requirements have to be fulfilled in all the operative conditions of the burner, where several issues like extinction phenomena, combustion instabilities, enhanced wall heat transfer, ect., may occur at anytime.

4.2.1 Numerical Results

The GT burner investigated in the present work is a real burner of an industrial gas turbine: G30 Dry Low Emission Combustor. For optical and laser measurements it was equipped with an optical access. It operates at high mass flows and with preheated air under high-pressure conditions.

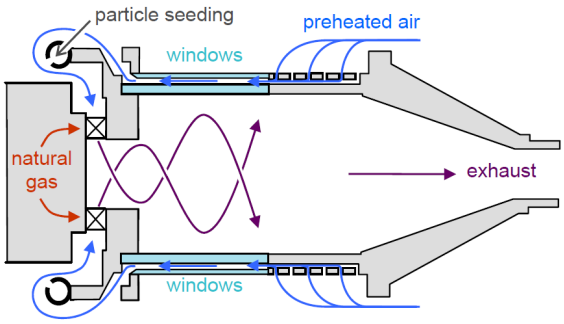

Figure 4.2.1: Experimental setup of the G30 Dry Low Emission Combustor.

The test case was experimentally investigated by Stopper et al. [21, 75] in the DLR laboratories. The burner comprises three main parts as shown in Fig. 4.2.1: the radial swirler, the combustion chamber and the exit duct of the exhaust gas. Before entering the radial swirler, air is preheated to 400°C by forcing its passage through a small gap between the quartz windows. Thus, due to the heat produced by the combustion the air inlet temperature increases, producing a cooling of the burner walls. Eventually, the incoming flow reaches the burner plenum and enters the swirling zone. The fuel, which is natural gas at room temperature, is introduced through various thin injector holes, placed perpendicularly to the

swirler. Combustion in a lean premixed mode occurs in the rectangular chamber located after the swirl zone. The chamber was equipped with four quartz windows to allow optical access from the four sides for laser diagnostics. The last part of the burner comprises a water-cooled exit duct, which connects the burner with a long exhaust channel.

In order to understand the behavior of the system under lean-premixed combustion, several operating conditions were investigated controlling both the pressure and the equivalence ratio inside the burner. The detailed list with all the measured operating points is available in ref. [76].

The present work focuses on a particular well-documented condition, indicated as "Case A", where an acoustically stable swirled flame is observed. According to [76], this kind of flame is obtained with an operating pressure of 3bar and an overall equivalence ratio of $\lambda_{b+pan} = 1.67$.

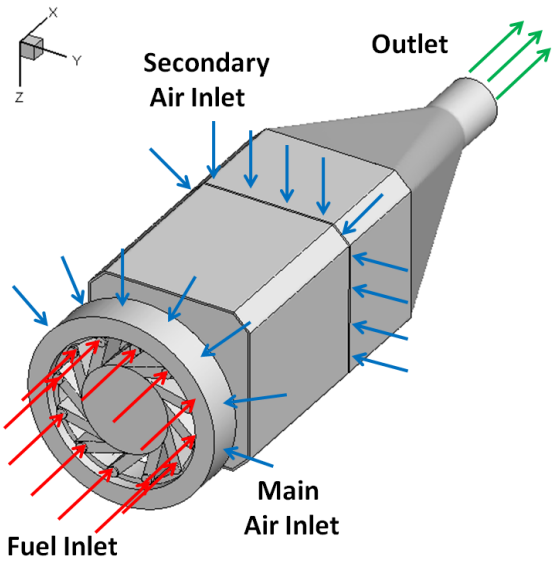

Figure 4.2.2: Geometry of the computational domain for the G30 Dry Low Emission Combustor.

In the "Case A", the air mass flow is distributed through the three inflows of the burner as follows: the main air mass flow passing through the swirl vanes ($\dot{m}_{air} = 0.16Kg/s$) with an inflow temperature of $T_{in} = 681K$; a first leakage air through the gap of the quartz windows and the metallic walls ($\dot{m}_{wind} = 1.6^{-2}kg/s$) with a $T_{win} = 700K$ and the leakage for cooling the burner panel ($\dot{m}_{pan} = 1.5^{-2}kg/s$) with $T_{pan} = 681K$. Fuel mass flow is equally distributed between the holes located in each swirler vane, with an inflow value of ($\dot{m}_f = 6^{-3}kg/s$), and is injected without pre-heating at room temperature $T_f = 318K$.

The computational domain is simplified in order to reduce the number of the elements

for the space discretization. Thus, all the cooling channels, the auxiliary systems before the swirler region and the air/fuel feed supply lines were not considered in the numerical simulations. It is assumed that the impact of these elements on the flow and combustion is negligible. The final configuration of the burner is illustrated in Fig. 4.2.2. Regarding the numerical mesh, two fully tetrahedral grids were generated with the commercial code ICEM-CFD. The first (grid 1) was provided by SIEMENS Lincoln [77], and comprises around 4.6M elements (ca. 1M points). The second grid (grid 2) has 21M elements instead and about 4M node points and was refined in order to resolve the large structures of the turbulence. The numerical calculations were focused on the influence of the combustion models and on the sensitivity of the grid dimensions (Grid 1/ Grid 2). Unsteady simulations were performed with a hybrid URANS/LES approach using the the SST-SAS for modeling of the turbulence, whereas the combustion was solved by means of the EDM, EDC and FM models. The computations were done with a constant time step of $\Delta t = 10^{-6}$s. To obtain a converged time-averaged solution, a physical time span of 10 residence times was considered. As mentioned, fuel consists of natural gas, which is approximated in the calculations by pure methane. Fuel chemistry was modeled with two different chemical kinetic mechanisms: a 2-step global mechanism (Nicols et al.[78]) and a 19-species chemistry mechanism DRM-19 [79].

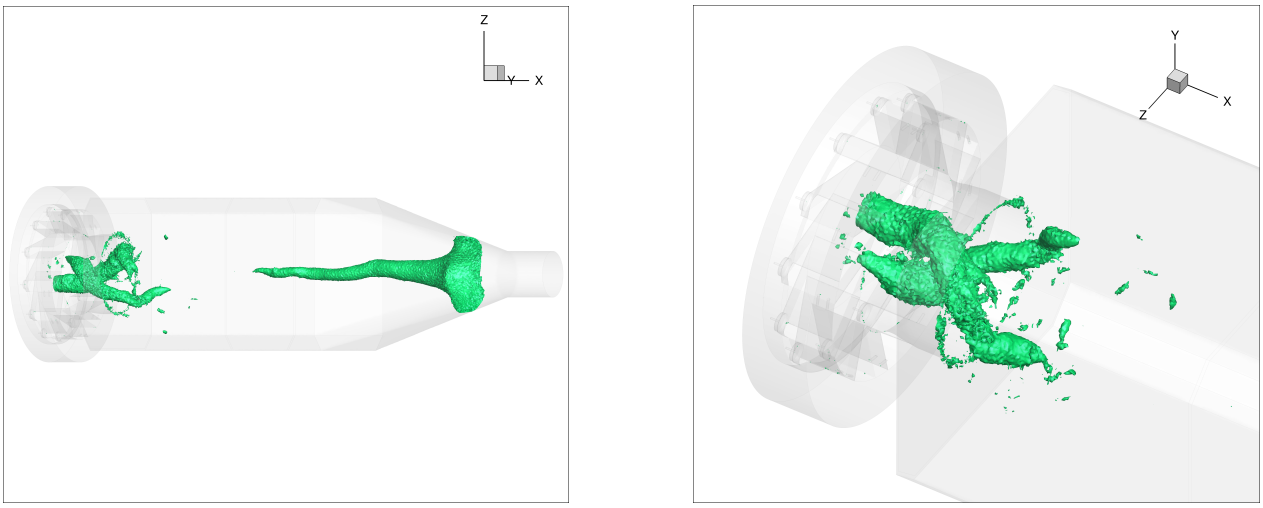

(a) (b)

Figure 4.2.3: Instantaneous pressure isosurface showing the typical PVC movement of the swirling flows.

The swirl influences deeply the flame shape and the flow pattern in the burner, and it may provide the flame stabilization or the occurrence of flashback instability. These opposite flame behaviors are dependent on the degree of the swirling intensity. Mathematically, it can be determined by a dimensionless quantity defined as Swirl number S_w, representing the ratio of the axial flux of angular momentum to the axial flux of axial momentum. This represents

an indication of the tangential flow rate injected in the combustor compared to the overall mass flow rate. An increase of this parameter leads to a significant increase of the instability, as reported in [80]. Normally with a small Swirl number, the flow is pushed into the chamber by a macro-vortex that can eventually break down in a large recirculation zone around the axial axis. Higher values of S_w lead to an increase of the turbulent fluctuations and to an upstream movement of the central recirculation zone toward the inflow region, causing flow instabilities or even a flashback of the flame into the inflow region.

In swirl flow a precessing vortex core (PVC) can arise. This flow instability is a three-dimensional unsteady vortex characterized by a helicoidal structure that occurs when the vortex center precesses around the central axis at a well-defined frequency. Due to its tangential movement, the PVC increases the mixing between air and fuel, thus increasing the combustion rate. Further downstream, the macro-vortex collapses and breaks down into smaller eddies for viscous effects. This PVC structure was recognized also for the present burner, plotting the instantaneous iso-surface of the pressure field, as shown in Fig. 4.2.3. The spiral center twists around the x-axis with a frequency of approximately 2500 Hz. The latter was obtained by means of the Fast-Fourier transform of the pressure signal acquired through monitor points placed in the main combustion chamber. It was also observed that the two vortexes may collapse into a single PVC structure due to the high centrifugal forces.

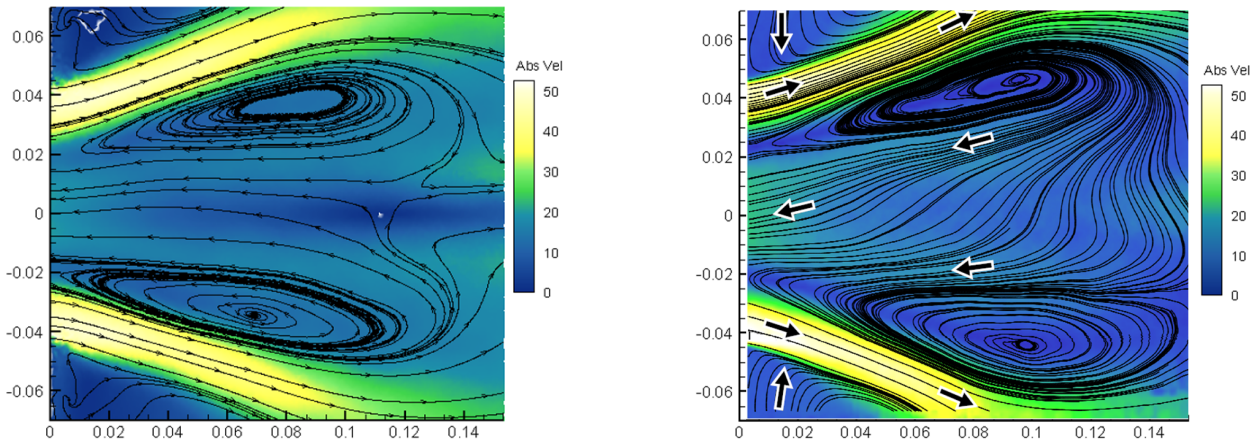

(a) (b)

Figure 4.2.4: Averaged velocity field obtained with numerical simulation (a) and through PIV measurements (b).

According to the PIV measurements, the macro-structure generated from the swirler looks different if combustion occurs. A large fast rotating central vortex core (CVC) was experimentally observed for a not reacting mixture inside the burner, becoming shorter and less pronounced with combustion [21, 75]. The latter case is shown in Fig. 4.2.4.b where the mixture enters the combustion chamber with high absolute velocity and forms a cone-shaped

distribution. In the inner part of this structure a recirculating region is clearly observable. This zone consists in two symmetrical low-speed regions, which push the fluid from the center of the burner in the direction of the pre-chamber zone. This backward flow helps to anchor the flame and to avoid possible flame blow off. One small recirculation zone (ORZ) originates also in the corners between the burner panel and the side walls. This region is due to the pressure velocity change and is also necessary for the flame stabilization. The numerical results for the average velocity field is illustrated in Fig. 4.2.4 under reacting conditions. This figure also shows a comparison between the computed mean flow and the PIV measurements. As it can be noticed, the numerical simulation is able to predict the mean flow distribution very well, reproducing perfectly both the large IRZ and the ORZ. The recirculation zones are not only well determined in terms of position, but also in intensity, since their absolute velocity seems in accordance with the experimental data. Observing the PIV figure, the angle at which the velocity enters in the chamber is approximately 20 degrees, whereas the numerical run exhibits a slightly lower value that leads to larger outer recirculating bubbles with a small over-prediction of the location of the reattachment point.

For evaluating the grid quality, Pope [81] derived a parameter based on the ratio of the resolved turbulent energy to the total turbulent energy. In order to ensure that the numerical simulation is working in a LES mode, this parameter has to be larger than 0.8 [81]. This is defined as follows:

$$R_T = \frac{1/2\left(\overline{u''^2} + \overline{v''^2} + \overline{w''^2}\right)}{1/2\left(\overline{u''^2} + \overline{v''^2} + \overline{w''^2}\right) + \overline{k}} \tag{4.2.1}$$

In Fig. 4.2.5 the Pope parameter contour R_T for estimating the percentage of the resolved turbulence is illustrated. The figure is composed of two sub plots, representing R_T for the coarse (grid 1 in the upper part) and the fine grid (grid 2 in the bottom). The coarse mesh indicates part of the computational domain with a value lower than 0.7, especially in the outer recirculation zones. In the region of the inner recirculation zone and in the pre-chamber R_T is instead slightly smaller than 0.8. These results demonstrate that the mesh (grid 1) is too coarse for capturing the turbulent vortices. Using the finer mesh (grid 2) leads to a different distribution for the R_T, since large part of the combustor has a value higher than 0.8. Therefore, the cell size in the crucial zone of interest such as the jet-injection, swirler region, is adequate for working in an LES-mode.

Figure 4.2.6 presents the time averaged temperature distributions in the symmetry plane for different simulations. In each picture a comparison between the Bulat et al. [82] results with an LES solver and the current computation is presented. The LES calculation is shown

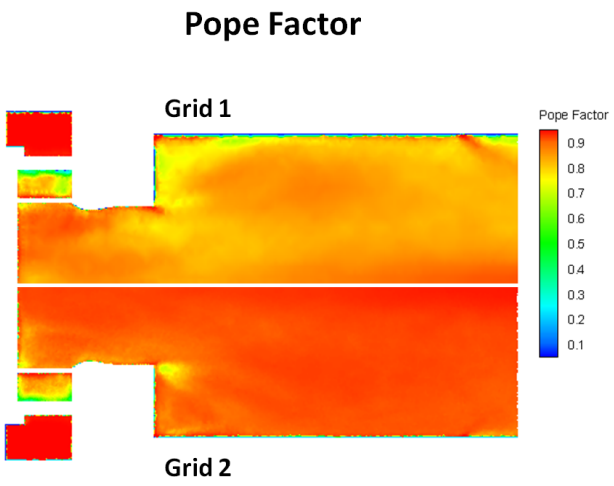

Figure 4.2.5: Pope parameter contour R_T for evaluating the percentage of resolved turbulence. In the upper part the distribution obtained with grid 1 (1M nodes), in the lower part for grid 2 (4M nodes).

on the upper part, whereas on the bottom different runs varying the combustion model (EDC/EDM) and grid size (grid 1/grid 2) are displayed. For the sake of simplicity, the results of the case with the FM model are not shown in this work, since they are similar to those obtained with EDC simulations. All the SAS numerical runs are in a fairly good agreement with the simulation from Bulat. They reveal the presence of hot gases also in the pre-chamber due to the backward flow and the swirl movement. Most of the conversion process from reactants to products occurs instead in the combustion chamber, where a maximum temperature value of approximately 2100K is observable. The main differences among the simulations are represented by the penetration length of the fresh reactants into the burning zone. The results calculated using the finer grid are clearly in a better agreement with the LES simulation.

To detect the portion of the combustion chamber where most of the chemical reactions occur, OH^* chemiluminescence (CL) pictures have been recorded. These radicals are excited by the laser technique and have a relatively short lifetime. They are investigated since they provide information on the location of the flame front and the position of the exothermic reactions of the combustion process. OH^* images are reported in terms of local radiation intensity for OH, whereas the heat release rate is expressed as a volumetric mass rate. The contours for the different simulations are presented in Fig. 4.2.7. As previously said, each picture contains a comparison between the LES simulation of Bulat and the current computations. The plots reveal a region with an elevated amount of heat release right in correspondence of the jet-injection in the main chamber, between the inner and outer shear layers. The use of global chemistry (i.e., EDM model) for modeling the fuel oxidation leads

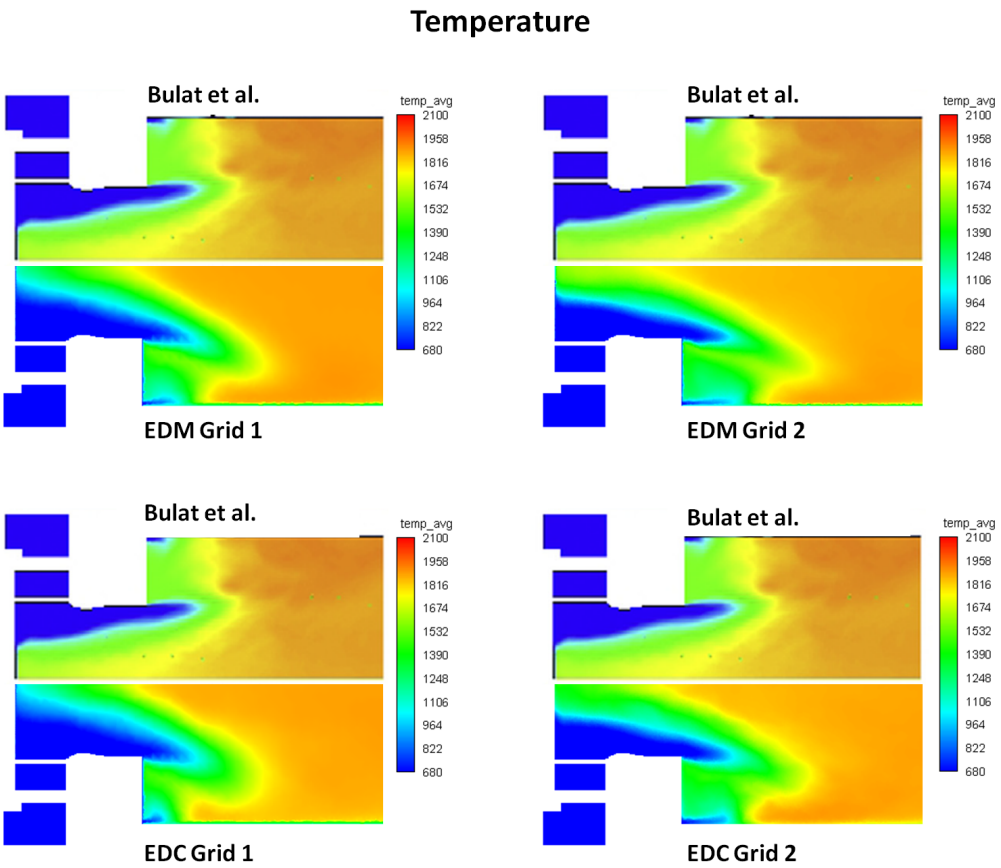

Figure 4.2.6: Temperature contours for different simulations: influence of numerical grids and combustion modeling.

to a small discrepancy in the form of the heat release. This is observed both in the coarse and in the finer grid. Conversely, the detailed model seems to perform a better approximation of this zone, similarly to the Bulat's computation.

In order to validate the models used for the simulations, 1D profiles of the most significant computed variables are compared with the experimental data. The information for the velocity fields (both in the axial and radial direction) as well as their corresponding root mean square values are measured through PIV technique. The profiles are acquired at five distinct locations at $x = 0{,}01$m, $x = 0{,}02$m, $x = 0{,}05$m, $x = 0{,}10$m and $x = 0{,}15$m. The 1D Raman technique was used for measuring species concentrations and temperature. Raman data were taken at different positions than the PIV data, focusing particularly on the field close to the injection in the chamber. In this case the measurements were recorded at $x = 0{,}0187$m, $x = 0{,}0387$m, $x = 0{,}0587$m, and $x = 0{,}0887$m. In Fig. 4.2.8 the sections interested by the laser acquisitions using PIV or Raman are illustrated.

The axial velocity profiles at the previous locations are shown in Fig. 4.2.9 and Fig. 4.2.19, respectively for grid 1 and grid 2. At the first position the presence of the anular

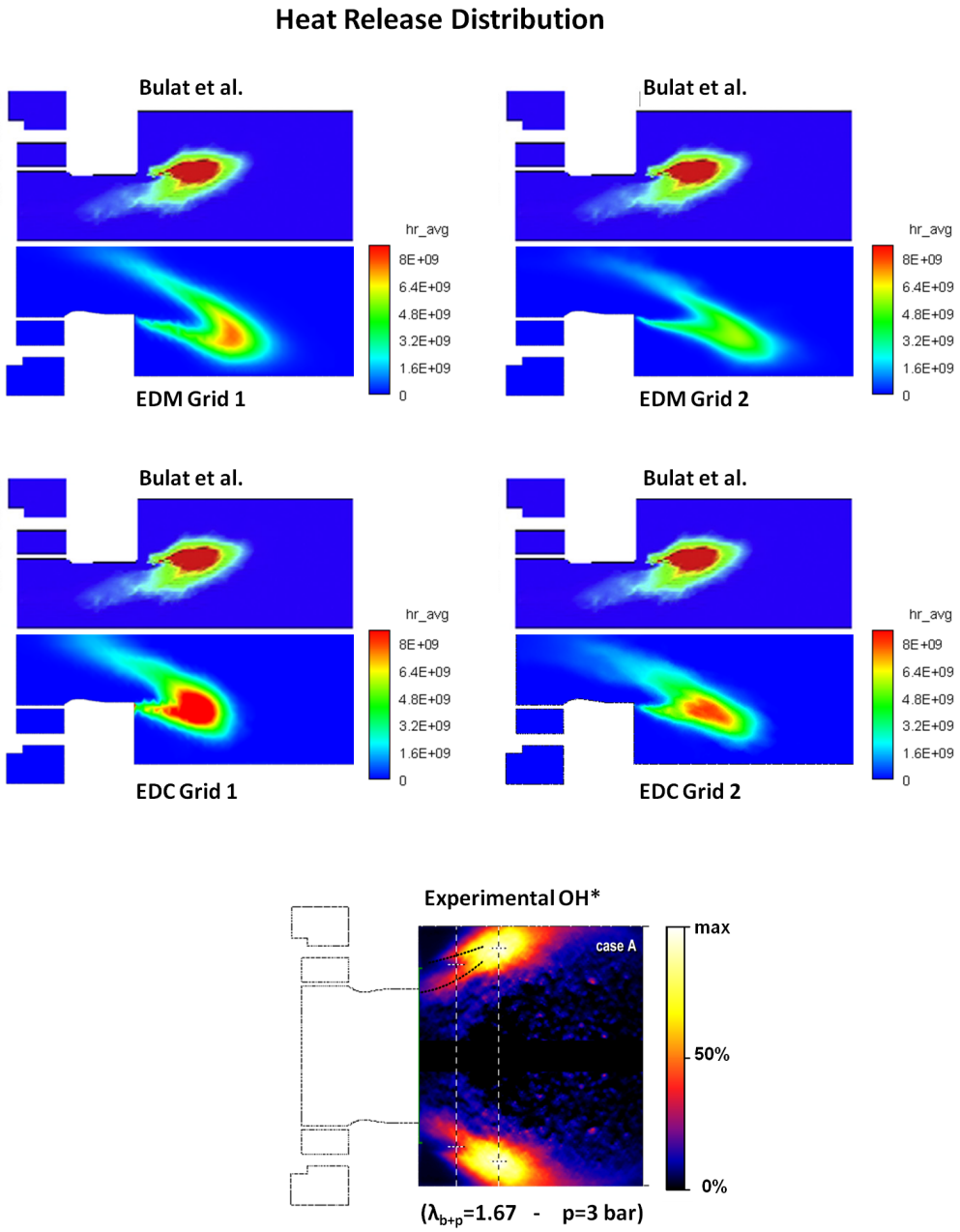

Figure 4.2.7: Heat Release contours for different simulations: influence of numerical grids and combustion modeling. Comparison with the OH^* chemiluminescence picture.

jet-injection is clearly observable, as well as the large recirculation zone in the middle zone with a minimum velocity of about -20 m/s. Further downstream, the velocity remains high close to the wall and tends to homogenize in the low-speed domain. The recirculating zone completely disappears after $x = 0{,}15$m and a flat profile develops. The simulations carried out with global and detailed chemistry using both grids are in close agreement with the experiments. Results with grid 2 (fine) are similar to those obtained with the coarser one,

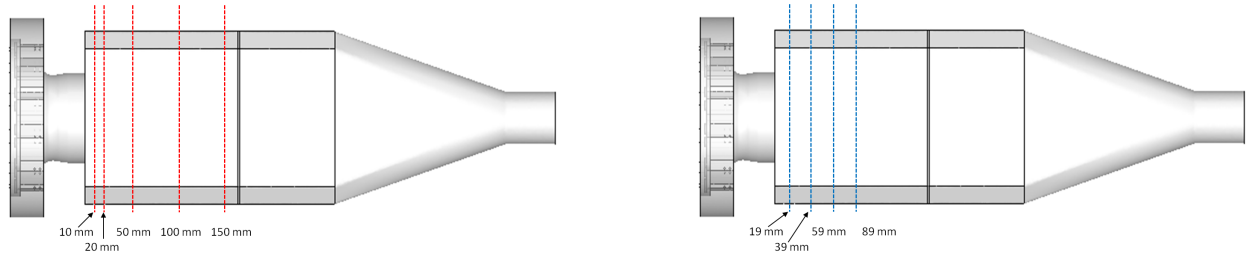

(a) (b)

Figure 4.2.8: Locations of the profiles extracted for a validation of the numerical results against the PIV data for the flow fiels (a) and against the Raman data for the species/temperature distributions (b).

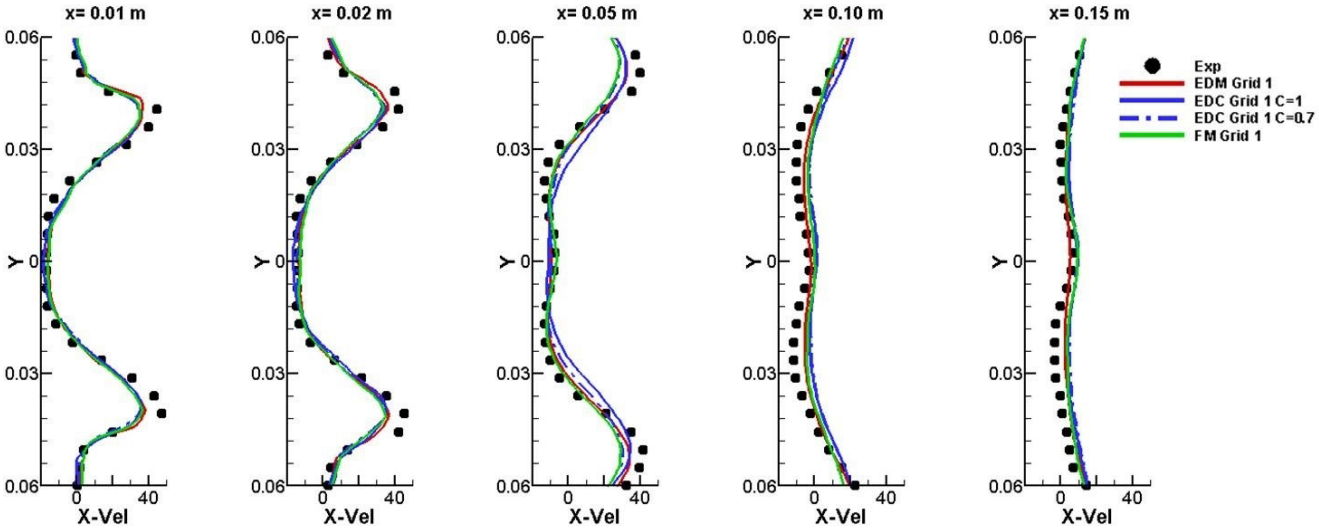

Figure 4.2.9: Axial velocity profiles extracted at different location downstream the injection for grid 1. Red solid line EDM simulation, blue solid line EDC with $C_{EDC} = 1$, blue dashed line EDC with $C_{EDC} = 0.7$, green solid line FM and in dot experimental data.

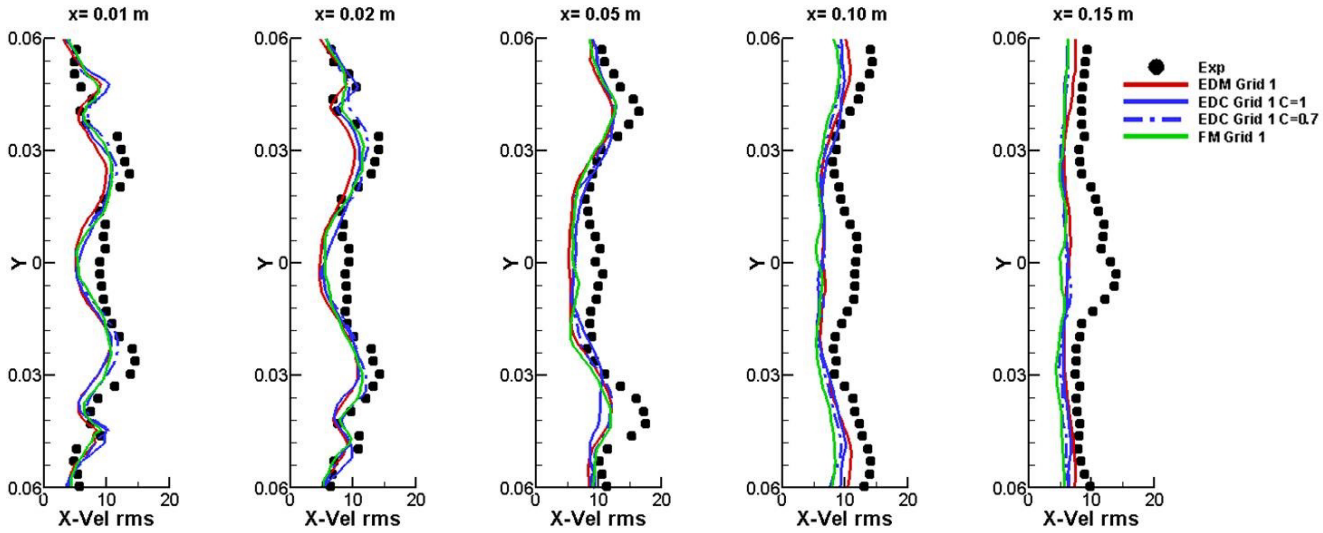

Figure 4.2.10: RMS values for the axial velocity extracted at different location downstream the injection for grid 11. Red solid line EDM simulation, blue solid line EDC with $C_{EDC} = 1$, blue dashed line EDC with $C_{EDC} = 0.7$, green solid line FM and in dot experimental data.

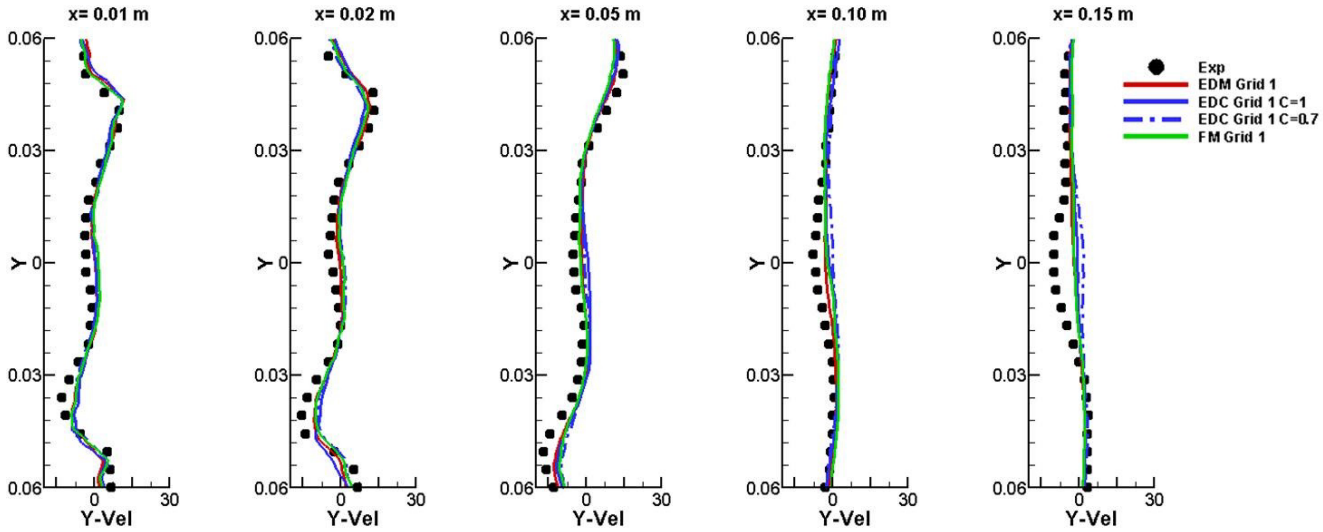

Figure 4.2.11: Radial velocity profiles extracted at different location downstream the injection for grid 1. Red solid line EDM simulation, blue solid line EDC with $C_{EDC} = 1$, blue dashed line EDC with $C_{EDC} = 0.7$, green solid line FM and in dot experimental data.

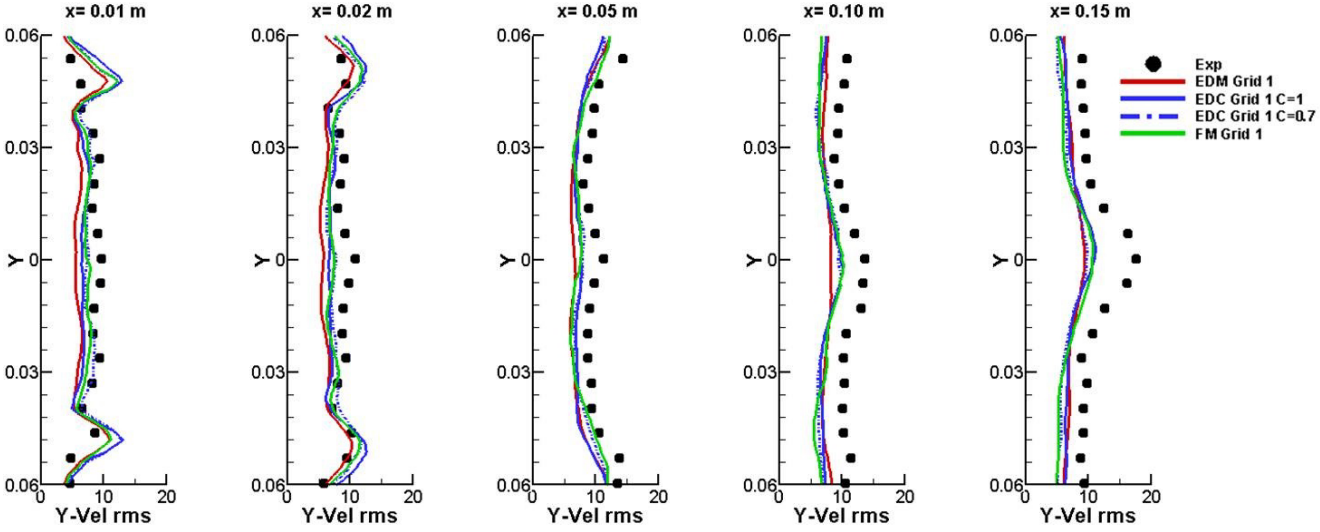

Figure 4.2.12: RMS values for the radial velocity extracted at different locations downstream the injection for grid 1. Red solid line EDM simulation, blue solid line EDC with $C_{EDC} = 1$, blue dashed line EDC with $C_{EDC} = 0.7$, green solid line FM and in dot experimental data.

and do not show a better accuracy against the experimental data.

The corresponding rms profiles for the axial velocity are reported for coarse and fine grid in Fig. 4.2.10 and Fig. 4.2.20 respectively. These present high values in correspondence of the inner and outer shear layer where the velocity presents spatial and temporal gradients. Close to this region, the velocity changes rapidly both in magnitude and direction, creating a substantial vorticity. Other locations, where the rms is particular intense, lie in the re-circulation bubble, due to the high fluctuations of the axial velocity. The profiles become less pronounced at $x = 0{,}15$m, assuming in the outer zone low values and near the symmetry axis a strong intensity. The results with the fine grid provide a better accuracy in the downstream region capturing the behavior of the rms along the main axis. The reason of the discrepancy with respect to the experimental data lies in fact on the grid resolution. A finer grid can capture and resolve more the turbulence fluctuations, allowing the model to work in an "LES-like" mode.

Regarding the radial velocity, the simulations are in good agreement with the experimental data, results for grid 1 are presented in Fig. 4.2.11 and for grid 2 in Fig. 4.2.21. The corresponding magnitudes are lower compared to the axial profiles, presenting peaks located in the inner shear layer. In the center region, the velocity almost vanishes due to the large recirculating bubble that creates strong variations only for the axial component. Downstream of the low-speed region, the mean values are approximately zero with the exception of the center plane where a minim value of -10m/s is observable. The rms profiles are reported in

Fig. 4.2.12 and Fig. 4.2.22. They show large fluctuations originated by the unsteadiness of the shear layer and by the inner recirculating zone. This behavior indicates the three-dimensional movement of the fluid, which is due to the swirl region. In conclusion, even for the radial rms a qualitative agreement with the measurements could be found.

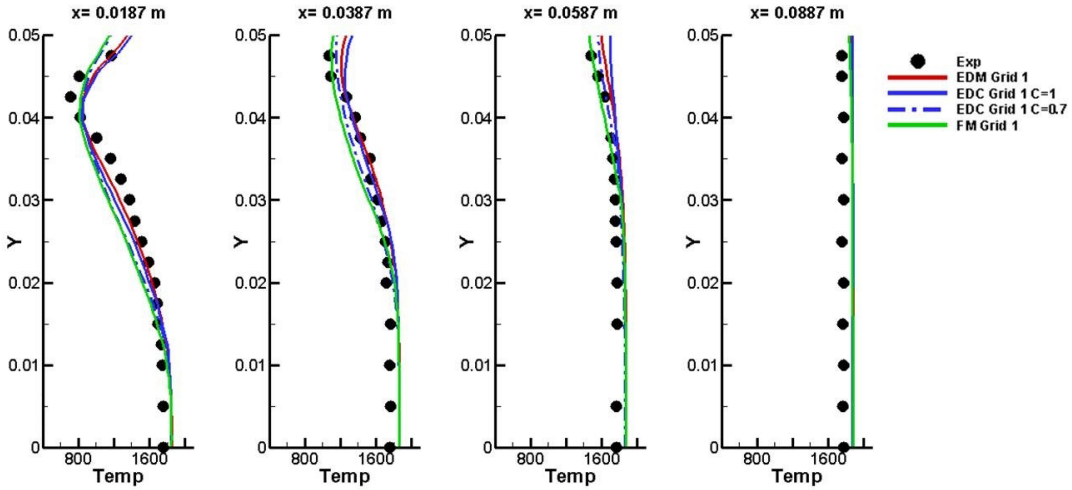

Figure 4.2.13: Temperature profiles extracted at different locations downstream the injection for grid 1. Red solid line EDM simulation, blue solid line EDC with $C_{EDC} = 1$, blue dashed line EDC with $C_{EDC} = 0.7$, green solid line FM and in dot experimental data.

More interesting for the combustion modeling validation are the temperature and species evolutions in the combustor. The mean temperature profiles are presented in Fig. 4.2.13 and Fig. 4.2.23, for the coarse and the fine grid respectively. Due to their symmetric distribution, they are reported only for one half of the combustor height (from the center axis up to 0.045m). The latter position corresponds approximately at the pre-chamber size, thus the measured points provide information on the flame shape in the outer shear layer. At the first location, the experimental data indicate a uniform profile in the inner recirculation region with a constant temperature of 1800K and a significant drop when approaching the shear layer. Here the temperature reduces to about 600K because of the injection of fresh mixture in the chamber. The numerical simulations are in good accordance with the data. A small over-prediction of about 50K is found in the low-speed zone both with global and detailed chemistry. This discrepancy decreases if the simulations are performed with the finer grid. The same situation is present in the flame brush zone, where a deviation of less than 200K is observable. The application of detailed chemistry models (EDC-FM) shows a small improvement of the accuracy in particular in the jet-injection zone, whereas the remaining part is similar to the simulations with EDM. Thus, the calculations with finer grid seem to not provide any benefits in terms of agreement with the measurements. Downstream of

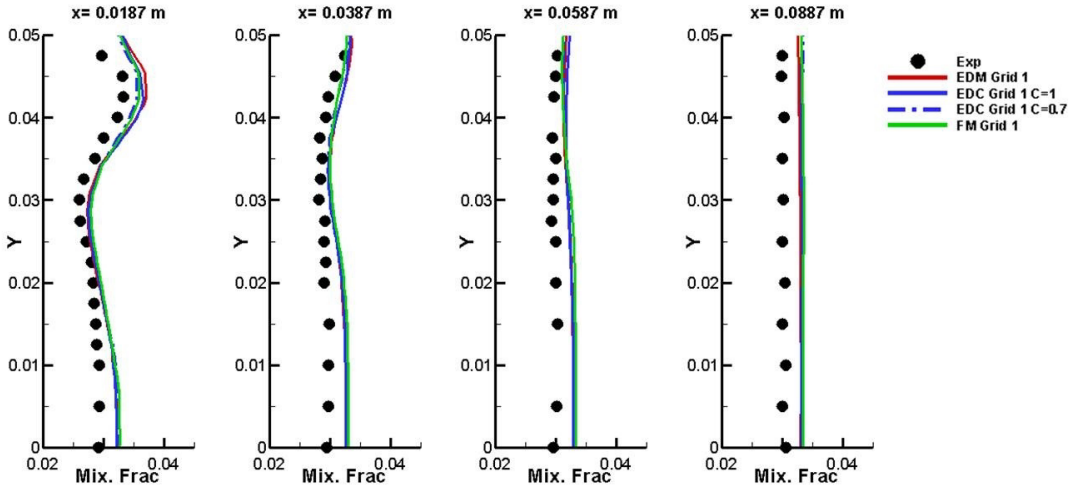

Figure 4.2.14: Mixture fraction profiles extracted at different locations downstream the injection for grid 1. Red solid line EDM simulation, blue solid line EDC with $C_{EDC} = 1$, blue dashed line EDC with $C_{EDC} = 0.7$, green solid line FM and in dot experimental data.

location 1, the fresh mixture ignites and burns: the profiles are then more homogeneous and the temperature drop reduces significantly.

The mixture fraction profiles are illustrated in Fig. 4.2.14 and Fig. 4.2.24. Observing the plots at different locations, the mixing mainly occurs because of the high vorticity in the outer shear layer for the macro-vortex and in the inner recirculating zone. The mixture enters the combustion chamber in lean condition and close to the pre-chamber walls assume the highest value, allowing the ignition of the flame. Even for this case, the profiles show a perfect accord with the experiments.

The experimental Raman technique allowed to detect not only the point-wise temperature but also the major species such as: CH_4, CO_2, O_2, H_2O. The profiles obtained through numerical simulations are presented from Fig. 4.2.15 to 4.2.18 for the coarse grid and from Fig. 4.2.25 to 4.2.28 for the fine one.

In conclusion, all the numerical simulations with global/detailed chemistry and with coarse/fine mesh predict the flow field and the mean quantities very well. As expected, a slight improvement of the accuracy in terms of the mean and rms velocity was found with the finer grid, whereas a better estimation of the temperature as well as the major species concentrations was obtained using detailed chemistry combustion models (EDC/FM).

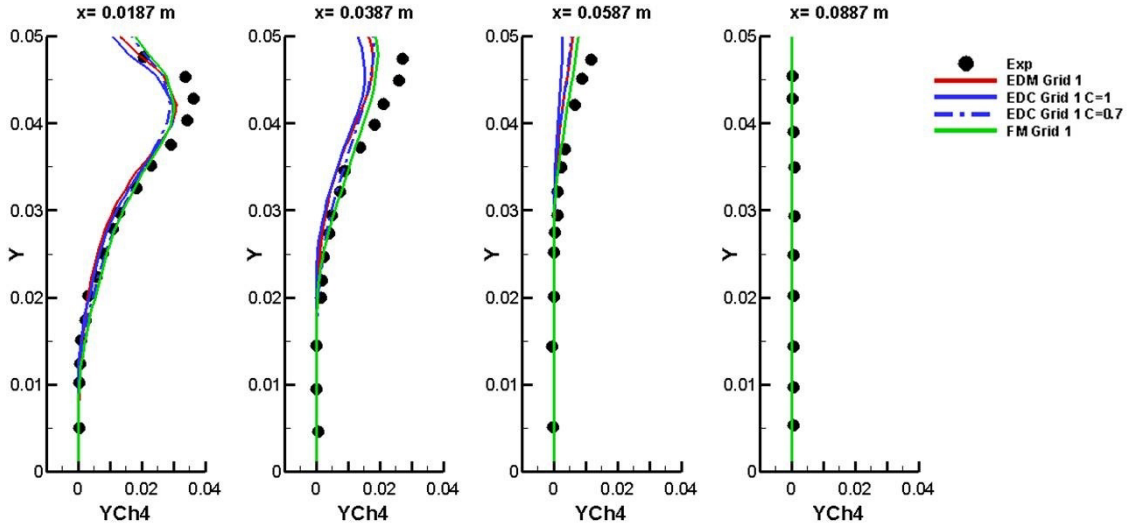

Figure 4.2.15: CH_4 mass fraction profiles extracted at different location downstream the injection for grid 1. Red solid line EDM simulation, blue solid line EDC with $C_{EDC} = 1$, blue dashed line EDC with $C_{EDC} = 0.7$, green solid line FM and in dot experimental data.

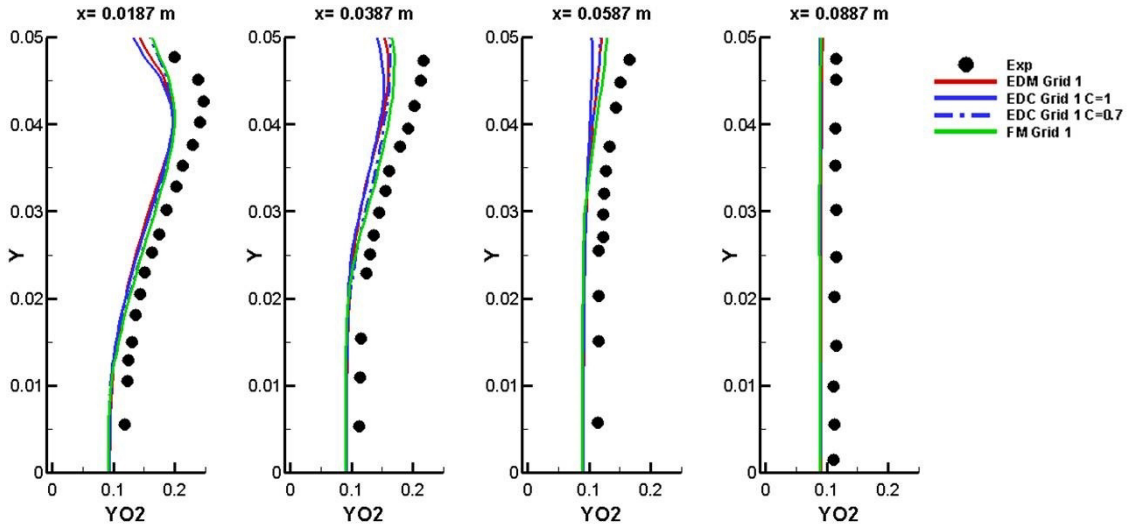

Figure 4.2.16: O_2 mass fraction profiles extracted at different location downstream the injection for grid 1. Red solid line EDM simulation, blue solid line EDC with $C_{EDC} = 1$, blue dashed line EDC with $C_{EDC} = 0.7$, green solid line FM and in dot experimental data.

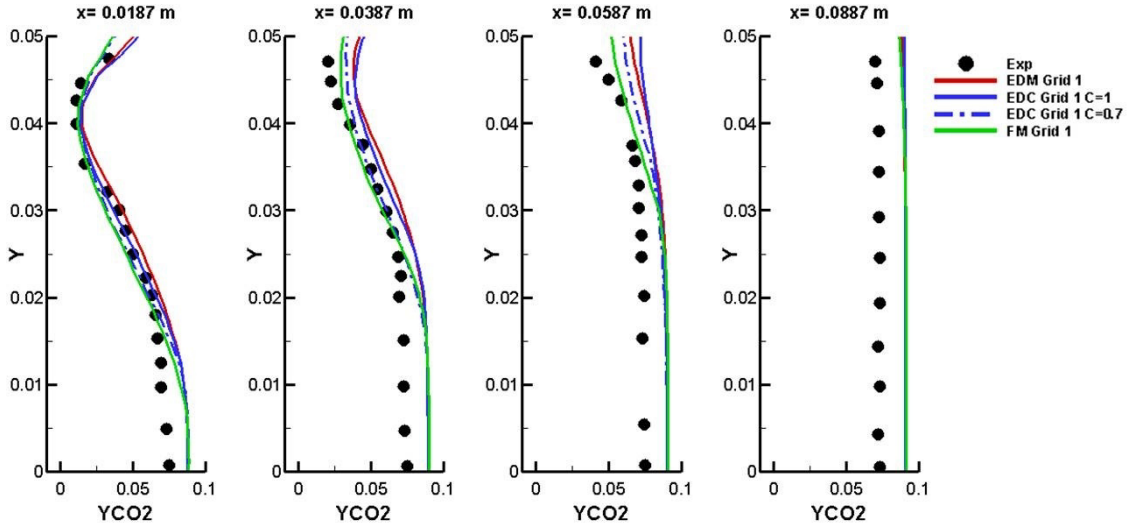

Figure 4.2.17: CO_2 mass fraction profiles extracted at different location downstream the injection for grid 1. Red solid line EDM simulation, blue solid line EDC with $C_{EDC} = 1$, blue dashed line EDC with $C_{EDC} = 0.7$, green solid line FM and in dot experimental data.

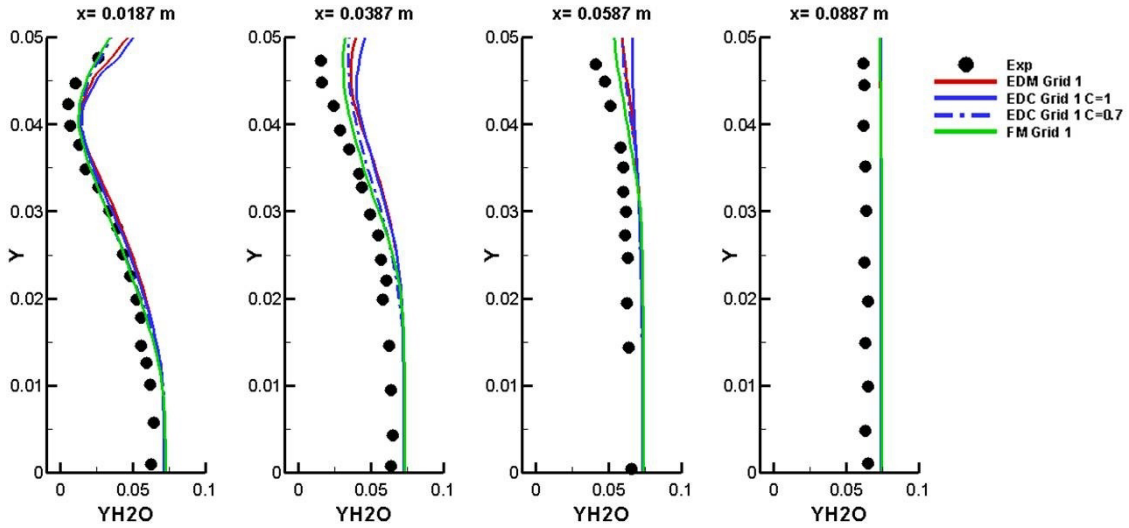

Figure 4.2.18: H_2O mass fraction profiles extracted at different location downstream the injection for grid 1. Red solid line EDM simulation, blue solid line EDC with $C_{EDC} = 1$, blue dashed line EDC with $C_{EDC} = 0.7$, green solid line FM and in dot experimental data.

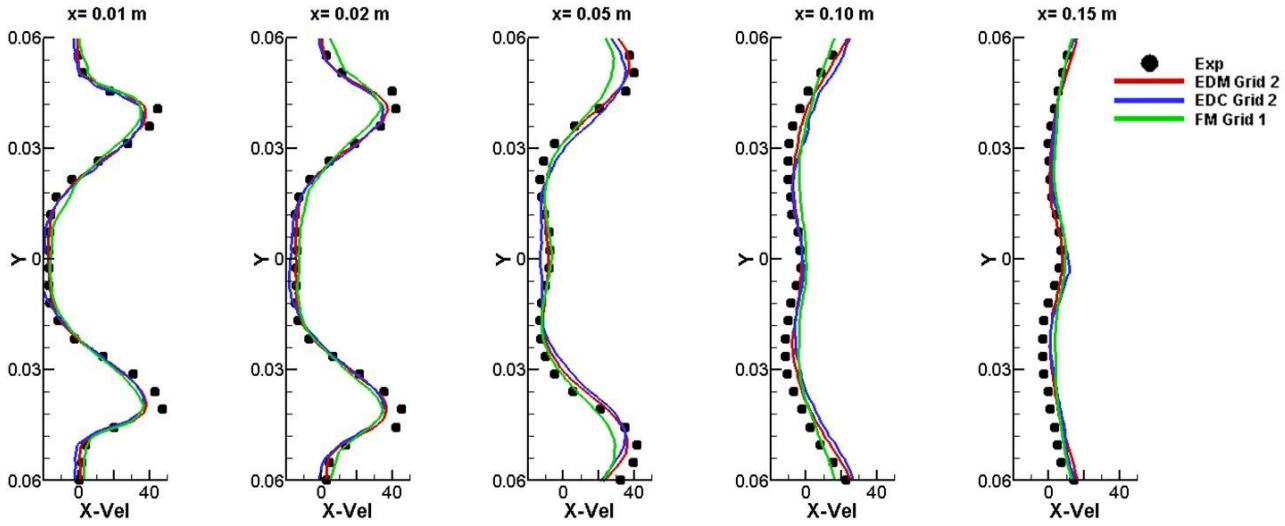

Figure 4.2.19: Axial velocity profiles extracted at different location downstream the injection for grid 2. Red solid line EDM simulation, blue solid line EDC with $C_{EDC} = 0.7$, green solid line FM and in dot experimental data.

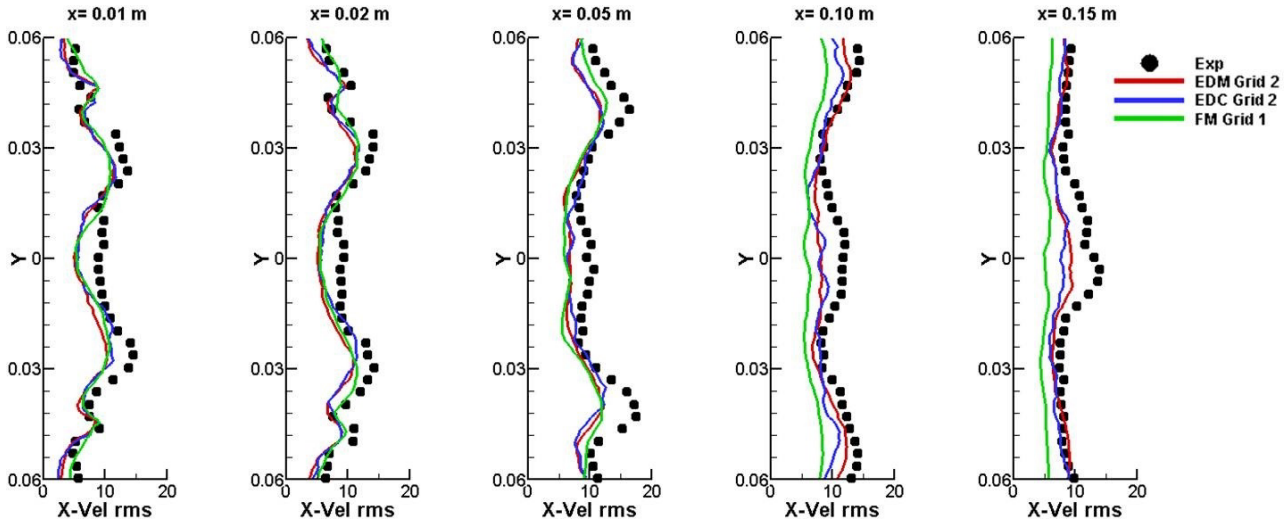

Figure 4.2.20: RMS values for the axial velocity extracted at different location downstream the injection for grid 2. Red solid line EDM simulation, blue solid line EDC with $C_{EDC} = 0.7$, green solid line FM and in dot experimental data.

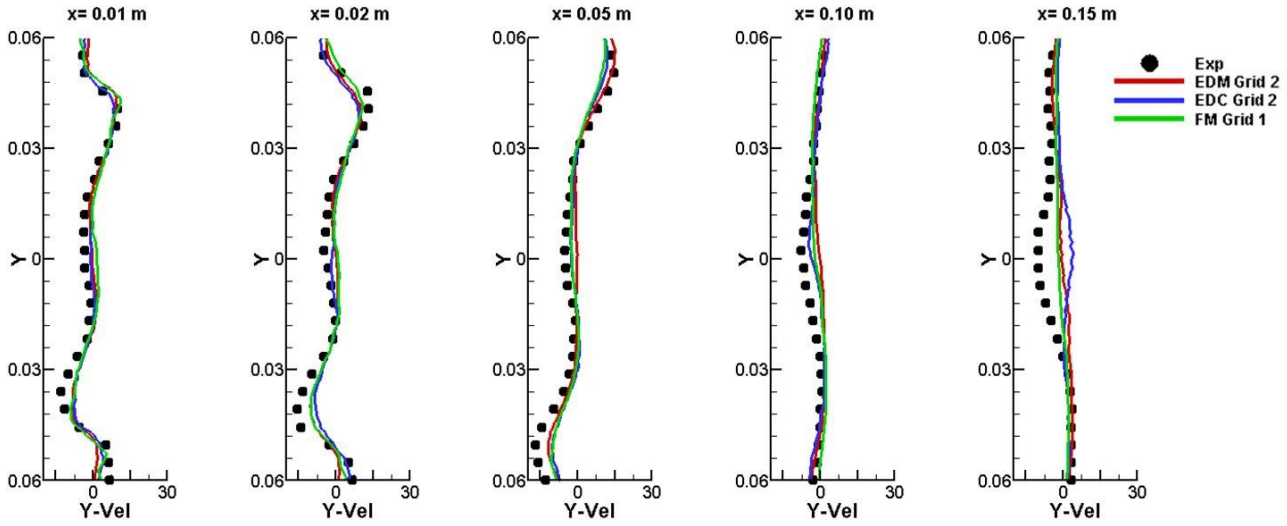

Figure 4.2.21: Radial velocity profiles extracted at different location downstream the injection for grid 2. Red solid line EDM simulation, blue solid line EDC with $C_{EDC} = 0.7$, green solid line FM and in dot experimental data.

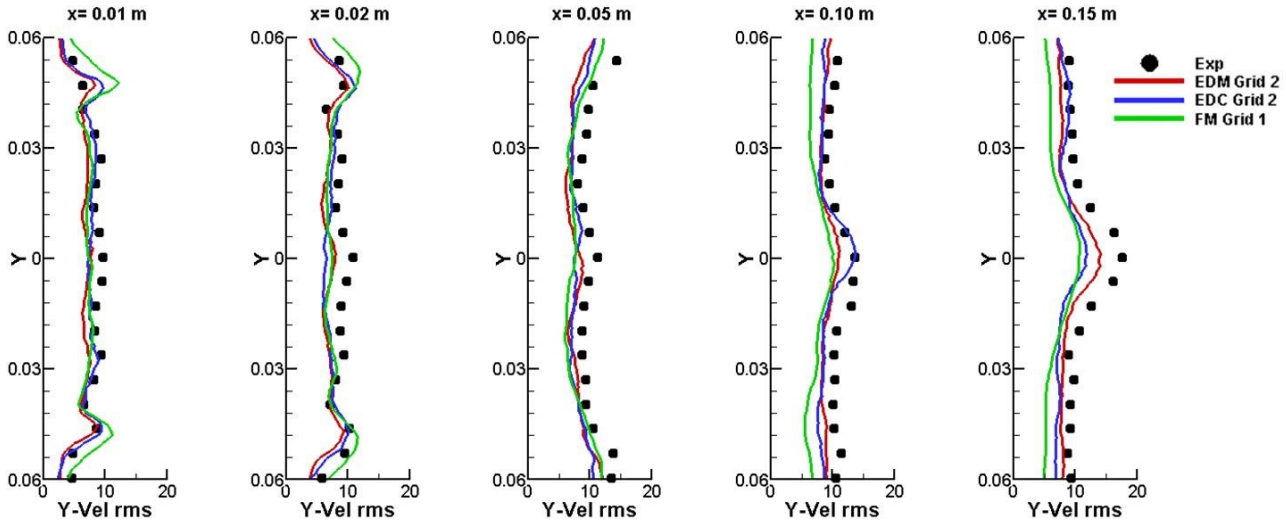

Figure 4.2.22: RMS values for the radial velocity extracted at different locations downstream the injection for grid 2. Red solid line EDM simulation, blue solid line EDC with $C_{EDC} = 0.7$, green solid line FM and in dot experimental data.

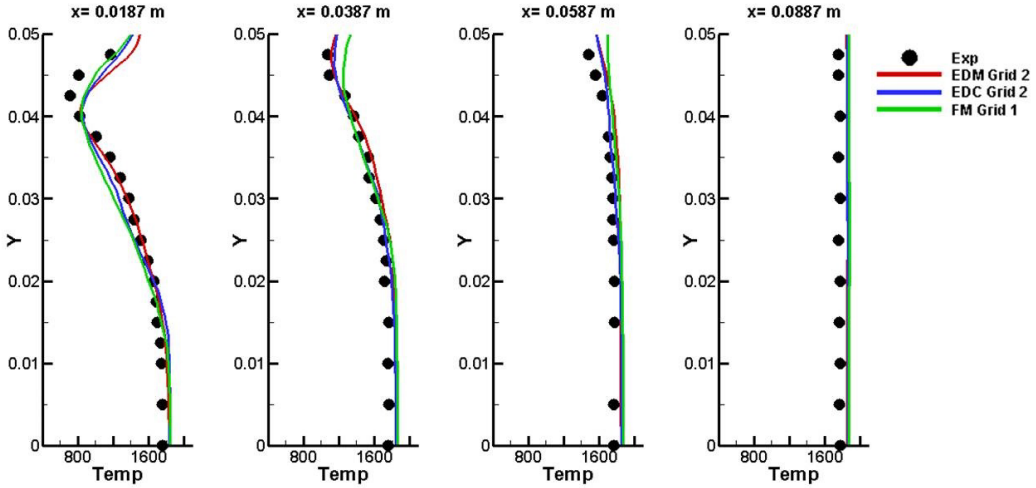

Figure 4.2.23: Temperature profiles extracted at different locations downstream the injection for grid 2. Red solid line EDM simulation, blue solid line EDC with $C_{EDC} = 0.7$, green solid line FM and in dot experimental data.

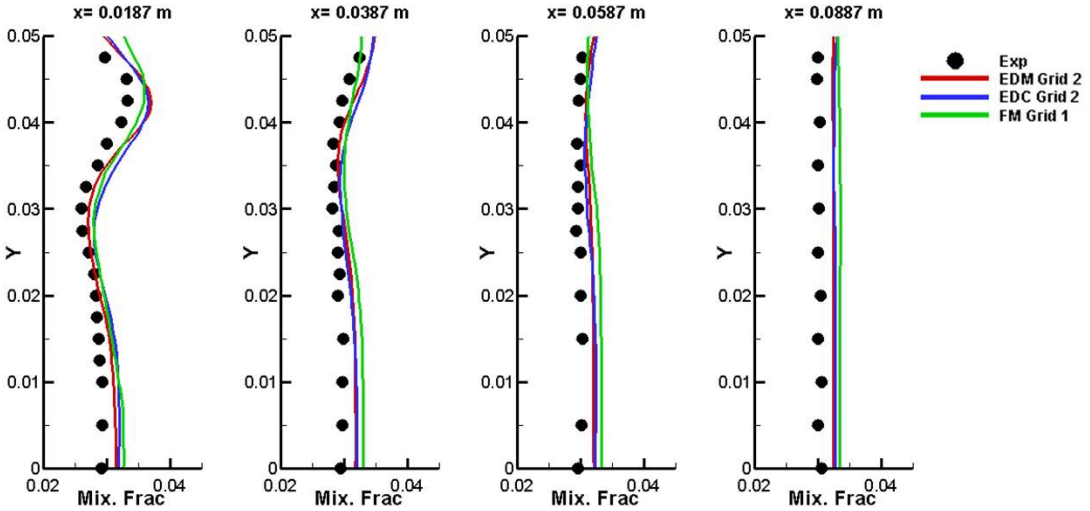

Figure 4.2.24: Mixture fraction profiles extracted at different locations downstream the injection for grid 2. Red solid line EDM simulation, blue solid line EDC with $C_{EDC} = 0.7$, green solid line FM and in dot experimental data.

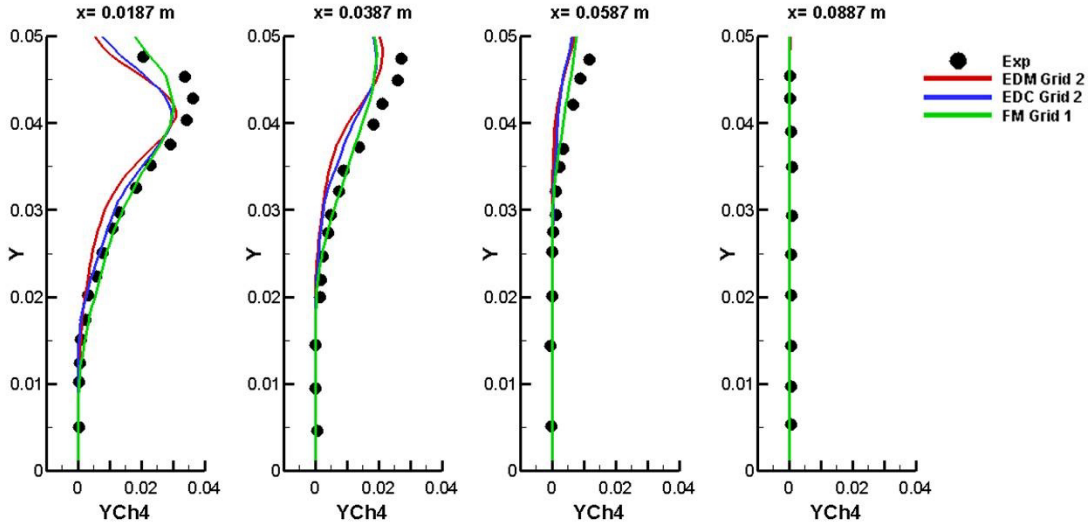

Figure 4.2.25: CH_4 mass fraction profiles extracted at different location downstream the injection for grid 2. Red solid line EDM simulation, blue solid line EDC with $C_{EDC} = 0.7$, green solid line FM and in dot experimental data.

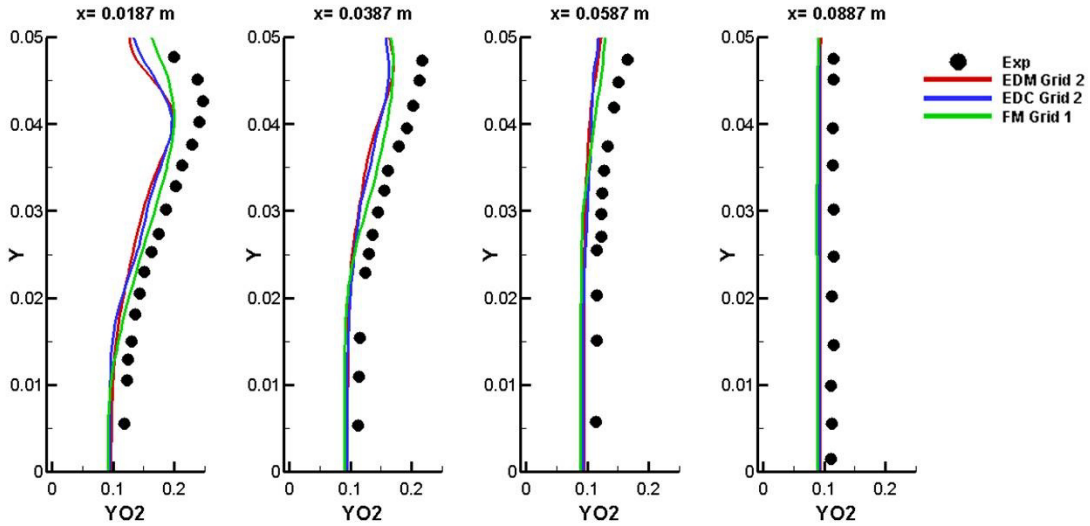

Figure 4.2.26: O_2 mass fraction profiles extracted at different location downstream the injection for grid 2. Red solid line EDM simulation, blue solid line EDC with $C_{EDC} = 0.7$, green solid line FM and in dot experimental data.

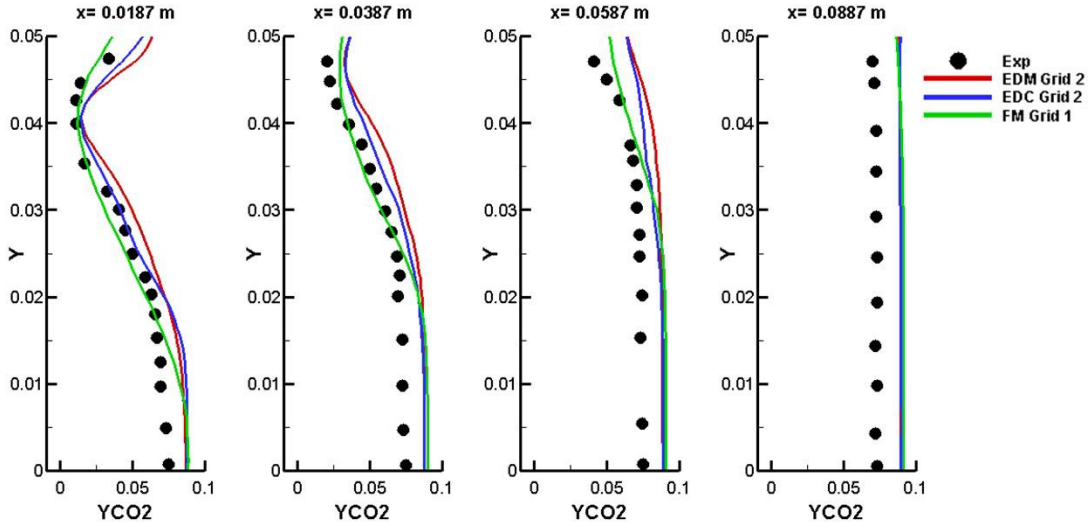

Figure 4.2.27: CO_2 mass fraction profiles extracted at different location downstream the injection for grid 2. Red solid line EDM simulation, blue solid line EDC with $C_{EDC} = 0.7$, green solid line FM and in dot experimental data.

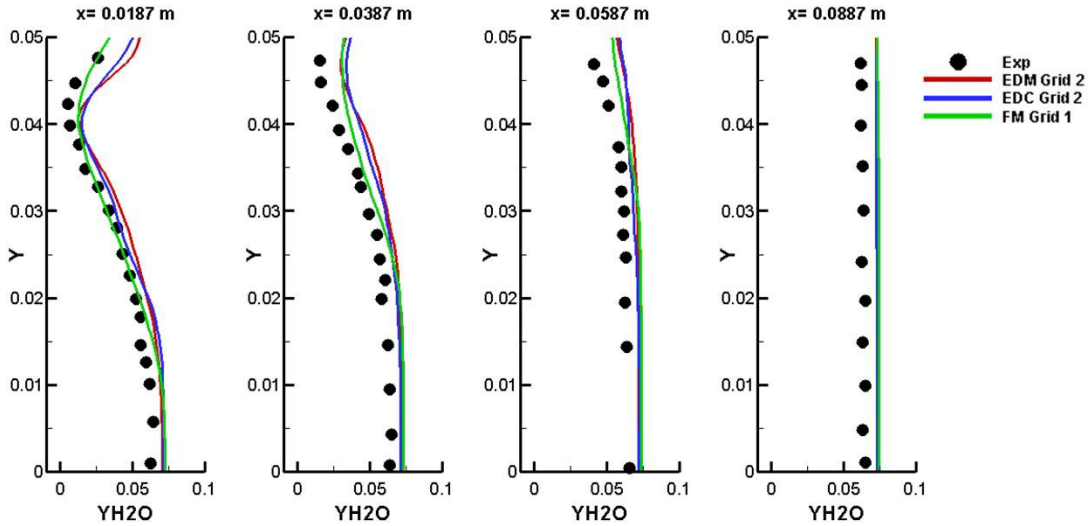

Figure 4.2.28: H_2O mass fraction profiles extracted at different location downstream the injection for grid 2. Red solid line EDM simulation, blue solid line EDC with $C_{EDC} = 0.7$, green solid line FM and in dot experimental data.

5 Validation of near wall models

Flows with separation and reattachment occur in many practical engineering applications. For example a detachment of flow occurs when the boundary layer separates from a blunt body's surface to form a vortex filled wake further downstream. This mechanism typically happens when a positive adverse pressure gradient occurs in the main direction of flow.

In these conditions the correct estimation of the physical phenomena occurring in the boundary layer has a great importance not only for the further development of the flow field, but also for the wall heat transfer. For an accurate prediction of the thermal boundary layer the only use of an efficient turbulence model for the modeling of the Reynolds stresses may not often be sufficient. In literature thermal models for closing the turbulent heat fluxes are often used in wall heat transfer problems. The turbulent heat fluxes $\widetilde{u_k''T''}$ are additional unknown quantities that arise from the RANS closure. These are often modeled in a simple way via the eddy viscosity closure presuming a constant value for the turbulent Prandtl number:

$$\overline{\rho}\widetilde{u_k''T''} = -\frac{\mu_t}{Pr_t}\frac{\partial \overline{T}}{\partial x_k} \tag{5.0.1}$$

where the turbulent Prandtl number is defined by the turbulent heat transfer eddy diffusivity α_t:

$$Pr_t = \frac{\mu_t/\rho}{\alpha_t} \tag{5.0.2}$$

However, the assumption of a constant turbulent Prandtl number in separating flows is quite questionable. Indeed, it was shown by Atonia et al. [83], [84] and also by [34], [61] that this simplification used in conjunction with the k-ε model may lead to a wrong estimation of the phenomena acting in the thermal boundary layer. Recent measurements [22], [34] have suggested values for Pr_t from 0.7-0.9 in the turbulent region and about 1.10 close to the solid boundary.

Therefore for an accurate prediction of the heat transfer in complex turbulence flows, it is required:

- a Low-Re model to solve the near-wall regions;

- a variable turbulent Prandtl number to improve the thermal field prediction in the boundary layer.

5.1 Near Wall modeling: Low Re Number k-ε Model

Despite its wide use in industrial applications, the RANS k-ε model suffers from several limitations for the prediction of complex turbulent flow. The standard formulation has been derived for high Reynolds number flows under the assumptions of isotropic and homogeneous turbulence. In the near wall regions the turbulence is far from isotropic and the model fails, unless some modifications in the near wall regions are applied. In the boundary layer it results in a large value of the turbulent viscosity that leads to erroneous results for the prediction of the velocity profile close to the wall [85]. In Chap. 2 it has been suggested to use the wall functions for resolving the boundary layer, considering local equilibrium of the production and dissipation of the turbulent kinetic energy. The assumption of equilibrium is, however, not valid since a non-equilibrium flow is present near the walls. Therefore, Low-Reynolds number models have been developed with the intent to resolve the flow right down to the viscosity-dominated sublayer without considering any wall functions approach. A representative example consists in the models of Launder and Sharma (1974), Lam and Bremhorst (1981), Chien (1982) and Lien and Leschziner (1993).

The common formulation for such models consists in the classical RANS equations for the turbulent kinetic energy k and its dissipation rate ε, with the addition of some modifications in the ε equation:

$$\frac{\partial \rho k}{\partial t} + u_j \frac{\partial \rho k}{\partial x_j} = \frac{\partial}{\partial x_j}\left[\left(\mu + \frac{\mu_t}{\sigma_k}\right)\frac{\partial k}{\partial x_j}\right] P_k - \rho\varepsilon \tag{5.1.1}$$

$$\frac{\partial \rho \varepsilon}{\partial t} + u_j \frac{\partial \rho \varepsilon}{\partial x_j} = \frac{\partial}{\partial x_j}\left[\left(\mu + \frac{\mu_t}{\sigma_\varepsilon k}\right)\frac{\partial \varepsilon k}{\partial x_j}\right] + C_{\varepsilon 1} f_{\varepsilon 1}\frac{\varepsilon}{k} P - C_{\varepsilon 2} f_{\varepsilon 2}\rho\varepsilon\frac{\varepsilon}{k} \tag{5.1.2}$$

The equation 5.1.2 differs from the 2.2.14 by the presence of the near wall damping functions $f_{\varepsilon 1}$ and $f_{\varepsilon 2}$. The terms $f_{\varepsilon 1}$ and $f_{\varepsilon 2}$ are introduced to recover the behavior of the turbulent quantities μ_t, k and ε in the near wall regions. According to the model the turbulent viscosity is also damped through the f_μ function:

$$\mu_t = C_\mu f_\mu \frac{k^2}{\varepsilon} \tag{5.1.3}$$

The modeling of f_μ is very challenging since the experimental curve shows a non analytical trend in the boundary layer: a constant value for $y^+ < 15$, a linear increase up to $y^+ = 60$ and a logarithmic behavior for high y^+ [86].

In the current work two Low-Re numbers models were considered for the simulations: the Lam-Brenhorst approach [87] and the Abe-Kondoh-Nagano model [88]. The models are very similar and present differences only in the formulation of the damping functions. These are formulated as a combination of exponential functions that tend to unity far from the wall. The corresponding values for these coefficients are summarized in Tab. 5.1.

Model	f_μ	$f_{\varepsilon 1}$	$f_{\varepsilon 2}$
ST	1.0	1.0	1.0
LB	$\left(1-e^{-0.0165R_y}\right)^2\left(1+20.5/R_T\right)$	$1+\left(0.05/f_\mu\right)^3$	$1-e^{-R_T^2}$
AKN	$\left(1-e^{-y^*/14}\right)^2\left[1+\frac{5}{R_T^{3/4}}e^{-(R_T/200)^2}\right]$	1.0	$\left(1-e^{-y^*/3.1}\right)^2\left[1-0.3e^{-(R_T/6.5)^2}\right]$

Table 5.1: Coefficients for the k-ε models: ST (Standard), LB (Lam-Bremhorst), AKN (Abe, Kondoh, Nagano)

The dimensionless parameters in the above expressions are given in [88]. The model constants for the k-ε (low and high Re number) formulations are instead reported in [88], [87].

Referring to the boundary conditions, the models assign for the turbulent kinetic energy at the wall a no-slip condition, whereas several relations can be found for the dissipation rate ε. Lam-Bremhorst have proposed a Neuman condition for ε that is easy to implement and provides reasonable results:

$$\left.\frac{\partial \varepsilon}{\partial y}\right|^{LB} = 0 \tag{5.1.4}$$

The AKN model prescribes instead:

$$\varepsilon^{AKN} = \nu \frac{\partial^2 k}{\partial y^2} \tag{5.1.5}$$

that can be simplified to the following relation:

$$\varepsilon^{AKN} = \frac{2\nu k}{y^2} \tag{5.1.6}$$

The main characteristic of the Low-Re approaches is the ability to reproduce the correct wall asymptotic relations of turbulence. These models provide: $k \propto y^2$, $\varepsilon \propto y^0$, $\mu_t \propto y^3$, in accordance with DNS results and experimental observations [61], [89]. Using the standard formulation the previous quantities are instead over-predicted.

5.2 Two equation model for thermal field

In the following paragraph a method for an accurate evaluation of the thermal field and the wall fluxes is proposed. As previously pointed out, the turbulent heat fluxes are often computed with the general RANS closure form in (5.0.1), with the assumption of a constant turbulent Prandtl number for the computation of the turbulent eddy viscosity $\alpha_t = \nu_t / Pr_t$. This hypothesis may lead to large discrepancies with the experimental data, since the turbulent Prandtl number in the boundary layer is often not constant. The wall characteristics, in fact, could be underestimated, since the temperature fluctuations, responsible of the wall heat transfer, are not well predicted. Therefore, in order to improve the thermal boundary layer modeling, two-equation models for the thermal field have been progressively developed over the last decades. These consist in two additional equations, solving for the temperature fluctuation variance $k_\theta = \frac{1}{2}\overline{T'^2}$ and its dissipation rate $\varepsilon_\theta = \alpha \overline{\frac{\partial T'}{\partial x_j}\frac{\partial T'}{\partial x_j}}$ [34], [61]

$$\frac{\partial \rho k_\theta}{\partial t} + u_j \frac{\partial \rho k_\theta}{\partial x_j} = \underbrace{\frac{\partial}{\partial x_j}\left[\left(\rho\alpha + \frac{\rho\alpha_t}{\sigma_h}\right)\frac{\partial k_\theta}{\partial x_j}\right]}_{Turbulent-Molecular\ Diffusion} \underbrace{-2\rho\overline{u_j T'}\frac{\partial T}{\partial x_j}}_{Production} \underbrace{-2\rho\varepsilon_\theta}_{Dissipation} \tag{5.2.1}$$

$$\begin{aligned}\frac{\partial \rho \varepsilon_\theta}{\partial t} + u_j \frac{\partial \rho \varepsilon_\theta}{\partial x_j} \quad = \quad & \underbrace{\frac{\partial}{\partial x_j}\left[\left(\rho\alpha + \frac{\rho\alpha_t}{\sigma_\phi}\right)\frac{\partial \varepsilon_\theta}{\partial x_j}\right]}_{Turbulent-Molecular\ Diffusion} + \\ & \underbrace{-C_{P1}\rho\frac{\varepsilon_\theta}{k_\theta}\overline{u_j T'}\frac{\partial T}{\partial x_j} - C_{P2}\rho\frac{\varepsilon_\theta}{k}\overline{u_i u_j}\frac{\partial U_i}{\partial x_j}}_{Turbulent\ Production} + \\ & \underbrace{-C_{D1}\rho\frac{\varepsilon_\theta^2}{k_\theta} - C_{D2}\rho\frac{\varepsilon\varepsilon_\theta}{k}}_{Turbulent\ Diffusion}\end{aligned} \tag{5.2.2}$$

where the unknown terms are modeled with a gradient diffusion approach:

$$\overline{u_j T'} = \alpha_t \frac{\partial T}{\partial x_j} \tag{5.2.3}$$

$$\overline{u_i u_j} = \nu_t \left(\frac{\partial U_i}{\partial x_j} + \frac{\partial U_j}{\partial x_i}\right) - \frac{2}{3}\delta_{ij}\left(k + \mu_t \frac{\partial U_k}{\partial x_k}\right) \tag{5.2.4}$$

Similar to the turbulent problem formulation for evaluating the turbulent viscosity μ_t, the turbulent heat diffusivity can be generally expressed by means of an appropriate turbulent length and velocity scale. A common approach is to assume the turbulent velocity scale proportional to the square of the turbulent kinetic energy and the length scale obtained as a

combination of the velocity and a characteristic time scale τ_m:

$$\alpha_t \propto U_c l_c = \sqrt{k}\left(\sqrt{k}\tau_m\right) \tag{5.2.5}$$

The characteristic time scale τ_m combines the effects of the velocity and temperature field time scale: the first depends on the turbulent quantities k and ε, ($\tau_t = k/\varepsilon$), the second is related to the temperature fluctuation variance and its dissipation, ($\tau_\theta = k_\theta/\varepsilon_\theta$). Thus the time scale characterizing the heat transfer was proposed to be a function of the τ_t and τ_θ with the generalized formula [22]:

$$\tau_m \propto \left(\tau_t^l \tau_\theta^m\right) = \tau_t R^m \quad \text{with} \quad l + m = 1 \tag{5.2.6}$$

where $R = \tau_\theta/\tau_t$ is the time scale ratio. Substituting the expression for τ_m in 5.2.5, we obtain a simple relation, originally proposed in the work of Nagano et al. [22], for the turbulent diffusivity. It depends on the temperature fluctuation variance k_θ, its rate of dissipation ε_θ, the turbulent quantities k-ε and the near-wall function f_λ (which accounts for the effects introduced by the wall proximity):

$$\alpha_t = C_\lambda f_\lambda k \tau_m = C_\lambda f_\lambda k \left(\frac{k}{\varepsilon}\frac{k_\theta}{\varepsilon_\theta}\right)^{1/2} \tag{5.2.7}$$

The choice of f_λ is crucial, since it has to reproduce the near wall asymptotic behavior of y^3 for α_t in the boundary layer. Thus it has to be of order y^{-1} for reproducing correctly the turbulent fluctuations [22].

In conclusion, the correct estimation of the turbulent heat fluxes from the model depends on several parameters, whose determination is not easy to obtain. The general formula for the τ_m, in fact, has been an object of research for a long time, and various authors have proposed alternative formulations with respect to those proposed by Nagano, obtaining significant improvement in the wall heat transfer prediction. In the following part, a brief description of these approaches will be presented, highlighting the different expressions for the turbulent heat transfer time scale τ_m and also for the near wall function f_λ.

5.2.1 Models based on the dissipation rate ε_θ and the temperature fluctuation variance

The exact transport equations for the temperature fluctuation variance k_θ and the appropriate dissipation rate ε_θ were derived by Launder for homogeneous turbulent flows without mean velocity and are reported in [85, 90]. In the following section two different approaches in modeling the production term $\mathcal{P}_{\varepsilon_\theta}$ in the ε_θ equation proposed by different authors [91, 22, 92]

are discussed.

According to the work of Launder, the production term for the temperature dissipation rate is a combination of the velocity and temperature fluctuations gradients and unfortunately it represents an unknown term of the problem that requires modeling:

$$\mathcal{P}_{\varepsilon_\theta} = 2\alpha \overline{\frac{\partial u_i'}{\partial x_j}\frac{\partial T'}{\partial x_j}\frac{\partial T'}{\partial x_i}} \tag{5.2.8}$$

Several proposals have been made to approximate it, with the general assumption that both the thermal and the mechanical time scale and also the corresponding production rates can influence the production term $\mathcal{P}_{\varepsilon_\theta}$ in the ε_θ equation. The production rate due to mean shear $\tilde{\mathcal{P}}$ and temperature $\mathcal{P}_\theta$ are indicated as follows:

$$\tilde{\mathcal{P}} = -\overline{u_i' u_j'}\frac{\partial \overline{U_i}}{\partial x_j} \quad \text{and} \quad \mathcal{P}_\theta = -\overline{u_j' T'}\frac{\partial \overline{T}}{\partial x_j} \tag{5.2.9}$$

In the early works from Newaman et alia [91], only the thermal time scale τ_θ and the production rate $\mathcal{P}_\theta$ were considered to model $\mathcal{P}_{\varepsilon_\theta}$. They proposed the following relation:

$$\mathcal{P}_{\varepsilon_\theta} = C_p \frac{\varepsilon_\theta}{k_\theta}\overline{u_j' T'}\frac{\partial \overline{T}}{\partial x_j} = C\frac{1}{\tau_\theta}\mathcal{P}_\theta \tag{5.2.10}$$

A first modification was proposed by Nagano and Kim [22]. Since the production term $\mathcal{P}_{\varepsilon_\theta}$ represents the generation of the turbulent interactions due to the thermal and velocity fluctuations, both production rates have to be considered in the modeling:

$$\mathcal{P}_{\varepsilon_\theta} = C_{P1}\frac{\varepsilon_\theta}{k_\theta}\overline{u_j' T'}\frac{\partial \overline{T}}{\partial x_j} + C_{P2}\frac{\varepsilon_\theta}{k}\overline{u_i' u_j'}\frac{\partial \overline{U_i}}{\partial x_j} \tag{5.2.11}$$

$$= C_{P1}\frac{\varepsilon_\theta}{k_\theta}\mathcal{P}_\theta + C_{P2}\frac{\varepsilon_\theta}{k}\tilde{\mathcal{P}} \tag{5.2.12}$$

A more general form includes an additional term that considers a mixed product between the turbulent time scale τ_t with the thermal production rate $\mathcal{P}_{\varepsilon_\theta}$:

$$\mathcal{P}_{\varepsilon_\theta} = C_{P1}\frac{\varepsilon_\theta}{k_\theta}\mathcal{P}_\theta + C_{P2}\frac{\varepsilon_\theta}{k}\tilde{\mathcal{P}} + C_{P3}\frac{\varepsilon}{k}\mathcal{P}_\theta \tag{5.2.13}$$

The latter term is often neglected, since it does not provide any significant contribution to the turbulent production. Another alternative approach was proposed by Deng et al. [92]. He suggested to model the production rate using the mixed time scale $\sqrt{\tau_t \tau_\theta}$ in combination with $\mathcal{P}_\theta$:

$$\mathcal{P}_{\varepsilon_\theta} = C_p\sqrt{\frac{\varepsilon_\theta}{k_\theta}\frac{\varepsilon}{k}}\overline{u_j'T'}\frac{\partial\overline{T}}{\partial x_j} \tag{5.2.14}$$

$$= C_p\sqrt{\frac{\varepsilon_\theta}{k_\theta}\frac{\varepsilon}{k}}\mathcal{P}_\theta \tag{5.2.15}$$

The models proposed above will be indicated with the following abbreviation: the Abe, Kondoh, Nagano model with AKN and the Deng formulation with DWX. The two different approaches differ also in the modeling of the characteristic time scale τ_m, in order to obtain improvements on the turbulent heat fluxes prediction. For the AKN model:

$$\tau_m^{AKN} = \tau_t\frac{2R}{0.5+R} \tag{5.2.16}$$

For the DWX model, the following expression was proposed instead:

$$\tau_m^{DWX} = \sqrt{2\tau_t\tau_\theta} \tag{5.2.17}$$

It is worth to point out that the equations 5.2.1 and 5.2.2 are not suited to reproduce the behavior at and near the wall. They represent the classical High-Reynolds-number formulation, that has to be modified in order to be valid in the boundary layer region and to simulate appropriately the turbulent fluctuating quantities in this region. This can be realized in a manner analogous to the Low-Reynolds-number approach for the k-ε model. The k_θ equation presents terms that are of the order of y in the near-wall region; this is assured through the balance of the viscous diffusion and dissipation term. As a consequence, no modification for the temperature fluctuation variance equation is required for modeling the flow in the boundary region. Regarding the ε_θ equation, the exact formulation for production and dissipation could provide a behavior of y^0, but the corresponding modeled terms tend to infinite when the wall is approached. This is due to the finite value for ε and ε_θ and the imposed zero value for k and k_θ at the wall. To remove the singularity, a modification at the wall for both ε and ε_θ is needed. This can be avoided by replacing ε and ε_θ in the velocity and thermal time scale with the limited values of:

$$\tilde{\varepsilon} = \nu\left(\frac{\partial\sqrt{k}}{\partial y}\right)^2 \quad \text{and} \quad \tilde{\varepsilon_\theta} = \alpha\left(\frac{\partial\sqrt{k_\theta}}{\partial y}\right)^2 \tag{5.2.18}$$

Under this assumption, the singularity is resolved and the dissipation term in the ε_θ equation approaches the zero value at the wall, still in contrast with the exact formulation that ensures a finite value of order of y^0. This formulation behaves, therefore, similarly to the

High-Reynolds-number form of the ε equation. In order to simulate then the behavior close to the wall, a particular set of damping functions has to be developed and included in the model. This can be achieved using the following damping functions (f_{P1},f_{P2},f_{D1},f_{D2}) that multiply the different production and destruction terms in the ε_θ equation for approximating the near-wall flows:

$$\begin{aligned}\frac{\partial \rho\varepsilon_\theta}{\partial t} + u_j\frac{\partial \rho\varepsilon_\theta}{\partial x_j} &= \underbrace{\frac{\partial}{\partial x_j}\left[\left(\rho\alpha + \frac{\rho\alpha_t}{\sigma_\phi}\right)\frac{\partial \varepsilon_\theta}{\partial x_j}\right]}_{Turbulent-Molecular\,Diffusion} + \\ &\underbrace{-C_{P1}f_{P1}\rho\frac{\varepsilon_\theta}{k_\theta}\overline{u_jT'}\frac{\partial T}{\partial x_j} - C_{P2}f_{P2}\rho\frac{\varepsilon_\theta}{k}\overline{u_iu_j}\frac{\partial U_i}{\partial x_j}}_{Turbulent\,Production} + \\ &\underbrace{-C_{D1}f_{D1}\rho\frac{\varepsilon_\theta^2}{k_\theta} - C_{D2}f_{D2}\rho\frac{\varepsilon\varepsilon_\theta}{k}}_{Turbulent\,Diffusion}\end{aligned} \tag{5.2.19}$$

Nagano et al. also proposed a Low-Reynolds-number formulation for the AKN model, based on particular damping functions to recover the behavior of the turbulent flow at the wall. In Tab. 5.2 the corresponding values for the damping functions are indicated.

f_{p1}	f_{P2}	f_{P3}	f_{D1}	f_{D2}
$\left(1-e^{-y^*}\right)^2$	1.0	0.0	$\left(1-e^{-y^*}\right)^2$	$\frac{1}{C_{D2}}\left(C_{\varepsilon 2}f_2-1\right)\left[1-e^{-y^*/5.7}\right]^2$

Table 5.2: Damping functions expressions for the AKN model in the Low-Re formulation

The model also suggested a new relation for the turbulent heat diffusivity α_t. It consists in the classical form as the relation expressed in 5.2.7, but presents a significant modification for the characteristic time scale τ_m for taking into account Low-Re number problems. Regarding the near-wall function f_λ, the expression is of order y^{-1}, providing the right near-wall behavior of y^3 for α_t.

$$\alpha_t = C_\lambda k\underbrace{\left[\frac{k}{\varepsilon}\left(\frac{2R}{0.5+R}\right) + 3\frac{1}{\sqrt{k}}\left(\frac{\nu^3}{\varepsilon}\right)^2\frac{\sqrt{2R}}{\sigma}f_d\right]}_{\tau_m}\underbrace{\left[1-e^{-y^*/14}\right]\left[1-e^{-\sqrt{\sigma}y^*/14}\right]}_{f_\lambda} \tag{5.2.20}$$

Different damping functions are employed instead in the model of Deng et al. (DWX), which perform better in the boundary layer region and provide an improvement of the accuracy. These are reported in Tab. 5.3:

f_{p1}	f_{P2}	f_{P3}	f_{D1}	f_{D2}
1.0	1.0	0.0	$\left(1-e^{-y^*/1.7}\right)^2$	$\frac{1}{C_{D2}}\left(C_{\varepsilon 2}f_2-1\right)\left[1-e^{-y^*/5.8}\right]^2$

Table 5.3: Damping functions expressions for the DWX model in the Low-Re formulation

The turbulent heat diffusivity α_t for the DWX model is given as follows:

$$\alpha_t = C_\lambda k \underbrace{\frac{k}{\varepsilon}\sqrt{2R}}_{\tau_m} \underbrace{\left[1-e^{-y^*/16}\right]^2\left[1+\frac{3}{Re_T^{3/4}}\right]}_{f_\lambda} \tag{5.2.21}$$

For both of the formulations, the model constants C_{P1}, C_{P2}, C_{D1}, C_{D2} used in the ε_θ equation have to be chosen. They are summarized, depending on the model, in Tab. 5.4. A slight difference for C_{P1} values can be observed between the models: this is mainly due to the modeled production term. In case of the DWX model, the latter consists in a unique term (since C_{P2} is zero), requiring therefore a higher constant value for producing the same production rate with respect to the AKN model. Instead the other constants remain the same. Their values are obtained through experimental measurements in decaying homogeneous scalar turbulence and temperature fluctuation variance in grid turbulence and they are validated against different types of high Reynolds-number flows [90].

Model	C_λ	C_{P1}	C_{P2}	C_{P3}	C_{D1}	C_{D2}
AKN k_θ-ε_θ	0.1	1.9	0.6	0.0	2.0	0.9
DWX k_θ-ε_θ	0.1	2.4	0.0	0.0	2.0	0.9

Table 5.4: Constants for the k_θ-ε_θ models: AKN (Abe, Kondoh, Nagano), DWX (Deng, Wu, Xi)

Finally, the boundary conditions for k_θ and ε_θ have to be indicated: zero value at the inflow and zero gradient at the boundaries for k_θ, whereas the temperature dissipation rate ε_θ is limited at the wall as follows:

$$\varepsilon_\theta\rfloor_w = \alpha\left(\frac{\partial\sqrt{k_\theta}}{\partial y}\right)^2 \tag{5.2.22}$$

To avoid confusion between the Low-Re number formulation developed also by Abe et al. and the above thermal model, in the following sections the abbreviation AKN (or AKN-k-ε) will indicate the low-Re turbulence model and AKN_t (or AKN-k_θ-ε_θ) the thermal model.

5.2.2 Models based on the specific dissipation rate ω_θ and the temperature fluctuation variance

As illustrated in Chap. 2, the standard two-equation turbulent models based on the k-ε formulation have showed a lack in the prediction of boundary-layer flows with large adverse pressure gradients, leading to incorrect values of the turbulent variable in the near-wall regions. This is mainly due to the ε variable used for the definition of the turbulent length-scale. Better results are obtained with the definition of the specific dissipation rate ω, defined as a combination of the turbulent kinetic energy and its dissipation: $\omega = \varepsilon/k$ [25].

Similarly to turbulent problems, in the thermal model the determination of the variable for the length-scale equation may be crucial and can significantly affect the accuracy of the results, providing a wrong prediction of the law of the wall for the temperature [23]. According to Bradshaw, the best choice for obtaining the right reproduction in the near wall regions is represented by the specific dissipation rate ω_θ rather than ε_θ. This is defined as follows:

$$\omega_\theta = \frac{\varepsilon_\theta}{k_\theta} \tag{5.2.23}$$

Huag and Bradshaw derived a heat transfer model (HB model), solving for the temperature fluctuation variance k_θ and its specific dissipation rate ω_θ. The corresponding governing equations for k_θ and ω_θ are:

$$\frac{\partial \rho k_\theta}{\partial t} + u_j \frac{\partial \rho k_\theta}{\partial x_j} = \underbrace{\frac{\partial}{\partial x_j}\left[\left(\rho\alpha + \frac{\rho\alpha_t}{\sigma_h}\right)\frac{\partial k_\theta}{\partial x_j}\right]}_{Turbulent-Molecular\ Diffusion} \underbrace{-2\rho\overline{u_j T'}\frac{\partial T}{\partial x_j}}_{Production} \underbrace{-2\rho k_\theta \omega_\theta}_{Dissipation} \tag{5.2.24}$$

$$\begin{aligned} \frac{\partial \rho \omega_\theta}{\partial t} + u_j \frac{\partial \rho \omega_\theta}{\partial x_j} \quad = \quad & \underbrace{\frac{\partial}{\partial x_j}\left[\left(\rho\alpha + \frac{\rho\alpha_t}{\sigma_\phi}\right)\frac{\partial \omega_\theta}{\partial x_j}\right]}_{Turbulent-Molecular\ Diffusion} + \\ & \underbrace{-C_{P1}\rho\frac{\omega_\theta}{k_\theta}\overline{u_j T'}\frac{\partial T}{\partial x_j} - C_{P2}\rho\frac{\omega_\theta}{k}\overline{u_i u_j}\frac{\partial U_i}{\partial x_j}}_{Turbulent\ Production} + \\ & \underbrace{-C_{D1}\rho\omega_\theta^2 - C_{D2}\rho\omega\omega_\theta}_{Turbulent\ Diffusion} \end{aligned} \tag{5.2.25}$$

The unknowns in the above equations related to the turbulent shear stress $\overline{u_j u_i}$ and the turbulent heat flux $\overline{u_j T'}$ are closed with a gradient diffusion approach as described in 5.2.4 and 5.2.3.

In order to have a definition for the turbulent heat diffusivity α_t valid for the HB model,

Huag and Bradshaw have considered the general form provided by Nagano [22], and have replaced the variables for the turbulent and thermal time scale with the definitions of ω and ω_θ. They obtained the following relation for α_t:

$$\alpha_t = C_\lambda k \left(\frac{1}{\omega} \frac{1}{\omega_\theta} \right)^{1/2} \tag{5.2.26}$$

The model constants related to the corresponding coefficients in the ω_θ equation are obtained analyzing the near-wall regions through the analytical integration of the transport equations. It results in an algebraical relation between the coefficients C_{D1} and C_{D2} with the turbulent Prandtl number at the wall $Pr_{t,w}$.

$$Pr_{t,w} = \frac{C_\mu}{C_\lambda} \sqrt{\frac{C_2 - C_{D2} Pr}{C_{D1} Pr}} \tag{5.2.27}$$

Using the DNS results for $Pr_{t,w}$ and imposing $C_{D1} = 0.1$, Bradshaw found the optimum value for the C_{D2}, and through an iterative method the other remaining constants for the production terms. The values are summarized in Tab. 5.5.

Model	C_λ	C_{P1}	C_{P2}	C_{P3}	C_{D1}	C_{D2}
HB k_θ-ω_θ	0.11	-0.2	0.94	0.0	0.1	0.83

Table 5.5: Constants for the k_θ-ω_θ HB model (Huag-Bradshaw)

5.3 Numerical Validation

5.3.1 Test case 1: Heat transfer predictions in cavities

The first test case considered for the validation of the turbulent models in conjunction with the two-equation thermal model is a numerical example of heat transfer in cavities [93]. For the numerical simulations, the test-case was simplified and the geometry consists in a channel flow with a two-dimensional cavity. The inflow has a constant height H and is placed at $1H$ upstream the cavity. At the inlet, a fully turbulent velocity profile with a constant static temperature of $T_{in} = 350K$ is prescribed. Pure air was used for the experiments and thus, for the numerical simulations. Its inflow properties (density ρ, molecular viscosity μ, thermal conductivity κ and specific heat C_p) are calculated at the inflow temperature T_{in}. The cavity resembles the space between two turbine blades, whereby a large recirculation zone takes place. Its dimension W is a multiple of the inflow height and was fixed at $W = 10H$. Regarding the cavity depth D, two configurations were considered with different aspect ratios: $D/W = 0.1$ and $D/W = 0.2$. The outlet region, instead, has the same geometry as the inflow,

with an outflow located $1H$ downstream the cavity. The computational domains is illustrated in Fig. 5.3.1.

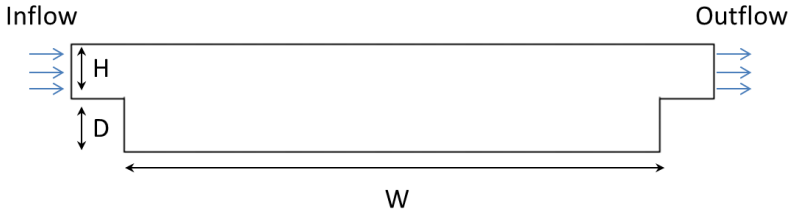

Figure 5.3.1: Sketch of the simplified geometry of a flow in a cavity.

The Reynolds number based on the bulk velocity U_{bulk} and the height H of the channel at the inlet is the same as the one that was considered by Metzger et al. in the experimental setup [94]:

$$Re_{in} = \frac{\rho U_{bulk} H}{\mu} = 15000 \tag{5.3.1}$$

The wall boundaries in the cavity were modeled as isothermal with a temperature of $T_w(x) = 293K$. Since no information for the upper wall temperature was available in literature, the remaining walls are treated as adiabatic. Two structured grids are used for the numerical simulations depending on the aspect ratio.

The experiments were conducted by Metzger et al.[94] focusing on the determination of the local Nusselt number distribution along the cavity wall for both the configurations ($D/W = 0.1$ and $D/W = 0.2$). In order to validate the simulations against the experimental data, a numerical definition for the Nusselts number is required. It can be defined as the ratio of the convective and the conductive heat transfer based on the characteristic length scale H:

$$Nu = \frac{h(x) H}{\lambda} \tag{5.3.2}$$

with the local heat transfer coefficient $h(x)$ related to the temperature difference $T_w(x) - T_{in}$ and the heat flux $\dot{q}(x)$ by:

$$h(x) = \frac{\dot{q}(x)}{T_w(x) - T_{in}} \tag{5.3.3}$$

The numerical simulations were conducted with the intent to obtain an accurate solution for the prediction of the heat transfer in a cavity flow. Steady state RANS simulations were performed with various turbulence models in conjunction with the two-equation scalar model. The k-ε model was used only with its standard formulation (results indicated in Fig.5.3.2 with a red line) without considering any near wall modification for Low-Reynolds

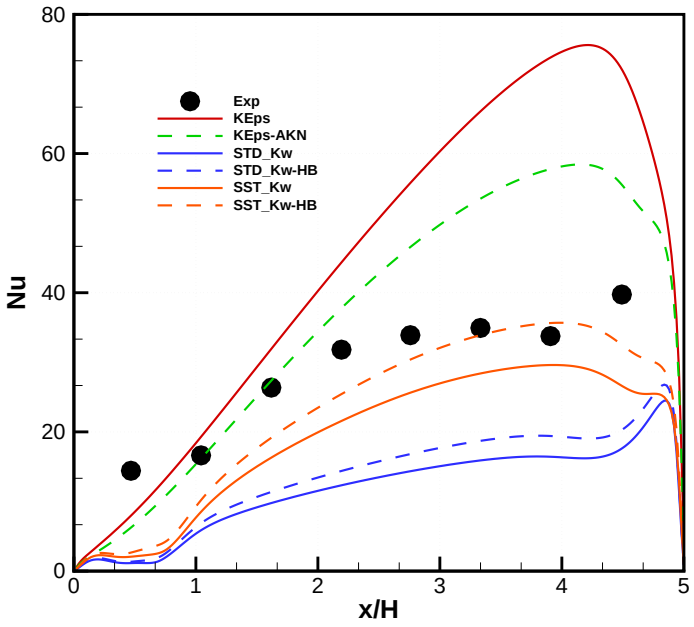

(a)

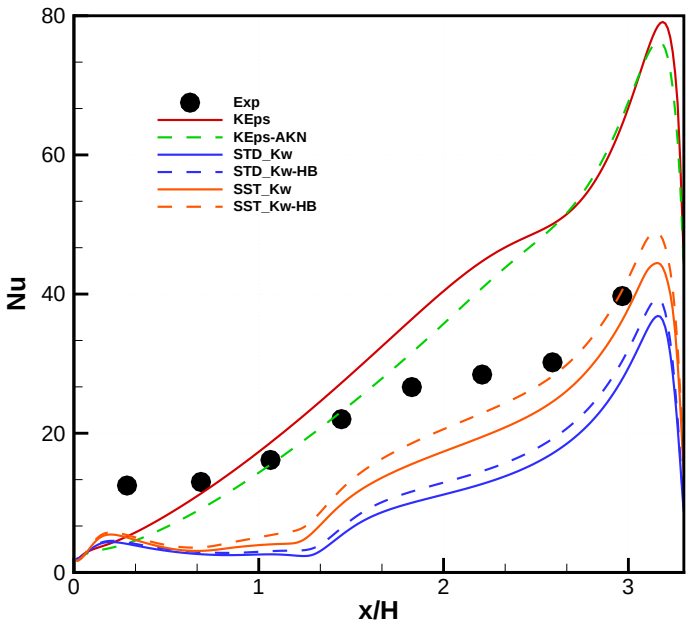

(b)

Figure 5.3.2: Nusselt number distribution on the lower wall of the cavity for $D/W = 0.1$ (a) and $D/W = 0.2$ (b)

numbers flows. The scalar model solves for the temperature fluctuation variance and its dissipation, thus avoiding the concept of constant turbulent Prandtl number. This was employed together with the k-ε model and the results are compared with those obtained assuming a fixed turbulent Prandtl number. These are hereinafter referred to with a red dashed line. Simulations with the k-ω model are also presented. They were carried out with the standard STD-k-ω approach and with Menter's formulation SST k-ω, (blue and orange lines respectively). A non-constant Pr_t in conjunction with the k-ω approach was modeled with the Huag-Bradshaw (HB) scalar model and the corresponding results are indicated with dashed lines. Convergence was assessed by the residual criteria. A target value of 1e-6 was considered for all the simulations.

Fig. 5.3.2(a) and (b) show the resulting heat transfer prediction on the lower wall of the cavity for the two different configurations with aspect ratio $D/W = 0.1$ (a) and $D/W = 0.2$ (b) (see Fig. 5.3.1). These represent the local Nusselt number distribution over the length of the cavity W, which is made dimensionless with respect to the total height of the cavity $C = D + H$ in Fig. 5.3.1 . The experimental results demonstrate an enhancement of the heat transfer moving from the left to the right of the cavity, with a maximum located just before the wall. Qualitatively, Nusselts' profiles for both the configurations are similar. The only difference lies in the growth rate for the Nu along the wall. While the configuration with $D/W = 0.1$ has a steeper gradient, the second indicates a slower increase of the heat transfer in the first part of the cavity with a progressive growth until the maximum is reached.

Numerically, the Nusselt number distribution obtained with the standard k-ε model is over-predicted: in both cases the region close to the first wall shows a good accuracy with the experimental data, while the remaining domain is largely overestimated. The peak, in fact, is approximately the double of that measured by Metzger [94]. The use of the Abe-Nagano-Kondoh k_θ-ε_θ (AKN-k_θ-ε_θ) model for closing the turbulent heat fluxes seems to slightly improve the distribution but the over-prediction remains still too large. Different results are obtained with the k-ω turbulence models. The STD-k-ω model under-predicts the heat transfer found experimentally, whereas the SST formulation seems to perform better. The latter, although the Nusselt number values are still low, exhibits the same trend and growth rate compared to the experiments. Better results are obtained coupling the turbulent effects with the thermal model from Huag and Bradshaw (HB). These simulations clearly highlight the advantage of their use: both the calculations show an improvement of the predicted Nusselt number with respect to the runs without the HB model. This is especially evident in the case with smaller aspect ratio, where the differences in the prediction are more pronounced and the results with HB model seem to better fit the experimental data.

The axial velocity distributions for $D/W = 0.1$ and $D/W = 0.2$ are illustrated in Fig. 5.3.3

and Fig. 5.3.4. Here a comparison of the numerical results for the flow fields obtained with the standard k-ε and the SST-k-ω models is presented. For the configuration with smaller aspect ratio, the axial velocity distribution with standard k-ε is very similar to that with the SST-k-ω. In this case both simulations show a flow separation with a large recirculation bubble that extends over nearly all the length of the cavity. A curved separated shear layer develops immediately downstream of the wall, creating the main bubble and two small recirculation zones in correspondence of the two corners of the cavity. This behavior was found in the simulation with the standard k-ε model, whereas in the SST-k-ω calculation the first recirculation zone, located close to the first cavity wall, is more pronounced and is then followed by the large bubble that impinges on the lateral solid boundary (Fig. 5.3.3).

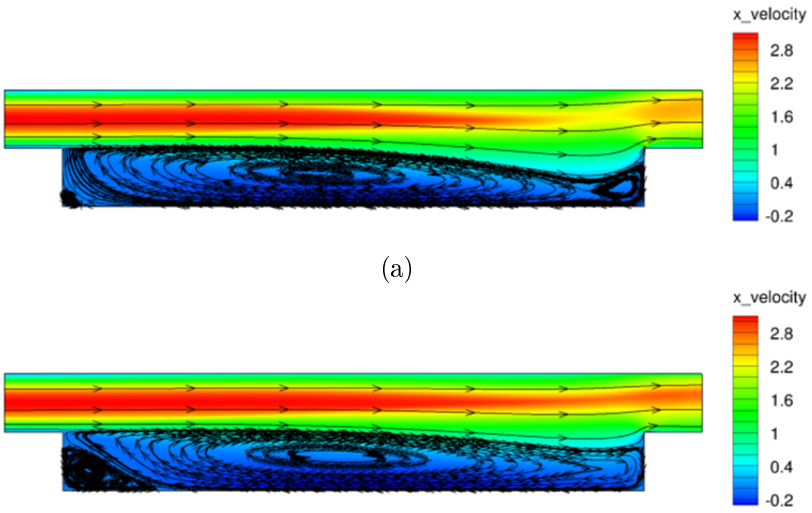

Figure 5.3.3: Axial velocity distribution for $D/W = 0.1$ with k-ε (a) and SST-k-ω in conjunction with the Huag-Bradshaw (HB) thermal model (b)

As a consequence, the small recirculation bubble on the right side close to the corner disappears. The effects of the first recirculation region affect the heat transfer distribution, leading to a flat profile for the Nusselt number until the bubble ends. This behavior can be clearly noticed observing the profiles for the Nusselt number in the Fig. 5.3.2(a). However, the simulations with aspect ratio $D/W = 0.2$ reveal significant differences in the downstream region after the wall for the axial velocity. With the k-ε model, the flow separates at the wall and reattaches on the side of the wall in the outlet region, creating a large unique recirculation zone. With the SST-k-ω model, whose result in term of velocity is presented in Fig. 5.3.4, the flow field presents after the flow separation, two counter-rotating vortexes in the cavity, which modify deeply the structure of the axial velocity and the heat transfer distribution.

Because of the first low-speed region, in fact, the heat transfer at the wall is not favored

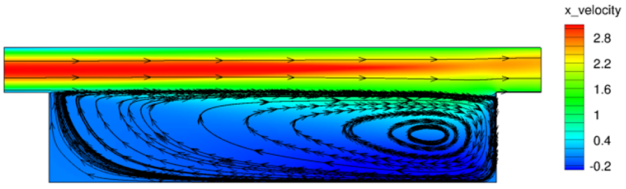

(a)

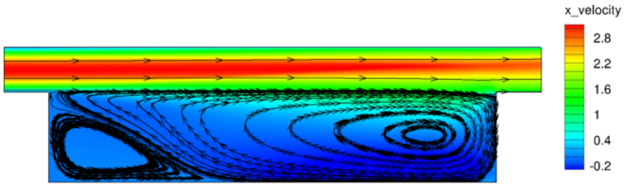

(b)

Figure 5.3.4: Axial velocity distribution for $D/W = 0.2$ with k-ε (a) and SST-k-ω in conjunction with the Huag-Bradshaw (HB) thermal model (b)

through the convective transport and the resulting Nusselt number remains constant in this first zone. Since no information for the velocity field was provided experimentally, it is difficult to know which flow field takes place in the cavity. However, the vortexes in the cavity have a great influence in the local enhancement of the Nusselt number distribution. This behavior is qualitatively well reproduced by the simulations with the k-ω formulation in conjunction with the thermal model for calculating the turbulent Prantdl number (HB model). In the following sections other test cases will be considered with the intent to investigate the ability of the AKN-k_θ-ε_θ or HB-k_θ-ε_θ thermal model to predict the wall heat transfer under different configurations and conditions.

5.3.2 Test case 2: Heat transfer predictions in a pipe expansion

The second test case considered for the numerical validation is a flow through a pipe expansion. Similarly to the case discussed previously, the flow presents an essentially two dimensional behavior with a flow separation and a recirculation zone in the larger pipe. At the inlet boundary pure air is inserted at a temperature of $T_{in} = 300K$ through a small pipe of diameter d, flowing parallel to the axis until it enters the main chamber, which is a coaxial cylindrical tube with diameter D. The resulting expansion ratio between the two zones has been fixed at $D/d = 2.5$. The flow separates at the edges of the small pipe right at the injection in the chamber. Experiments reveal an increase of the heat transfer in correspondence of the recirculation zone, with a peak located approximately at the reattachment points [95]. The measurements were conducted by Baughn et al. [96], focusing on the influence of the expansion ratio (and consequently the Reynolds number) on the local heat transfer. In this work it will be illustrated only the case corresponding at $D/d = 2.5$ and Reynolds number

of 17300, since both the experimental data for the temperature and the velocity fields are available in literature.

Due to the symmetry of the problem only a segment of the pipe was considered in the simulation, as shown in Fig.5.3.5. The computational domain consists of a small inlet region with a constant section $d/2$ and an expansion region, which axially extends for $16D$. The parameter H is defined as $H = (D-d)/2$. A sketch of the computational domain is illustrated in Fig. 5.3.5 and 5.3.6.

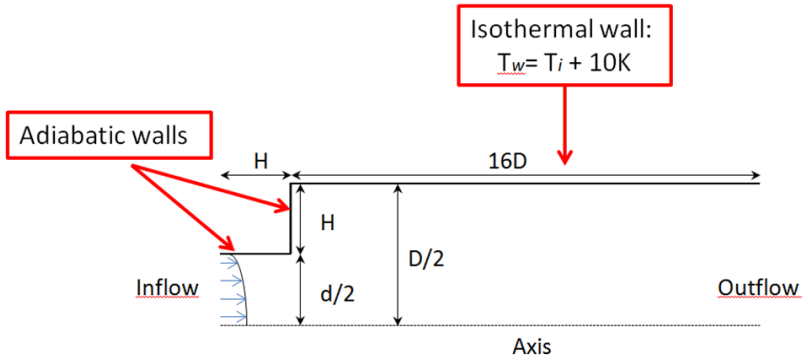

Figure 5.3.5: Geometry for the turbulent flow in an abrupt expansion.

Corrections:

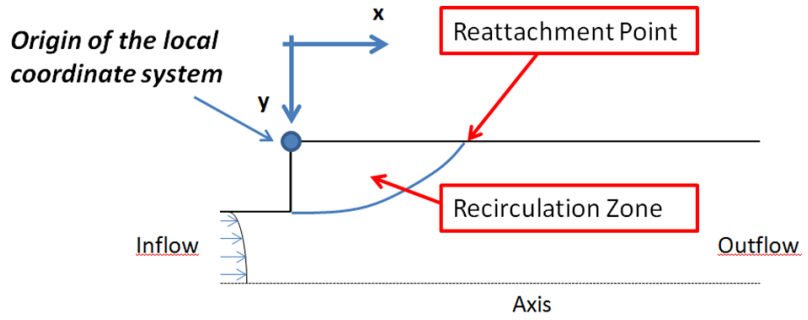

Figure 5.3.6: Coordinate system considered for the extraction of the numerical 1D profiles.

All the wall boundaries have been treated as adiabatic, except for the wall in the expansion region (Fig.5.3.5). The latter was set as isothermal prescribing a wall temperature value as indicated in the experiments of Baughn [96]. He measured the temperature and the velocity fields in the abrupt expansion under isothermal conditions. A uniform temperature at the wall was obtained through two cylindrical heaters set around the measurements chamber in order

to achieve a difference between the wall temperature and the inlet air temperature ($T_w - T_{in}$) of about 10K. At the symmetry axis, the radial velocity vanishes and the condition of zero gradient was imposed for all the other variables. At the solid walls the no-slip boundary condition is employed, leading to a zero value for the velocity and the turbulent kinetic energy.

Since no information was indicated concerning the velocity at the inflow, a mean axial velocity profile was prescribed using the one-seventh law with the assumption of zero radial profile. This profile ensures a condition similar to that observed under fully-developed turbulence. The experiments, in fact, showed the presence of a turbulent flow in the upstream pipe but with a low level for turbulence intensity. This suggests to use the following empirical values for the turbulent variables at the inlet [97]:

$$k_{in} = 0.003 u_{in}^2 \tag{5.3.4}$$

$$\varepsilon_{in} = \frac{C_\mu k_{in}^{1.5}}{0.03R} \tag{5.3.5}$$

where R is the radius of the pipe and C_μ is a model constant for the STD-k-ε model.

For the numerical prediction of the heat transfer process, steady-state simulations were run using RANS turbulence models: STD-k-ε, STD-k-ω and SST-k-ω. The convergence of the solution was monitored by checking the residuals history prescribing a value of 1e-6 as convergence criteria. The aim of the investigation mainly addressed to assess the accuracy of the thermal model for the k-ε (AKN-k_θ-ε_θ Model) and for k-ω (HB-k_θ-ε_θ Model) and to verify the improvement in the boundary layer region provided through a Low-Reynolds number formulation. The latter was applied by means of the AKN-k-ε model for Low-Reynolds number flows and the results are indicated with a green solid line in Fig.5.3.7 and 5.3.8. The reference simulations have been carried out without considering any model for the temperature fluctuation variance and its dissipation. Under this condition, the turbulent heat fluxes were modeled with the eddy-diffusivity approximation assuming a constant turbulent Prandtl number of 0.7. Since the previous numerical results for the test-case 1 have demonstrated an improvement of the wall heat transfer predictions, the test-case 2 was also simulated with the scalar model for the temperature fluctuation variance. The numerical results for the flow and temperature field predictions are validated against the experimental data of Baughn [96] and are reported in the next sections.

5.3.2.1 Numerical Results with k-ε approach

The measurements of Baughn et al.[96] consist in a collection of data for the temperature and axial velocity field, recorded at different locations downstream of the abrupt expansion.

Considering the local coordinate system shown in Fig.5.3.6, 1D profiles were extracted at: $x/D = 0.075$, $x/D = 0.030$, $x/D = 1.80$, $x/D = 3.00$, $x/D = 4.20$, $x/D = 6.00$.

Due to the velocity, the thermal load is convected from the wall to the center of the pipe, leading to a local increase of the fluid temperature. In the region right after the expansion region, the fluid preserves its inflow value T_{in}, whereas in the upper side of the pipe the transport of the thermal energy is favored due to a large recirculation zone. Between the two regions a steeper temperature gradient occurs and the temperature varies from $T = 300$K to almost $T = 305$K. Moving downstream, the mixing phenomenon becomes more relevant and the temperature gradient is smoother. This can be observed in Fig. 5.3.7 at $x/D = 0.075$. After $x/D = 1.80$, the temperature field appears instead more homogeneous and the effect of higher wall temperature leads progressively to an increase of the value on the axis. Fig. 5.3.7 shows the comparison of the simulated profiles with the STD-k-ε, AKN-k-ε and with AKN-k-ε in conjunction with the AKN-k_θ-ε_θ thermal model against the experiments (AKN_t). The profiles are qualitative well predicted by all the models: the STD-k-ε over-predicts the temperature in the recirculation region, where the turbulent fluctuations play a significant role in the heat transfer mechanism, and it also shows an erroneous temperature gradient at the wall. In the further downstream zone, the simulated profiles present a good agreement with the experimental data, with the only exception of the zone near the axis of the pipe, where the temperature is slightly under-predicted. On the other hand the Low-Reynolds number model (AKN) presents the worst results in term of radial profiles with a larger deviation from the right measured points. Better results are obtained combining the previous model with the thermal model (AKN_t); in this case the deviation is completely recovered. The simulation, in fact, shows profiles similar to the calculation with the STD-k-ε model and also provides a better estimation of the temperature along the axis.

In Fig. 5.3.8 the axial velocity profiles, extracted at the same locations as for the previous temperature profiles, are illustrated. These are non-dimensionalized with the maximum velocity in the simulations and compared against the experiments. As previously mentioned, the transverse profile for the axial velocity shows clearly at $x/D = 0.075$ the presence of two regions corresponding at the injection (with higher velocity) and at the recirculation zone (with low speed). The reattachment point is located at approximately $x/D = 3.00$. After the position $x/D = 6.60$ no significant variations for the axial velocity field could be found, as also confirmed by Chang [97], and a flat uniform profile originates in the pipe, propagating without modifications until the outlet region. The behavior of the numerical simulations for the velocity field is similar to what happens for the temperature. The Low-Reynolds number model (AKN) is not able to provide a good accuracy leading to a small underestimation, whereas the STD-k-ε seem to reproduce very well the behavior of the flow

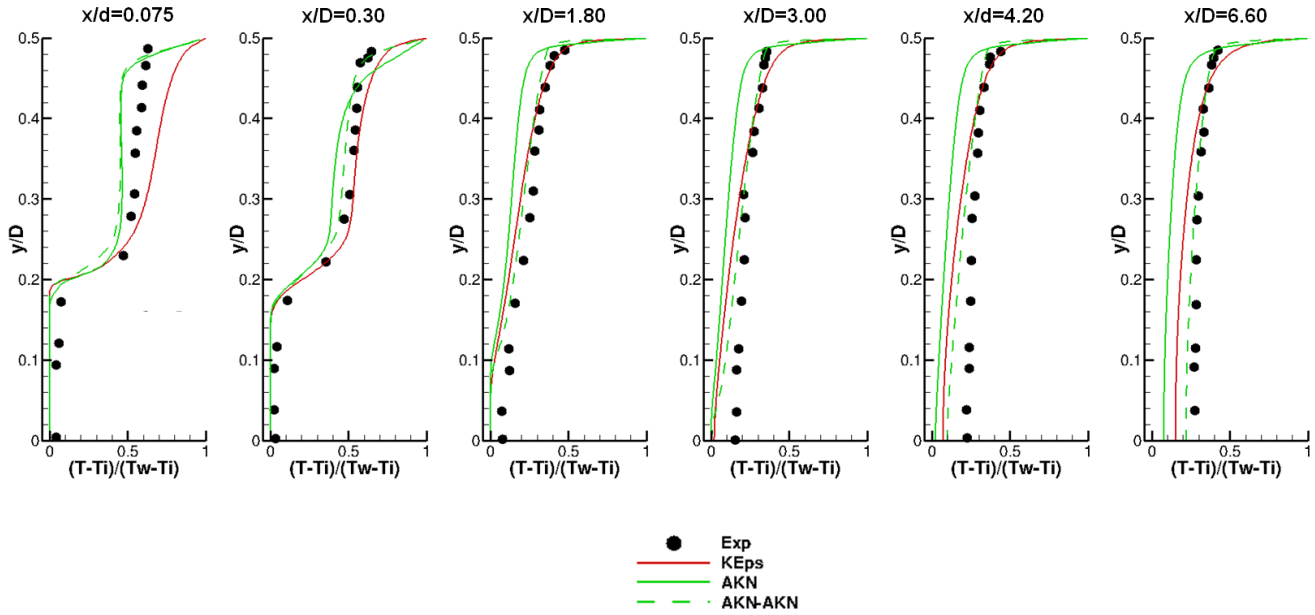

Figure 5.3.7: Comparison of the simulated temperature profiles with k-ε approach against the experimental data at different locations. In red line simulation with STD-k-ε, in green solid line calculation with AKN Low-Reynold number model and in green dashed line computation with AKN Low-Reynold number model in conjunction with the AKN_t thermal model.

field. This deviation is probably due to the damping functions in the Low-Reynolds number formulation, that reduce the turbulent viscosity in the near-wall region but also influence the central flow region leading to the small discrepancies found against the experiments.

5.3.2.2 Numerical Results with k-ω approach

In Fig. 5.3.9 and Fig. 5.3.10 the axial velocity and temperature profiles calculated with the k-ω formulation are shown. The reference simulations are computed with the standard STD and Menter's SST formulation with a constant Pr_t: they present a good agreement in the injection zone in terms of temperature values, but under predict significantly the thermal field in the further downstream region. However, the axial velocity calculated with the standard STD presents a good accuracy with the experimental data, as well as the simulation with SST, although the latter deviates a little from the experiments at the location $x/D = 6.60$. The use of the thermal model (HB) provides some improvements in matching the measurements in the near-wall region, but it does not influence significantly the temperature field.

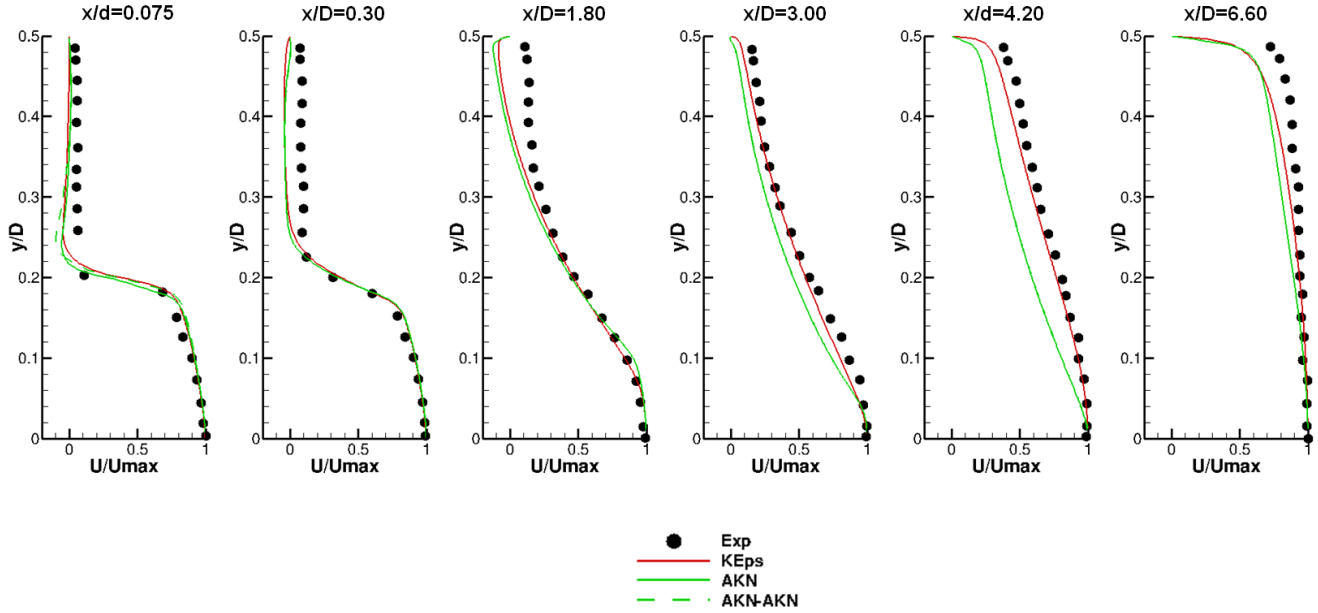

Figure 5.3.8: Comparison of the simulated velocity profiles with k-ε approach against the experimental data at different locations. In red line simulation with STD-k-ε, in green solid line calculation with AKN Low-Reynold number model and in green dashed line computation with AKN Low-Reynold number model in conjunction with the AKN_t thermal model

5.3.3 Test case 3: Heat transfer predictions in a backward facing step

Another interesting test case for studying the performance of the heat transfer and turbulence modeling is the flow after a backward facing step. Similar to the case of a flow in an abrupt expansion, the flow is essentially two-dimensional and is subjected to a sudden expansion. Due to the increase of the cross-sectional area, the flow separates at the edge of the expansion, creating downstream a shear layer and a large recirculation bubble. The recirculation zone consists in a low-speed region with low pressure and high level of turbulent fluctuations. After this zone, the flow reattaches to the wall and re-develops as in a channel flow. In the following section, the capability to predict the reattachment length and the wall heat transfer for this test case will be tested using the turbulent models with and without their Low-Reynolds number formulation and in combination with their thermal models. The test case under investigation is the flow field downstream of a backward facing step with an expansion ratio of 1.25. The computational domain is illustrated in Fig.5.3.11 and consists in an inlet and outlet region and an expansion zone. The length of the total domain is approximately $40H$, the inflow is located $1.1H$ upstream of the step and the expansion ratio $(W/(W-H))$ is 1.25. The Reynolds number based on the step height $H = 0.038m$ is 28000 and corresponds to an

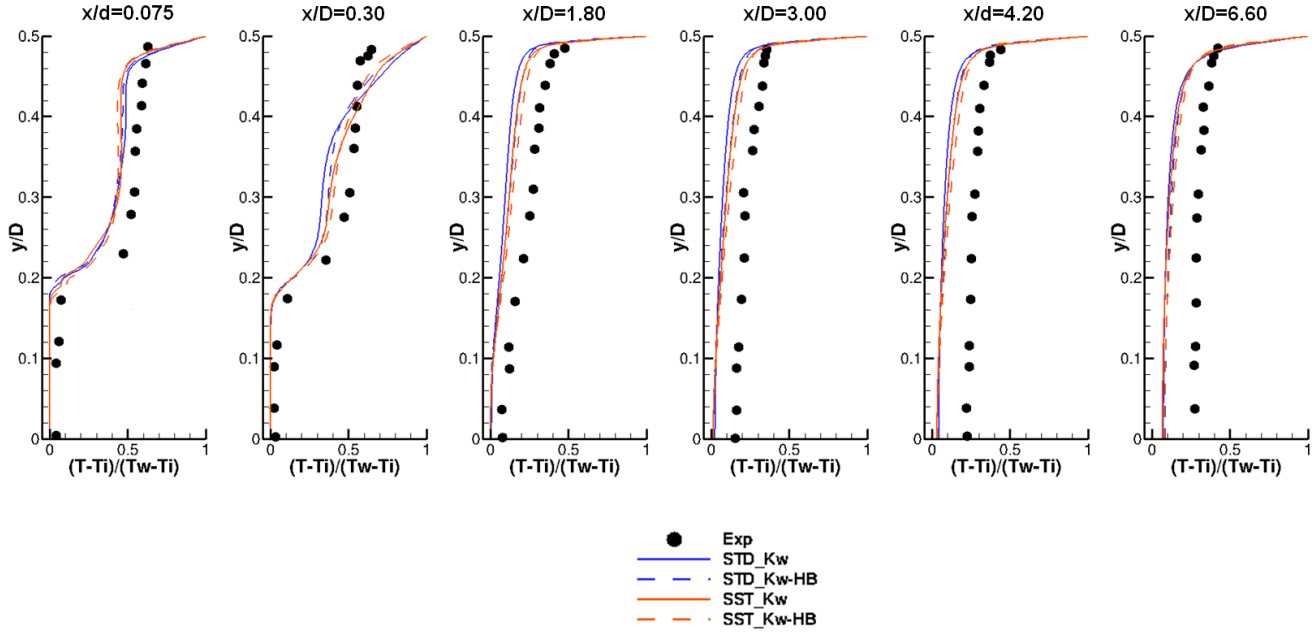

Figure 5.3.9: Comparison of the simulated temperature profiles with k-ω approach against the experimental data at different locations. In blue line simulation with STD-k-ω, in blue dashed line calculation with STD-k-ω with HB, in orange line computation with SST-k-ω and orange dashed line SST-k-ω with HB.

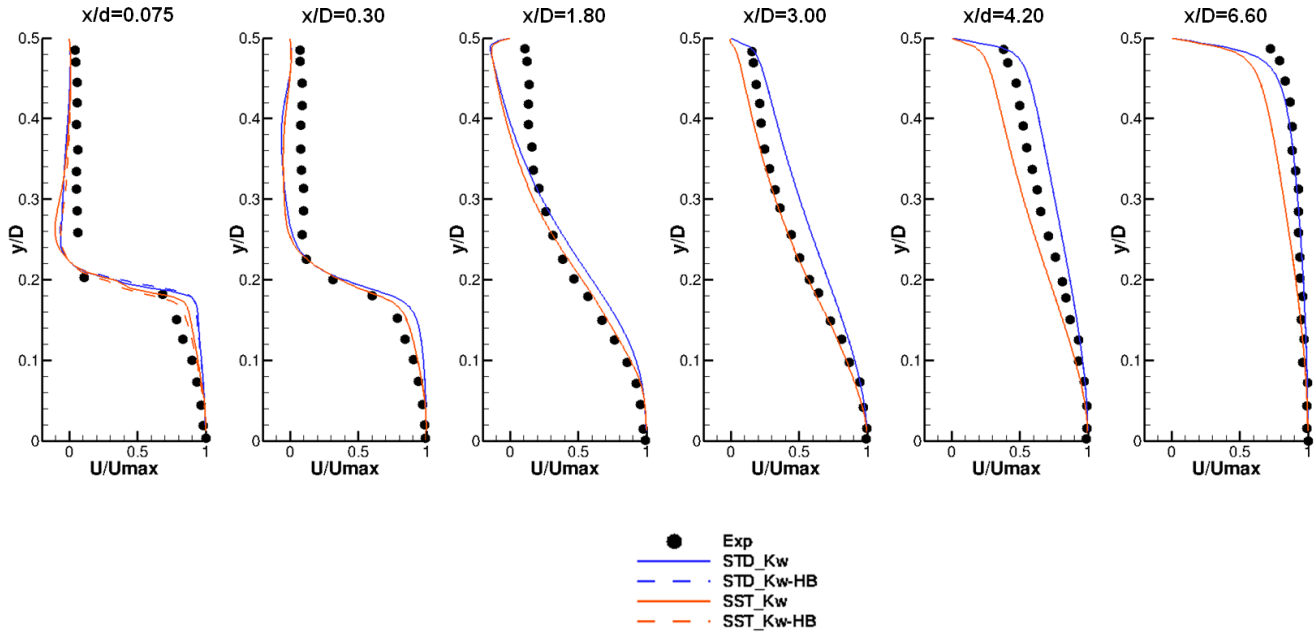

Figure 5.3.10: Comparison of the simulated velocity profiles with k-ω approach againt the experimental data at different locations. In blue line simulation with STD-k-ω, in blue dashed line calculation with STD-k-ω with HB, in orange line computation with SST-k-ω and orange dashed line SST-k-ω with HB.

inflow velocity of 11 m/s. At the inlet, pure air is inserted with a constant static temperature of $T_{in} = 293K$. For the inflow conditions, velocity and turbulent kinetic energy profiles for a fully-developed channel flow have been specified in order to match the experimental values in [98].

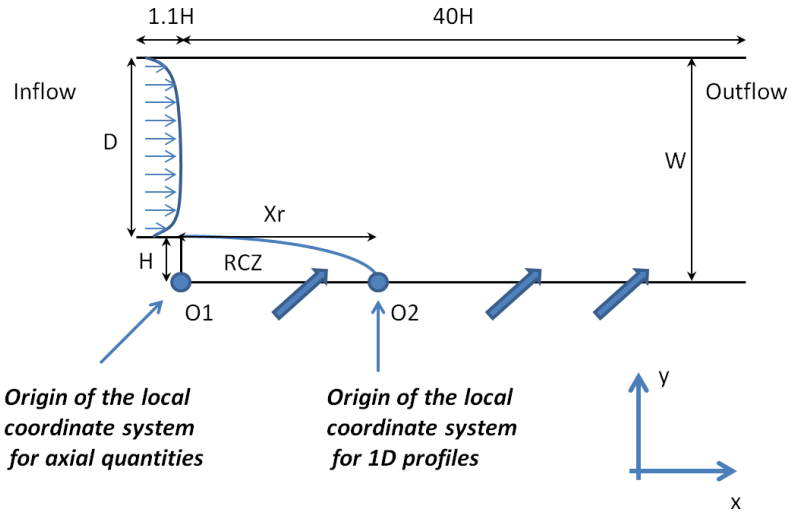

Figure 5.3.11: Geometry sketch for the turbulent flow over a backward facing step.

Steady state simulations were carried out with RANS-based turbulence models, whereas the convergence of the solution was monitored with the standard residual criteria (convergence for values lower than 1e-6).

For the computational mesh, the same grid adopted in the work of Panara [34] was used: this presents approximately 44000 nodes (about 200000 cells). The wall boundaries have been set to adiabatic, whereas a constant heat flux $q = 270W/m^2$ has been prescribed at the bottom wall after the expansion. This influences significantly the temperature distribution close to the solid boundaries and slightly the values in the center region.

The experiments for this test case were performed by Vogel and Eaton [99]. They focused on the determination of the heat transfer mechanism and on the analysis of the flow and the temperature field in the near wall region. The experimental data consist in a set of data for the friction coefficient and the Stanton number distribution along the bottom wall. In addition, 1D measurements for velocity and the temperature are also available at different positions in the expansion region. More in detail, considering the local coordinate system with origin in the reattachment point $O2 = X_r$ in Fig.5.3.11, 1D profiles were measured at $X_* = -0.95$, $X_* = -0.75$, $X_* = -0.35$, $X_* = -0.05$, $X_* = 0.45$ and $X_* = 1.25$. X_* is defined as follows:

$$X_* = \frac{X - X_r}{X_r} \tag{5.3.6}$$

The skin friction coefficient C_f, is a dimensionless quantity of the wall shear stress τ_w. It is the ratio of the wall shear stress τ_w and the dynamic pressure of the oncoming flow.

$$C_f = \frac{\tau_w}{\frac{1}{2}\rho U_\infty^2} \tag{5.3.7}$$

The Stanton number St, instead, is also a dimensionless quantity and relates the heat transfer coefficient to the heat capacity of the fluid stream per of unit cross-sectional area and per unit of time. This is particularly used in general problem dealing with the forced convection calculations and it is expressed as follows:

$$St = \frac{h\,(x)}{U_{ref}\rho c_p} \tag{5.3.8}$$

where $h(x)$ is the local heat transfer coefficient, ρ the density of the fluid, c_p the specific heat of the fluid and U_{ref} is the reference velocity of the fluid. In general the Stanton number is derived by a combination of the Nusselt number Nu, the Reynolds number Re and Prandtl number Pr:

$$St = \frac{Nu}{Re \cdot Pr} \tag{5.3.9}$$

5.3.3.1 Numerical Results with k-ε approach

The results of the simulations with the k-ε formulations in terms of skin friction coefficient C_f and Stanton number St are reported here below (Fig. 5.3.12 and Fig. 5.3.13). Several simulations have been performed for investigating the ability of the k-ε models alone or in conjunction with the two-equation thermal models. The aim was to correctly reproduce the experimental data and to accurately predict the wall heat transfer. With this intent, the numerical calculations were divided in three sets: for each set the turbulent model was fixed (standard STD, the Low-Reynolds number AKN and LB derivations respectively) whereas the thermal models varies. More in detail, four possible variations for the latter could be adopted:

- AKN_t model (indicated in the figures as AKN with dashed line);
- AKN_t model with damping functions at the wall (AKN-Low with dashed line and circle symbols);
- DWX_t model (DWX with dash-dot-dot line);

- DWX_t model with damping functions at the wall (DWX-Low with dash-dot-dot line and triangular symbols).

All the simulations indicate the flow separation occurring at the edge of the expansion region and the presence of a large recirculation zone. The location of the reattachment point X_r is crucial for the wall heat transfer prediction. The groups of calculations with the STD-k-ε, AKN-k-ε and LB-k-ε reveal a slight change in the determination of the X_r. The best results were provided by the AKN-k-ε approach that shows a reattachment point of $5.94H$. Similarly the STD-k-ε leads to a value of $5.65H$. The model of Lam-Bremhorst (LB) on the other hand strongly underpredicts strongly the reattachment point with an error of almost 20%.

Model	X_r	X_r/H	$Error$ %
STD $k\varepsilon$	0.21459	5.64703	15.34
STD $k\varepsilon$-AKN_t	0.21460	5.64734	15.33
STD $k\varepsilon$-AKN_t-Low	0.21458	5.64677	15.34
STD $k\varepsilon$-DWX_t	0.21459	5.64712	15.34
STD $k\varepsilon$-DWX_t-Low	0.21461	5.64768	15.33
AKN $k\varepsilon$	0.22582	5.94253	10.91
AKN $k\varepsilon$-AKN_t	0.22581	5.94245	10.91
AKN $k\varepsilon$-AKN_t-Low	0.22583	5.94289	10.90
AKN $k\varepsilon$-DWX_t	0.22580	5.94211	10.91
AKN $k\varepsilon$-DWX_t-Low	0.22581	5.94237	10.91
LB $k\varepsilon$	0.20473	5.38769	19.23
LB $k\varepsilon$-AKN_t	0.20475	5.38803	19.22
LB $k\varepsilon$-AKN_t-Low	0.20474	5.38797	19.22
LB $k\varepsilon$-DWX_t	0.20472	5.38747	19.23
LB $k\varepsilon$-DWX_t-Low	0.20473	5.38763	19.23
Experiment	0.25346	6.67	0.00

Table 5.6: Results for the reattachment lenghts X_r, the dimensionless values X_r/H and relative errors in respect to the experiments.

The use of the AKN_t or DWX_t thermal model, even with the Low-Reynolds damping functions, seems to produce insignificant variations in the resulting X_r. This is actually expected, since the thermal model, solving for the temperature fluctuation variance and its dissipation, influence deeply the temperature fields in particularly in the boundary layer and just slightly the velocity distribution. In Tab.5.6 all the results in terms of length of recirculation X_r, its dimensionless value with the step height X_r/H and the relative error in respect to the experimental data are summarized.

In Fig. 5.3.12 the behavior of the skin friction coefficient C_f along the heated wall in the expansion region is represented. The best agreement with the experiments is obtained with the Low-Reynolds number models.

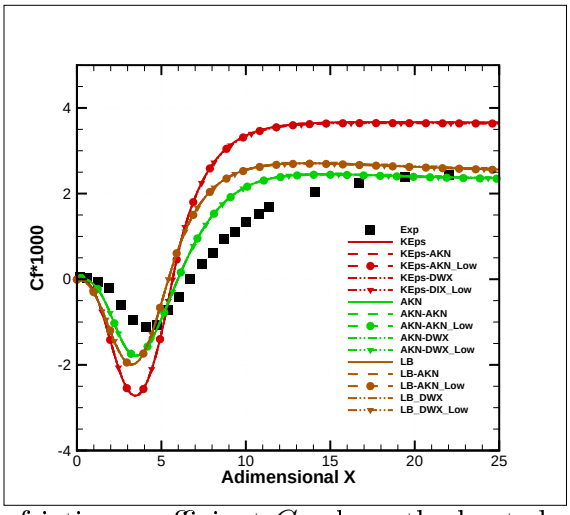

Figure 5.3.12: Skin friction coefficient C_f along the heated wall downstream of the step

Regarding the wall heat transfer estimation, each simulation presents a diverse behavior for St. The results related to the k-ε group of calculations are illustrated in 5.3.13(a). The standard formulation STD has the maximum deviation with respect to the experimental data; improvements are obtained combining the model with the AKN_t or DWX_t. The results provided by the Low-Renoldys formulation for the AKN_t or DWX_t follow the experiments very well. In contrast with the k-ε group, the reference simulations with the AKN model perform very well, predicting accurately the trend of the experimental St. Furthermore, the simulation with Low-Renoldys formulation for the DWX_t presents an excellent agreement, estimating correctly the maximum for St and the behavior in the region downstream the peak. The results for the AKN simulations are represented in 5.3.13(b). Regarding the last set of runs with the LB formulation (Fig. 5.3.13(c)), similarly to the previous cases the simulations with the thermal model provide significant improvements in the prediction of the St-number with respect to the calculations performed without.

The temperature distribution at different locations downstream of the step is analyzed in Fig. 5.3.14. The simulations match the experimental data very well in the two positions ($X* = -0.35$, $X* = -0.75$) located in the middle of the recirculation zone. Instead a discrepancy was found for the location closer to the wall ($X* = -0.95$), where all the turbulent models, despite of the employ of the wall damping functions, fail in the reproduction of the boundary layer and lead to an over-prediction of the temperature values. Downstream of the recirculation bubble, the flows redevelops and the effects of the heated wall become less pronounced. In this region, $X* = 0.05$, $X* = 0.45$ and $X* = 1.25$, the numerical simulations show again a good agreement with the measured values.

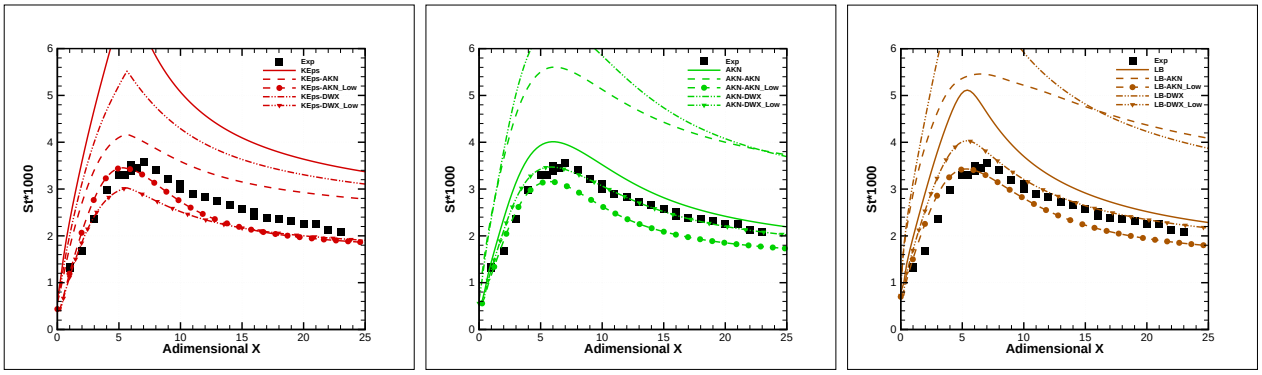

(a) (b) (c)

Figure 5.3.13: Stanton number St along the heated wall downstream of the step with the STD-k-ε (a), AKN-k-ε (b) and LB-k-ε (c) formulations.

5.3.3.2 Numerical Results with k-ω approach

Similar to the previous case, the simulations with the k-ω approach were classified in two groups: the first with the standard STD model and the second with the Menter SST formulation. Since the turbulent models do not present any Low-Reynolds number formulation, each set of calculations consists in a run with the model alone (solid line) and a simulation in conjunction with the Huag-Bradshaw (HB) model (dashed line). In contrast with the previous simulations, the results carried out with the k-ω approach reveal an improvement for the reattachment point X_r. The standard STD model generates a recirculation zone with an extension $X_r/H = 6.19$ with only 7.21% of error, whereas the SST over-predict the measured value of only 5%. Concerning the thermal model HB, instead, the calculations do not show any particular advantage for the prediction of X_r, but seem to lower the reference value computed with the STD and to slightly worsen the X_r of the SST model. In Tab.5.7 all the numerical results for the reattachment point X_r and the relative error in respect to the experimental data, obtained with the k-ω approach, are listed.

Model	X_r	X_r/H	$Error$ %
STD $k\omega$	0.23519	6.18925	7.21
STD $k\omega$-HB_t **1**	0.22172	5.83463	12.52
STD $k\omega$-HB_t **2**	0.22172	5.83463	12.52
SST $k\omega$	0.26612	7.00311	-4.99
SST $k\omega$-HB_t **1**	0.26935	7.08805	-6.27
SST $k\omega$-HB_t **2**	0.26935	7.08805	-6.27
Experiment	0.25346	6.67	0.00

Table 5.7: Results for the reattachment lenghts X_r, the dimensionless values X_r/H and relative errors in respect to the experiments.

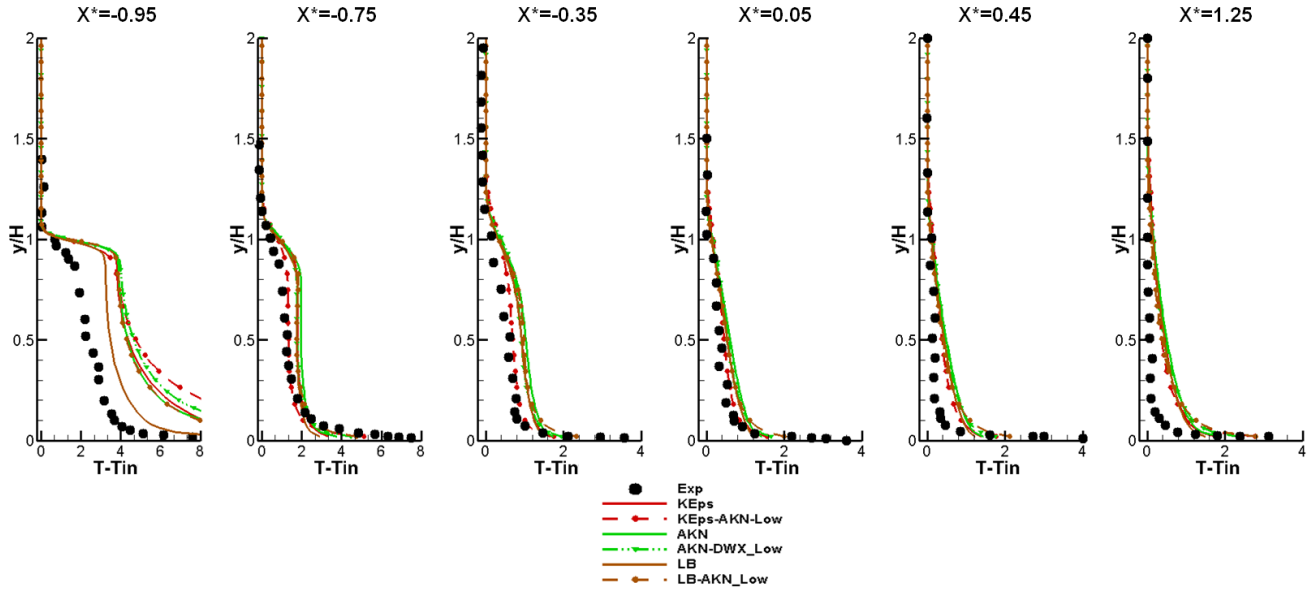

Figure 5.3.14: Comparison of the simulated temperature profiles against the experimental data at different locations.

Fig. 5.3.15(a) shows the numerical results for C_f and its measured values. The skin friction coefficient C_f calculated with the STD model presents a moderate gap for the maximum negative value in the recirculation zone and a significant deviation for the asymptotic value in the downstream region with the experiments. The behavior of C_f with the SST approach instead, shows a great concordance in the results obtained with the SST model alone or in combination with the HB. Both simulations predict the correct location of the minimum and also the numerical value for C_f in the low-speed region in front of the step. The downstream region, on the other hand, differs a little and is underestimated in respect to the experimental data.

The Stanton number distribution, as previously verified, is influenced by the use of the thermal model. The behavior is illustrated in Fig. 5.3.15(b). The simulations carried out with the sole turbulent models (both STD and SST) under-predict the magnitudes of the St; but the location of maximum Stantdon number obtained with both models coincides approximately with the experimental results. The HB model, together with the previous turbulent models, does not show particular improvements in the results of the thermal boundary layer. This is indicated in the plot in Fig. 5.3.15(b) with the dashed line and the name $HB-1$. The latter, in fact, makes use of the standard limiting value for the dissipation of the temperature fluctuation variance at the wall, described in [23]:

$$\omega_{\theta 1} = \left(1 - \frac{C_{D2} P_r}{\beta}\right) \frac{6}{C_{D1} P_r y^2} \tag{5.3.10}$$

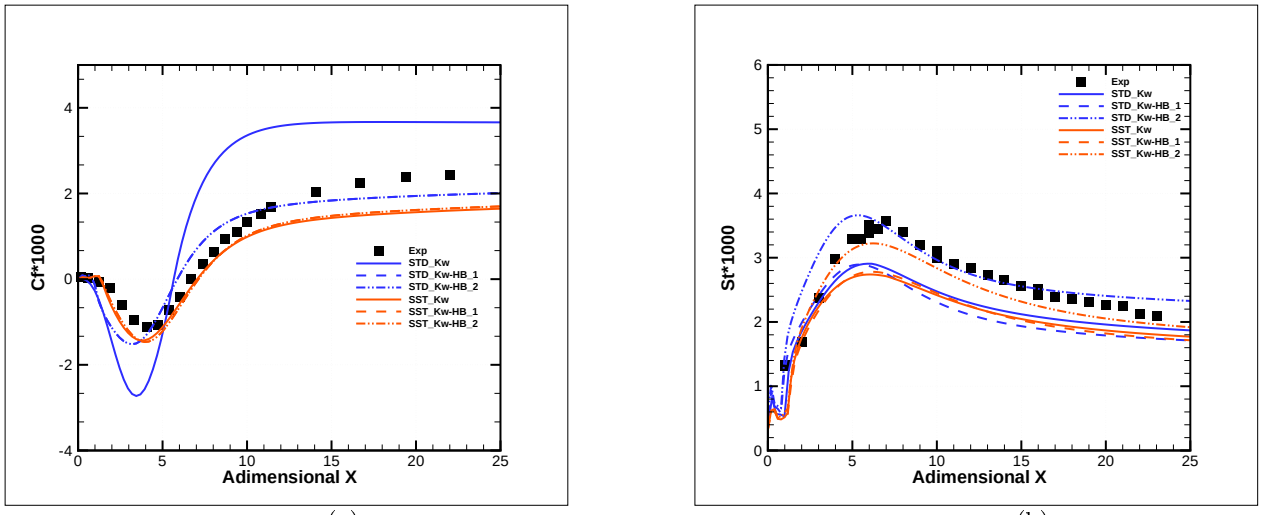

(a) (b)

Figure 5.3.15: Skin friction coefficient C_f (a) and Stanton number St along the heated wall downstream of the step with the STD-k-ω and SST k-ω (b).

This relation seems to be not suited for the thermal evaluation in the boundary layer, since it restricts significantly the value assumed by the turbulent Prandtl number and leads to an underestimation of the turbulent heat fluxes. With this consideration, the author slightly changed the previous wall values with a rearrangement of the limiting condition for the ε_θ as follows:

$$\omega_{\theta 2} \propto \frac{\alpha}{y^2} \tag{5.3.11}$$

and the relative results are indicated with the dash dot-dot line and the name $HB-2$. The use of this new limiting value shows a significant improvement in the Stanton number for the wall heat flux. In this case the simulation reveals a considerable increase in magnitude for St and provides excellent agreement with the experimental data, although the position of the maximum seems affected by this modification. This is shown in the simulation with the STD, in which the peak is shifted on the left side influencing also the position of the skin friction factor and the recirculation length X_r.

The temperature distributions at different locations downstream of the step are instead indicated in Fig. 5.3.16. All models predict accurately the experimental data, with small deviations at the boundaries. The deviations are partially recovered if the HB is used in conjunction with the turbulence models. Regarding the portion of the field in the redevelopment region, this is predicted very well both in the zone right after the reattachment point and further downstream. About the recirculation bubble: the simulation STD-HB shows the best comparison with the experiments at the location $X* = -0.35$, whereas moving in

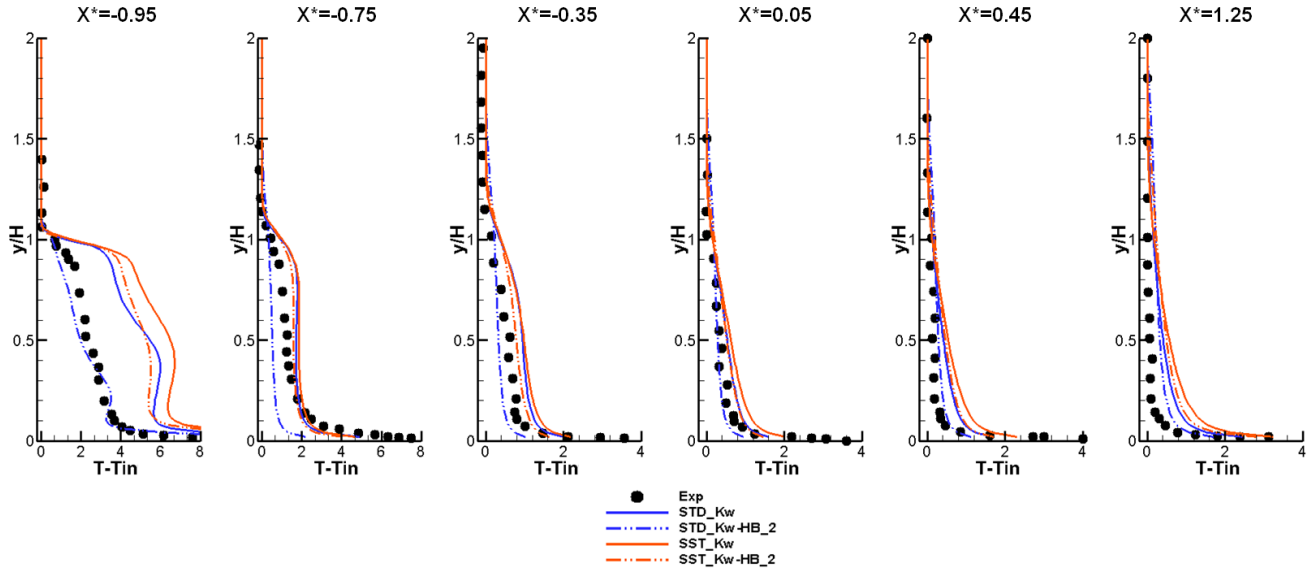

Figure 5.3.16: Comparison of the temperature profiles against the experimental data at different locations.

the middle of the bubble the profiles extracted at $X* = -0.75$ agree perfectly if the $SST\text{-}HB$ is used.

5.3.4 Test case 4: Heat transfer predictions in a pulsating flow

As last validation of the HB model, a pulsating test case was considered for showing the effects of the amplitude of the oscillations on the heat transfer mechanism. The test case investigated was researched experimentally by Ishino et al. [9], in order to prove the heat transfer enhancement in pulsating flows. Ishino, in fact, performed several measurements campaigns at different operative conditions, varying progressively the frequency f (from 15 to 20 Hz), the oscillation amplitude U_b of the pulsating flow and also the value of the initial main stream velocity U_m, with the intent to examine the influence of the inflow variations on the thermal distribution. The experiments were conducted on a long circular pipe, equipped with different optical techniques for measuring both the flow and temperature field. The inlets of this experimental apparatus consist in two elements: a normal air inflow that injects the main stream with a constant velocity U_m and a pulsating flow generator that creates the oscillations. The latter is none other than a piston-cylinder system driven by an electrical motor. To generate a heat propagation from the wall to the fluid, the walls of the pipe are heated up in order to have a significant gradient with the inflow temperature.

The main aim of the experiments was to calculate the increase of the Nusselt number due to the various amplitude ratios U_b/U_m in respect to a reference Nusselt number, measured during steady condition ($U_b = 0$).

Concerning the numerical simulations, the computational domain was simplified to a long pipe with only one inlet, in which the effects of the pulsating flow are superimposed on the main air stream. This corresponds to impose a sinusoidal velocity profile with a nonzero mean at the inlet. Unsteady simulations were carried out with a URANS approach using $k-\omega$ turbulence models. The time step for all simulations was set to $\Delta t = 10^{-5}$s. The computations were initialized by a RANS solution and were done for more than seven residence times. After a duration of two residence times, the averaging phase of the numerical solution was activated. The time-averaged solution of the flow field was achieved considering a physical time span of five residence times. The gird is made up by unstructured elements with several prism layers around the walls.

For calculating the effects of the heat transfer enhancement due to the pulsations on the Nusselt number Nu_b, Ishino considered the overall heat transfer coefficient h_b, which depends on the mass flow rate m, on the cross-sectional averaged Temperature T_m at the inlet and outlet, on the logarithmic mean temperature $\Delta\theta$ and on the area of heat transfer surface S according to [9]:

$$h_b = mc_p \frac{(T_{m2} - T_{m1})}{S\Delta\theta} \tag{5.3.12}$$

where T_m and $\Delta\theta$ are defined as follows:

$$T_m = \frac{2\pi}{U_m A} \int_0^R U(y)T(y)(R-y)dy \tag{5.3.13}$$

For the numerical simulations only one of the cases investigated by Ishino was considered [34]. This corresponds to: a mean velocity $U_m = 5$ and a pulsating frequency of $f = 20$Hz. The amplitude of the pulsation U_b was varied, as indicated in the experiments, in order to range from low amplitude ratios to high oscillating regimes. More in details, $U_b/U_m = 1.38$, $U_b/U_m = 3.00$, $U_b/U_m = 4.50$ and $U_b/U_m = 6.00$ or using the Reynolds numbers: $Re_b/Re_m = 1.38$, $Re_b/Re_m = 3.00$, $Re_b/Re_m = 4.50$ and $Re_b/Re_m = 6.00$.

The unsteady calculations were performed with the SST-k-ω and SST-k-ω with HB model and the results are compared against the experimental data in terms of Nu_b/Nu. The numerical comparison is reported in Fig. 5.3.17, which shows the heat transfer enhancement relatively to each of the four amplitude ratios for both the computations. At low ratios, i.e. U_b/U_m=1.38, the simulation with the sole SST-k-ω slightly over-predicts the measurement, that is, on the other hand, in great accordance with the simulation performed in conjunction with the thermal model HB. Similar is the situation for $U_b/U_m = 3.00$, with again a small deviation from the experimental data for the SST-k-ω with HB model and a larger one for the run performed with the sole turbulence model. At U_b/U_m=4.50, both the simulations

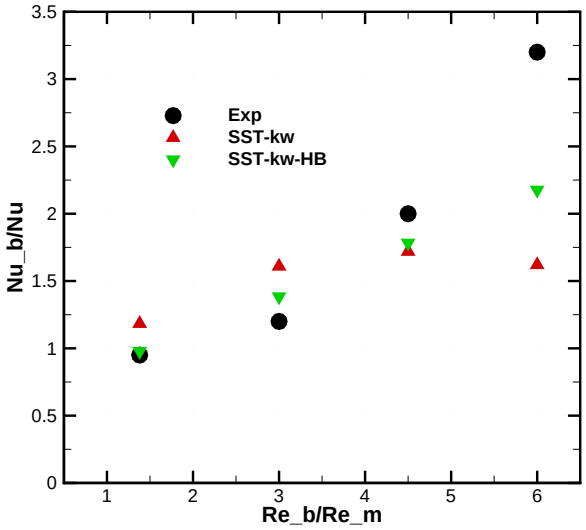

Figure 5.3.17: Numerical comparison of the heat transfer enhancement due to different amplitude ratios using SST-k-ω and SST-k-ω with HB model.

under-estimated the real heat transfer enhancement but are still close to the measured value with a discrepancy of only 10%. Considering the case at high amplitude oscillations instead, U_b/U_m=6.00, the SST-k-ω fails in predicting the temperature distribution in the long pipe and thus the heat transfer due to convection, exhibiting a relative error of approximately 50%. On the other hand, the run with the thermal model HB seems to perform much better. Despite the under-prediction against the experimental data, it recovers part of the deviation and presents an error less of 34%.

It can be concluded that, observing all of the numerical results provided for the different test-cases, the HB model provides promising results for heat transfer problems under stationary conditions and also for pulsating flows. As a consequence, the model will be used and tested in the next section for evaluating the wall heat transfer and also the thermal distribution in a more complex test case considering a regime of self-excited oscillations due to the coupling between combustion and acoustics. This particular condition is referred to in literature as thermo-acoustics regime.

6 Thermo-acoustic and Combustion instabilities

The generic definition of combustion instabilities consists in any fluctuation (in term of space and time) of the physical variables values that govern the system, referring to continuous flow combustors in stationary conditions. Pressure is one of the physical variables which can range significantly, since it is strongly influenced during the propagation of acoustic waves. The pressure variation inside the combustion chamber causes fluctuations in the heat release as altering the mass flow rates of the reactants. These kinds of fluctuations can interact with one of the natural modes of the structure and thus cause macroscopic pressure oscillations that completely change the thermo-fluid dynamic field inside the combustor.

In combustors, designed to work under a steady-state regime, the occurrence of the combustion instabilities worsen the performance of the system causing:

- mechanical vibrations, which are source of noise and thus environmental pollution, and fatigue stress for the structure;
- formation of hot spots on the walls of the combustion chamber, i.e., local overheating which considerably reduce components life;
- increase in pollutant emissions and consequent reduction in combustion efficiency caused by the incompleteness of the oxidation reactions through time.

6.1 Acoustic Modeling

In order to predict accurately the thermo-acoustic instabilities inside the burner an efficient compressible solver has to be applied. The numerical strategy for solving the Navier-Stokes equations is based on pressure or -density based solvers. The first solvers were developed for low-speed incompressible flows that are typical of combustor chambers. Under these conditions, density variations are not a function of pressure variations in the flow field. This results in an infinite propagation in the domain of any perturbation. The density-based approach instead was mainly developed for high-speed compressible flows. In the limit of

the Mach number approaching to zero, compressible (density-based) flow solvers suffer from severe deficiencies, both in efficiency and accuracy. Recently both methods have been extended and reformulated to solve and operate for a wide range of flow conditions beyond their traditional or original intent [100, 101, 102]. For the density based method, two distinct techniques have been proposed to capture solution convergence for low Mach-number regimes: preconditioning [103, 104] and asymptotic [105, 106]. In contrast, for pressure-based solvers a first attempt of extension for compressible flows is attributed to the work of Harlow and Amsden [107], based on a semi-implicit finite difference algorithm. This approach, like other developed subsequently, either are too dissipative due to the first-order time discretization [108] or require a significant number of inner iterations to converge [109]. A new approach that overcomes the above limitations was proposed by Moureau et al.[102] based on the characteristic splitting of the acoustic and advective modes. Since the DLR in-house THETA code was originally developed as incompressible solver based on the pressure-based algorithm [49, 61], a modification for taking into account the compressibility effects is then needed. Lourier in his work [110] dealed with this issue and implemented in THETA an extension of the algorithm proposed by Moureau. Lourier showed the good capability of this method for simulations of combustion instabilities in terms of accuracy and reduction of computational time [102]. This approach, which is called Semi-Implicit Characteristic Splitting (SICS), is second order accurate for linear acoustics and low Mach advection without inner loop iterations [110]. It invokes a fractional step method [111] based on characteristic splitting of acoustic and advective modes. Further details can be found in Lourier [110].

6.2 Combustion instabilities: fundamental and possible origins

Combustion instabilities often manifest as large amplitude pressure and heat release oscillations, which may lead to structure failure or reduce the life time of the combustor. They can occur at any time during the running of the combustor and are caused by a closed feedback loop between two or more physical processes involving combustion. Because lean combustion is intrinsically sensitive to perturbations, small oscillations of the flame heat release may occur, creating a pressure disturbance inside the combustor. These pressure perturbations propagate at speed of sound from the reactive zone inside the burner and can be partially or fully reflected at the boundaries. A self-excited instability process can take place in the combustion chamber as consequence of a closed feedback mechanism. Depending on the acoustic boundary conditions, pressure waves can be in fact more or less reflected, feeding/removing energy to/from the system at each cycle. If the amount of the energy dissipated is lower

compared to the one gained, the amplitude of instabilities will grow in time until it saturates. There are several mechanisms responsible of perturbations of the heat release (i.e. combustion instabilities) in the combustor. Generally speaking, any velocity or pressure perturbation leads to fluctuations in the heat release [4]:

- Fuel Feed Line-Acoustic Coupling: pressure oscillations may alter the pressure drop across the unchocked fuel nozzles, which in turn deliver oscillating fuel mass flow into the system. This influences the combustion process driving instability.
- Equivalence Ratio Oscillations: pressure oscillations propagating into the premixing chamber may modify the mixing process, producing a mixture with an equivalence ratio oscillating periodically in time.
- Vortex Shedding: interaction of turbulence and flame front (i.e. vortical structures distort the flame) causes surface area oscillations, thus producing heat release oscillations.

6.3 Rayleigh Criterion

The Rayleigh criterion permits to state approximately if the combustion is subjected to an unstable behavior due to thermo-acoustic oscillations. The criterion states that: if the fluctuating heat release is more in phase than out of phase with the pressure oscillations, conditions are right for feeding energy into the system [14]. A mathematical relation was proposed by Putnam and Dennis [112]:

$$R = \int_0^\tau p'(t)\, q'(t)\, dt > 0 \tag{6.3.1}$$

where τ is the period of oscillation, p' and q' represent the unsteady pressure and heat release fluctuations, respectively and R is the Rayleigh index. A positive value of R indicates an amplification of the pressure wave amplitude due to the fluctuating heat release rate whereas a negative Rayleigh's index denotes a damping of the oscillations. The above relation represents a non complete statement of the Rayleigh criterion: even though the equation is satisfied mathematically, the occurrence of strong thermo-acoustic instabilities in the burner could not arise. This demonstrates that these instabilities also depend on other important factors, whose neglection may lead to erroneous interpretations of the dynamic of the system. In detail, the spatial variations of the pressure and heat release quantities as well as the energy dissipation due to viscous effects could be considered in a more general formulation of the criterion:

$$\int_0^\tau \int_V p'(\vec{x},t)\, q'(\vec{x},t)\, dtdV > \int_0^\tau \int_V \Phi(\vec{x},t)\, dtdV \tag{6.3.2}$$

According to this equation, a system is prone to instability if the rate of the energy release into the system is high and the rate of dissipation is low. Under this condition, the amplitude of the oscillations grows exponentially, leading consequently to oscillations in the heat release and wall heat flux, until it saturates due to dissipative and non linear effects (viscous dissipation, heat transfer and acoustic radiation, etc.), reaching a new equilibrium point where gains and losses of system are equal. This situation, in which the amplitude and frequency of the oscillations are almost constant in time, is referred to in literature as Limit Cycle behavior.

6.4 Investigations on Thermo-Acoustic instabilities in a model combustor

One of the measures to achieve the reduction of the pollutant emissions is represented by the lean-combustion regime. This kind of burning mode contributes to decreasing significantly the NOx but, on the other hand, to enhancing the presence of CO due to the low adiabatic temperature. In this condition, however, the system becomes more sensitive to perturbations. This may give rise to combustion instabilities, which can lead to structure vibrations, enhancement of heat transfer, blow-off and flash back events. As previously mentioned, these instabilities represent self-sustained pressure fluctuations which occur during unsteady combustion [4]. The causes of these mechanisms are not completely known yet and a more in depth research is needed. Especially the study of the heat transfer occurring during a cycle of a pressure oscillation has not been thoroughly investigated so far and it represents one of the major impacts on the energy balance of a combustion chamber. The pressure fluctuations can drive a perturbed thermal boundary layer which can expose the structure to a thermal fatigue and, eventually, to its failure. The question is how strongly heat transfer is affected by fluctuations during stable and unstable combustion and how to simulate it.

A model combustor was designed and built in the framework of the EU-funded project LIMOUSINE to study self-excited oscillations and its consequences in an academic configuration by Kok et al. [5, 6, 11, 12]. The LIMOUSINE burner is basically similar to the Rijke tube (an open cylinder resonator) [13], [14] but it operates with one end closed, turning part of heat fluctuations into sound fluctuations thus creating a self-amplifying standing wave.

The self-excited oscillations can modify the structure of the flame, eventually leading to pulsating combustion. As a consequence, a high-amplitude limit-cycle oscillation in the hot fluid causes a temporal thinning of the boundary layers in transient motion, and enhances the heat transfer from the fluid to the combustor liner. The major aim of the present work is to investigate this physical process and the variable heat flux on the wall.

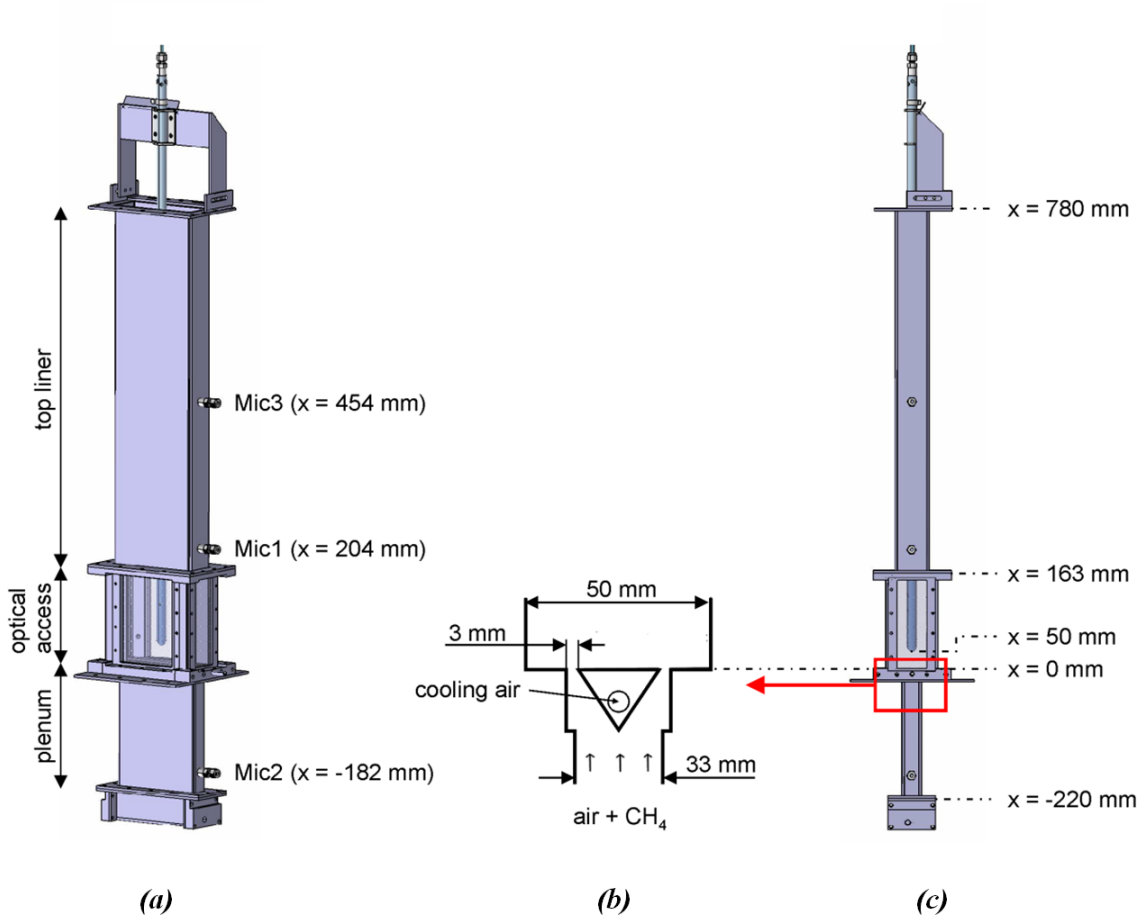

Figure 6.4.1: Sketch of the geometry of the LIMOUSINE burner (a) and of the bluff body (b). The picture (c) illustrates the position of the microphones to detect the acoustics in the burner.

As mentioned, the model combustor LIMOUSINE was designed and built as a combustion-driven Rijke tube and set up in a vertical position. The burner operates with an air/methane mixture; it was initially designed for a lean partially premixed operation and later on it was converted at DLR into a fully premixed burner. The burner comprises three main frames shown in Fig. 6.4.1.a: a plenum, an optical access and a top section. A bluff body (Fig. 6.4.1.b) is located at approximately one third of the whole length of the combustor (at x = 0 mm) and acts as a flame holder, creating a low-speed region that helps to stabilize the flame and to ignite the fresh mixture. Following the flow direction, the subsequent section is a rectangular combustion chamber where, in the interval between x = 0 mm and x = 150 mm, four quartz windows are incorporated to allow optical access from the four sides. A top liner is finally integrated downstream of the optical access section up to a height of x = 780 mm. The premixed operation of the flame is practically fulfilled by mixing the fuel and the air further upstream.

In order to detect the wall heat flux experimentally, a cylindrical air-cooled stainless steel probe was introduced in the combustion chamber. The probe is 1083 mm long and has an outer diameter of 16 mm and consists of a hollow cylindrical body with a semi-spherical tip and a second body represented by a 6 mm diameter cylindrical tube that runs coaxially inside the first body and carries the cooling fluid. The air flows out of the inner pipe and flows back in the inner annular gap (1 mm) to the upper end of the probe and is exhausted. A simplified sketch of the probe tip is shown in Fig. 6.4.2. The external body of the probe includes two parts which can be dismantled: the first element consists in a long tube that supports structurally the active module of the probe. This part, which is 181 mm long, is the one used for the measurement and where three thermocouples are allocated to monitor the temperature in the solid wall of the outer cylinder. These three thermocouples (type K) measure the thermal state of the primary module of the probe at three different locations. If one takes the probe tip as reference, the three thermocouples are at 14 mm, 69 mm and 124 mm. The probe is fastened on the top liner by means of a purpose-built rectangular flange welded on the upper aperture of the Limousine top liner. A schematic of the cooling system of the probe tip is depicted in Fig. 6.4.2. The air is fed through a 4 mm pipe at approximately 270 l/min so that the outer surface temperature during operation was kept under 600°C.

From an experimental point of view, a complete dataset for the acoustics in term of frequency and amplitude of oscillations is available and used for a comparative study with numerical results. OH* chemiluminescence (CL) pictures were recorded (as phase lock averaging and standard averaging) for different operating conditions and provide interesting information about the position of the heat release zone. The temperature field was investigated through the Coherent Anti-Stokes Raman Scattering (CARS) technique for the gas phase temperature. PIV data are available only for the LIMOUSINE partially premixed version, and therefore they cannot be used for comparison in the fully premixed case. Despite the lack of PIV information, the agreement between simulations and OH* pictures also provides a qualitative validation for the velocity field, since the possible accordance for the reaction zones depends on the interaction between the flow and thermal field.

The numerical simulations of the present work were performed through a commercial (ANSYS-CFX) and an in-house code (THETA), and address at three main operating conditions of the burner in order to predict accurately the thermal field and the primary reaction zone during stable and unstable combustion. The combustor exhibits an unstable behavior in the range of the air excess ratio λ from 1.2 to 1.3 at a thermal power of 36 kW with a dominant frequency of about 150 - 181 Hz depending on λ. The stable flame regime occurs instead for $\lambda > 1.43$. The experimental behavior of the burner under both regimes is

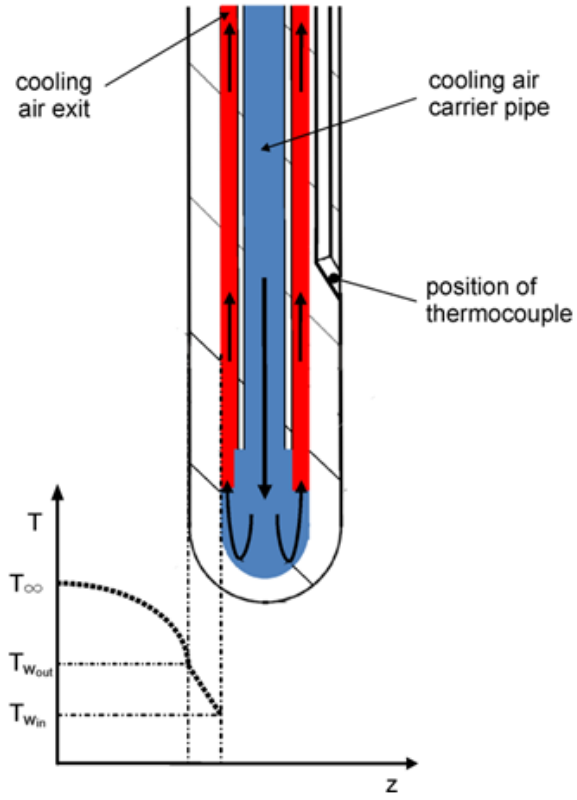

Figure 6.4.2: Detailed view of probe tip with depiction of the cooling process of the probe and expected temperature profile.

presented in Fig. 6.4.3.

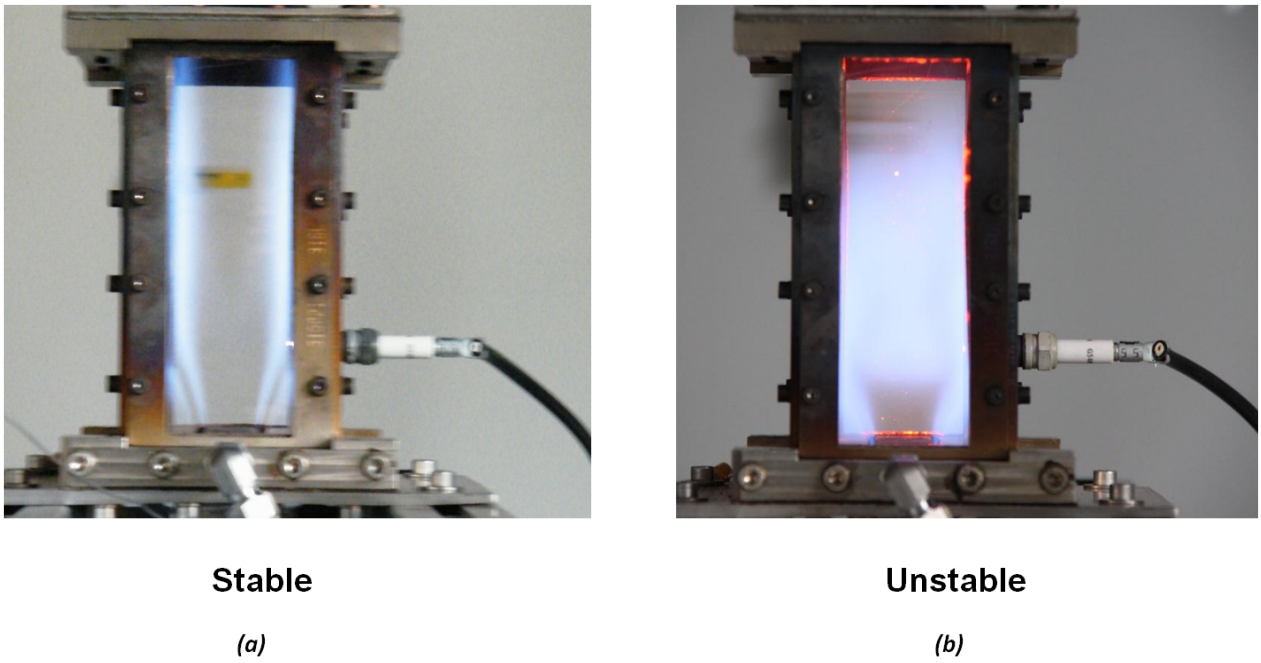

Figure 6.4.3: Experimental setup with visualization of the flame profile under stable (a) and unstable regime (b).

The OH* chemiluminescence (CL) pictures taken from the side walls (Fig. 6.4.4), confirm the attitude of the burner, passing from unstable to stable depending on the air excess ratio of the mixture. In the unstable regime, the flame is shortened and confined in the lower part of the burner, pulsating with a resonant characteristics frequency related to the geometry. Observing the OH* images in fact, the flame reaction zone appears distributed homogeneously with a uniform intensity after few centimeters from the bluff body. This condition is presented in the first two pictures in Fig. 6.4.4 corresponding to $\lambda = 1.2$ and 1.3 respectively. This unstable combustion mode was simulated to show the change in wall heat flux and the temperature fluctuations as a consequence of the response of the thermal boundary layer. It will be demonstrated that the heat release and pressure fluctuations are in phase and thus the Rayleigh criterion is satisfied. On the other hand, the stable regime presents a clearly different shape: the chemiluminescence pictures show a stretched flame shape which is stabilized through the geometry of the bluff body. The flame is then shifted upward with the consequence that combustion is delayed causing a longer flame length.

The stability characteristics of the burner varying the operating conditions for a fixed thermal power are summarized in Fig. 6.4.5:

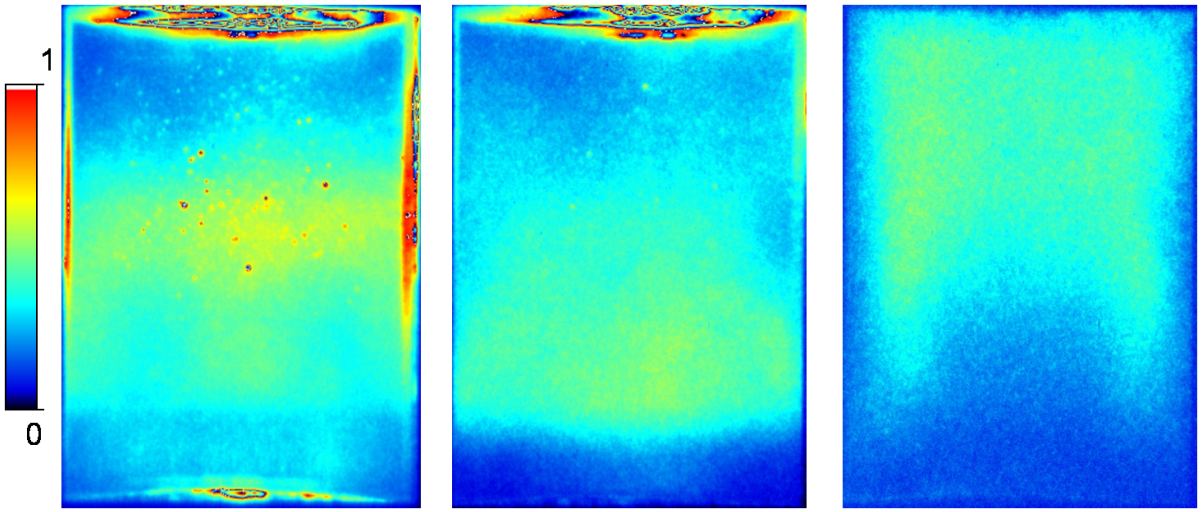

Figure 6.4.4: OH* chemiluminescence (CL) pictures taken from the side walls right after the bluff body position. First picture on the left hand side refers to $\lambda = 1.2$ (unstable), second picture to $\lambda = 1.3$ (unstable), and last image to $\lambda = 1.45$ (stable).

Case	Thermal Power - λ	Frequency	Air/Fuel inlet	Acoustic behavior
1	36 kW - 1.20	180 Hz	21°C	UNSTABLE
2	36 kW - 1.22	178 - 181 Hz	21°C	UNSTABLE
3	36 kW - 1.26	174 - 176 Hz	21°C	UNSTABLE
4	36 kW - 1.29	165 - 168 Hz	21°C	UNSTABLE
5	36 kW - 1.44	- Hz	21°C	STABLE
6	36 kW - 1.50	- Hz	21°C	STABLE

Figure 6.4.5: Stability characteristics of the burner varying the operating conditions.

6.4.1 Unstable case with $\lambda = 1.2$ (Case 1)

The main purpose of the simulations for Case 1 is the numerical determination of the flame limit cycle behavior, where strong pressure oscillations were detected experimentally. In order to get a better insight of the flame dynamics, the calculations were carried out with ANSYS-CFX and THETA, varying the thermal boundary conditions and observing the changes in the flow characteristics (pressure, temperature, wall heat flux) as consequence of the response of the thermal boundary layer. The simulations focus on the numerical prediction of the acoustic characteristics of the unstable combustion (acoustic frequency, pressure amplitude, heat release distribution).

6.4.1.1 Influence of the thermal losses through the side walls

In a first attempt, the commercial code ANSYS-CFX was used to investigate the burner under unstable conditions and to verify its ability in the prediction of a limit cycle behavior under different thermal boundary conditions. Two unsteady simulations were carried out with a Hybrid URANS/LES approach using the the SST-SAS for modeling the turbulence. Combustion was solved by means of the Burning Velocity Model BVM. The computations were calculated with a constant time step of $\Delta t = 10^{-6}$s. The computational domain and the description of the boundaries are depicted in Fig. 6.4.6. Since the intent was to understand the thermo-acoustic prediction no time-averaged solution was obtained and the simulations were stopped after 0.5s. For the thermal boundary conditions, a first calculation was run with the following conditions: adiabatic walls in the plenum region , isothermal wall for the thermal probe with $T_w = 700$K and adiabatic walls in the combustion chamber (side walls). Proper boundary conditions were considered at the intake and outlet of the numerical domain to mimic the experimental setup and the acoustic behaviour. At the inlet a constant mass flow was prescribed according to the experimental data for providing a fully premixed mixture with $\lambda = 1.2$. At the outlet the NSCBC method was applied to reproduce an open acoustic BC. The value for the reflection coefficient at the exit plane was set according the measurements performed at the University of Twente [113]. As mentioned, fuel consists in natural gas, which is simulated with pure methane.

According to the simulations, the flame starts to exhibit instabilities immediately due to the bluff body, generating coherent vortexes from the edges of the prism, as shown in the temperature contour in Fig. 6.4.9.a. The pair of stationary vortices formed in correspondence of the two shear layers leads to an asymmetric vortex shedding that interacts with the acoustic field and generates the instabilities in the burner. It is well known [4] that the vortex shedding can be the reason of the instabilities. Vortices in the combustion core distort the flame, causing its surface area to oscillate and further downstream to break down into smaller eddies. The process happens in a periodic manner with a characteristic time scale that could excite the natural acoustic frequency of the combustor. The pressure oscillations were monitored through two monitor points set a different heights, respectively at 20 mm and 40 mm above the bluff body. As shown in Fig. 6.4.7.a, its time evolution presents, for almost the whole simulated time, an amplitude of less than 500Pa with a periodic behavior that leads to an exponential growth of the pressure, which occurs approximately every 0.5 sec. The growth terminates with few oscillations at very high peak of pressure (higher than 1000Pa) and with a sudden decay of the oscillations, favoring again a stable behavior of the flame.

Fig. 6.4.8 could schematically explain what takes place in the combustion chamber. The

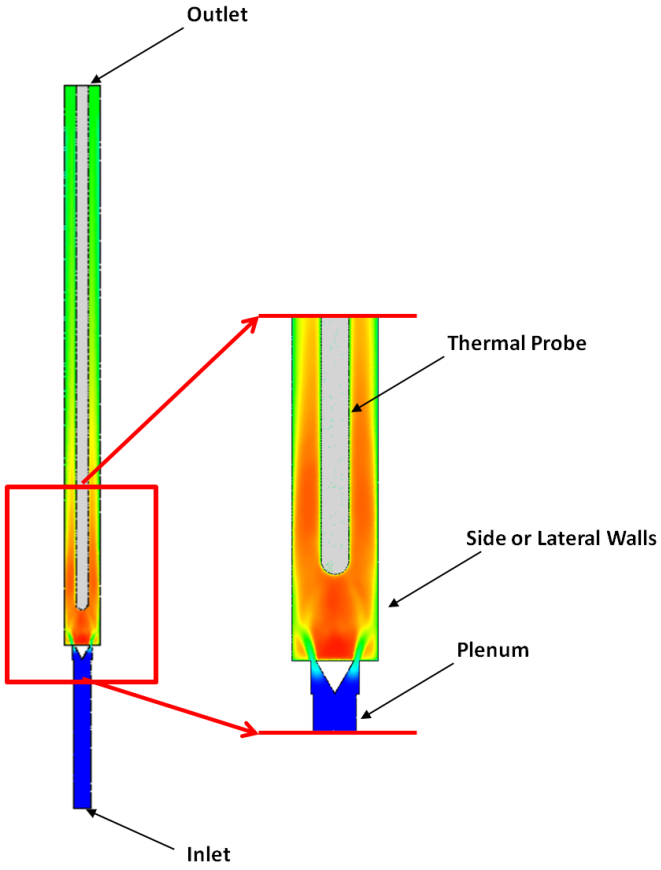

Figure 6.4.6: Computational domain of the LIMOUSINE burner.

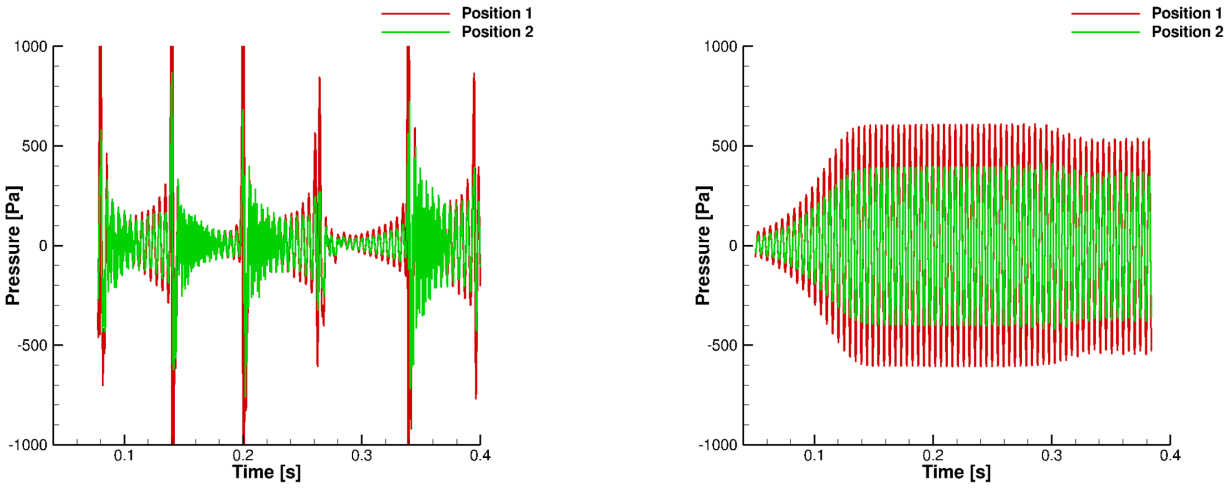

(a) (b)

Figure 6.4.7: Pressure signals over the time for the adiabatic (a) and isothermal case (b). Red line corresponds at location x=20 cm, green line x=40 cm.

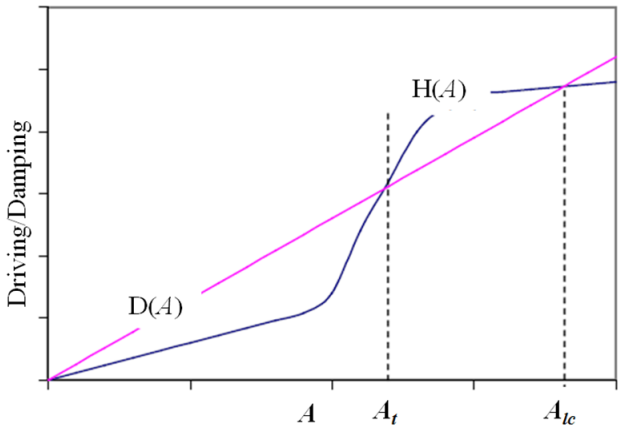

Figure 6.4.8: Schematic diagram of forcing $H(A)$ and damping $D(A)$ mechanisms as function of instability amplitude for a nonlinear system. The damping forces are assumed to be linear with the amplitude A [4].

graph plots the hypothetical dependence of the energy gain $H(A)$ and losses $D(A)$ of a nonlinear system over the amplitude A. The system presents three equilibrium points that have different effects on the stability of the system: $A = 0$ is a stable point, since all the disturbances with an amplitude lower than A_t will be damped to $A = 0$. In contrast to that, at $A = A_t$ the system is unstable and the perturbations are enhanced in time until they reach a stable equilibrium point where the gain matches the losses and a stable limit cycle appears; $A = A_{lc}$ is also a stable point, since all the disturbances with an amplitude higher than A_{lc} will be damped to $A = A_{lc}$. The behavior of the simulation can be explained as the part of the graph limited by the trigger amplitude A_t and A_{lc}, where a small perturbation can lead to an enhancement or damping of the fluctuations.

Numerically, it was observed that the high pressure fluctuations of the reflected acoustic wave decreases the flow rate at the combustion inlet (Fig.6.4.9.b-c) and then regenerates, with a time delay, an oscillatory flame as well as vortices (Fig. 6.4.9.d). This behavior occurs periodically and can be explained observing the time evolution for the pressure, temperature and reaction rate signals, as showed in Fig. 6.4.10. At the beginning, the pressure amplitude enhances as long as it is in phase with the reaction rate and the damping is smaller than the pressure gain.

Eventually, when the value of the reaction rate signal tends to zero, the pressure amplitude decays suddenly (as shown in Fig. 6.4.9.b-c). This fulfills the Rayleigh criterion according to which the intensity of the oscillations is damped when p' and q' are out of phase. After 0.02 s the flame is fully developed; the reaction rate starts to oscillate again and it couples finally with the pressure signals, amplifying it in an exponential manner and repeating the

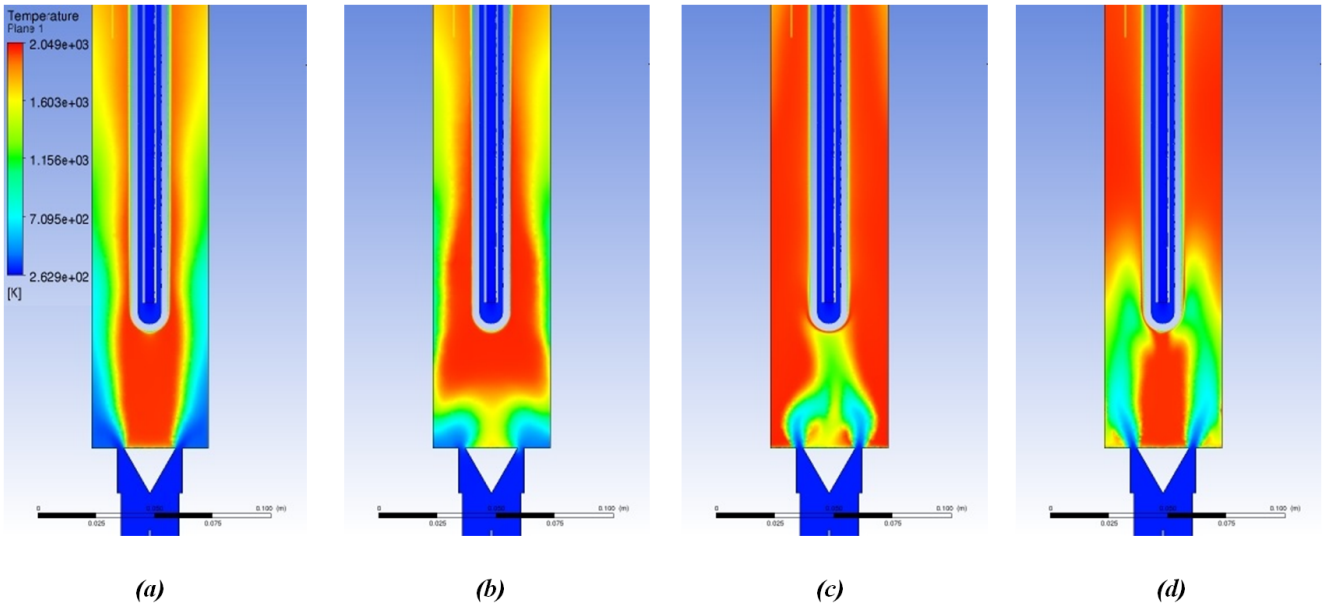

Figure 6.4.9: Temperature contours for different time steps show the transition from stable to unstable regime for adiabatic case.

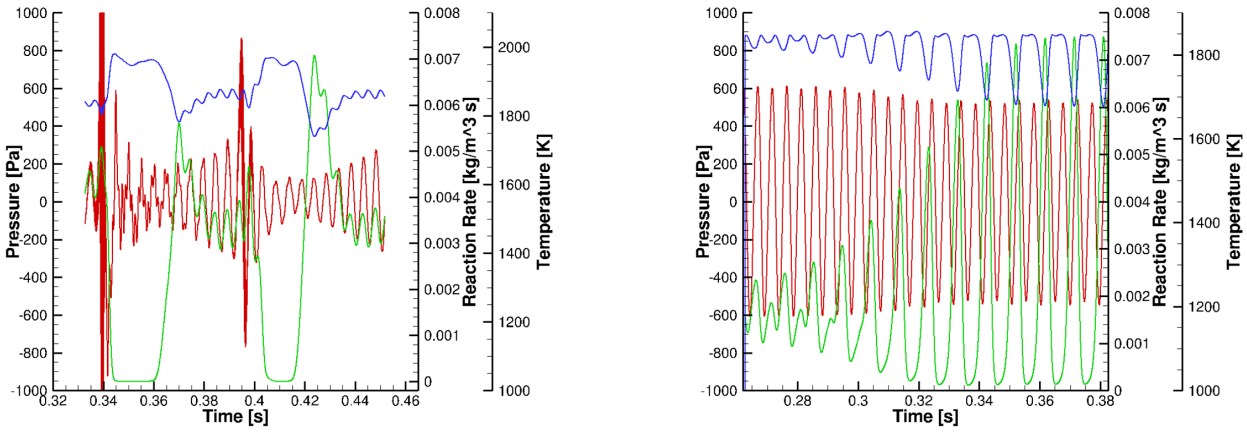

(a) (b)

Figure 6.4.10: Pressure (red line), Temperature (blue line), Reaction Rate (green line) signals over the time for the adiabatic (a) and isothermal case (b).

mechanism described above.

As mentioned, the pressure amplitude were measured through two microphones mounted in the combustion chamber and one in the plenum region, as showed in Fig.6.4.1.a. According to Heckl et al.[114], due to the area blockage between the plenum and the combustion chamber, the upstream and downstream parts are acoustically decoupled and acoustics is determined only by the combustion chamber. However, due to the geometrical characteristic of close inlet-open outlet the lowest fundamental mode has the shape of a quarter-wave, whereas the

other modes will present the form and frequency:

$$\lambda_n = \frac{4L}{n+1} \tag{6.4.1}$$

$$f_n = \frac{c}{4L} \cdot n + 1 \tag{6.4.2}$$

The positions of the microphones were chosen with the intent to record not the maximum or minim level but to be able to evaluate the resonance frequency and to reconstruct from the FFT the shape of the first and third harmonics.

The proof to verify which kind of instabilities occurs in the combustor is represented by the Rayleigh criterion. The criterion is computed by means of the cross-correlation of the pressure and reaction rate signals. Its value is converted in the spectrum domain by the FFT and it shows the spectral energy distribution, highlighting the dominant frequencies. In order to satisfy the criterion, the phase angle of the cross spectrum has to be confined between $-\pi/2$ and $\pi/2$, thus leading to an amplification of the disturbances in the system. Furthermore, this has to be verified not only temporally but even spatially, demonstrating that the combustion instabilities are amplified in the whole combustor and not just locally. The phase angle of the cross spectrum at a characteristic frequency assumes a value of 0.8 $\pi/2$. This value is within the limit -$\pi/2$ and $\pi/2$, which may lead to instability and resonance of the system. The Fourier analysis (Fig. 6.4.12.a) highlights a dominant peak at 199 Hz and several other peaks at higher frequencies, (respectively at 400 Hz, 800 Hz) whose amplitude is lower but contributes to the acoustic spectrum. The experimental frequency is about 180 Hz.

A second calculation was performed for considering the lateral side walls as isothermal with a prescribed constant temperature of 700K. The main purpose was to investigate the effect of these thermal losses in the dynamic behavior of the flame. In comparison to the adiabatic case, some larger differences in the flame characteristics have been found, but the driving mechanism for the instabilities remains the vortex shedding process due to the geometry of the burner. More in detail, the process of instabilities in the LIMOUSINE burner was identified as self excited [113],[115] since no external forces are acting on the system. Under these conditions the pressure oscillations grow spontaneously in time until a limit cycle behaviour occurs. The mechanism leading to the instabilities is due to the combination and interaction of different physical processes between aerodynamics, combustion and structure. Near the trailing edges of the prism, coherent structures are formed at the edges of the bluff body leading to a symmetric vortex shedding. This produces distortion in the flame, causing its

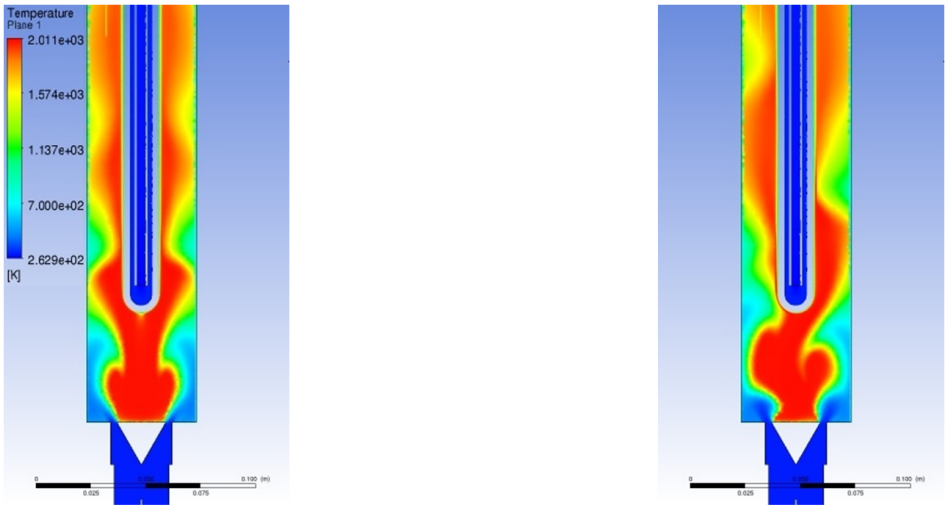

(a) *(c)*

Figure 6.4.11: Temperature contours for different time steps show the transition from oscillating flame (a) to unstable regime (b) for the isothermal case.

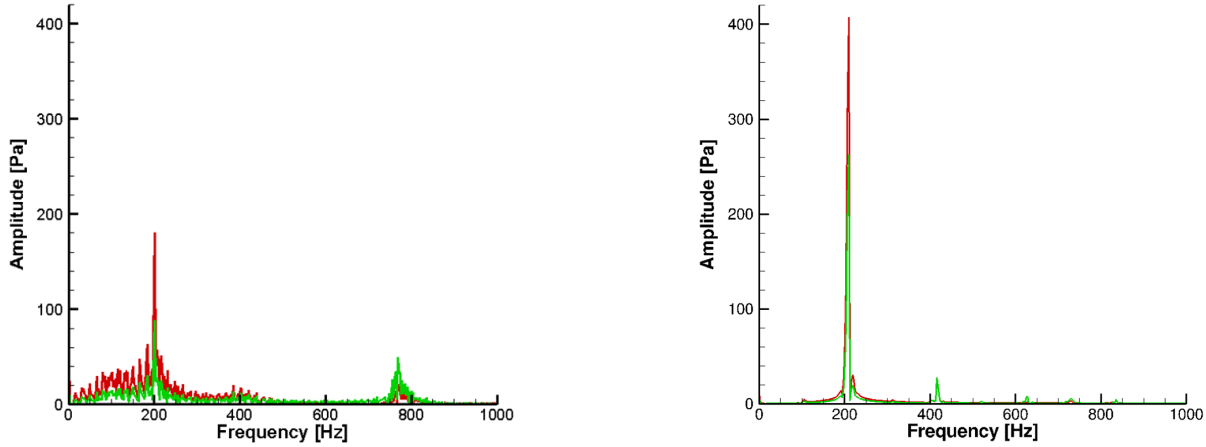

(a) (b)

Figure 6.4.12: FFT of the pressure signals for the adiabatic (a) and isothermal case (b). Red line corresponds at location x=20 cm, green line x=40 cm.

surface area to oscillate and thus producing heat release oscillations. The process happens in a periodic manner with a characteristic time scale that in some operative conditions excites a natural acoustic frequency of the burner, driving oscillations in the burner itself. Due to the excitation of the first acoustic mode, the oscillations are amplified. At $t = 0.15s$ the growth in time stops, since the driving source (combustion) saturates and a stable limit cycle oscillation is observed. This means that all perturbations with an amplitude higher than A_{lc} will be damped out until their amplitude attains the value of $A = A_{lc}$ again. When

a stable limit cycles occurs, self-sustained oscillations take place in the burner, modifying the structure of the flow dynamics. The simulation shows clearly that the transition from exponential growth of the perturbations to LCO (Limit Cycle Oscillations) changes radically the flame shape, in contrast with the adiabatic case. This is evident in the two plots in Fig. 6.4.11 that indicate the flame shape during unstable (with amplification of the oscillations) and LCO phase.

Fig. 6.4.10.b illustrates the evolution of the pressure, temperature and reaction rate for the isothermal case; although the pressure signal oscillates with constant amplitude and frequency over the time (proving the Limit Cycle Oscillations regime), the temperature and reaction rate show an exponential growth of their fluctuations that seem to saturate due to dissipative and non linear effects at 0.35s. In order to understand if the pressure and reaction rate are in phase, a spectral analysis (FFT) was performed as for the adiabatic case.

Fig. 6.4.12.b shows the energy distribution in the frequency domain, and reveals a dominant peak at 208 Hz with very high amplitude compared to the adiabatic case. The higher harmonics (2nd, 3th and 4th harmonic respectively at 410, 620 and 830 Hz) have a low contribution in the spectrum showing low amplitudes, thus still supporting the theory that oscillations occur with "only" one constant frequency. Instead, as already discussed, the adiabatic case shows a high peak amplitude at 800 Hz (corresponding approximately to the 4th harmonic of the burner), and could be the evidence that more than one acoustic mode is excited at the same time.

Additionally, the excitation of the flame fluctuations is elaborated by means of the Rayleigh criterion with the cross-correlation of the pressure and reaction rate signals. The cross correlations provide a measure of the coupling of the two waves as a function of a time-lag applied to one of them. This helps to establish the phase shift between the signals, necessary for the Rayleigh analysis. Fig.6.4.13 illustrates two examples of cross spectrums for pressure and heat release signals calculated in the simulation with adiabatic and isothermal condition for the side wall in the combustion chamber (see Fig.6.4.6).

6.4.1.2 Influence of the thermal losses through the probe wall

In the previous paragraph (6.4.1.1) the influence of the thermal boundary conditions for the side walls (Fig.6.4.6) on the amplitude of the thermo-acoustic oscillations was investigated using the ANSYS-CFX code. It was found that setting an adiabatic condition might be not appropriate for modeling the acoustic behavior of the LIMOUSINE combustor. In the following section, a parametric study varying the wall temperature on the probe surface is conducted, while the side walls in the combustion chamber are treated isothermal with $T_w = 700K$. The aim was to investigate how the limit cycle behaviour can vary by changing the

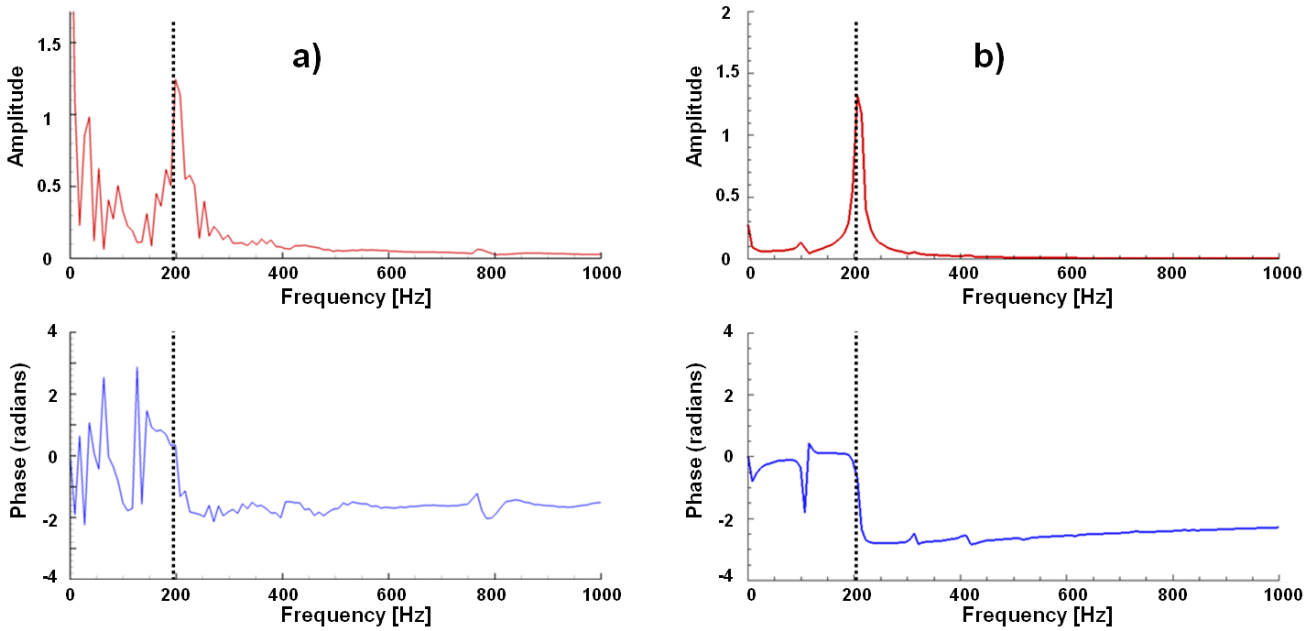

Figure 6.4.13: Cross spectrum of the pressure and reaction rate signals for the adiabatic (a) and isothermal case (b). Top: Magnitude. Bottom: phase angle.

thermal conditions only on the probe surface. Unsteady numerical simulations are performed with the in-house THETA code, using the the SST-SAS approach for modeling the turbulence. The turbulence-chemistry interaction was solved by means of the combustion models EDM or EDC depending on the chemical mechanism considered. To obtain a converged time-averaged solution, a physical time span of 10 residence times was considered. As mentioned, fuel consists of natural gas, which is simulated with pure methane. Fuel chemistry was modeled with two different chemical kinetic mechanisms: a 2-step global mechanism, Nicols et al.[78], and a 19-species chemistry mechanism DRM-19 [79], reduced from the GRI-3.0 mechanism [69] (detailed chemistry approach). The numerical boundaries imposed are coherent with the previous case: a constant mass flow is prescribed at the inlet and an impedance BC is applied at the outlet.

Three simulations were conducted with different wall temperature for the probe wall: a first calculation was performed with $T_w = 500K$ (S1), a second with $T_w = 700K$ (S1) and the last assuming $T_w = 900K$ (S3). The remaining walls in the plenum regions are kept adiabatic, while the side walls of the combustion chamber are isothermal with $T_w = 700K$.

The premixed mode is achieved by mixing fuel and air before they enter the burner. The fresh mixture is injected at the inlet at room temperature, flowing through the plenum until reaching the combustion zone. The bluff body acts as a flame holder. As observed in the

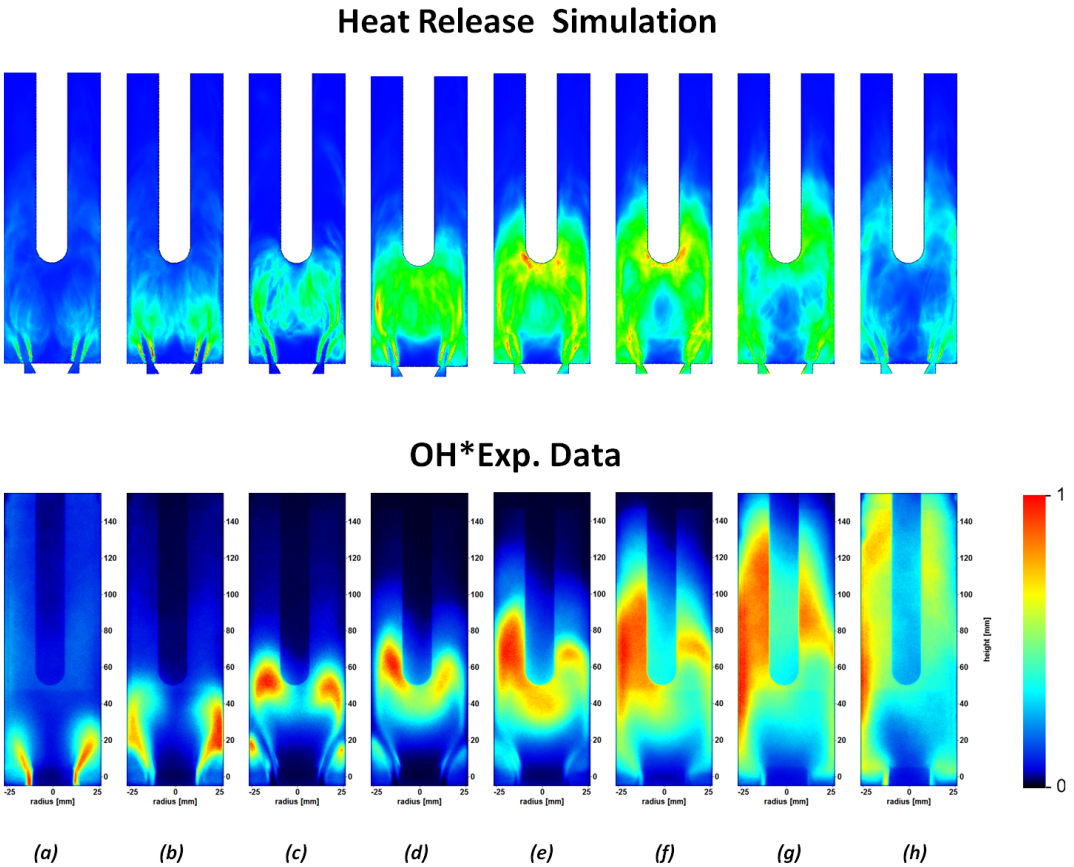

Figure 6.4.14: Phase averaged (in time) images for the measured OH* chemiluminescence (lower part) and the simulated heat release (upper part).

CFX calculations, a pair of two vortices are formed in correspondence of the bluff body edges. They propagate downstream and break down into smaller structures that interact with the flame front, causing oscillations in the heat release. This is one of the possible mechanisms leading the thermo-acoustics.

The flame dynamics is represented in detail in Fig. 6.4.14, where the upper part of the picture corresponds to the numerical simulation and the lower one to the experimental data. It should be noted here that two different quantities are compared: heat release and OH*. Though the OH* is often taken as a good indicator for heat release, it allows only for a rather qualitative comparison of experiments and simulations. The figure illustrates, in eight phases of one complete oscillation (phase-lock), the OH* chemiluminescence and the simulated flame heat release; the different phases increase from left to right. The OH* chemiluminescence pictures have been taken from the short side window with an intensified CCD camera. As already discussed, the experimental data confirm that the flame is stabilized due to the prism edges. Initially the reaction zone takes place in very small vortex sheets that propagate from the small gap between the bluff body and the lateral walls (Fig. 6.4.14.a). Later on, due to

flow instabilities, this pair of stationary structures lead to a symmetrical vertical pattern (Fig. 6.4.14.b), that induces the vortices to roll up and to undergo pairing (Fig. 6.4.14.c). During this process the flame is wrinkled and its surface area increases rapidly, favoring the turbulent mixing and combustion. The process continues convecting the vortices downstream until they reach the probe, placed in the middle of the burner. According to Fig. 6.4.14.d the reaction zone is confined further downstream and only a light signal is recorded in proximity of the prism. After that (Fig. 6.4.14.e and Fig. 6.4.14.f), the combustion zone is confined between the side walls and around the probe, where a strong OH* CL signal has been experimentally detected. The last step of this periodical process consists in the vanishing of the reaction zone (Fig. 6.4.14.h): at this moment no reactions occur in the burner since everything is burnt. The cycle starts over again when fresh mixture enters through the small gaps of the burner. Some deviations were found numerically: the initial phase, when the vortices are formed from the trailing edges and their further development into vertical structure is very well reproduced (Fig. 6.4.14.a-b-c). The secondary phase, when the flame front is convected further downstream, seems to overestimate the reaction zone instead, and consequently to over-predict the flame heat release close to the bluff body, as it can be noticed in Fig. 6.4.14.d-e-f. The reason of the discrepancies may lay in different factors: global chemistry, grid effects, wrong turbulent-combustion interaction, radiation neglected.

6.4.1.2.1 Numerical results with global chemistry The axial velocity distribution shows downstream of the bluff body a central large recirculation zone (CRZ) that extends until the probe tip. Two outer recirculation zones are also observed in the corner between the side walls and the burner plenum. Fig. 6.4.15 reports the distributions corresponding to S1-S2-S3 runs.

- Case S1: $T_w = 500K$;
- Case S2: $T_w = 700K$;
- Case S3: $T_w = 900K$.

The effect of the difference T_w at the probe wall has a significant influence on the dimension of the CRZ. With lower T_w (case S1) the maximum length for the recirculating bubble is found; it extends for most of the downstream region impinging the probe wall. The velocity, as a consequence, is forced to flow in the small passage between the shear layer and side walls, accelerating and expanding after approximately 8 cm from the bluff body. Case S2 is analogous to the previous run, showing almost the same distribution with a slightly smaller recirculation zone. Conversely, the S3 run exhibits a significant reduction for the CRZ due to the lower thermal losses in the burner that modifies the flow field structure. This influences

the velocity distribution further downstream: the flow accelerates less and the maximum velocity is reduced.

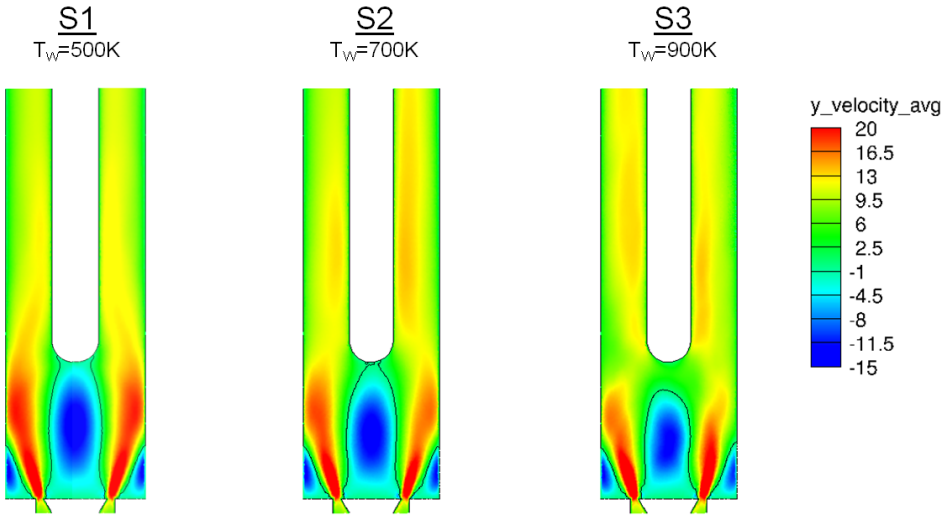

Figure 6.4.15: Time averaged axial velocity contour for S1-S2-S3 runs with global chemistry.

6.4.1.2.2 Numerical results with detailed chemistry In order to prove that the detailed chemistry plays a significant role in the determination of the acoustics in the burner, a further simulation (S4) was conducted using a complex chemistry approach and imposing for the probe wall an isothermal condition ($T_w = 700K$). In contrast, the S1, S2, S3 calculations were performed considering a simple global mechanism for the oxidation of methane in air. In Fig. 6.4.16.a-d the time averaged heat release for the S1-S4 simulations is reported and compared with the experimental OH* (CL) image in Fig. 6.4.16.e. The images confirm that the flame is compact and shortened, and, due to its pulsation, the reaction zone occurs until a height of 10 cm from the bluff body. The global chemistry (S1, S2, S3) computations illustrates a reaction zone comprises until 70 mm from the burner, in the detailed chemistry simulation (S4) instead this region is a bit wider. The asymmetrical behavior of the OH* images was due to the high temperature close to the bluff body surface. The high thermal load caused deformations of the surface that modified the size of the overture between the bluff body and the wall. In this condition the flow was found to be asymmetric between the left and right side of the combustor (Fig. 6.4.16.e).

6.4.1.2.3 Acoustic Measurements The acoustic behavior of the burner was investigated both numerically and experimentally. As shown in Fig. 6.4.1.a, three microphones were set at different heights with respect to the bluff body and they were able to measure the pressure oscillations in the burner. Two of these were placed downstream (Mic1, Mic3) in the

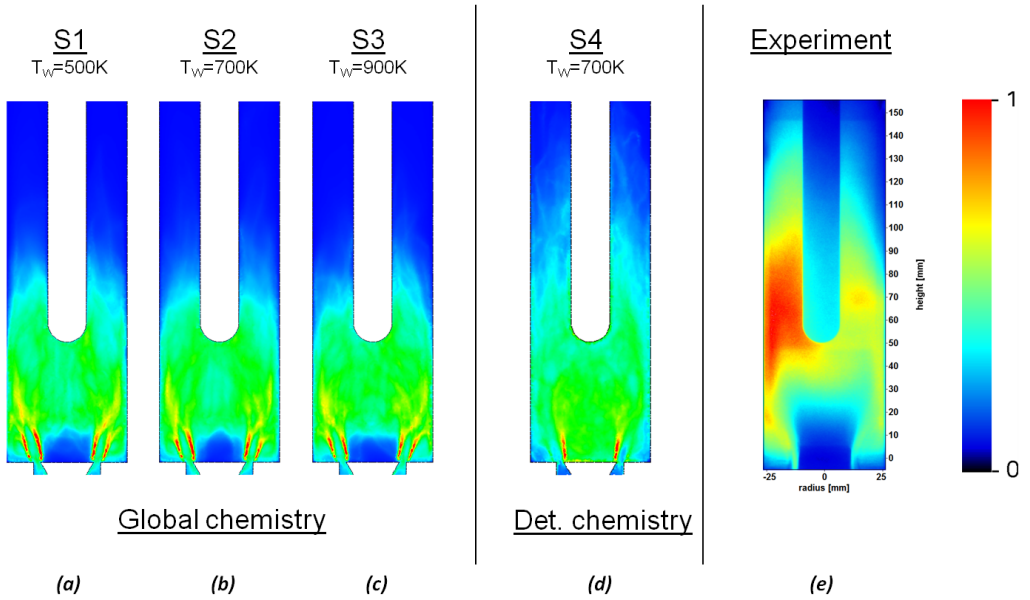

Figure 6.4.16: Time averaged images for the measured OH* chemiluminescence (CL) and the simulated heat release.

combustion chamber, whereas the Mic2 is inserted in the plenum, monitoring and recording the pressure upstream the wedge. The experimental signals were then post-processed with the FFT for obtaining the the resonance frequencies of the combustor. According to Heckl et al.[114], plenum and combustion chamber are acoustically decoupled and can be treated separately.

In Fig. 6.4.17 the numerical simulations are summarized in terms of amplitude of the oscillations and their fundamental frequency f_a. The burner reveals, at the operating condition of $\lambda = 1.2$, an acoustic frequency of $f_a = 181$ Hz that represents the first resonance frequency of the burner. As described in Ref.[116], due to its excitation the system resonates, converting thermal energy released from the combustion into mechanical energy (sound). This mechanism promotes instabilities and enhances the oscillations amplitude until it saturates because of nonlinear effects, leading finally to stable oscillations in the combustor (limit cycle oscillations). The pressure measured in the three microphones decreases along the flow direction. The strongest oscillation takes place close to the inlet where the rms indicates 7454 Pa, and the amplitude of the pressure at the frequency f_a 6150 Pa. At Mic1 the experimental value is about 4630 Pa and even lower in Mic3 with 3598 Pa. This pressure trend, decreasing from the close end to the open end of the combustor, indicates that the system has been excited at the first acoustic mode and is acting like a quarter-wave resonator [116]. It was shown by Sashi [113] that the Limousine burner is excited also at first fundamental mode (see Fig.6.4.18).

Lambda 1.2		Mic2 (-182 mm)	Mic1 (204 mm)	Mic3 (454 cm)	Frequency (f_a)
Experiment	Amplitude [Pa]	6150	4630	3598	181 Hz
	P_{rms} [Pa]	7454	4054	2984	
S1 (T_w = 500 K)	Amplitude [Pa]	-	1222	927	249 Hz
	P_{rms} [Pa]	-	1661	1279	
S2 (T_w = 700 K)	Amplitude [Pa]	3385	1310	995	258 Hz
	P_{rms} [Pa]	3368	1727	1350	
S3 (T_w = 900 K)	Amplitude [Pa]	-	1502	1130	267 Hz
	P_{rms} [Pa]	-	1679	1295	
S4 (T_w = 700 K) (Detailed Chemistry)	Amplitude [Pa]	4205	3900	3092	185 Hz
	P_{rms} [Pa]	4800	3260	2275	

Figure 6.4.17: Pressure amplitude at the fundamental frequency and rms values at different positions in the burner. Comparison between experimental data and numerical results.

For the numerical simulations three monitor points record the pressure signal at the same height of the microphones. The numerical results for S1-S2-S3 are able to capture the same decreasing trend, but unfortunately not the appropriate amplitude. The maximum amplitude at Mic1 is about 1222 Pa for S1, 1310 Pa for S2 and 1502 Pa for S3, quite distant from the experimental data of 4630 Pa. Despite that, the influence of the thermal boundary conditions on the amplitude of the oscillations, which increases with the wall temperature, was observed. This phenomenon shows the importance of setting the right thermal boundary conditions when dealing with thermo-acoustic problems, since it may lead to big discrepancies in the solution. The same behavior was found for the acoustic frequency. Similarly, its value depends on the wall temperature imposed on the thermal element and increases with T_w. This is included between 249 Hz ($T_w = 500K$) and 267 Hz ($T_w = 900K$), and presents a discordance of 38% with respect to the experimental data.

So far it has been demonstrated that the amplitude is partially affected from T_w (about 25% of the maximal amplitude changes with enhancing T_w from 500 to 900 K), not justifying the significant discrepancy with the measured values. In order to try to get better results, a simulation with detailed chemistry for methane oxidation was performed and the results are shown in Fig. 6.4.17. The chemical mechanism used is the DRM19 [79], developed by reduction of the original GRI-Mech with the goal of developing a smallest set of reactions to reproduce closely the main combustion characteristics predicted by the full mechanism, GRI-Mech-3.0 [69]. In this case the simulation revealed that oscillations originate in the

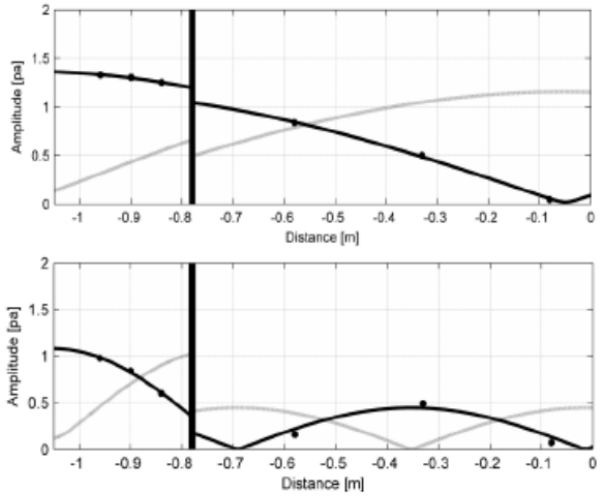

Figure 6.4.18: Pressure (black line) and velocity (gray line) mode shape at the first fundamental frequency (top) and at the third quater wave mode (bottom) for the LIMOUSINE burner.

burner with a main frequency of 185 Hz. This result matches the experimental data of 181 Hz with less than 2% of error. A good agreement has been found even for the amplitude at the fundamental frequency: the simulation indicates values of 3900 Pa at Mic1 with respect to 4630 Pa for the experiment. This value is very promising since the difficulties in catching the right amplitude in thermo-acoustic problems are well known in literature and the EDC model used in the simulations provides very good results both for the amplitude and for the frequency. In Fig. 6.4.17 the results for the pressure at Mic2 and Mic3 are also reported, demonstrating that the model is able to predict the amplitude in other positions of the burner very well.

The improvement of this prediction lies in using a combustion model with complex chemistry that provides better accuracy for the combustion and its interaction with turbulence. Its use modifies the temperature/pressure distribution and leads to a better prediction of the flame characteristics. Without the CARS temperature measurement, it is difficult to affirm if the global chemistry simulations are under- or over-predicting the real temperature: the different distribution could be the main cause of the discrepancy in pressure amplitude and acoustic frequency values, but it can be certainly stated that detailed chemistry plays a crucial role in determining the right acoustic behavior of the burner.

In Fig. 6.4.19 the FFT of the pressure signals is presented. In order to show the influence of the chemical mechanism on the simulations, only the plots related to global and detailed chemistry (respectively, simulation S2 and S4) are reported and compared with the FFT of the experimental signal (Fig. 6.4.19.c). For the sake of simplicity, the other computations

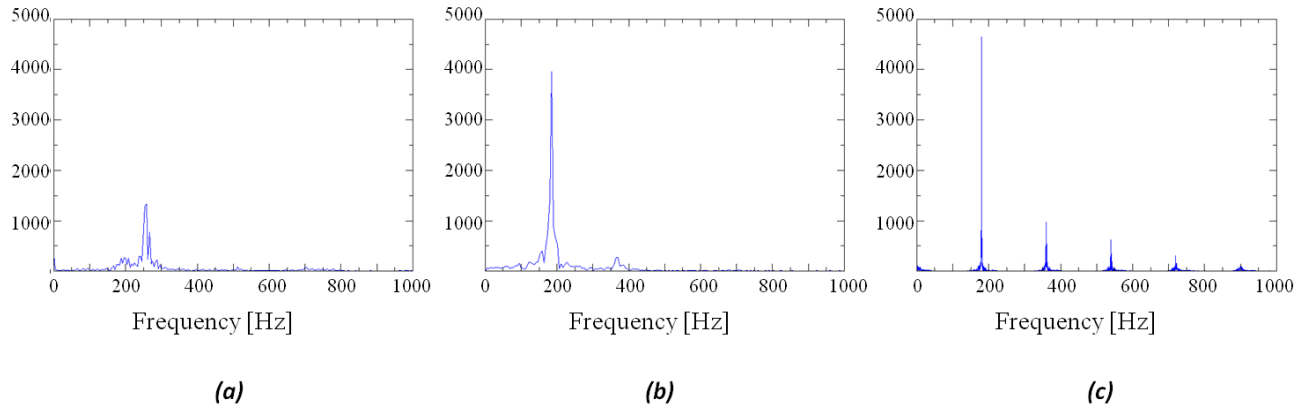

Figure 6.4.19: FFT of the pressure signal for simulation with global chemistry (S2-T_w = 700K) (a), detailed chemistry (S4-T_w = 700K) (b) and experimental data (c) at Mic1 (204 mm from the bluff body).

(S1-S3 respectively with $T_w = 500$ and $900K$) are not presented here, since they present the same trend of the FFT and they do not reveal significant differences in the amplitude with respect to the S2 run. The FFT of the case with global chemistry has an energy spectrum with a dominant peak at 250 Hz and relative amplitude of 1300 Pa. Other harmonics have a very low contribution and they cannot be distinguished because of their low amplitude. On the other hand, the simulation with a complex kinetic mechanism approximates the experimental value of 181 Hz very well, and the FFT exhibits a value of about 3900 Pa, in perfect agreement with the data in Fig. 6.4.19.c. Moreover, a second high peak at around 370 Hz can be clearly detected, which corresponds to the second harmonic of the burner and is not identified by the S2 computation.

In order to evaluate the Rayleigh criterion, an investigation on the pressure p and heat release q was performed. Pressure is recorded as for the FFT signals at different heights downstream the bluff body, whereas the simulated heat release signal is the result of the volume integration over the combustion chamber. The Rayleigh criterion states that instabilities are promoted if the phase angle between these two signals is in the interval of $-\pi/2$ and $\pi/2$. In Fig. 6.4.20.a the trends of p and q in case of global chemistry are presented. The pressure has a sinusoidal behavior that oscillates between -2000 and +2000 Pa; similarly, the global heat release is periodical and sinusoidal with a positive phase shift lower than $\pi/2$ with respect to p. Considering the S4 simulation, the pressure shows an analogous oscillating behavior as for the global chemistry case; the q signal presents fluctuations that are not constant over the time but are almost in phase with the pressure peaks as shown in Fig. 6.4.20.b. This coupling yields to the maximum amplification of the disturbances in the combustor.

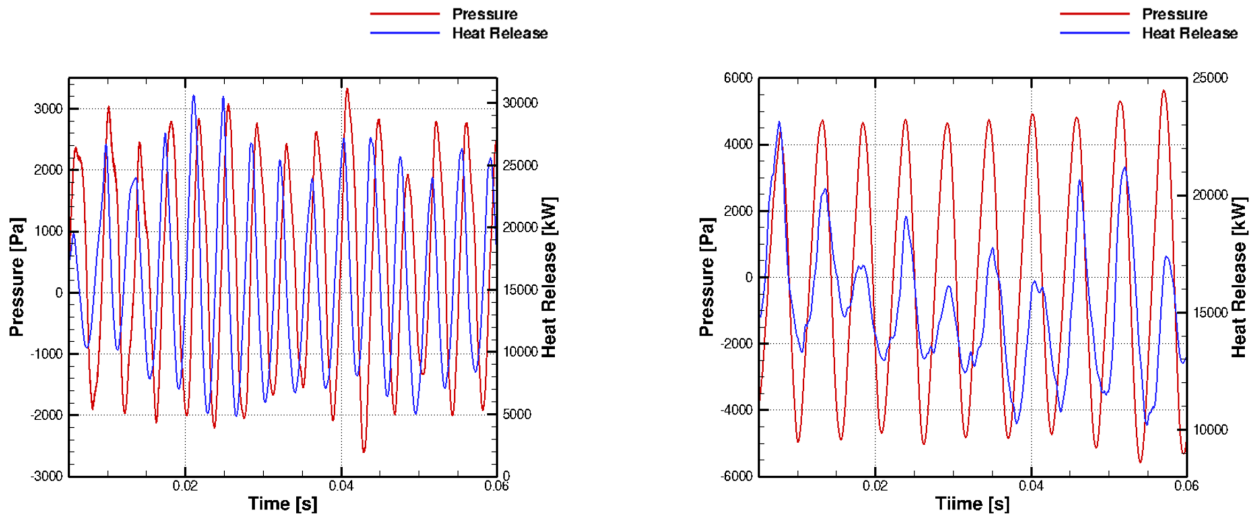

(a) (b)

Figure 6.4.20: Simulated pressure and global heat release trend for global (a) and detailed chemistry case (b) at Mic1 (204 mm from the bluff body).

6.4.1.2.4 Heat Transfer and wall temperature The determination of the wall heat load in the combustor chamber is very challenging. Many physical processes affect the heat transfer during the operation of the burner. Most of these processes are related to the turbulent fluctuations, whose modeling is still under investigation. To overcome this problem in literature many empirical relations have been introduced for simple test cases under steady conditions, correlating for example the Nusselt number, defined as the ratio between the convective heat flux and the conduction heat flux, with the Reynolds and Prandtl number. The most common relation, valid under steady conditions, is based on the following expression [34]:

$$Nu = CRe^{\alpha}Pr^{\beta} \tag{6.4.3}$$

The determination of the coefficients α and β is strictly dependent on the flow field (turbulent or laminar flow) and geometry conditions. If the complexity of the problem increases, empirical correlations fail and the numerical modeling is the only mean to predict the heat transfer.

Thermo-acoustic oscillations enhance the complexity of the problem in predicting accurately the wall heat transfer. During this unstable regime, the combustion process and acoustic field are coupled together and a pulsating flame originates in the burner. The consequence of having a pulsating flow is the oscillation of the boundary layer thickness, therefore

an increase of the wall heat flux that may cause a shortened lifetime of the combustor. This was shown by Panara in a recent study [34] analysing the heat transfer in an oscillating flow. He found a significant increment of the wall heat transfer when the amplitude of the oscillations is larger than the mean flow velocity.

For the determination of the wall heat transfer during a thermo-acoustic regime, the LIMOUSINE burner was investigated by means of Fast Real Wall Method (RW). The Fast Real Wall method is based on the assumption that the walls react fast at any changes of the temperature close to the surface. It is a simple method that allows to obtain good results without having any mesh for the solid part and is based on the electrical analogy, where both the fluid and the solid are schematically modeled as resistances. With this approximation the global wall heat flux can be evaluated as follows:

$$\begin{cases} \dot{q}_{sol} = \dfrac{k_{sol}}{t_c}\left(T_{wall} - T_{sol}\right) = h_c\left(T_{wall} - T_{sol}\right) \\ \\ \dot{q}_{gas} = \left.\dfrac{\lambda_{gas}}{C_p}\right|_{P0} \dfrac{T_{P0} - T_{wall}}{\Delta x_{P0-Wall}} = \alpha_{gas}\left(T_{sol} - T_{wall}\right) \end{cases} \tag{6.4.4}$$

In the previous equations, $\dot{q}_{sol}$ is the heat flux within the solid (gas-solid interface and the outer wall), $\dot{q}_{gas}$ is the heat flux between the first grid point and the interface, k_{sol} is the conductivity, t_c the thickness of the material, the ratio k_{sol}/t_c is referred as heat transfer coefficient indicated as h_c and $\Delta x_{P0-wall}$ is the normal distance between the cell point next to the surface and the interface T_{wall}, $\dot{q}_{sol}$, $\dot{q}_{gas}$ represent the unknowns of the problem. Assuming a steady state condition, the heat flux from the gas part $\dot{q}_{gas}$ turns out to be equivalent to the heat flux in the solid $\dot{q}_{sol}$ and consequently combining together the two expressions in 6.4.4 it is easy to get the expression 6.4.5 where all the variables are known and the wall heat flux can be calculated. Once the wall heat flux is known, the wall temperature can be calculated from the solver.

$$\dot{q}_{wall} = \frac{1}{\dfrac{1}{h_c} + \dfrac{1}{\alpha_{gas}}}\left(T_{P0} - T_{sol}\right) \tag{6.4.5}$$

The numerical results in terms of wall temperature along the thermal probe for stationary simulations is indicated in Fig. 6.4.21.a. The Real Wall model (RW, see eq.6.4.5) was used to calculate the change in the wall temperature due to the high pressure oscillations in the combustion chamber. This plot represents the simulated wall temperature distribution in a three dimensional view.

It can be observed that the temperature increases from the probe tip until the outlet

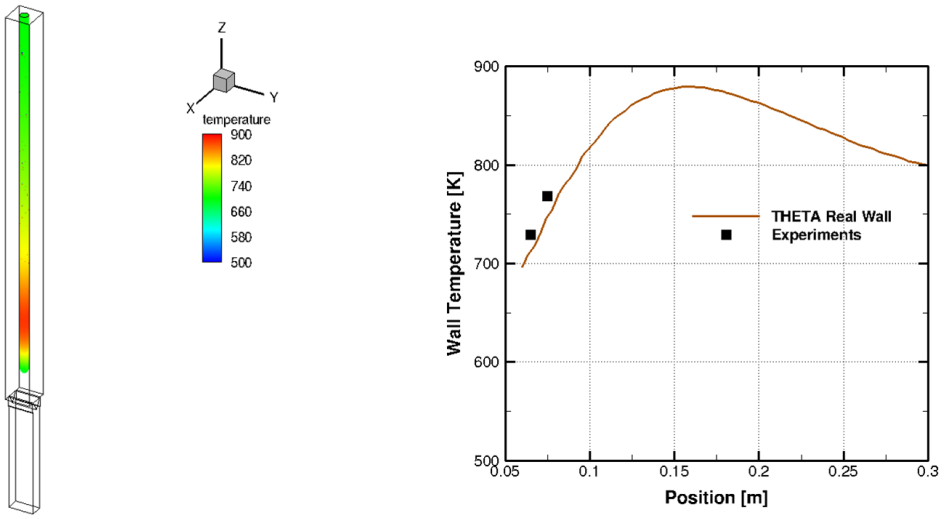

(a) (b)

Figure 6.4.21: Wall temperature along the thermal probe for stationary simulations using RW method in THETA (a). Extracted wall temperature using RW method in THETA (b).

region: the value enhances from 700K reaching a maximum at 900K and then decreases progressively approaching the end of the burner. In order to establish the accuracy of the previous simulation, the wall temperature has been extracted along one line parallel to the axis of the thermal probe for comparison against the few experimental data available. The measurements were performed using thermographics phosphors [117].

In Fig. 6.4.21.b the comparison between the numerical results of the wall temperature and the experimental values is presented. The simulation shows a very good agreement with the experimental data: it captures the right tendency for the wall temperature and presents only 50K deviation respect to the experiments.

The unsteady wall heat transfer is calculated with the Fourier equation imposing a constant wall temperature $T_w = 700$K, In Fig. 6.4.22.a the trend of the heat transfer over the time is illustrated for the simulation with complex chemistry. The plot shows that its value is oscillating around an averaged value of $2400 W/m^2$ with amplitude of about $200 W/m^2$. More interesting is the graph in Fig. 6.4.22.b that represents its FFT. This exhibits a dominant peak at 180Hz, and contributions at 360 and 550 Hz (2nd and 3rd harmonic). These frequencies correspond to the acoustic frequencies of the burner described in the previous section.

6.4.2 Unstable case with $\lambda = 1.3$ (Case 4)

A second operative condition that was investigated experimentally and numerically is at $\lambda = 1.30$. Unsteady simulations were carried out with the THETA code with similar numerical

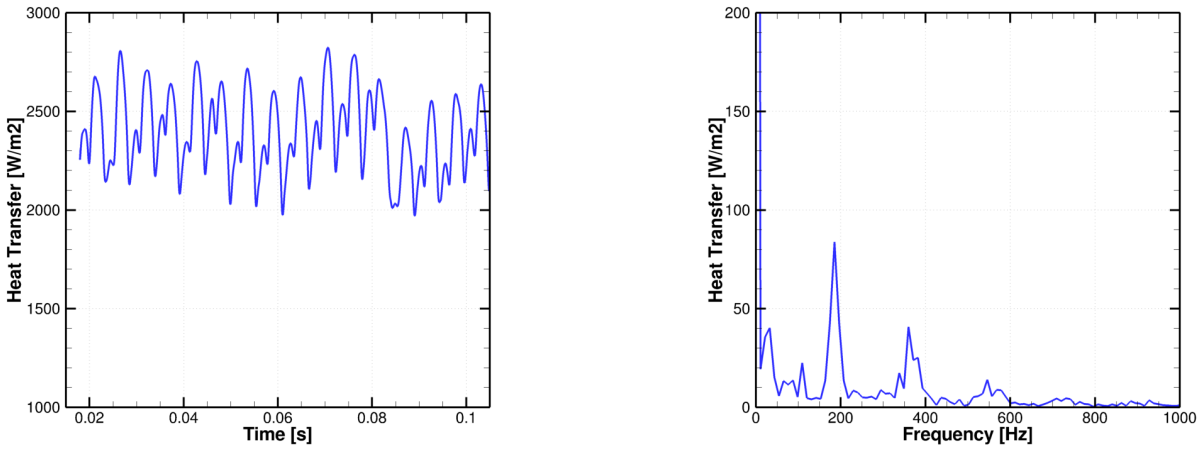

(a) (b)

Figure 6.4.22: Heat release trend over the time for detailed chemistry case (a). FFT of the unsteady heat transfer to the wall (b)

setup as for the case with $\lambda = 1.2$. Turbulence was modeled with the hybrid URANS/LES approach using the the SST-SAS model, whereas the combustion was solved by means of the combustion models EDM or EDC depending on the chemical mechanism considered. To obtain a converged time-averaged solution, a physical time span of 10 residence times was considered. Fuel chemistry was modeled with two different chemical kinetic mechanisms: a 2-step global mechanism (Nicols et al.[78]) and a 19-species chemistry mechanism DRM-19 [79], reduced from the GRI-3.0 mechanism [69] (detailed chemistry approach). The numerical boundaries consist of a constant mass flow prescribed at the inlet and an impedance BC at the outlet. The thermal boundary conditions consider adiabatic walls in the plenum region , isothermal wall with $T_w = 700$K both for the probe wall and the side walls in the combustion chamber (see Fig.6.4.6). In this case, the flame regime is still unstable and presents a significant lower amplitude (almost half of the previous case) of the thermo-acoustic oscillations. This has allowed to perform a laser diagnostics technique such as CARS, for the measurements of the gas phase temperature.

The dynamics behavior of the unstable flame resembles the condition at $\lambda = 1.2$. This is represented in terms of phase averaged images for OH* (CL) and heat release in Fig. 6.4.23.

The fresh mixture enters the combustion chamber and burns immediately, creating a pair of vortexes that propagate symmetrically from the edges of the bluff body. Downstream, these structures enlarge continuously and eventually roll up into only one macro-vortex. The effect of the thermo-acoustic oscillations in the burner leads to an upstream movement of the flow, generating a large recirculating region. When it occurs, the phase averaged OH*

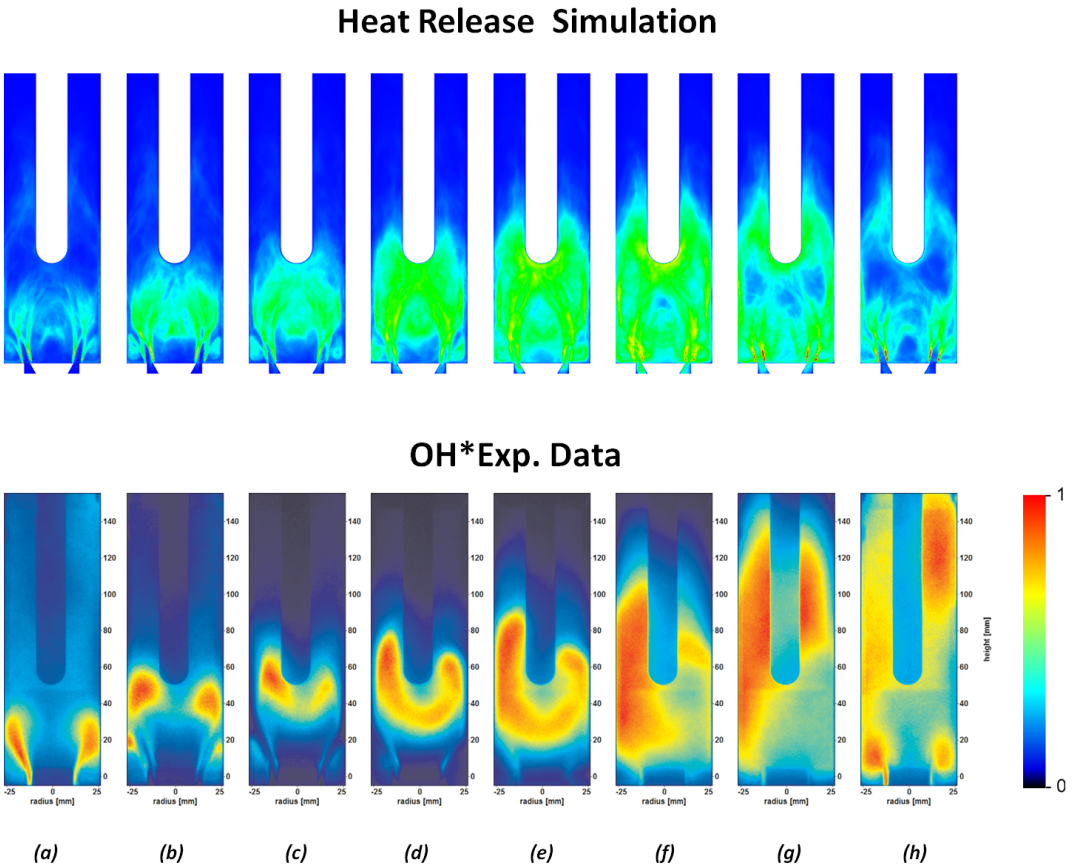

Figure 6.4.23: Phase averaged images for OH* chemiluminescence (lower part) and heat release (upper part) with global chemistry.

(CL) images reveal that the combustion process is not well-confined in space and time but oscillates with a constant frequency of 165 Hz. The frequency value is slightly lower compared to the case with $\lambda = 1.20$. This is mainly due to the lower mean temperature value inside the combustor chamber, which reduces the speed of sound and as consequence the acoustic frequency. Numerically, the simulation done with global chemistry (EDM) reveals in Fig. 6.4.23 a qualitatively good agreement with respect to the experimental data. All of the eight phases of the unstable regime are captured by the calculations very well, from the vortex formation to the burning in the recirculation zone and around the thermal probe, and show an analogous periodic behavior of the flame dynamics.

The combustion model also plays a significant role in the determination of the combustion zone. This aspect is shown in Fig. 6.4.24, showing the phase averaged results of the heat release using detailed chemistry and the EDC model. The simulation is able to reproduce the flame dynamics pretty well, increasing the zone interested by the chemical reactions. Compared to the global chemistry calculation, the combustion zone appears longer and stretched in the main stream direction, approximating better the experimental data for the OH*(CL).

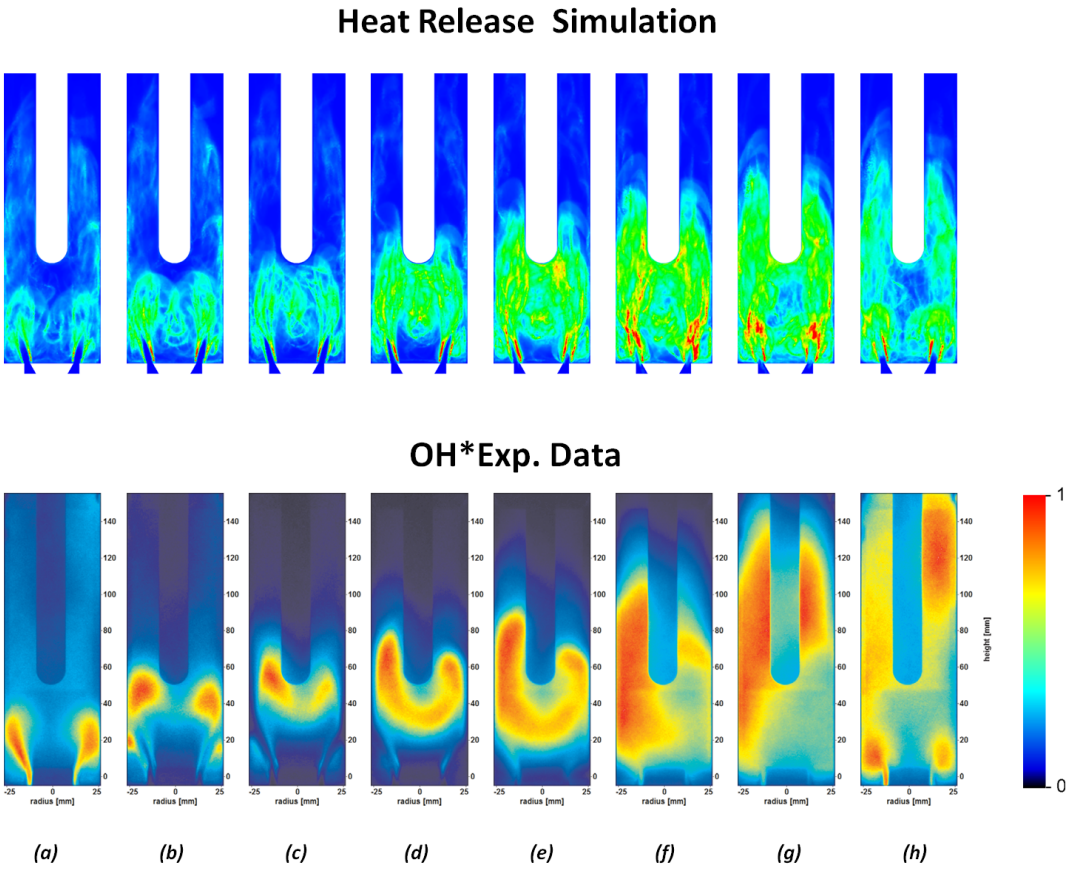

Figure 6.4.24: Phase averaged images for OH* chemiluminescence (lower part) and heat release (upper part) with detailed chemistry.

In order to evaluate the reaction zone in the burner, the instantaneous OH* (CL) images related to all the phases were added and analyzed for obtaining a time-averaged result. The numerical heat release values were also time-averaged. The results are presented in Fig. 6.4.25 and Fig. 6.4.26, respectively with global and detailed chemistry. More in detail, for each simulation with one particular combustion model (EDM or EDC), two further calculations were performed considering either the Real Wall method (RW) or the Turbulent mixing model (HB) for the temperature fluctuations. The Real Wall method was tested in the previous case for a stationary condition, providing encouraging results in the wall temperature calculation.

The HB model (Huag-Bradshaw) [23] was tested intensively and validated in Chap. 5 for various test cases, showing the influence of the turbulent heat fluxes in the accurate calculation of the heat transfer. The pictures in Fig. 6.4.25 show the comparison against the time-averaged OH* (CL) of the three simulations with global chemistry: EDM, EDM with RW and EDM with HB model. The three computations are in a qualitatively good agreement with the experiments and show the same maximum level of intensity for the heat release distributions. On the other hand in Fig. 6.4.26 the same comparison is presented, but

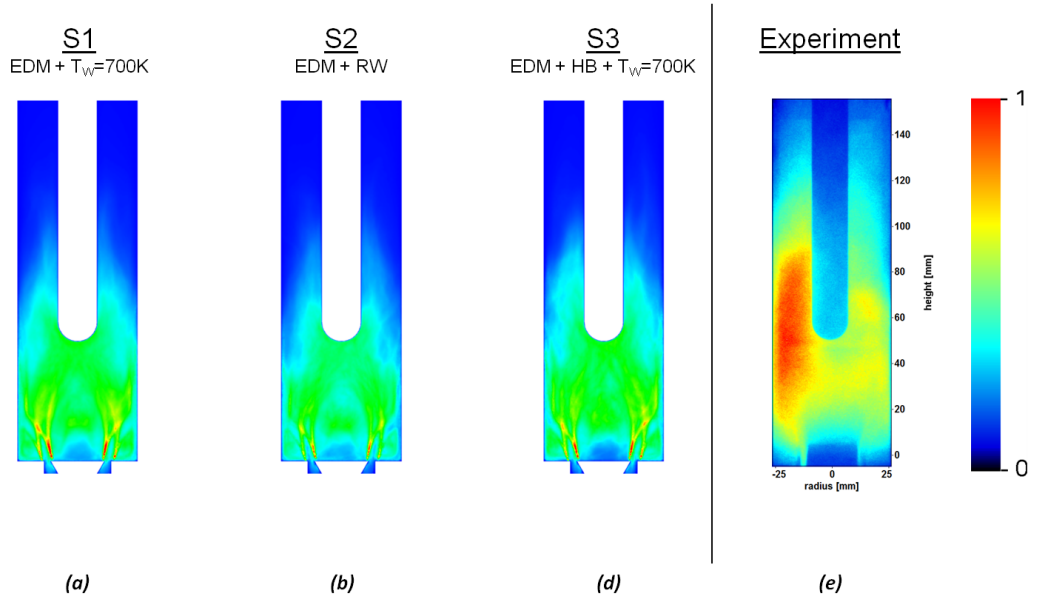

Figure 6.4.25: Time averaged images for the measured OH* chemiluminescence (CL) and the simulated heat release with global chemistry.

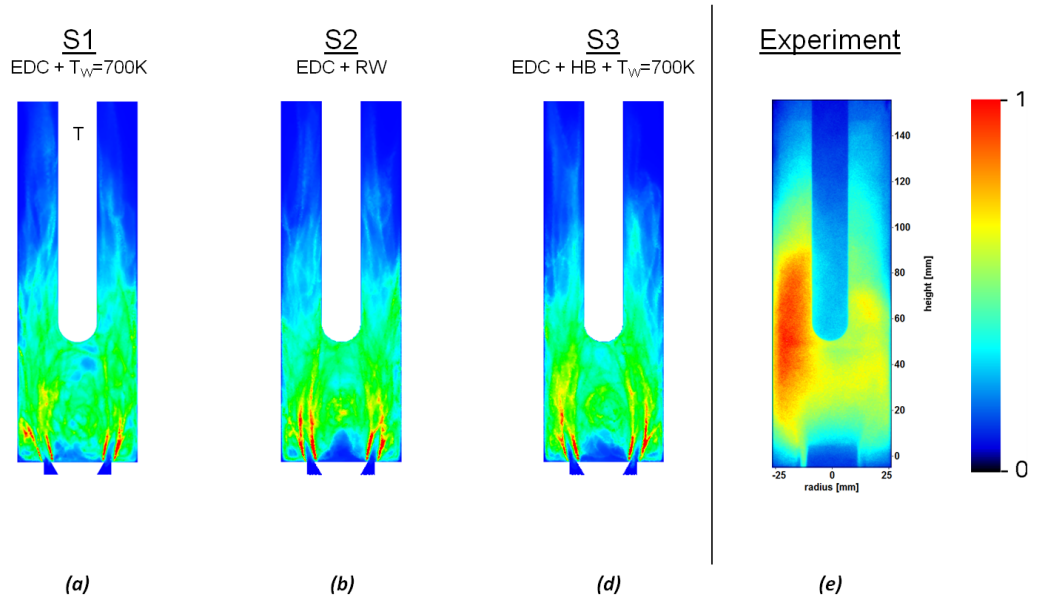

Figure 6.4.26: Time averaged images for the measured OH* chemiluminescence (CL) and the simulated heat release with detailed chemistry.

using detailed chemistry and the EDC as combustion model. No relevant deviations in the heat release distributions are present among this set of computations. However, the results are closer to the experimental data, since they show a longer portion of the combustor where chemical reactions occur. It has to be pointed out that the experimental data for the OH* presents again an asymmetrical behaviour. This was due to the thermal deformation of the surface of the bluff body that modifies the flow distribution between left and right side of the combustor.

6.4.2.1 Acoustic data

All the acoustic data recorded during the experiments and monitored in the simulations (both with global and detailed chemistry) are briefly summarized in Fig. 6.4.27. The experiments for this operative condition ($\lambda = 1.30$) have given a characteristic frequency $f_a = 165$ Hz, i.e., slightly lower than the case with $\lambda = 1.20$. The microphones were set at the same positions, as indicated in Fig. 6.4.1. The measured amplitudes of the pressure oscillations are: 1399 Pa, 1707 Pa and 1611 Pa, for microphone Mic2, Mic1 and Mic3 respectively.

Lambda 1.3		Mic2 (-182 mm)	Mic1 (204 mm)	Mic3 (454 cm)	Frequency (f_a)
Experiment	Amplitude [Pa]	1399	1707	1611	165 Hz
	P_{rms} [Pa]	5371	3715	3252	
Case1 (EDM)	Amplitude [Pa]	2850	1411	1151	258 Hz
	P_{rms} [Pa]	2271	1114	1279	
Case 2 (EDM- HB)	Amplitude [Pa]	2525	1282	1039	249 Hz
	P_{rms} [Pa]	2205	1105	898	
Case 3 (EDM - RW)	Amplitude [Pa]	1806	1220	1130	246 Hz
	P_{rms} [Pa]	2316	1136	1295	
Case 4 (EDC) (Detailed Chemistry)	Amplitude [Pa]	2025	1238	1089	199 Hz
	P_{rms} [Pa]	1847	1115	814	
Case 5 (EDC - HB) (Detailed Chemistry)	Amplitude [Pa]	1314	1242	613	188 Hz
	P_{rms} [Pa]	1571	962	718	
Case 4 (EDC - RW) (Detailed Chemistry)	Amplitude [Pa]	1955	1192	879	192-198 Hz
	P_{rms} [Pa]	1493	905	676	

Figure 6.4.27: Pressure amplitude at the fundamental frequency and rms values at different positions in the burner.

Numerically, the set of simulations with global chemistry reveals a resonant frequency, which is higher compared to the experiments: the computation performed with the EDM model exhibits an acoustic frequency of 258Hz; the run with EDM in conjunction with the RW model presents a lower value, that is 249Hz; the run using the EDM model together

with the HB model has recorded oscillations with a frequency of 246 Hz. The relative error committed regarding the experimental f_a is high: 56% for the standard simulation with EDM, 50% for the EDM with the RW model and 49% in combination of the HB model for the temperature fluctuations. Despite that, the computations carried out with either the RW or HB model show the good tendency of the thermal models in improving the accuracy with respect to the real behavior of the burner. Regarding the calculations with detailed chemistry, they show a significantly lower frequency compared to the EDM runs, getting closer to the experimental frequency. The standard EDC case reveals oscillations with 199 Hz; the other two computations, i.e., the EDC with RW and EDC with HB model, perform even slightly better leading to frequencies of 188 and 192 Hz respectively. Obviously the relative error reduces considerably, the value passes from almost 20% obtained with the standard EDC to only 13% using the previous model in combination with the Real Wall method. The latter results show therefore, as the detailed chemistry combustion models may influence deeply the acoustic simulations of the burner, leading to a reduction of the deviation of the numerical frequency with the measured one. The increase in the accuracy in terms of acoustic reflects a better prediction of the temperature distribution in the burner, as well as of the reaction zone, as previously discussed. In conclusion, it is remarkable that the use of the thermal models (Real Wall method or Huag-Bradshaw model) leads again even for the simulations with detailed chemistry to slight improvements, enhancing the quality and the accuracy of the numerical results.

6.4.2.2 Heat Transfer and Wall Temperature

Also for this operative condition ($\lambda = 1.30$), experimental data for the wall temperature along the thermal probe are available by thermographic-phosphor measurements. The numerical validation was performed for the steady case considering again the RW-method. The results in terms of the wall temperature are illustrated in Fig. 6.4.28.a and Fig. 6.4.28.b. In the first plot a three-dimensional view of the burner with focus on the thermal probe is presented. The wall temperature exhibits a similar behavior as in the case $\lambda = 1.20$, with a monotonic increase of the values from the tip of the probe to a maximum located at $x = 0.15$m, followed by a slight reduction of the temperature in the downstream region. This curve trend was also confirmed by the experiments. Due to the limited optical access of the burner, the experimental data were taken at different points on the surface of the probe up to $x = 0.12$m above the bluff body. Despite that, the simulation with the RW method is able to reproduce the measurements correctly, predicting accurately the temperature along the thermal element as indicated in Fig. 6.4.28.b.

Finally the wall heat transfer time evolution is illustrated in Fig. 6.4.29.a. Similarly to

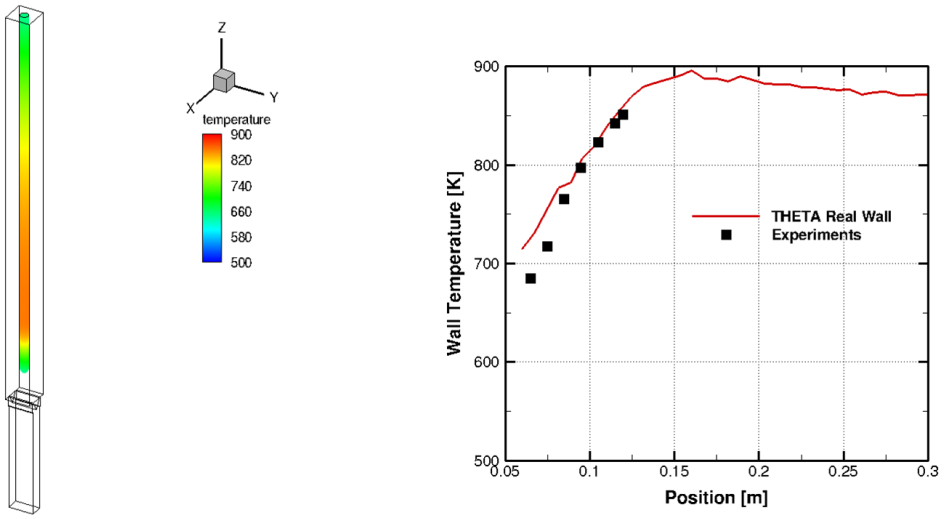

(a) (b)

Figure 6.4.28: Wall temperature along the thermal probe for stationary simulations using RW method in THETA (a). Extracted wall temperature using RW method in THETA (b).

the case with $\lambda = 1.20$, the values oscillate around an averaged value of $2400 W/m^2$ but with a significant lower amplitude. The Fast-Fourier Transform of this signal reveals a frequency of approximately 190Hz, in line with the acoustic resonance frequency of the burner. The spectra analysis is reported in Fig. 6.4.29.b.

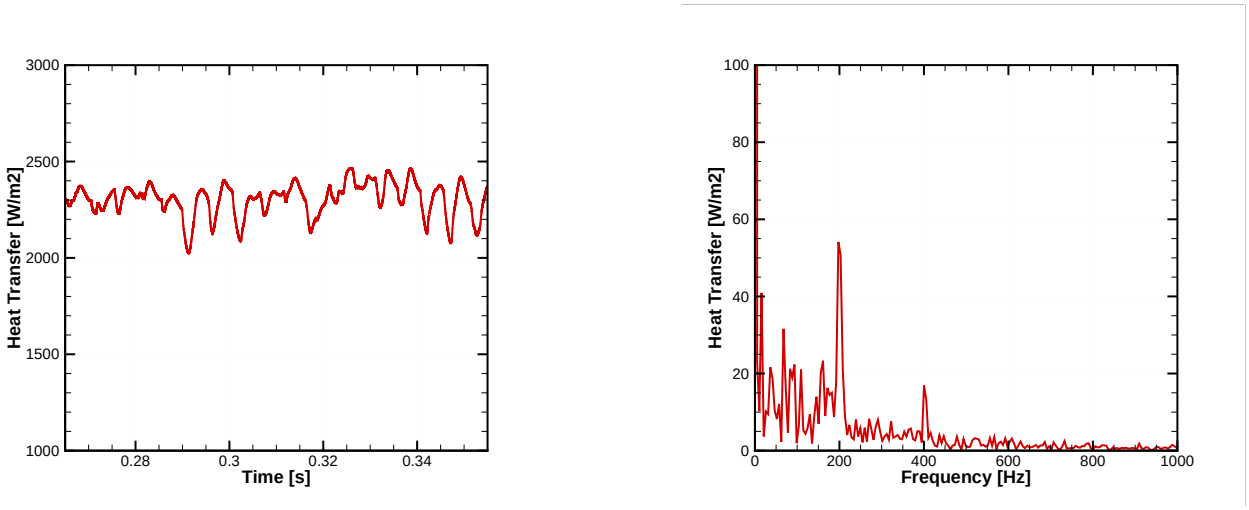

(a) (b)

Figure 6.4.29: Calculated heat release over the time for detailed chemistry case (a). FFT of the unsteady heat transfer to the wall (b)

6.4.2.3 Gas-Phase Temperature: numerical results comparison against measurements

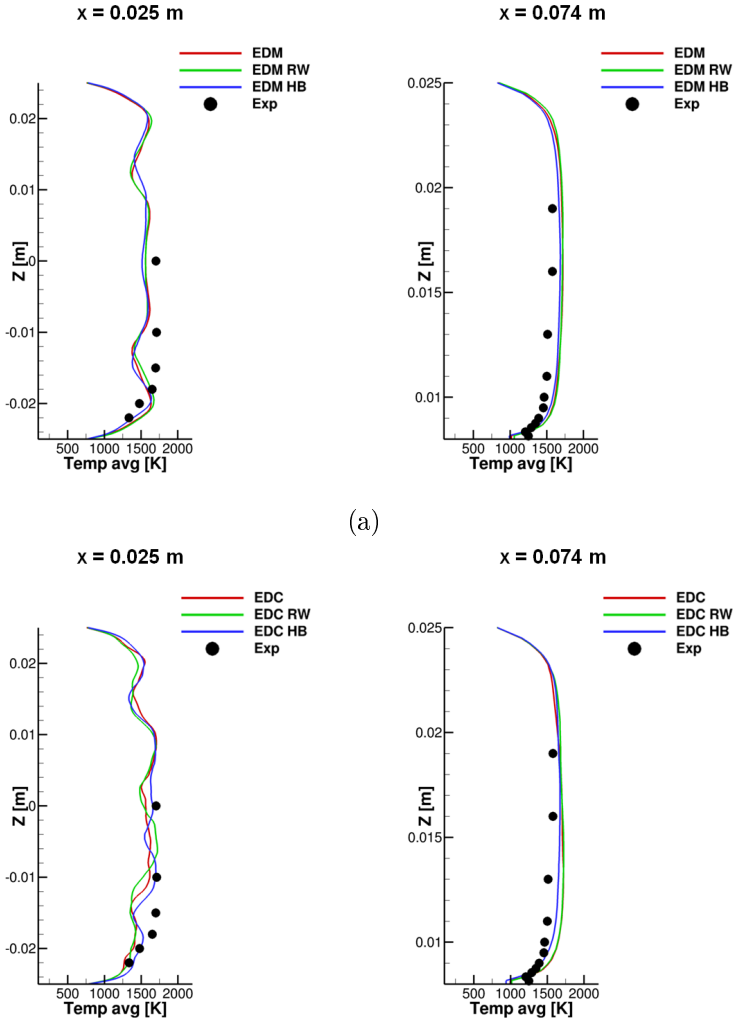

(a)

(b)

Figure 6.4.30: Averaged temperature profiles at x=0.025m and x=0.074m for global chemistry calculation (a) and detailed chemistry calculation (b). In red line simulation performed with the combustion model (*EDM* or *EDC*), in green line in conjunction with the *RW* model, in blue with the *HB* thermal model and in dot experimental data.

For validating the simulations, gas-phase temperature values were taken experimentally through the CARS technique at different locations downstream of the bluff body. The two planes considered for the measurements were $x = 0.025$ m and $x = 0.074$m. The first position is located in the middle between the probe tip and the bluff body, where a large recirculation zone is observed. The second one is placed in the downstream region with the intent to measure the thermal boundary layer near the wall of the thermo-element. A

numerical comparison of the time-averaged temperature is shown in Fig. 6.4.30.a and Fig. 6.4.30.b, respectively for global and detailed chemistry. The simulations plotted refer to the calculation with the combustion model (EDM or EDC), to the computation in conjunction with the RW wall model and to the run together with the HB thermal model. A qualitatively good agreement was found for all of the simulations at both the positions. Furthermore, phase-averaged data were also recorded at the same locations for showing the change of the temperature field over one cycle of the limit-cycle oscillation. The plots, related to eight temperature phases, are illustrated in Fig. 6.4.31 and Fig. 6.4.32 for $x = 0.025$ m and $x = 0.074$. The numerical simulations present again a fairly good accordance regarding to the experimental data.

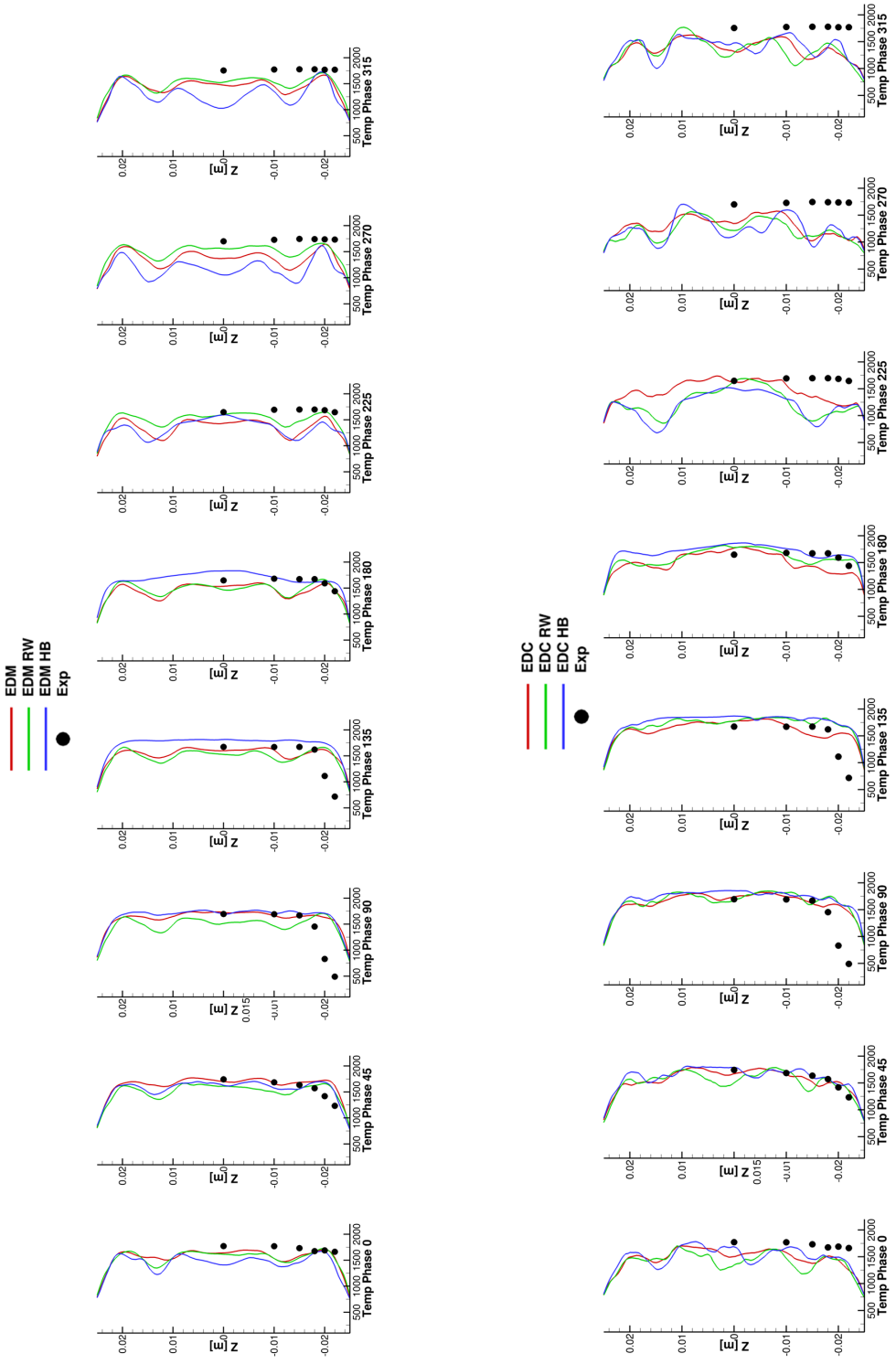

Figure 6.4.31: Phase averaged temperature profiles at x=0.025m for global chemistry calculation (a) and detailed chemistry calculation (b). In red line simulation performed with the combustion model (*EDM* or *EDC*), in green line in conjunction with the *RW* model, in blue with the *HB* thermal model and in dot experimental data.

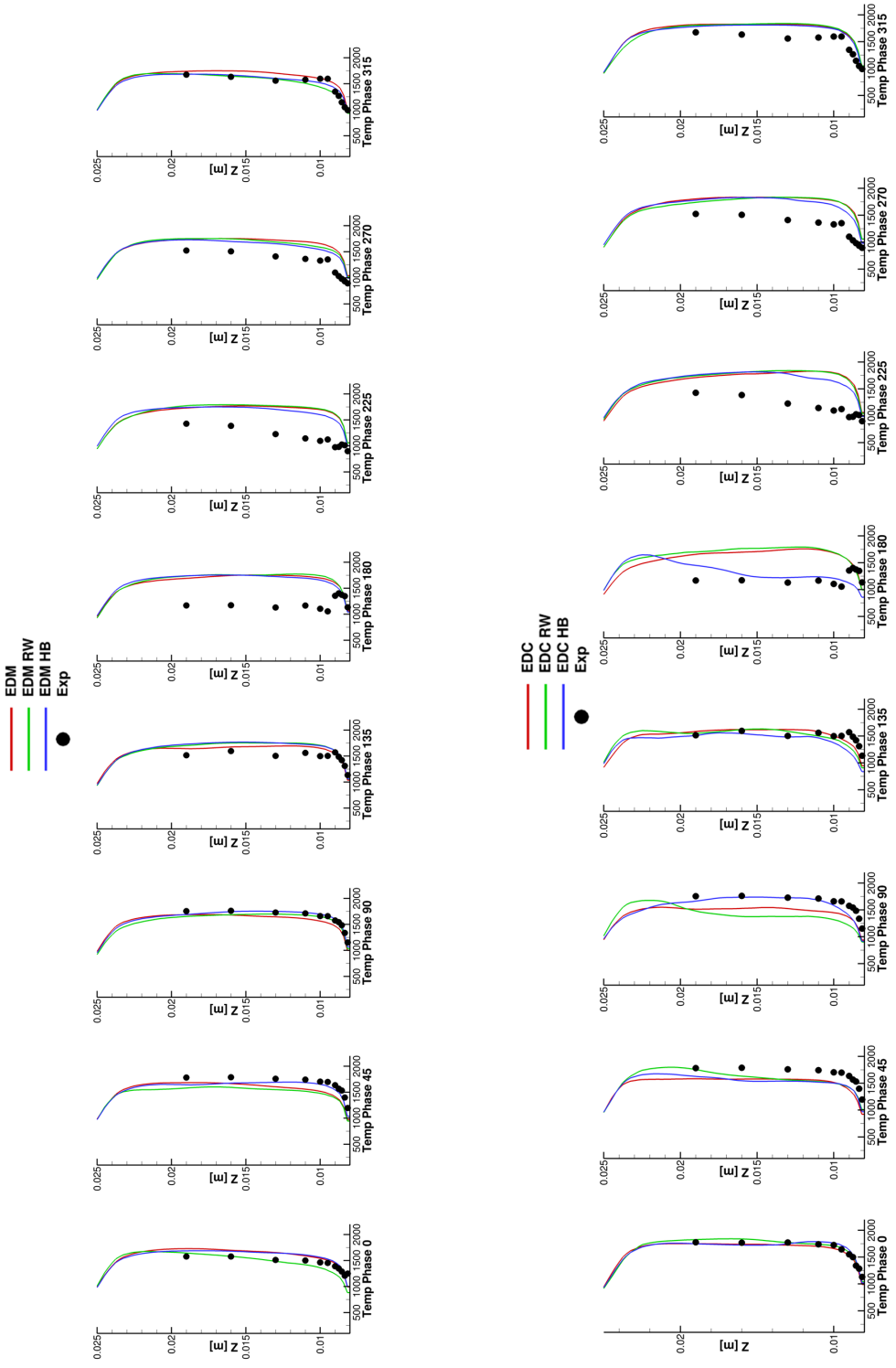

(a) (b)

Figure 6.4.32: Phase averaged temperature profiles at x=0.074m for global chemistry calculation (a) and detailed chemistry calculation. In red line simulation performed with the sole combustion model (*EDM* or *EDC*), in green line in conjunction with the *RW* model, in blue with the *HB* thermal model and in dot experimental data.

6.4.3 Stable case with $\lambda = 1.45$ (Case 5)

The operating condition $\lambda = 1.45$ at thermal power of 36kW leads to a stable burning regime, characterized by a long flame. For this case, no thermo-acoustic oscillations were observed in the burner, since the FFT of the pressure signal reveals an energy spectrum without any relevant peak. Numerically unsteady simulations were performed with the SST-SAS turbulence model in conjunction with different combustion models: Eddy Dissipation Model (EDM), Eddy Dissipation Concept Model (EDC), Finite Rate Chemistry Model for laminar flame (FRC), Joint-presumed PDF model (JPDF). Fuel chemistry was modeled with two different chemical kinetic mechanisms: a 2-step global mechanism Nicols et al.[78] (global chemistry approach) and a 19-species chemistry mechanism DRM-19 [79], reduced from the GRI-3.0 mechanism [69] (detailed chemistry approach). At the inlet a constant mass flow was prescribed providing a mixture with $\lambda = 1.45$. At the outlet standard pressure outlet condition was imposed since no acoustic interaction was observed experimentally [1] The thermal boundary conditions consider adiabatic walls in the plenum region , isothermal wall with $T_w = 700$K both for the probe wall and the side walls in the combustion chamber (see Fig.6.4.6). The computations were initialized by a RANS solution and were calculated for more than seven residence times. After a duration of two residence times, the averaging phase of the numerical solution was activated. The time-averaged solution was obtained considering a physical time span of five residence times.

The main aim of the calculations was focusing on the determination of the reaction zone and testing the accuracy of the combustion models against the time-averaged OH*. As mentioned, the computations were performed using both global and detailed chemistry and the results are reported in Fig. 6.4.33.

The EDM model is able to predict the same shape for the reaction zone as the experiments, presenting however deviations in the position of the maximum heat release. According to the simulation, the latter is located approximately at 20 cm above the bluff body. The OH* (CL) image presents instead, a strong intensity of the radial OH* between x=5 and x=15 cm, indicating that the burning process extends for a large portion of the combustor. This discrepancy in detecting the right zone interested by reactions motivated the investigation of the test case with detailed chemistry models. The first calculation was performed neglecting the turbulent-chemistry interaction using the Finite Rate Chemistry Model. The result is presented in Fig. 6.4.33.b, and represents a worsening of the EDM due to the reduction

[1] Under these conditions, simulations were performed with an incompressible solver using the THETA code. THETA was in fact developed initially as incompressible solver, where pressure and density variations were decoupled. Density could vary only due to temperature and mixture modifications but not due to pressure fluctuations. Practically speaking, this results in an infinite propagation of the pressure perturbations inside the domain that does not permit the calculation of any thermo-acoustic instabilities.

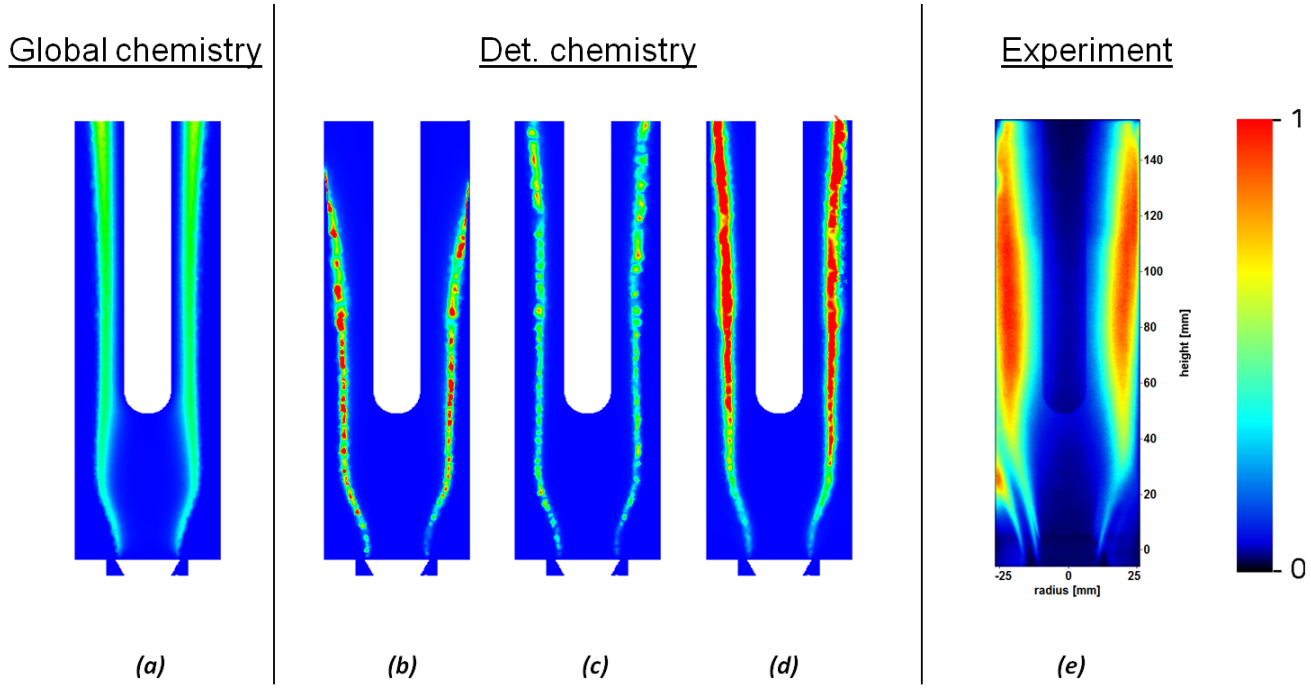

Figure 6.4.33: Time averaged images for the measured OH* chemiluminescence (CL) and the simulated heat release with detailed chemistry under a stable flame regime ($\lambda = 1.45$). (a) Simulation with Eddy Dissipation Model for global chemistry, (b) Finite Rate Chemistry Model, (c) Joint-presumed PDF model, (d) Eddy Dissipation Model for detailed chemistry and (e) experimental data.

in the flame length. This indicates the strong influence of the turbulence in such a kind of flame. As a consequence, the JPDF model was used and the result is showed in Fig. 6.4.33.c: this provides a flame length comparable with that of the experiments but underestimates the intensity of the chemical reactions in the region where the OH* image presents the strongest signal. A further computation was performed with the Eddy Dissipation Model for detailed chemistry (EDC), Fig. 6.4.33.d. The heat release distribution predicted by the model is in great accordance with the OH* image. In this case both the flame length and intensity of the chemical reactions are reproduced very well. The latter model delivers therefore the best result in terms of accuracy against the experiments with respect to the all other combustion models employed for the simulations.

7 Conclusion

In this work an investigation on lean-premixed combustion for various model combustors was conducted. The regime of lean-premixed combustion is nowadays one of the most promising approaches to reduce the pollutant emission. However, lean premixed flames are prone to the so-called thermo-acoustic instabilities. These instabilities can generate high pressure oscillations, which modify the flow field, and drive fluctuations of the heat release. Thermo-acoustic instabilities are generated as a result of the closed feedback between acoustics, aerodynamics and combustion [5, 6, 11].

With the intent to accurately predict the dynamics behavior of the combustor under this unstable condition, several numerical turbulent-combustion and thermal models were implemented in the DLR combustion code THETA.

About the combustion models, the validation against experimental data for the "Eddy Dissipation Concept Model" (EDC), the "Fractal Model" (FM) and the "Linear Eddy Mixing" (LEM) is discussed in detail in Chap. 4. The first test-case analyzed is a non-premixed, unconfined, turbulent hydrogen-air flame: the "H3-Flame" [7]. The numerical results of the different combustion models differ only slightly. This is due to the fact that the combustion rates are mainly controlled by the turbulent mixing rather than by the chemical kinetics. A second test case that was considered is a real size gas turbine (GT) combustor. In this burner, the swirl of the flow is responsible for the flame stabilization by forming a central recirculation flow region. A macro-vortex rotating around the central axis of the chamber (the Precessing Vortex Core - PVC) is observed here. This instability increases the mixing and thus, the combustion rate. The numerical simulations with global (EDM) and detailed chemistry model (EDC) are able to predict the mean flow distribution very well, reproducing the inner and outer recirculation zone. For validating the combustion models, the numerical heat release, temperature and species distributions are compared against measurements [21, 75]. The use of global chemistry (EDM) for this testcase leads to visible deviations with respect to the experimental data. Conversely, the detailed combustion model simulations (EDC, FM) provide a better accuracy.

In Chap. 5 a brief overview of the most used thermal models in literature is described. Two models in particular, the AKN_t (Abe, Kondoh, Nagano model [22]) and the HB (Huag and

Bradshaw model [23]), are discussed and validated against the experiments. The aim was to verify the increase of the numerical accuracy in the thermal boundary layer when these models are used under stationary and pulsating flow. These models are tested first in simple heat transfer problems: cavity flow, flow in abrupt expansion and flow with a backward facing step. In all the simulations, the models have allowed to obtain a better estimation of the Nusselt number and a better agreement with the measurements. On the other hand, the computations performed without the thermal model show a consistent discrepancy in the wall heat transfer determination. A further validation is performed considering a pulsating flow with heat transfer [9]. This is done to observe the sensitivity of the model in predicting the heat transfer with the increase of the amplitude of the oscillations. Also in this condition, the thermal model simulations highlight better results with respect to the computation performed without. As a consequence, this model is used in conjunction with the turbulent-combustion model, in Chap. 6, for evaluating the wall heat transfer under thermo-acoustic instabilities.

In Chap. 6, a numerical analysis of the thermal field in the LIMOUSINE model combustor [5, 6, 11, 12] under stable and unstable conditions is considered. Three operative conditions ($\lambda = 1.20$, $\lambda = 1.30$, $\lambda = 1.45$) are simulated. The combustor exhibits an unstable behavior in the range of the air excess ratio λ from 1.20 to 1.30 at a thermal power of 36 kW with a dominant frequency of about 150 - 181 Hz. On the other hand, the leanest condition $\lambda = 1.45$ is a stable condition characterized by a turbulent flame. For the case with $\lambda = 1.20$, several simulations with various thermal boundary conditions (considering different wall temperature values T_w) using the *EDM* model are performed. This investigation has shown different acoustic behavior in function of the prescribed wall temperature T_w and significant deviations with respect to the experimental data. As a consequence, a computation using detailed chemistry with the *EDC* combustion model is carried out. This calculation reveals an improvement in the estimation of the acoustic characteristics compared to the case with the *EDM*. Experimentally a frequency of 181 Hz is observed, the calculated frequencies are 185 Hz with the *EDC* and about 250 Hz with the *EDM*. A good agreement is found also for the amplitude at the fundamental frequency: the *EDC* simulation indicates amplitude values of 3900 Pa at Mic1, whereas in the experiments an amplitude of 4630 Pa was measured.

A second operative condition that was experimentally and numerically investigated is at $\lambda = 1.30$. In this case, the flame regime is unstable but presents a significant lower amplitude (almost half of the previous case) for the thermo-acoustic oscillations. This has allowed to perform temperature measurements by CARS. The dynamics behavior of the flame resembles the condition with $\lambda = 1.20$, with a pulsating flame confined in the lower part of the burner. In order to determine an accurate numerical solution of the acoustics of the burner, this is investigated both with global and detailed chemistry. Simulations with the thermal model

HB (see chap. 5) and the real wall approach *RW* (see chap. 6) are also performed. For this operative condition, the best agreement with the measurements is found with the EDC model using detailed chemistry, which presents a deviation with respect to the acoustic frequency of only 20%. If the *EDC* model is coupled with the *HB* or *RW* method, the results are even better, with a reduction of error to 13%. The main reason for this improvement is demonstrated in this work and lies in the high sensitivity of the acoustic results with the thermal boundary conditions imposed (see paragrah 6.XX, 6.XX). Furthermore, it is also shown in Chap. 5 that such thermal models are capable of resolving the unsteady heat flux in the boundary layer during thermo-acoustic instabilities as well. As a consequence, their use in conjunction with the turbulent-combustion model using detailed chemistry leads to an improvement of the numerical results.

The operating condition $\lambda = 1.45$ leads to a stable burning regime, characterized by a long turbulent flame. For this case, no thermo-acoustic oscillations are observed in the burner, since the fluctuating heat release is out of phase with the pressure oscillations and conditions are not right for feeding energy into the system. The flame is influenced only by the turbulent unsteadinesses, generated by the sharp edges of the bluff body geometry. Since OH* chemiluminescence (CL) were also taken for this stable case, it was worth to validate again the combustion models with global and detailed chemistry (*EDM*, *FRC*, *JPDF*, *EDC* respectively) against the experimental data. The best agreement is found with the *EDC* model, showing a great accordance for the predicted flame length and the zone where the chemical reactions occur.

The main conclusions that can be drawn for an efficient simulation during thermo-acoustic instabilities are:

- the use of global chemistry shows a significant over-prediction of the resonance frequency;
- detailed chemistry combustion models are able to provide an improvement in the estimation of the acoustic characteristics compared to the models with global chemistry. This is due to the fact that the heat release calculated by detailed chemistry is much more accurate and as a consequence the acoustics of the combustor is better predicted.
- the acoustic characteristics are very sensitive to the thermal boundary conditions;
- thermal models (see chap. 5) are capable of resolving the unsteady heat flux in the boundary layer also during thermo-acoustic instabilities. The use of these models in conjunction with detailed chemistry leads to better results in terms of wall temperature and acoustic characteristic.

Bibliography

[1] S.B. Pope. *Turbulent Flows.* Cambrige University Press. 2000.

[2] S. Vaidyanathan. *Sub-grid Combustion Modeling for Compressible Two-Phase Reacting Flows.* PhD thesis, School of Aerospace Engineering. Georgia Tech Istitute, 2003.

[3] B. Muehlbauer. *Numerische Simulation von Verbrennungslaerm.* PhD thesis, Stuttgart University, 2012.

[4] T. Lieuwen and V. Yang. *Combustion instabilities in gas turbine engines. operational experience, fundamental mechanisms and modeling.* In Prog. in Astronautics and Aeronautics AIAA, Volume 210. 2005.

[5] Alemeda J. Casado and J. Kok. *Combustion dynamics coupled to structural vibration.* The 17th Internation Congress On Sound and Vibration. 2010.

[6] J.Kok S.Kumar, P.R.Alemela. *Dyanmics of a flame stabilized bluff body in part. Premixed.* Asme GT2011-46241. 2011.

[7] B. Noll M. Aigner A. Filosa, M. Di Domenico. Numerical simulation of non-premixed, turbulent hydrogen-air flame using an extension of the linear eddy mixing model. *Proceedings. 6th European Combustion Meeting (ECM), 25.-28.06.2013, Lund, Sweden.*, 2013.

[8] A. Filosa, B. Noll, M. Di Domenico, and M. Aigener. Numerical investigations of a low emission gas turbine combustor using detailed chemistry. *50th AIAA/ASME/SAE/ASEE Joint Propulsion Conference, 28.-30.07.2014, Cleveland (USA).*

[9] Y. Ishino, M. Suzuki, T. Abe, N. Ohiwa, and S. Yamaguchi. Flow and heat transfer characteristics in pulsating pipe flows. *Heat Transfer-Japanese Research. 25(5)*, 1996.

[10] Ann P. Dowling. *The challenges of lean premixed combustion.* Proc. International Gas Turbine Congress. 2003.

[11] J. Casado Tufano S. and J. Kok. *Combustion instabilities in gas turbine engines. operational experience, fundamental mechanisms and modeling.* Asme GT2012-69501. 2012.

[12] I. Hernandez. Les and acoustics analysis of the thermoacoustics instab. *3rd Colloquium INCA. Toulouse.*, 2012.

[13] M.Soundhaus. Über die schallschwingungen der luft in erhitzten glasrohren und in gedeckten pfeifen von ungleicher weite. *Pogendorff's Annalen der Physik und Chemie, vol. 79, pages 1-34.*, 1850.

[14] B. Rayleigh J W. Sturtt. *The Theory of Sound.* ed New York, New York: Dover Publications , 230-231. 1945.

[15] I.R.Gran and B.F.Magnussen. *A numerical study of a bluff-body stabilized diffusion flame. part 2. influence of combustion modeling and finite-rate chemistry.* Combustion Science and Technology.119. 1996.

[16] H.Schütz R.Lückerath B.Noll and M.Aigner. Complex chemistry simulation of flox®-'flameless oxidation' combustion. *International Journal on Energy for a Clean Environment,Volume 8, Number 3, 2007, pp. 239-259*, 2007.

[17] V. Battaglia E. Giacomazzi and C. Bruno. *The coupling of turbulence and chemistry in a premixed bluff-bosy flame as studied by LES.* Combustion and Flame, 138:320 – 335. 2004.

[18] E. Giacomazzi . *Modellistica e simulazione della combustione turbolenta.* PhD thesis, University of Rome. 1999.

[19] http://www.cantera.org/docs/sphinx/html/index.html.

[20] Gerlinger. P Aigner M. Fioliktatis A., Ess P. *Transported PDF Calculations of a Turbulent, Non-Premixed, Non-Piloted, Hydrogen-Air Flame with Differential Diffusion.* AIAA paper 2012-0179. 2012.

[21] W. Meier R.Sadanandan M. Stöhr U.Stopper, M. Aigner and S. Kim. *Flow field and combustion characterization of premixed gas turbine flames by planar laser techniques.* ASME Conference Proceedings. 2008(43130):419–429. 2008.

[22] Y.Nagano and C.Kim. *A two equation model for heat transport in wall turbulent shear flows.* J.Heat Trassfer 110, 583-589. 1988.

[23] P. G. Huang and P. Bradshaw. *Law of the wall for turbulent flows in pressure gradients.* AIAA Journal. Vol. 33, 624-632. 1995.

[24] Karima Khusnutdinova. *Mathematical Reviews Seminar.* Department of Mathematical Sciences, Loughborough University, UK. 2009.

[25] David C. Wilcox. *Turbulence Modeling for Cfd.* DCW Industries, Incorporated. 1994.

[26] Osborne Reynolds. *On the Dynamical Theory of Incompressible Viscous Fluids and the Determination of the Criterion.* Philosophical Transactions of the Royal Society of London. A, v. 186. 1895.

[27] J. Boussinesq. *Théorie de l'écoulement tourbillant.* N°XXIII-46, 1877.

[28] T. Saad. *Turbulence modeling for beginners.* Lectures Notes. University of Tennesee. 2009.

[29] W.P. Jones and B.E. Launder. *The prediction of laminarization with a two-equation model of turbulence.* Int. J. Heat Mass Transfer, 15:301–314. 1972.

[30] E. Launder and B.I. Sharma. *Application of the energy-dissipation model of turbulence to the calculation of flow near a spinning disc.* Letters Heat Mass Transfer, 1(2):131–138. 1974.

[31] PV Lanspeary RC Morgans BB Dall, GJ Natha. *Application of the revised Wilcox k-omega Turbulence.* Second International Conference on CFD in the Minerals and Process Industries. 1998.

[32] F.M. White. *Viscous fluid flow.* McGraw-Hill. 1991.

[33] Santiago Beatove. *Computation Fluid Dynamics: Slide on Turbulent Boundary Layer.* 2000.

[34] D. Panara. *Boundary Layer Response to Combustion Instabilities and Associated Heat Transfer.* Phd thesis, University of Stuttgart. 2010.

[35] F. R. Menter. *Influence of freestream values on k-omega turbulence model predictions.* AIAA Journal (Impact Factor: 1.08). 07/1992; DOI:10.2514/3.11115. 1992.

[36] F. R. Menter. *Two-Equation Eddy-Viscosity Turbulence Models for Engineering Applications.* AIAA Journal, Vol. 32, No. 8, pp. 1598-1605. 1994.

[37] M. Kuntz F.R. Menter and R. Langtry. *Ten Years of Industrial Experience with the SST Turbulence Model.* In Turbulence, Heat and Mass Transfer 4. Bergell House. 2003.

[38] Schlichting H. Gersten K. *Boundary Layer Theory.* Springer; 8th edition (March 22, 2000). 2000.

[39] F. R. Menter and Y. Egorov. *A scale-adaptive simulation model using two-equation models.* AIAA Paper 2005-1095. 2005.

[40] F.R.Menter and Y.Egorov. *Advances in Hybrid RANS-LES Modeling, chapter Development and application of SST-SAS turbulence model in the DESIDER project.* Springer Verlag Beriln Heidelberg. 2007.

[41] Leonard A. *Energy cascade in large-eddy simulations of turbulent fluid flows.* Advances in Geophysics. 1974.

[42] F. Nicoud F. Ducros and T. Poinsot. *Numerical Methods for Fluid Dynamics VI., chapter Wall adapting local eddy-viscosity models for simulations in complex geometries.* Oxford University Computing Laboratory, Wolfson Building, Parks Road, Oxford. 1998.

[43] Franz Joos. *Technische Verbrennung.* Springer-Verlag Berlin Heidelberg. 2006.

[44] Fluent-ansys manual, 2000.

[45] B.F. Magnussen and B.H. Hjertager. *On mathematical modelling of turbulent combustion with special emphasis on soot formation and combustion.* In Proceedings of the 16th International Symposium on Combustion, pages 719–729. The Combustion Institute. 1976.

[46] D.B.Spalding. *Mixing and chemical reaction in steady confined turbulent flames.* In 13th Symp. (Int'l.) on Combustion. The Combustion Institute. 1970.

[47] Felsch C. *Investigation of Boundary Conditions and Pressure Waves in Numerical Modelling of Compressible Turbulent Flow with Combustion.* Master Thesis, Norwegian University of Science and Technology. 2003.

[48] S.A.Orszag V.Yakhot W.S.Flannery F.Boysan D.Choudhury J.Maruzewski and B.Patel. *Renormalization group modeling and turbulence simulations.* International Conference on Near-Wall Turbulent Flows. 2003.

[49] M. Di Domenico. *Numerical Simulation of Soot Formation in Turbulent Flows.* Phd thesis, University of Stuttgart. 2008.

[50] P .Gerlinger. Investigation of an assumed pdf approach for finite-rate chemistry. In *AIAA Paper, 2002-0166.*, 2002.

[51] P.Gerlinger B.Noll and M.Aigner. *Assumed PDF modelling and PDF structure investigation using finite-rate chemistry.* Progress in Computational Fluid Dynamics,5:334-344. 2005.

[52] S .Girimaji. Assumed *beta*-pdf model for turbulent mixing: Validation ad extension to multiple scalar mixing. In *Combustion Science and Technology, Vol. 78, pp. 177–196*, 1991.

[53] A.N. Lipatnikov V.L. Zimont. Chem. Phys. Reports 14 (7) 993-1025. 1995.

[54] *Ansys Manual: Introduction to CFX.* 2000.

[55] I.Porumbel and S. Menon. Large eddy simulation of bluff body stabilized premixed flame. *AIAA paper 2006-152*, 2006.

[56] S. Menon T.M. Smith. One-dimensional simulations of freely propagating turbulent premixed flames. *Combustion Science and Technology, 128:1, 99 -130*, 1999.

[57] O. Stein. Large eddy simulation of combustion in swirling and opposed jet flows. *PhD thesis, Imperial College London*, 2009.

[58] A.R. Kerstein. Linear eddy modeling of turbulent transport ii. *Combustion and Flames, Vol 75, pp 397-413.*, 1989.

[59] Di Domenico M. *Numerical Simulations of Soot formation in Turbulent Flows.* PhD thesis, University of Stuttgart. 2007.

[60] *ANSYS CFX solver manager user's guide.Release 14.0.* 2011.

[61] E. Ivanova. *Numerical Simulations of Turbulent Mixing in Complex Flows.* Phd thesis, University of Stuttgart. 2012.

[62] J. D. Lambert. *Numerical Methods for Ordinary Differential Systems.* New York: Wiley. 1992.

[63] F. Creta. *Computational Methods In Chemical Kinetics Reduction And Analysis For Combustion Modeling And Applications To Hydrocarbon System.* PhD thesis, University of Rome, Italy, 2005.

[64] S .D. Cohen and A. C. Hindmarsh. Cvode, a stiff/nonstiff ode solver in c. In *Computers in Physics, 10(2), pp. 138-143.*, 1996.

[65] S .H. Lam and D. A. Goussis. The csp method for symplifying kinetics. In *International Journal of Chemical Kinetics, vol. 26, pp. 461-486*, 1994.

[66] A. Filosa. *Analisi di ignizione di propellenti liquidi per LRE.* Master Thesis, Universita Roma La Sapienza. 2009.

[67] Alan C. Hindmarsh and Radu Serban. *User Documentation for cvode v2.7.0.* Center for Applied Scientific Computing Lawrence Livermore National Laboratory. 2012.

[68] R.A.Yetter F.L.Dryer and H.Rabitz. *Comb. Sci. Tech., vol. 79, pp. 97-128.* 1991.

[69] http://www.me.berkeley.edu/gri-mech/version30/text30.html.

[70] J.M. Simmie W.J. Pitz C.K. Westbrook. M. O conaire, H.J. Curran. *A comprehensive Modeling Study of Hydron Oxidation.* Int. J. Chemical Kinetics 36, no. 11, 603-622. 2004.

[71] Prucker S. Cao M.-H. Meier, W. and W. Stricker. *Characterization of Turbulent H2/N2/Air Jet Diffusion Flames by Single-Puls Spontaneous Raman Scattering.* Combustion Science and Technology, Vol. 118, 293-312. 1996.

[72] T. Coffee and J. Heimerl. *Transport Algorithms for Premixed Laminar Steady State Flames.* Combustion and Flame, Vol. 43, 1981, pp. 273-289. 2004.

[73] B.E. Lauder and D.B. Spalding. *The Numerical Computation of Turbulent Flows.* Computer Methods in Applied Mechanics and Engineering. 269-289. 1974.

[74] S .B. Pope. An explanation of the turbulent round—jet/plane-jet anomaly. In *AIAA Journal, Vol. 16, No. 3, pp. 279-281.*, 1978.

[75] W. Meier R.Sadanandan-M. Stöhr U.Stopper, M. Aigner and S. Kim. *Flow field and combustion characterization of premixed gas turbine flames by planar laser techniques.* Journal of Engineering for Gas Turbines and Power, 131(2):021504. 2009.

[76] M. Stöhr U.Stopper, R.Sadanandan and alia. *TurChemi: Final Report.* Internal DLR report. 2009.

[77] Siemens Industrial Turbomachinery Ltd 2010. *Mesh Details-TurChemi.* Internal report. 2010.

[78] A. J. Hamer R. J Roby D. G. Nicol, P. C. Malte and R. C. Steele. Development of a five-step global methane oxidation-no formation mechanism for lean- premixed gas turbine combustion. *Journal of Engineering for Gas Turbines and Power*, 1999.

[79] http://www.me.berkeley.edu/drm.

[80] Y. Huang and V. Yang. *Effect of swirl on combustion dynamics in a lean-premixed swirl-stabilized combustor.* Proceedings of the Combustion Institute, V.30, 1775–1782. 2005.

[81] S .Pope. Ten questions concerning the large-eddy simulation of turbulent flows. In *New Journal of Physics 6, 35*, 2004.

[82] A.J. Marquis. G. Bulat, W.P. Jones. *NO and CO formation in an industrial gas-turbine combustion chamber using LES with the Eulerian sub-grid PDF method.* Combustion and Flames: article in press. 2014.

[83] L.V Krishnamoorthy and R.A. Atonia. *Temperature dissipation measurements in a turbulent boundary layer.* J.Fluid Mech. Vol. 176, pp. 265-281. 1987.

[84] R.A. Atonia. *Behavior of the turbulent Prandtl number near the wall.* Int. J. Heat Mass Transfer, 23, pp. 906-908. 1980.

[85] B. E. Launder. *Heat and mass transport.* Topics in Applied Physics, 232-287. Springer-Verlag, Berlin – Heidelberg, 1976.

[86] G. Scheuerer V. C. Patel, W. Rodi. *Turbulence Models for Near-Wall and Low-Reynolds- Number Flows: A Review.* AIAA Journal; 23, S. 1308-1319. 1985.

[87] C. K. G Lam and K. A. Bremhorst. *Modified form of the k-eps Model for predicting wall turbulence.* Journal of Fluids Engineering, Vol. 103, pp 456-460. 1981.

[88] Y. Nagano K. Abe, T. Kondoh. *A new turbulence model for predicting fluid flow and heat transfer in separating and reattaching flows-II. Thermal field calculations.* International J. Heat Mass Transfer. Vol 38, pp. 1467-1481. 1994.

[89] Kondoh T. Abe, K. and Nagano. *A new turbulence model for predicting fluid flow and heat transfer in separating and reattaching flows – 1. Flow field calculations.* Int .J. Heat and Mass Transfer. Vol.37, No.1, pp. 139 -151. 1994.

[90] Y.G. Lai T.P. Sommer, R.M.C. So. *A Near-Wall Two Equation Model for Turbulent Heat Fluxes.* Internation J.Heat Mass Transfer. Vol.35-12, 3375-3387. 1992.

[91] B. E. Launder G. R. Newman and J. L. Lumley. *Modelling the behaviour of homogeneous scalar turbulence.* J. Fluid Mech. Vol.111, 217-232. 1992.

[92] W. Wu B. Deng and S. Xi. *A near-wall two-equation heat transfer model for wall turbulent flow.* Int. J. Heat Mass Transfer. Vol. 44, 691-698. 2001.

[93] G. Iaccarino A. Ooi and M. Behnia. *Heat transfer predictions in cavities.* Center for Turbulence Research Annual Research Briefs. 1998.

[94] D.E. Metzger, R.S.Bunker, and R.K.Chyu. *Cavity Heat Transfer on a Transverse Grooved Wall in a Narrow Flow Channel.* Journal Heat Transfer. Vol. 111, 73-79. 1989.

[95] P. Momeni. *Modelling the effect of the pulsation on flow and heat transfer in turbulent separated and reattaching flows.* University of Manchester. 2008.

[96] J. W. Baughn, B. E. Launder, M. A. Hoffman, and R. K. Takahashi. Local heat transfer downstream of an abrupt expansion in a circular channel with constant wall heat flux. *J. Heat Transfer. Vol. 106(4), 789-796*, 1984.

[97] W.D. Hsieh and K.C. Chang. *Calculation of wall heat transfer in pipe expansion turbulent flows.* International Journal of Heat and Mass Transfer. Vol. 39(18), 3813-3822. 1996.

[98] J. P. Johnston E. W. Adams and J. K. Eaton. Experiments on the structure of turbulent reattaching flow. *Tech. Report MD-43, Stanford University*, 1984.

[99] J. C. Vogel and J. K. Eaton. *Combined Heat Transfer and Fluid Dynamic Measurements Downstream of a Backward-Facing Step.* J. Heat Transfer. Vol. 107(4), 922-929. 1985.

[100] S. de B. Alves. Review of numerical methods for compressible flow equations at low mach numbers. In *XII Computational Modelling Meeting - EMC, Rio de Janeiro*, 2009.

[101] F. Belblidia I.J. Keshtiban and M.F. Webster. Compressible flow solvers for low mach number flows - a review. In *Online Report-http://www.cs.swan.ac.uk/reports/yr2004/CSR2-2004.pdf*, 2004.

[102] V. Moureau, C. Bérat, and H. Pitsch. An efficient semi-implicit compressible solver for large-eddy simulations. volume 226, pages 1256 – 1270, 2007.

[103] E. Turkel. Preconditioned methods for solving the incompressible and low speed compressible equations. *Journal of Computational Physics*, 72(2):277 – 298, 1987.

[104] W. Lee B. Va and P. Roe. Characteristic time-stepping or local preconditioning of the euler equations. *AIAA Journal-10th Computational Fluid Dynamics Conference*, 91:260 – 282, 1991.

[105] C.L. Merkle Y. Choi. Time-derivative preconditioning for viscous flows. *AIAA Technial Paper 91-1652*, 1991.

[106] C.L. Merkle Y. Choi. The application of preconditioning in viscous flows. *Journal of Computational Physics*, 105(2):207 – 223, 1993.

[107] F.H. Harlow and A.A. Amsden. A numerical fluid dynamics calculation method for all flow speeds. *Journal of Computational Physics*, 8(2):197 – 213, 1971.

[108] S.Y. Yoon and T. Yabe. The unified simulation for incompressible and compressible flow by the predictor-corrector scheme based on the cip method. *Computer Physics Communications*, 119(2):149 – 158, 1999.

[109] R. Codina M. Vázquez P. Ortiz O.C. Zienkiewicz, P. Nithiarasu. The characteristic-based-split procedure: an efficient and accurate algorithm for fluid problems. *International Journal for Numerical Methods in Fluids*, 31(1):359–392, 1999.

[110] J.M. Lourier. *Numerische Simulation von thermoakustischen Instabilitäten in Gasturbinenbrennkammern mithilfe von Impedanzrandbedingungen.* PhD thesis, University of Stuttgart, 2016.

[111] A.J. Chorin. Numerical solution of the navier-stokes equations. *Mathematics of Computation*, 22:745–762, 1968.

[112] E. C. Fernandes and M. V. Heitor. *Unsteady flames and the Rayleigh criterion.* Unsteady Combustion (Dordrecht, the Netherlands: Kluwer Academic Publishers. 1996.

[113] M. Shashi. *Modelling of Complex Physics and Combustion Dynamics in a Combustor with a Partially Premixed Turbulent Flame.* PhD thesis, Twente University, 2014.

[114] M. Heckl A. Neuber G. Krieger E. Hassel and J. Janicka. the rijke tube: A green's function approach in the frequency domain. *Acta Acustica united with Acustica*, 96(4):pp. 743–752, 2010.

[115] I. Hernandez. *Soot modeling in flames and Large-Eddy Simulations of thermo-acoustic instabilities*. PhD thesis, Toulouse University, 2011.

[116] A.Filosa B.Noll M.Aigner J.Kok M.Shahi. Numerical studies of unsteady heat transfer with thermoacoustics oscillations. *International Congress on Sound and Vibration.*, 2013.

[117] S .W. Allison and G. T. Gillies. Remote thermometry with thermographic phosphors: instrumentation and applications. In *Rev. Sci. Instrum*, 1997.